

UNIVERSITY OF BIRMINGHAM

NANOPARTICLE-BASED FORMULATION FOR THE TREATMENT OF OSTEOARTHRITIS: A TRIBOLOGICAL STUDY

By

Konstantina Simou

A thesis submitted to

the University of Birmingham

for the degree of

DOCTOR OF PHILOSOPHY

School of Chemical Engineering

The University of Birmingham

May 2022

UNIVERSITY OF
BIRMINGHAM

University of Birmingham Research Archive

e-theses repository

This unpublished thesis/dissertation is copyright of the author and/or third parties. The intellectual property rights of the author or third parties in respect of this work are as defined by The Copyright Designs and Patents Act 1988 or as modified by any successor legislation.

Any use made of information contained in this thesis/dissertation must be in accordance with that legislation and must be properly acknowledged. Further distribution or reproduction in any format is prohibited without the permission of the copyright holder.

ABSTRACT

Osteoarthritis is an incurable disease, which deteriorates the lubrication of the joints, resulting in pain and progressive loss of mobility. A tribological intervention mechanism was established in this thesis to address osteoarthritis development.

The effect of patients' physical characteristics on the lubrication properties was established from the analysis of osteoarthritic synovial fluid samples. Age above 60 years and Body Mass Index above 30 (obesity) were identified as the dominant risk factors resulting in the degeneration of synovial fluid, and thus, the development of osteoarthritis. Synovial fluid's viscosity decreased by 58% with age and 38% with BMI, while the shear-thinning index increased by 40% and 7%, respectively. The adhesion energy, which is positively correlated to the coefficient of friction, increased by 172% with age and 234% with Body Mass Index.

Nanoparticle-based formulations were evaluated to remedy the poor lubrication of osteoarthritic joints. The proposed formulations could be delivered to the pathological joints via intra-articular injection, the most effective treatment at the early stages of osteoarthritis. Nevertheless, the current supplements used in intra-articular injection therapy are unable to provide lubrication improvement under low velocities because they are squeezed out of the joints.

Commercially available silica and latex nanoparticles were used to prove the principle that nanoparticles can improve the tribological performance when used on contact surfaces simulating the natural and artificial joint's contacts. Silica and latex nanoparticles reduced the coefficient of friction by 50.8% and 36.8%, respectively. The

maximum reduction in the coefficient of friction is attributed to its surface polishing by the nanoparticles and was achieved on the rough silicone elastomer. A steel ball-silicone elastomer substrate configuration was used for further testing to replicate the bone-cartilage contact at the beginning of the osteoarthritis when the cartilage is partially removed.

The optimised formulation consisted of 0.5 % w/v biocompatible polymer nanoparticles made of Polymethylmethacrylate, Polycaprolactone, or Polylactic acid dispersed into a 0.1% w/v Hyaluronic acid solution with 0.5% w/v Sodium Dodecyl Sulfate. Nanoparticles reduced the coefficient of friction, owing to the polishing effect. The Hyaluronic acid restored its physiological concentration in the osteoarthritic synovial fluid. Sodium Dodecyl Sulfate enhanced the stability of the formulation by electrostatic interactions. All three biocompatible nanoparticles reduced the coefficient of friction at low velocities. Maximum reduction of the coefficient of friction was achieved at high adsorption of nanoparticles, high Zeta Potential and nanoparticles with low Young's modulus. As a next step, the biocompatible nanoparticles were loaded with a model drug (Celecoxib). The drug-loaded nanoparticle formulations reduced the coefficient of friction of the human articular cartilage by 32%, prolonged the release of the drug up to 9 days, and demonstrated excellent biocompatibility, with 82-86% viability to synovial chondrocytes, highlighting their potential use as intra-articular supplements to treat early osteoarthritis.

ACKNOWLEDGMENTS

First of all, I would like to thank my supervisors Dr Zhenyu J. Zhang and Professor Jon Preece, for their continuous technical and emotional support all those years. Also, I want to thank them for giving me the opportunity to conduct a PhD at their team that changed my professional and personal life.

I want like to thank Dr Simon Jones and his team for providing the synovial fluid, articular cartilage and cells used for my experiments. I would like to thank Piaopiao Pan from the Guangzhou University of Chinese Medicine in China, who synthesised the nanoparticles I used for my experiments. I would also like to thank Bryan Gan from the School of Computer Science at the University of Birmingham, who created a statistical analysis tool to help me explain my experimental data.

I would like to thank Dr Thomas Mills and Professor Karl Dearn for allowing me to use some instruments of their group to complete the experimental part of this thesis. I could not have progressed my thesis so far without their help.

I would like to acknowledge the School of Chemical Engineering for the funding I received that enabled me to pursue my PhD and the postgraduate administration team of the School of Chemical Engineering for the support they provided me all those years.

I would like to thank my family (George, Anna, Dimitra) for inspiring me to pursue this PhD and supporting me all way long.

Finally, a big thank you to my partner Panagiotis for his support during all the difficult times I had during the PhD and for proofreading this thesis. Without him, I would never have managed to overcome the difficulties and be here.

TABLE OF CONTENTS

1. INTRODUCTION 1
1.1 Motivation 1
1.2 Aim and objectives of the project 3
1.3 Thesis layout 4
1.4 Literature review 7
1.4.1 Introduction to tribology 7
1.4.1.1 Working principle of sliding tribometer 8
1.4.1.2 Lubrication regimes 9
1.4.2 Lubricants and lubricant additives 11
1.4.2.2 Nanoparticles 13
1.4.3 Diarhrodial joints 18
1.4.3.1 Articular cartilage 19
1.4.3.2 Synovial fluid 20
1.4.4 Mechanical properties of joints 21
1.4.4.1 Lubrication regimes of joints 21
1.4.4.2 Mechanical properties of articular cartilage 23
1.4.4.3 Rheology of synovial fluid 24
1.4.4.4 Articular cartilage boundary lubrication 24
1.4.5 Osteoarthritis and its effect on the joints 30
1.4.5.1 Factors affecting osteoarthritis 34
1.4.6 Treatment of osteoarthritis 36
1.4.6.1 Intra-articular injection therapy 37
1.5 Summary 45

2. METHODOLOGY 47
2.1 Atomic Force Microscopy 48
2.1.1 Introduction to Atomic Force Microscopy 48
2.1.2 Atomic Force Microscope cantilevers 49
2.1.3 Atomic Force Microscope working principle 51
2.1.4 Imaging modes 52
2.1.5 Force spectroscopy 55
2.2 Tribological testing 59
2.2.1 Mini-Traction Machine 59
2.2.2 High Frequency Reciprocating Rig 61
2.3 Contact mechanics 63
2.4 Rheology 66
2.4.1 Introduction to rheology 66
2.4.2 Steady-state shear rheometry 67
2.4.2.1 Types of shear viscosity 67
2.4.3 Oscillatory rheometry 71
2.4.4 Rheometer working principle 71
2.4.5 Types of rheological tests 73
2.4.5.1 Flow tests 73
2.4.5.2 Viscoelasticity tests 74
2.5 Particles size and Zeta Potential measurements 76
2.5.1 Size measurements - Dynamic Light Scattering 76
2.5.2 Benefits of Dynamic Light Scattering 79
2.5.3 Zeta Potential measurements - Electrophoretic Light Scattering 80

3. INVESTIGATION OF RHEOLOGICAL AND SURFACE PROPERTIES OF OSTEOARTHRITIC SYNOVIAL FLUIDS 84
3.1 Introduction 84

3.2 Materials and methods 88
3.2.1 Materials 88
3.2.2 Methods 89
3.2.2.1 Rheological measurements of synovial fluids 89
3.2.2.2 Surface interactions measurements of synovial fluids 91
3.2.2.3 Statistical analysis 92
3.3 Results and discussion 93
3.3.1 Rheological characterisation of synovial fluids 93
3.3.1.1 Effect of age 98
3.3.1.2 Effect of fat levels and Waist: Hip 100
3.3.1.3 Effect of obesity 102
3.3.1.4 Effect of gender 104
3.3.1.5 Effect of sample origin 104
3.3.1.6 Further statistical analysis 105
3.3.2 Surface interactions of synovial fluids 107
3.3.2.1 Effect of age 109
3.3.2.2 Effect of obesity and Waist: Hip 110
3.3.2.3 Effect of gender 112
3.3.2.4 Effect of sample origin 112
3.3.3 Correlations between rheological and surface properties of synovial fluids 113
3.4 Conclusions 115

4. NANOPARTICLES AS FRICTION MODIFIERS FOR OSTEOARTHRITIC JOINTS 118
4.1 Introduction 118
4.2 Materials and methods 120
4.2.1 Materials 120
4.2.2 Preparation of nanoparticle formulations 121
4.2.3 Surface morphology of substrates 122
4.2.4 Size and Zeta Potential measurements of nanoparticle formulations 122
4.2.5 Viscosity measurements of nanoparticle formulations 123
4.2.6 Contact angle measurements of nanoparticle formulations 124
4.2.7 Tribological measurements of nanoparticle formulations 124
4.2.8 Statistical analysis 126
4.3 Results and discussion 127
4.3.1 Substrates characterisation 129
4.3.2 Nanoparticle formulations characterisation 131
4.3.3 Coefficient of friction of nanoparticle formulations 135
4.3.3.1 Effect of pressure on the coefficient of friction 135
4.3.3.2 Effect of surface characteristics on the coefficient of friction 139
4.3.3.3 Effect of nanoparticle formulations on the coefficient of friction 140
4.3.3.4 Future usage of Machine Learning Analysis tool 148
4.4 Conclusions 150

5. NANOPARTICLE FORMULATION FOR INTRA-ARTICULAR TREATMENT OF OSTEOARTHRITIC JOINTS 153
5.1 Introduction 153
5.2 Materials and methods 155
5.2.1 Synthesis of polymer nanoparticles 155
5.2.2 Preparation of nanoparticle formulations 156
5.2.3 Tribological measurements of nanoparticle formulations 156
5.2.4 Size and Zeta Potential measurements of nanoparticle formulations 157
5.2.5 Imaging of substrates morphology 158
5.2.6 Viscosity measurements of nanoparticle formulations 158
5.3 Results and discussion 158

5.3.1 Characterisation of nanoparticle formulations....158
5.3.2 Effect of nanoparticle formulations on viscosity....162
5.3.3 Effect of nanoparticle formulations on the coefficient of friction....165
5.3.4 Effect of nanoparticle formulations on substrates' morphology....168
5.3.5 Effect of nanoparticles concentration on the coefficient of friction....170
5.3.6 Effect of nanoparticle type on the coefficient of friction....172
5.4 Conclusions....175

6. DUAL FUNCTIONAL FORMULATION FOR INTRA-ARTICULAR TREATMENT IN EARLY OSTEOARTHRITIS....177
6.1 Introduction....177
6.2 Methodology....179
6.2.1 Synthesis of polymer nanoparticles....179
6.2.2 Preparation of nanoparticle formulations....180
6.2.3 Size and Zeta Potential measurements of nanoparticle formulations....181
6.2.4 Generation of animal cartilage explants....181
6.2.5 Generation of human cartilage explants and primary cells....181
6.2.6 Tribological measurements of nanoparticle formulations....182
6.2.7 Surface adsorption of nanoparticle formulations....183
6.2.8 Imaging of sensors and cartilage explants....185
6.2.9 Surface properties of nanoparticle film....185
6.2.10 *In-vitro* cytotoxicity evaluation of nanoparticle formulations....186
6.3 Results and discussion....186
6.3.1 Surface roughness of human cartilage explants....186
6.3.2 Effect of formulation on the stability....188
6.3.3 Effect of nanoparticle formulation on the coefficient of friction of cartilage....191
6.3.4 Surface adsorption characteristics of nanoparticle formulations....194
6.3.5 Effect of nanoparticle formulation on cartilage's surface characteristics....197
6.3.6 Cytotoxicity of nanoparticle formulations....200
6.3.7 *In-vitro* drug release from the nanoparticle formulations....202
6.4 Conclusions....203

7. CONCLUSIONS AND FUTURE PERSPECTIVES....206
7.1 Conclusions....206
7.2 Recommendations for future work....210

APPENDIX....213
A.1 Ethical declaration....213
A.2 Supplementary data to Chapter 4....215
A.3 Supplementary data to Chapter 5....216
A.4 Supplementary data to Chapter 6....221

LIST OF REFERENCES....225

LIST OF FIGURES

Figure 1.1: Schematic diagram of the coefficient of friction against Hersey number, known as Stribeck curve. 10
Figure 1.2: Summary of NPs classification in terms of their dimension, morphology, composition and uniformity. Adopted from [49]. 14
Figure 1.3: Lubrication mechanisms of NPs grafted with amino group organic chains. Adopted from [58]. 16
Figure 1.4: Schematic diagram of a healthy knee joint, in which the AC covers the ends of the bones and the SF is viscous enough to separate them. Adopted from [68]. 18
Figure 1.5: Schematic representation of boundary lubrication on the AC. Collagen network is represented with orange colour, lubricin with fuchsia, HA with grey and PCs with green and blue. Adopted from [104]. 25
Figure 1.6: Chemical structure of HA. Adopted from [64]. 26
Figure 1.7: Schematic representation of lubricin structure. Adopted from [111]. 28
Figure 1.8: Chemical structure of γ-globulin. Adopted from [113]. 28
Figure 1.9: Chemical structure of HAS. Adopted from [115]. 29
Figure 1.10: Chemical structure of Phosphatidylethanolamide, Phosphatidylcholine, and Phosphatidylserine. Adopted from [118]……..……...30
Figure 1.11: Differences between a (a) healthy and (b) osteoarthritic knee joint. Adopted from [127]. 31
Figure 1.12: Topographies of human AC explants from (a) healthy, (b) mild osteoarthritic and (c) advanced osteoarthritic knee joint. Adopted from [135]. .. 32
Figure 1.13: Schematic representation of drug retention time offered by various delivery systems to the joints via IAI therapy. Adopted from [127]. 41
Figure 2.1: Experimental techniques used for the study of joints based on the Stribeck curve..... 47
Figure 2.2: SEM image of an AFM probe……50
Figure 2.3: Schematic representation of AFM basic principle. 52
Figure 2.4: AFM imaging modes (a) contact mode, (b) intermittent-contact mode, and (c) non-contact mode. 53
Figure 2.5: (a) Schematic representation of typical force curve for a hard surface, and (b) real force curve for PBS between a Silicon Nitride cantilever and a CoCr alloy substrate. 56
Figure 2.6: SEM picture of a typical colloidal probe with a borosilicate glass particle. 58
Figure 2.7: MTM basic principle (a) schematic representation, and (b) picture. The arrows show the direction of rotation of the shafts. 61
Figure 2.8: HFRR basic principle (a) schematic representation, and (b) picture adopted from [263]. 62
Figure 2.9: Schematic illustration of (a) Hertz, (b) JKR, and (c) DMT models in the case of a sphere in contact with another sphere or a planar surface [267]. Continuous lines represent the configuration under zero load and dotted lines under applied load. 65
Figure 2.10: Types of shear viscosity fluids……68

Figure 2.11: Schematic illustration of the ARES-G2 rheometer (TA Instruments, USA) and the 20 mm 2^{o} steel cone geometry used in this thesis. 72
Figure 2.12: Viscoelasticity of non-Newtonian fluids against angular frequency. Adopted by [271]. 75
Figure 2.13 Schematic representation of the basic principle of DLS. 78
Figure 2.14: Schematic illustration of the EDL on a negatively charged particle. The EDL consists of the Stern layer and the diffuse layer. The ZP is the potential measured at the slipping plane. 81
Figure 3.1: Viscosity of four indicative SF samples from patients suffering from OA and the reference PBS in relation to the shear rate. Circle: 57 yr, overweight, male, knee OA, fat 28.3%, W: H 1.12. Square: 74 yr, overweight, female, knee OA, W: H 0.97. Rhombus: 71 yr, overweight, female, knee OA, fat 37.8%, W: H 0.91. Triangle: 76 yr, overweight, male, knee OA, fat 24.8%, W: H 0.93. The data are fitted with the Power-law model. For every SF sample, the shear-thinning index (n) is presented. Each data point is the average viscosity value of three repetitions of the same sample. The error bars represent their standard error. 95
Figure 3.2: SF (a) viscosity at 2 s^{-1} and (b) shear-thinning index in relation to the age of patients with OA. Each viscosity data point is the average of three repetitions of the same sample. Each shear-thinning index data point was found using the Power-law model on three repetitions of the same sample. The error bars were omitted for presentation purposes. The R^2, P and the trendline were calculated using linear regression analysis in Microsoft Excel. 99
Figure 3.3: SF viscosity at 2 s^{-1} and shear-thinning index in relation to the (a,b) fat and the (c,d) W: H for patients with OA. Each viscosity data point is the average of three repetitions of the same sample. Each shear-thinning index data point was found using the Power-law model on three repetitions of the same sample. The error bars were omitted for presentation purposes. The R^2, P and the trendline were calculated using linear regression analysis in Microsoft Excel. 101
Figure 3.4: SF (a) viscosity at 2 s^{-1} and (b) shear-thinning index as a function of the weight status, the gender, and the origin of the sample of patients with OA. Each bar represents the average value of all the patients of the group (Normal weight (NW) N=11, Overweight (OW) N=21, Obese (OB) N=17, Male (M) N=22, Female (F) N=27, Knee N=29, Hip N=19). The error bars represent the standard error of the viscosity of the different SF samples within each group. 103
Figure 3.5: (a) Average adhesion energy of ten osteoarthritic SF samples as a function of the dilution factor. Each bar represents the average value of ten SF samples at the same dilution factor. The error bars represent their standard error. (b) Representative force curve of a human osteoarthritic SF (green). The black curve is the force curve of PBS. The measurements were performed between a silicon nitride cantilever and a titanium substrate. 109
Figure 3.6: Adhesion energy of ten SFs samples diluted ten times in PBS as a function of the age for patients with OA. Each adhesion energy point is the average from one hundred and fifty force curves made with the same sample. The error bars were omitted for presentation purposes. The R^2, P and the trendline were calculated using linear regression analysis in Microsoft Excel……..110
Figure 3.7: Adhesion energy of ten SFs samples diluted ten times in PBS as a function of patients' BMI. Each adhesion energy point is the average from one hundred and fifty force curves made with the same sample. The error bars were omitted

for presentation purposes. The R^2, P and the trendline were calculated using linear regression analysis in Microsoft Excel. 111
Figure 3.8: Average adhesion energy for ten-times diluted osteoarthritic SF samples as a function of the weight status, the gender and the origin of the sample. Each bar represents the average adhesion energy of all the patients of each group (Normal weight (NW) N=3, Overweight (OW) N=2, Obese (OB) N=5, Male (M) N=3, Female (F) N=7, Knee OA N=5, Hip OA N=5). The error bars represent the standard error of the adhesion energy of the different SF samples within each group. 112
Figure 3.9: Adhesion energy and viscosity of the same nine osteoarthritic SF samples. Viscosity was measured on neat SF samples, whereas adhesion energy on ten-times diluted samples. Each bar represents one SF sample. The error bars represent the standard error of three repetitions for the viscosity and one hundred and fifty for the adhesion energy of the same sample……114
Figure 4.1*:* Graphical abstract of ball-disc tribopairs. 125
Figure 4.2: Topography of MTM substrates. (a) CoCr, (b) Glass, and (c) SE. Images acquired by JPK AFM and analysed with Gwyddion software. 130
Figure 4.3: Contact angle of pure PBS, pure ASF, and PBS/ASF in the presence of SDS (0.5%) on the Glass, CoCr, and SE substrates. Each bar represents the average of three different samples tested on six different areas of each substrate. The error bars represent their standard error. 130
Figure 4.4: Contact angle of latex and silica NPs formulations on the Glass, CoCr, and SE substrates. The formulations consisted of NPs (0.5%) and SDS (0.5%) in PBS and ASF. Each bar represents the average of three different samples tested on six different areas of each substrate. The error bars represent their standard error. 131
Figure 4.5: (a) Size, (b) PDI, and (c) Zeta Potential of formulations with latex and silica NPs in water and ASF(AS). The concentration of NPs and SDS (S) was 0.5%. Each bar represents the average of five repetitions of three different samples. The error bars represent their standard error. 133
Figure 4.6: Viscosity of silica NPs in (a) ASF, (c) PBS, and latex NPs in (b) ASF, (d) PBS. The concentration of NPs was 0.01%, 0.1%, 0.5%, and 1%. Formulations contained NPs and SDS (0.5%). Each data point is the average viscosity of three repetitions of the same sample. The error bars represent their standard error.135
Figure 4.7: CoF against Hersey number for six material configurations using a formulation of latex NPs (0.1%) and SDS (0.5%) in PBS. The coefficient of friction for configurations with a steel ball is illustrated with filled symbols, whereas with a PE ball with unfilled symbols. The same shape of symbols is used for configurations with the same substrate. Each data point is the average CoF of six repetitions of the same sample. The error bars represent their standard error.137
Figure 4.8: Maximum reduction of the CoF achieved with silica and latex NPs formulations in PBS and ASF for six contact material configurations. The missing bars represent the cases when there was no reduction in the CoF. Each bar represents the average CoF reduction of six repetitions of the same sample. The error bars represent their standard error between the sliding velocities 1-100 mm s^{-1}. 141
Figure 4.9: Suggested lubrication mechanism of NPs formulations on the surface of the rough SE. 142

Figure 4.10: CoF against sliding velocity of the formulations 0.1% silica/latex NPs in PBS/ASF between (a) a steel ball and a SE disc and (b) a PE ball and a SE disc. Each data point is the average CoF of six repetitions of the same sample. The error bars represent their standard error. 144
Figure 5.1: (a) Size, (b) PDI, and (c) Zeta Potential of PMMA, PCL, and PLA NPs (0.5%) in water, water/SDS (0.5%), water/HA (0.01%), and water/HA (0.01%)/SDS (0.05%). Each bar represents the average of four repetitions of the same sample. The error bars represent their standard error. 159
Figure 5.2: Schematic representation of the microstructure and the interactions between polymer NPs (red circles), HA, and SDS in the formulation. 162
Figure 5.3: Viscosity of PMMA, PCL, and PLA NPs formulations at 37^{o}C. The formulations consisted of NPs (0.5%)/HA (0.1%)/SDS (0.5%) in PBS. Each data point represents the average viscosity of three repetitions of the same sample. The error bars represent their standard error. 163
Figure 5.4: Effect of (a) SDS, (b) HA, (c) SDS and HA on the CoF between a steel ball and a SE substrate as a function of sliding velocity. The concentration of NPs and SDS was 0.5% w/v, whereas the concentration of HA 0.1% w/v. Each data point represents the average CoF of six repetitions of the same sample. The error bars represent their standard error. 167
Figure 5.5: AFM images of SE (a) clean, (b) used with SDS (c) used with PLA NPs, (d) and (e) used with PLA NPs/HA/SDS. The concentration of NPs and SDS was 0.5%, whereas the concentration of HA 0.1%. All formulations were based on PBS. The size of the images is 400 μm^2. 170
Figure 5.6: (a) Effect of NPs concentration (0.1%, 0.5%, 1%) on the CoF developed between a steel ball and a SE substrate. Each data point is the average CoF of six repetitions of the same sample. The error bars represent their standard error. (b) Schematic representation of the suggested lubrication mechanism. The formulations were consisted of PLA NPs/HA (0.1%)/ SDS (0.5%) in PBS. 171
Figure 5.7: CoF of PMMA, PCL, and PLA NPs formulations between a steel ball and a SE substrate as a function of Hersey number. The formulations were consisted of NPs (0.5%)/HA (0.1%) /SDS (0.5%) in PBS. Each data point is the average CoF of six repetitions of the same sample. The error bars represent their standard error. 172
Figure 5.8: Reduction of the CoF caused by PMMA, PCL, and PLA NPs formulations against sliding velocity between a steel ball and a SE substrate. The formulations were made of NPs (0.5%)/HA (0.1%)/SDS (0.5%) in PBS. Each bar represents the average CoF reduction of six repetitions of the same sample. The error bars represent their standard error 175
Figure 6.1: HFRR setup for testing human and animal AC explants. (a) AC disc generated using a cork borer, (b) AC disc fixed on a steel disc, (c) AC fixed in the sample holder. 183
Figure 6.2: AFM topographies of the same human osteoarthritic AC explant at various sizes. (a) 4, (b) 25, (c) 2.5 10^3, and (d) 10^4 μm^2 188
Figure 6.3: (a) Size, (b) PDI, and (c) Zeta Potential of formulations with blank and drug-loaded PMMA, PCL, and PLA NPs. The filled bars represent the blank and the non-filled bars the DL-NPs. Each bar represents the average of five repetitions of three different samples. The error bars represent their standard error. 190

Figure 6.4*:* Effect of formulation's components on the CoF of porcine AC against a stainless steel ball. The formulations investigated consisted of PLA NPs (0.5%), PLA NPs (0.5%)/SDS (0.5%), PLA NPs (0.5%)/HA (0.1%), and PLA NPs (0.5%)/HA (0.1%)/ SDS (0.5%) in PBS. The percentages on the top of the bars represent the reduction of the CoF. Each bar represents the average CoF of a single sample at different time points within 30 minutes. The error bars symbolise their standard error. 191
Figure 6.5: CoF of human osteoarthritic AC against a stainless steel ball with (a) blank and (b) DL-PMMA, DL-PCL, and DL-PLA NPs formulations as lubricants. The formulations consisted of NPs (0.5%) /HA (0.1%)/SDS (0.5%) in PBS. The percentages on the top of the bars represent the reduction rate of the CoF. Each bar represents the average CoF of a single sample at different time points within 30 minutes. The error bars symbolise their standard error. 193
Figure 6.6*:* Representative QCM adsorption curve of a formulation consisting of 0.1% PMMA NPs in PBS on a (3-Mercaptopropyl) trimethoxysilane-functionalised QCM sensor. The force curve of a single measurement is presented here for presentation purposes. 195
Figure 6.7*:* AFM images of (3-Mercaptopropyl) trimethoxysilane-functionalised QCM sensors (a) clean, (b) used with a DL-PCL NPs formulation (c) used with a DL-PLA NOs formulation, and (d) used with a DL-PMMA NPs formulation. The size of the images is 100 μm^2. 197
Figure 6.8*:* Interferometer images of human osteoarthritic ACs (a) intact with surface roughness 1.25 μm, and (b) treated with a NPs formulation with surface roughness 0.45 μm. The NPs formulation consisted of PCL NPs (0.5%)/SDS (0.5%)//HA (0.1%) in PBS. The size of both images is 10^4 μm. 198
Figure 6.9: Representative force curve of a human osteoarthritic AC explant in PBS (black) and NPs formulation (blue). The force curves were created with a stainless steel colloidal probe. The force curve of a single measurement is presented here for presentation purposes. 199
Figure 6.10: Cytotoxicity of chondrocytes after one and five days of incubation with (a) different components of the formulation, and (b) NPs formulations with different types of DL-NPs. The filled bars represent the average number of cells after one day and the stripped patterned bars after five days of incubation. The formulation on (b) consisted of DL-NPs (0.5%)/HA(H) (0.1%)/SDS(S) (0.5%) in PBS. DL- PCL, DL-PLA, and DL-PMMA NPs were used. The error bars represent the standard error from three wells seeded with the same sample. 201

LIST OF TABLES

Table 1.1: Summary of reported nanoparticle formulations for simultaneous pharmacological treatment and lubrication improvement of joints. 43
Table 2.1: Contact radius, sample deformation, and adhesion force approximations based on Hertz, DMT and JKR models. 65
Table 3.1: Steady-state flow viscosity of osteoarthritic and healthy SF samples reported in the literature. Values annotated with (*) correspond to the average viscosity ± standard error. 86
Table 3.2*:* Characteristics of patients / donors of synovial fluid suffering from OA. .. 89
Table 3.3: Shear-thinning index (n) of SF samples from various groups of patients suffering from OA. 94
Table 3.4: Significant interactions of viscosity (η) and shear-thinning index (n) with patient groups acquired by ANOVA. The probability (P) and the Partial Eta Squared ($\eta p2$) are provided for each interaction. 106
Table 4.1: Mechanical and physical properties of silica and latex NPs. 121
Table 4.2: Summary of tested nanoparticle formulations. 122
Table 4.3: Mechanical and morphological properties of specimen and real joint contacts. 128
Table 4.4: Contact area and pressure for six materials' configurations based on the Hertz model. 136
Table 4.5: Coefficient of friction and its correlation coefficient with sliding velocity for six materials' configurations. 138
Table 4.6: Optimum lubricant for various materials configurations. 141
Table 4.7: Fitting parameters of the tribological behaviour of six contact surfaces configurations (MLA). 149
Table 5.1: Mechanical/physical properties of PMMA, PCL, and PLA NPs. 155
Table 5.2: Summary of tested nanoparticle formulations. 156
Table 5.3: Viscosity (η), consistency (m), Power-law index (n), and coefficient of determination (R^2) of nanoparticle formulations and PBS. 163
Table 6.1: Summary of tested nanoparticle formulations. 180
Table 6.2: Adsorbed mass of DL-PCL, DL-PLA, and DL-PMMA NPs formulations on a (3-Mercaptopropyl) trimethoxysilane-functionalised QCM sensor and CoF reduction on human osteoarthritic AC explants. 196
Table 6.3: Reduction of human osteoarthritic AC explants Young's modulus with blank and drug-loaded (DL) PCL, PLA, and PMMA NPs formulations. Formulations consisted of NPs (0.5%)/HA (0.1%)/0.5% SDS (0.5%) in PBS. 200

LIST OF ABBREVIATIONS

SYMBOL	NAME
AC	Articular cartilage
AFM	Atomic Force Microscopy
AGEs	Advanced glycation end-products
ANOVA	Analysis of variance
ASF	Artificial synovial fluid
BMI	Body Mass Index
CC	Correlation coefficient
CoCr	Cobalt-chromium
CoF	Coefficient of friction
DGS	D-glucosamine sulphate
DLS	Dynamic light scattering
DS	Diclofenac Sodium
ECM	Extracellular matrix
EDL	Electric Double Layer
ELS	Electrophoretic Light Scattering
FDA	US Food and Drug Administration
GAGs	Glycosaminoglycans
HA	Hyaluronic acid
HAS	Human serum albumin
HFRR	High-Frequency Reciprocating Rig
HPLC	High-Performance Liquid Chromatography
IAI	Intra-articular injection
MMPS	Matrix metalloproteinases
MRI	Magnetic resonance imaging
MTM	Mini-Traction Machine
NPs	Nanoparticles
NSAIDs	Non-steroidal anti-inflammatory drugs
PBS	Phosphate-buffered saline
PCL	Polycaprolactone
PCs	Saturated phosphatidylcholines
PDI	Polydispersity
PDMS	Polydimethylsiloxane
PE	Ultra-high-molecular-weight polyethylene
PLA	Polylactic acid
PMMA	Polymethylmethacrylate
PTFE	Polytetrafluoroethylene
PVA	Polyvinyl alcohol
RhB	Rhodamine B
ROS	Reactive oxygen species
SAPLs	Surface active phospholipids
SDS	Sodium dodecyl sulphate
SEM	Scanning Electron Microscopy
SPM	Scanning Probe Microscopy
SRR	Slide-to-roll ratio

SYMBOL	NAME
STM	Scanning Tunnelling Microscope
SZP	Superficial Zone Protein
W: H	Waist to Hip Ratio
ZP	Zeta Potential

NOMENCLATURE

SYMBOL	NAME	UNIT
A	Adhesion per unit area	N m^{-2}
C	Contact area	m^2
D	Translational diffusion coefficient	m^2 s^{-1}
$d(H)$	Hydrodynamic diameter	m
E_a	Activation energy	m N mol^{-1}
F	Force	N
f	Frequency	Hz
$f(k_a)$	Henry's function	-
G'	Storage modulus	Pa
G''	Loss modulus	Pa
$g(\tau)$	Time decay	s
h	Film thickness	m
He	Hersey number	-
I	Pre-exponential factor	s^{-1}
J	Nominal sensitivity	Kg Hz^{-1} m^{-2}
k	Boltzmann's constant	kg m^2 s^{-2} K^{-1}
k_c	Spring constant	N m^{-1}
M	Mass	kg
m	Consistency of viscosity	Pa s
n	Power-law/shear-thinning index	-
$\tilde{n}$	Refractive index	-
n_p^2	Partial Eta Squared	-
P	Probability value	-
p	Applied contact pressure	N m^{-2}
Q	Cantilever deflection	m
q	Propagation vector length	m^{-1}
R	Universal gas constant	m N K^{-1} mol^{-1}
R^2	Coefficient of determination	-
r	Radius	m
R_a	Surface roughness	m
S	Electric field strength	Volt m^{-1}
T	Absolute temperature	K
u	Speed	m s^{-1}
V	Volume	m^3
v	Poisson ratio	-
W	Indenter load	N
x_s	Stroke length	m
a	Contact radius	m
γ	Surface energy	N m^{-1}
$\dot{\gamma}$	Shear strain rate	s^{-1}

SYMBOL	NAME	UNIT
δ	Deformation	m
$\Delta\gamma$	Adhesion work	N m^{-1}
E	Young's modulus	N m^{-2}
ε	Dielectric constant	-
η	Viscosity	Pa s
ϑ	Scattering angle	^{o}
λ_o	Laser light's wavelength	m
μ_e	Electrophoretic mobility	m^2 s^{-1} $Volt^{-1}$
ρ	Density	g m^{-3}
σ	Shear stress	N m^{-2}
τ	Time	s
μ_e	Electrophoretic mobility	m^2 s^{-1} $Volt^{-1}$

1. INTRODUCTION

1.1 Motivation

Osteoarthritis (OA) is a pathological condition causing progressively degeneration in the joints, and leading to severe pain and diminished mobility. As OA progresses, articular cartilage (AC) loses its lubrication capacity and synovial fluid (SF) its viscoelasticity. In fact, a significant cause of pain in OA stems from the elevated Coefficient of Friction (CoF) between the articulating surfaces.

OA is a widespread disease with more than 500 million patients worldwide [1]. The cases of OA are anticipated to rise in the following years due to the sedentary lifestyle and the ageing population [1, 2]. Despite its prevalence and severity, there is no diagnostic method for OA at its early stages. Detecting the morphological changes in the joints indicating the presence of OA is only possible via Magnetic Resonance Imaging (MRI). However, even MRI cannot detect alterations in the early OA, which are visible only in molecular resolution [3-6]. As a result, the disease has progressed significantly at the time of the diagnosis, and the degeneration cannot be reversed.

Current therapies for OA are not effective enough to treat the damage of the joints entirely or decelerate their degeneration. At the beginning of the disease, patients follow a pharmacological treatment focused on pain relief, but it is not always effective. When pharmacological treatment fails, intra-articular injection (IAI) of therapeutic formulations in the diseased joints is utilised. Currently, IAI therapy is the most effective treatment at the early OA. Although it restores the viscoelasticity of SF, it cannot protect joints from CoF increase, especially during high-frequency activities

when the formulations squeeze out from the joint cavity and the articulating surfaces come in direct contact. Another drawback is that IAI therapy offers only temporary pain relief because the formulations diffuse quickly from the joints [7]. Arthroplasty is the only solution but is applied only when the disease has progressed to its latest stages, and pharmacological/IAI treatments fail. This procedure involves a surgical intervention during which artificial implants replace the whole joint or a part of it. Even though arthroplasty is the most effective solution at the last stage of OA, it has a limited lifespan of 15 years maximum [8].

Nanoparticles (NPs) incorporated into IAI formulations could act as alternative lubricant additives and improve the tribological performance of the osteoarthritic joints. Particulates of sub-micron size have demonstrated outstanding potential in reducing the CoF and wear of various systems like synthetic engine oils (e.g. poly-alpha-olefin) [9, 10], biolubricants (e.g. coconut oil, Pongamia oil) [11], and water-based lubricants for ceramics [12, 13]. Unlike classic therapeutic compounds, which diffuse away, NPs' small size could enable them to adsorb on the rough AC surfaces and offer prolonged lubrication characteristics. NPs could also improve the IAI therapy for OA in other ways. Instead of being injected directly into the joints, the drugs can be loaded on them and acquire a prolonged and controlled release [14]. Furthermore, the material of which NPs are made could also carry therapeutic properties for the joints. For example, sodium hyaluronate NPs have the additional advantage of restoring the viscoelasticity of the SF [15].

OA is a complex disease with unclear aetiology. Multiple factors, including age, obesity, gender, metabolism, previous traumatic incidents, and occupation, induce

joints deterioration [16]. The complexity of the disease, in combination with the lack of effective treatments and joints' self-repair capacity, highlight the need for further research and development in that field. The more is learnt about joint's tribology and its relationship with the pathophysiology of OA, the better the possibilities are for the development of effective treatments capable of stopping and reversing the progression of OA [3]. Simultaneously, non-invasive diagnostic tools for detecting OA at its early stages must be developed to prevent further development of OA or decelerate its progression. Changes occurring in osteoarthritic joints' mechanical properties or composition at the early stages of OA could serve as biomarkers. One example is the increase of protein biomarkers in joints at the early OA [17].

1.2 Aim and objectives of the project

This project aims to develop a physical intervention mechanism to mitigate the development of OA at its early stages by controlling the tribological characteristics of articulating joints. The first aim is to understand the requirements for the new treatment by expanding the current knowledge regarding the impact of OA on the joints' lubrication properties. The hypothesis is that OA acts differently on patients with different physical and anatomical characteristics, and identifying that will assist in establishing targeted treatments based on individual characteristics. The primary requirement for the new intervention mechanism is to treat the elevated CoF in the osteoarthritic joints, which is a major source of pain. To that end, an IAI formulation capable of restoring the viscoelasticity of SF and improving the lubrication performance of osteoarthritic joints needs to be developed. NPs will be the main ingredients of the formulation because it is hypothesised that they act as lubricant additives for the joints.

NPs are also used as drug delivery carriers and are expected to prolong the retention time of the therapeutic agent in the joints to increase its effectiveness, which is a secondary aim for the treatment.

The individual objectives are outlined below:

- Examine the impact of OA on the lubrication properties of the SF via rheological and surface interaction characterisation.
- Evaluate the impact of patients' physical characteristics on the lubrication properties of the SF and establish their range for each patient group.
- Identify the effect of surface materials replicating joint contacts on the lubrication performance (CoF, viscosity) of the NPs formulations.
- Evaluate the effect of NPs type, NPs concentration and solvent's viscosity on the lubrication performance of the NPs formulations.
- Develop a stable NPs formulation capable of providing the desired lubrication properties (CoF, viscosity) to the osteoarthritic joint.
- Evaluate the lubrication performance of formulations with blank and drug-loaded NPs on human osteoarthritic AC.
- Test the *in vitro* cytotoxicity and drug release of the developed drug-loaded NPs formulation to evaluate its biocompatibility and its capacity to prolong the retention time of drugs.

1.3 Thesis layout

- Chapter 1 - Introduction. This chapter includes the motivation, the aim, and the objectives of the project. Moreover, it comprises a literature review on the

tribology, NPs as friction modifiers, and the mechanical properties of the osteoarthritic joints. Focus is given on the IAI treatment for OA, in line with recent studies reporting potential IAI formulations for improved joints' lubrication.

- Chapter 2 - Methodology. This chapter outlines the working principle of the main techniques employed in this project. Those are Atomic Force Microscopy (AFM), Dynamic Light scattering, steady-state shear rheometry, CoF measurements, and Tribology. It also reviews previous studies, which employed those techniques to study the mechanical properties of the joints and characterise NPs formulations.
- Chapter 3 - Investigation of rheological and surface properties of osteoarthritic synovial fluids. This experimental chapter examines the rheological (viscosity, shear-thinning index) and surface properties (adhesion energy) of osteoarthritic SF samples. The results are grouped based on the patients' characteristics (age, gender, BMI, fat level, W: H, joint type), and correlations are identified.
- Chapter 4 - Nanoparticles as friction modifiers for osteoarthritic joints. This experimental chapter investigates the capacity of NPs formulations to improve the lubrication performance of surfaces simulating the natural and artificial joints. The impact of the NPs characteristics (size, Young's modulus, hardness), substrates' mechanical properties (surface roughness, Young's modulus), and solvents viscosity on the CoF are investigated.
- Chapter 5 - Nanoparticle formulation for intra-articular treatment of osteoarthritic joints. In this chapter, a potential IAI formulation is developed to treat the joints in early OA. A combination of polymer NPs, surface-active species and (Hyaluronic acid) HA is used to achieve the maximum CoF reduction between

substrates mimicking the bone-AC contact. The effect of each component on the CoF is evaluated using tribology, rheology, Dynamic light scattering (DLS) and AFM.

- Chapter 6 - Dual functional formulation for intra-articular treatment in early osteoarthritis. This chapter examines the efficacy of a drug-loaded NPs formulation as an IAI analgesic for patients in early OA. Its lubrication performance was tested *in vitro* in natural human osteoarthritic AC samples and its viability on synovial chondrocytes.
- Chapter 7 - Conclusions & future work. This chapter brings together all the findings of the project and discusses the outcome of those. In addition, it refers to the applicability of the findings to the industry and provides suggestions for future work.

Data from chapter 3 have been presented as follows:

Simou K., Jones S., Davis E., Preece J., Zhang Z "Nanomechanics of synovial fluids towards the treatment of osteoarthritis". Poster presentation at *World Congress of Biomechanics*, Dublin, 2018.

Chapters 3-6 will be published in peer-reviewed journals under the titles given in this thesis.

1.4 Literature review

1.4.1 Introduction to tribology

Tribology is a multidisciplinary field relating to the science and engineering of interacting surfaces in relative motion. Tribology studies the main principles of friction, wear, and lubrication and investigates its applications [18]. Tribology finds application in manufacturing [19], machine elements [20], energy consumption [21], automotive [22], aerospace [23], and even biology (e.g. synovial joints, skin) [24-26]. Friction is the force that causes resistance to the relative motion and demonstrates the kinetic energy dissipated during that movement [27]. Wear is the damage of solid surfaces due to their relative motion resulting in material loss [27]. Adhesion is a type of wear that happens when two moving surfaces stick together and then immediately separate [28]. The adhesion force scales proportionally with friction in most cases [29]. In this thesis, adhesion has been used as a measure of the degeneration of the osteoarthritic joints. Lubrication minimises the coefficient of friction (CoF) and wear between contacting surfaces by separating them using lubricants [30].

Friction is the most commonly used property for tribological characterisation of any moving system and is extensively examined in this thesis. The friction force F (N) is present in any moving system and is analogical to the vertically applied normal force W (N) based on the First Law of Friction:

$$F = \mu W \qquad (1.1)$$

where μ is the CoF [27]. CoF is evaluated by the friction force: normal force ratio between two interactive materials [26]. The second law of friction claims that the friction

force is irrespective of the nominal area of contact [27]. In general, CoF is affected by the temperature of the system, the loading magnitude, the speed of the interactive surfaces, the type of surfaces' movement (sliding/rolling mechanism), the contact geometry, the lubricants concentration, the lubricants viscosity, the materials' mechanical properties (surface roughness, Young's modulus) and chemical interactions [28, 30-32]. Surface roughness, R_a is a measure of surface texture that relates to surface geometries and indicates surface degradation [33, 34].

1.4.1.1 Working principle of sliding tribometer

A sliding tribometer measures the tribological performance of two surfaces in a relative and controlled motion. The friction force measured with a sliding tribometer is derived from the reciprocation between two surfaces, and it is used to calculate the CoF and material's wear [35]. Some applications of a tribometer include the development and evaluation of bearing materials, lubricants, coatings, and the investigation of the origin of friction and its interplay with wear [36].

The basic setup of a sliding tribometer includes two rubbing surfaces, one stationary and the other one moving relative to the other. The surfaces are usually a disc and ball or pin made of materials with mechanical properties similar to contacting surfaces of the real-life scenario the tribometer simulates. A lubricant is loaded on the disc, and a known normal force is applied from the pin/ ball [35]. The normal force is derived from a dead weight attached to the pin/ball [35]. The measured friction force is derived from the reciprocating between the rubbing surfaces [35]. The velocity drives the sliding motion of the pin/ball and the disc [18]. Dynamic friction can also be studied in the existence of servo-controllers [37]. Some tribometers enable the accurate control

of temperature and humidity in addition to the above. It has to be mentioned that the application of representative parameters can simulate almost any real tribological scenario and enable its study.

1.4.1.2 Lubrication regimes

The Stribeck curve is a concept commonly used to identify the lubrication mode followed in moving systems. More specifically, it describes the CoF behaviour against the operating conditions usually the entrainment speed or the Hersey number. The dimensionless Hersey number (*He*) is defined as

$$He = \frac{\eta U}{\overline{W}} \qquad (1.2)$$

where η is lubricant's viscosity (Pa s), U is the entrainment speed (m s^{-1}), and $\overline{W}$ is the normal load per length of the bearing (N m^{-1}). The lubrication modes and resulting CoF relate to parameters affecting the film thickness (h) formation (e.g. lubricant's viscosity) and the operating parameters (e.g. speed, normal load) [38]. Hersey number is used in the Stribeck curve instead of the film thickness because of its higher magnitude [38]. **Figure 1.1** is a schematic diagram of the Stribeck curve.

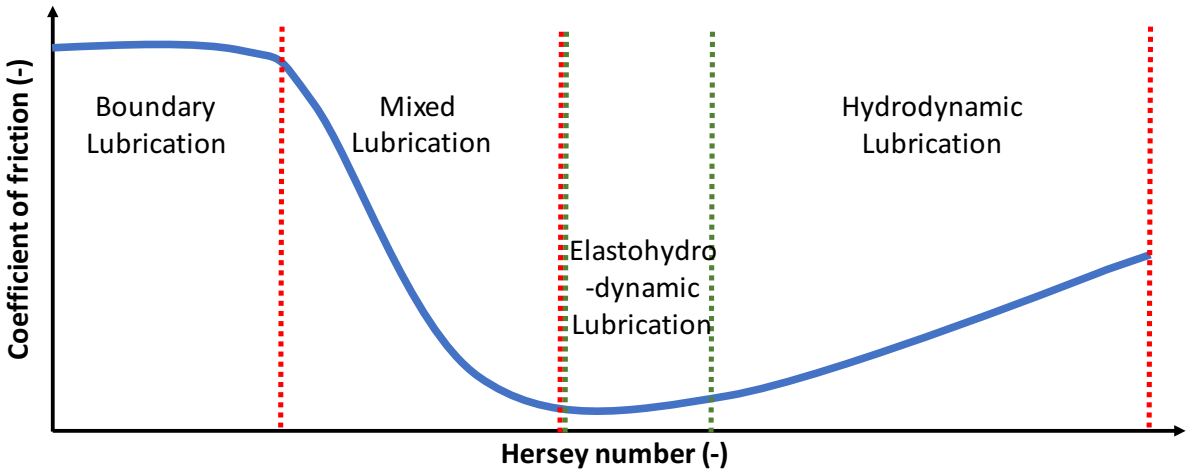


Figure 1.1: Schematic diagram of the coefficient of friction against Hersey number, known as Stribeck curve.

Most moving systems follow the four main lubrication modes described by the Stribeck curve: boundary, hydrodynamic, mixed, and elastohydrodynamic. The boundary regime appears under low sliding speeds or repeated loading and is characterised by significant wear and energy losses [28]. In the boundary lubrication, the asperities of the opposing surfaces are in direct proximity because, at low velocities, the lubricant is neither entrained (h < 70 nm) nor has the required pressure to keep the surfaces apart; as a result, the CoF is high [30]. On the contrary, under high sliding speed and low loading, the opposing surfaces are entirely separated thanks to the high viscosity of the lubricant and the high speed (h > 1 μm), and the hydrodynamic lubrication dominates [30]. The CoF is generally low and is affected by the lubricant's viscosity and microstructure. The wear in that regime is low, but there is fatigue because of the viscous dragging forces (cycling stresses) [28]. The elastohydrodynamic lubrication is found within the hydrodynamic regime and occurs on soft surfaces in rolling motion under high pressure [28]. In the elastohydrodynamic regime, the surfaces withstand elastic deformation owing to elevated hydrodynamic

pressure but are still separated (10 nm < *h* < 70 nm) [30]. The final region is the transitional regime between the boundary and the hydrodynamic, called mixed lubrication. As the speed increases when moving away from boundary lubrication, lubricant entrainment increases and the opposing surfaces separate. Although in the mixed lubrication regime, the CoF varies with the entrainment of the lubricant (70 nm < *h* < 1um), it is lower than the boundary and higher than the hydrodynamic regime at every point [30]. In the elastohydrodynamic/mixed regime, the thickness of the tribofilm is 1-3 times higher than the surface roughness [39].

1.4.2 Lubricants and lubricant additives

Lubricants improve the performance of machinery (reduced maintenance, downtime), reduce the operational cost (reduced fuel, prolonged lifetime), and minimise the impact on the environment (reduced emissions) [40]. Their primary functions include controlling the CoF, and protecting the surfaces against dirt, corrosion, overheating, and prolonging the lifetime of the moving elements [41].

The form of the lubricant is relevant to its application. In general, lubricants in the form of gas are used when there is low contact pressure between the contact pair [9]. Solid/semisolid lubricants are preferred under slow sliding speeds and high temperatures [9]. Liquid lubricants dominate the lubricant market and are used under high sliding speeds and loading conditions. Liquid lubricants also demonstrate the additional capability of surface self-repair (e.g. wear improvement). Some commonly used applications of liquid lubricants are in automotive, diesel engines, and marine engines [40].

Liquid lubricants consist of 80-95% base fluid and 5-20% lubricant additives [41]. The base fluid is usually a mineral oil (e.g. solvent-refined, hydro-processed, hydro-cracked), a synthetic oil (e.g. poly-alpha-olefin (PAO)) or a bio lubricant (natural triglycerides) [41]. Mineral oil is commonly used due to its low price, but it is not environmentally friendly [28, 42]. Synthetic oils perform well under extreme temperature conditions but they are also harmful to the environment [28, 42]. Biolubricants are made from plant oils, and apart from their exceptional lubrication performance, they are environmentally friendly and biodegradable [28, 42].

Various parameters contribute to lubricant's performance. Viscosity and density of the base fluids are also critical to lubricant's performance because they are positively correlated with the thickness of the tribo-film [43]. High viscosity correlates to thick tribofilm but low lubricant's efficiency because of poor fuel atomisation. Lubricants density also affects the thickness of the tribofilm but to a smaller extent. High viscosity index is critical for a lubricant's performance because it is associated to fewer changes in viscosity with increasing temperature; an usual issue during machine operation [44].

Lubricant additives are compounds, enhancing the performance of base fluids significantly in a cost-effective manner [41]. Their main functions include reducing the CoF and wear of the system, preventing its seizure, prolonging the lifetime of the parts in contact and the lifetime of the lubricant [41]. The additives could be in liquid or solid form [41]. Lubricant additives could be friction modifiers, extreme pressure, or anti-wear additives [45]. The friction modifiers create easily deformable and fragile protective films, which prevent surface contact and abrasion (wear when a hard surface pass over a soft surface causing material loss) [28]. The extreme pressure and

anti-wear additives react with the contacting surfaces creating thick and robust protective films, which offer load-carrying ability [42]. The friction modifiers provide a CoF lower than the other two types of lubricant additives under boundary conditions [46]. Typically, the lubricants are mostly efficient under boundary/mixed lubrication regimes and less under hydrodynamic regimes [45].

1.4.2.2 Nanoparticles

NPs have been recently proposed as lubricant additives. NPs could be categorised based on their composition, size, morphology, and uniformity. **Figure 1.2** is a schematic illustration of NPs belonging to those four categories. There are naturally occurring and synthetically made NPs [47]. The naturally occurring are mainly composites (consist of more than one material), whereas a single material or combination of materials could make the synthetic NPs [47]. According to their dimension, NPs could be zero-dimensional (e.g. filaments, atomic clusters), one-dimensional (e.g. nanotubes, nanowires), two-dimensional (e.g. nanosheets, nanoribbons), and three-dimensional (e.g. nanocones, nanocoils) [47]. More specifically, zero-dimensional are NPs with dimensions being smaller than 100 nm, one-, two-, three-dimensional are NPs with one, two, three dimensions above 100 nm [48]. NPs can be classified into low or high aspect ratios regarding their morphology [47]. The low aspect ratio NPs could be further divided into spherical, cubical, oval, colloids, prism-shaped, and pillar-like, whereas the high aspect ratio NPs into nanosprings, nanostars, nanorods, nanohooks, nanoplates, and nanohelices [47]. Finally, NPs could be isometric or inhomogeneous and can be found either in

dispersed aerosols or in the agglomerate phase; in the latter case, their behaviour is affected by the size of the agglomerates [47, 48].

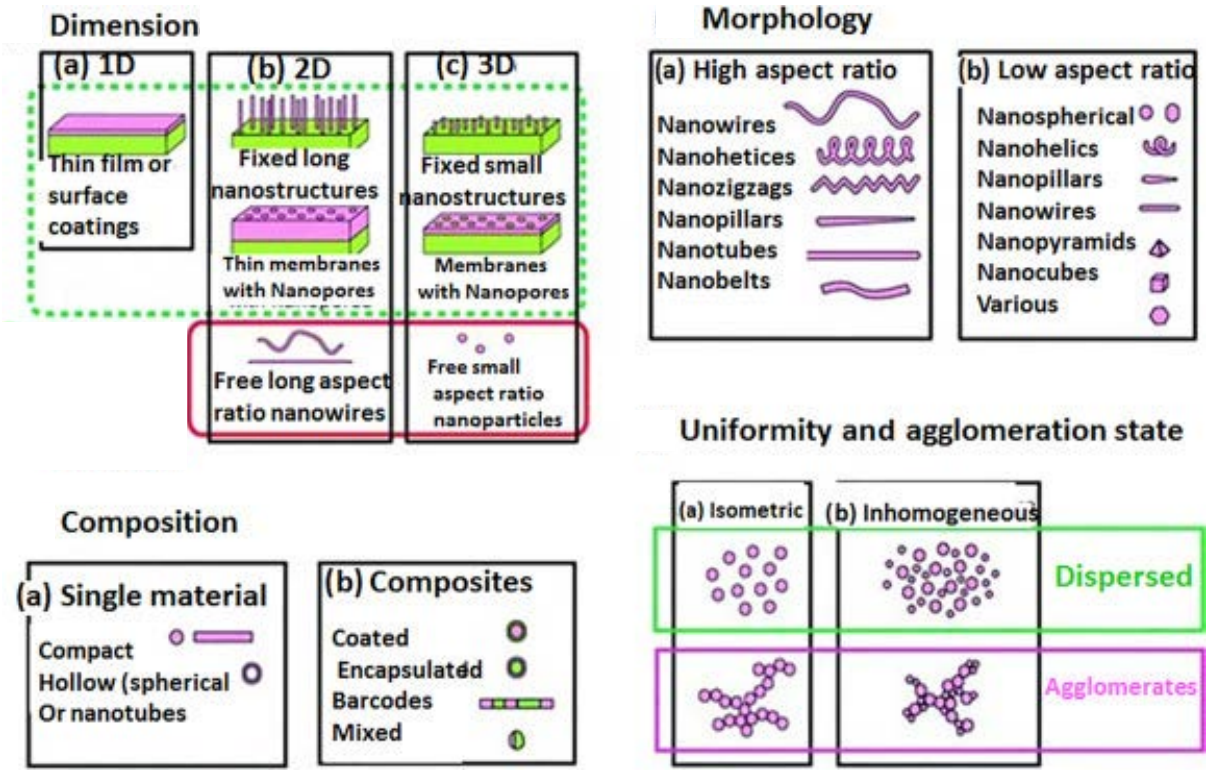


Figure 1.2: Summary of NPs classification in terms of their dimension, morphology, composition and uniformity. Adopted from [49].

Suspensions of solid NPs into base lubricants form the so-called nanolubricants. Nanolubricants are synthesized either in one or two steps. On the latter one, the initial step is the synthesis of the NPs in dry form and the second step is their dispersion into the base oil [50]. In the nanolubricants the size of the nanoparticles ranges from 1 to 100 nm and their concentration from 0.2 to 40% [40].

Nanomaterials were only used before as dry lubricants under extreme temperature conditions [51]. However, NPs work as solid additives in liquid lubricants as well [52, 53]. NPs based on metals (Fe, Cu, Co), metal oxides (CuO, TiO_2 ZnO, Al_2O_3, Fe_3O_4, $ZnAl_2O_4$), metal sulphides (MoS_2, WS_2, FeS, CuS), carbon (graphite,

graphene, diamond), boron nitrides, polymers (poly(dodecyl methacrylate), nanocomposites (Al_2O_3/ TiO_2, TiO_2/ SiO_2) and rare earth compounds ($CeVO_4$, LaF_3) are only a few of them exhibiting excellent tribological performance [9]. Especially, diamond, copper, boron, tungsten and molybdenum disulphide NPs are materials used already as commercial additives in oil lubricants for combustion engines (e.g. diesel, petrol, gasoline for vehicles), industrial gears, bearings, and compressors [40].

NPs demonstrate numerous benefits compared to other additives. First of all, they are not soluble in base oils allowing them to adsorb on the contacting surfaces and change their tribological characteristics [54]. Their small size (nanometer size) enables them to penetrate easily to any contact area [55]. They are time-efficient because they do not require elevated temperatures to start working [55]. They do not interact with other additives maintaining low antagonistic effects in the lubricant formula [55]. They are non-volatile and can be utilised under extreme temperatures [54]. NPs are also more environmentally friendly than the typical additives containing sulfur and phosphorus (e.g. organo-zinc phosphate) [44]. Finally, NPs can be made with a variety of materials and be suitable for every possible application. Nevertheless, one challenge is the price of the NPs being roughly 10% higher than the price of petroleum-based additives [44].

NPs are excellent lubricant additives; they are efficient in reducing the friction and wear of materials in relative motion. Over the past two decades, NPs were used as lubricant additives for oils, and numerous publications outline their improved tribological performance [9, 10]. For example, the friction of the engine lubricant poly-alpha-olefin with the addition of silica and titania NPs has been reduced up to 40% [56], and similar data have been published for paraffin [9].

Various lubrication mechanisms have been suggested so far for the NPs. The four most prevalent are illustrated in **Figure 1.3**. Under specific conditions, like low normal load and spherical NPs larger than the surface roughness, the NPs can roll over the contact area and reduce the sliding friction by transforming a part of it into rolling friction (Ball bearing/rolling effect) [9, 57]. NPs can deposit on the worn (because of the friction) rubbing surfaces, compensate for the mass loss and form films that protect the rubbing surfaces from penetrating the contact area (Mending effect) [9, 57]. Another mechanism suggests that protective films-tribofilms of NPs could be generated from the by-products of the interactions (e.g. tribochemical reaction) of NPs with the surfaces in contact (Protective film effect) [9, 57]. The last proposed lubrication mechanism is the polishing/smoothing effect. In that case, NPs fill the valleys of a rough surface, making it smooth and reduce its surface roughness [10].

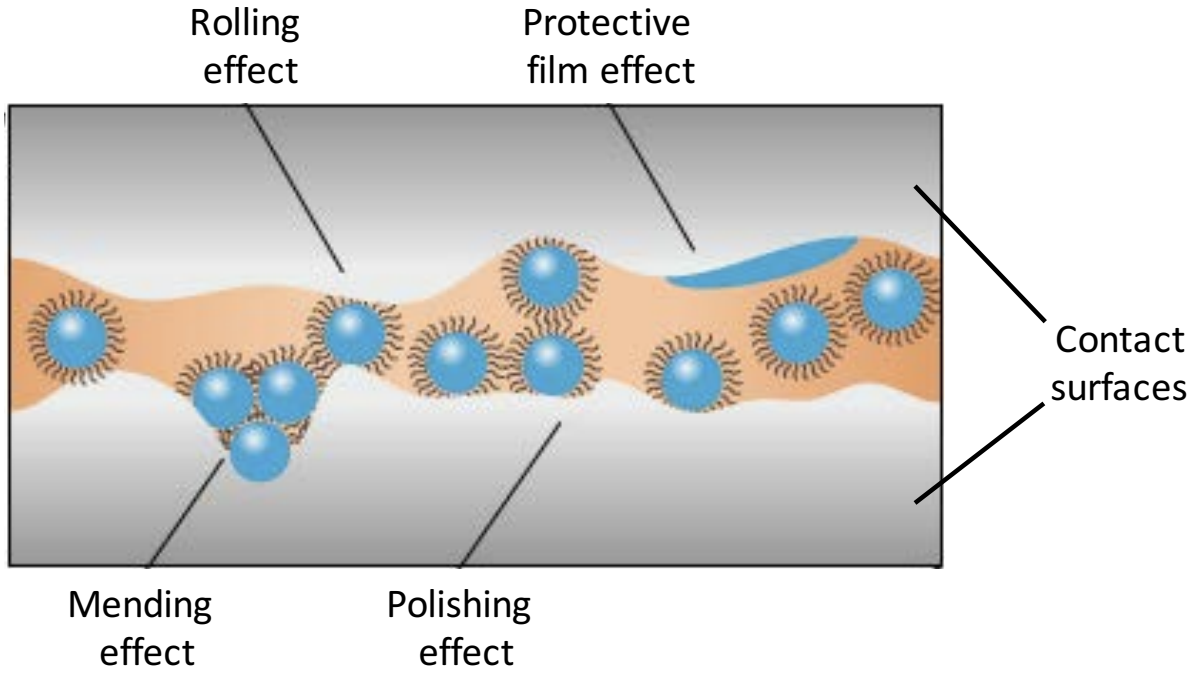


Figure 1.3: Lubrication mechanisms of NPs grafted with amino group organic chains. Adopted from [58].

The performance of nanolubricants is governed by NPs physicochemical properties, size, shape, and concentration [9]. Although the optimum concentration of NPs depends significantly on the application, a concentration lower than 2% has been found efficient in numerous cases [9]. When the concentration of NPs is less than the critical, the NPs cannot form a consistent protective film and smoothen the surfaces [59]. When the concentration of NPs is more than the critical, the contact area has more NPs than those needed, resulting in aggregates formation, uneven NPs distribution, and increased surface roughness [59]. NPs size should be smaller than the surface roughness of the contact surfaces to achieve proper coverage and lubrication [28]. The smaller the size, the better the dispersion stability of the nanolubricant [60]. The shape of the NPs is associated with their lubrication action [28]. Spherical NPs follow the rolling lubrication mechanism [28]. Onion NPs have a dispersion ability better than the spherical thanks to the absence of dangling bonds (unsatisfied valence on an immobilised atom) [61].

Dispersion of NPs into the lubricants is a challenge [9]. Due to their elevated surface energy and the attractive van der Waal interactions aggregation and sedimentation occur significantly weakening the performance of the nanolubricant [55, 62]. Steric repulsion using functionalized polymers (e.g. hybrid nanoparticles), electrostatic repulsion using surfactants, in situ synthesis are used to improve the stability of the nanolubricants [55]. Moreover, magnetic stirring, ultrasonic agitation, homogenization, high-shear mixing, and ball milling improve significantly homogenization and dispersion stability [28]. Polymer grafting is a technique used to control nanoparticles interactions and their dispersion's stability in aqueous and non-aqueous lubricants.

1.4.3 Diarhrodial joints

Diarhrodial joints are complex systems located in many parts of the body, where two bones come together. **Figure 1.4** represents the main parts of a physiological knee joint. The main components are the AC, the SF, and the subchondral bone. AC is a soft, slippery, and deformable thin tissue, which cushions the ends of the bones in diarthrodial joints [63, 64]. SF is the natural lubricant of the joint. It is a tissue fluid, a derivative of blood serum located between articulating AC surfaces [26, 65]. The bony parts of the joints covered by the AC are known as subchondral bones [66]. The subchondral bone lays directly beneath the calcified AC and provides the joint with mechanical support and part of its nutrition [66, 67]. This work is focused on the AC and SF, which are further analysed below.

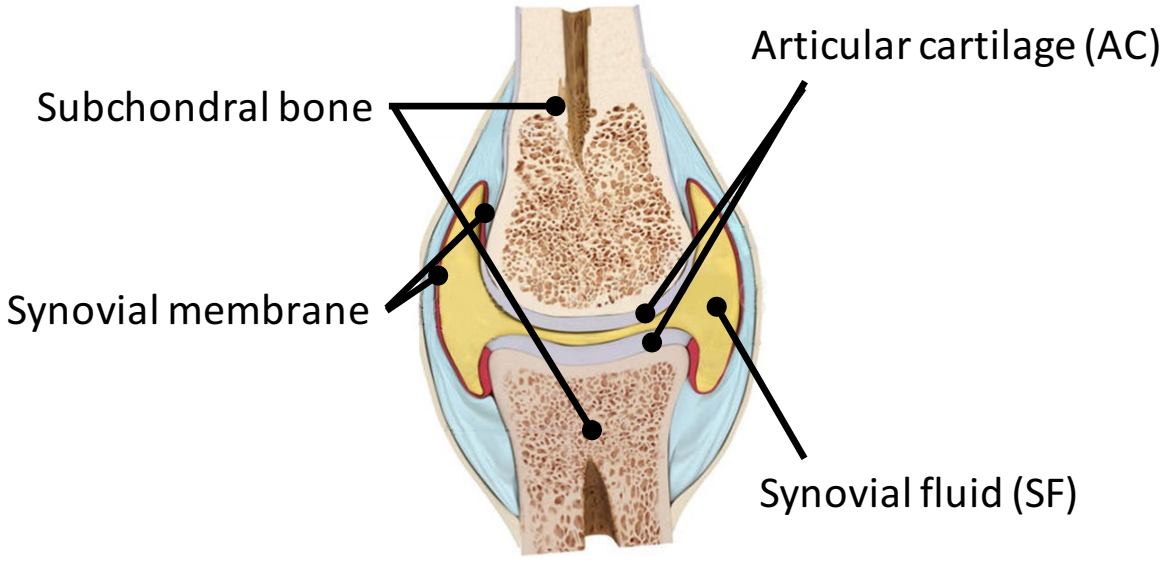


Figure 1.4: Schematic diagram of a healthy knee joint, in which the AC covers the ends of the bones and the SF is viscous enough to separate them. Adopted from [68].

1.4.3.1 Articular cartilage

AC is a multiphasic material. It consists of a solid phase (fibrillar collagen network, proteoglycans), a fluid phase (water), and an ion phase (ionic species of dissolved electrolytes) [69]. Water is its main component, since it consists 65-80% w/w of the AC [64, 70, 71]. Major components of the AC extracellular matrix apart from the water, are a fibrillar collagen network composed of type II collagen (10–20% w/w of the AC), and proteoglycans (10–20% w/w of the AC) [64, 70]. Aggrecans consist 10% w/w of AC and are considered the most important proteoglycans [64]. Other non-collagenous proteins, glycoproteins, and ions of dissolved electrolytes (Na^+, Ca^{2+}, Cl^-) are also present in small concentration [64, 70, 71]. Last but not least, chondrocytes, AC's cells, are 1–5% w/w [64, 70, 71]. Chondrocytes undertake the production, the preservation, "the turnover" of the extracellular matrix (ECM) constituents, and contribute to the movement of the joint [64].

The biomechanical characteristics of AC are ascribed to the ECM components and the AC structure. AC is composed of the superficial, middle, deep and calcified zone [64]. The superficial zone withstands the shearing load and inhibits adhesion [72]. In the middle zone the orientation of the collagen fibres change. The deep zone withstands the compressive load. and the calcified zone joins the AC to the bone and imparts its properties [73]. Moreover, the proteoglycan macromolecules (mainly the aggrecan) and the fibrillar collagen network provide the AC its load-bearing capability [3, 64]. On the contrary, chondrocytes low stiffness indicates that they have no impact on AC mechanical properties [52, 64].

AC provides low-CoF and wear-resistant properties to the joints [63, 64]. The exceptional lubrication AC offers is attributed to its ability to equally distribute the applied load [63, 64]. even under extreme conditions like complete shifts in the moving direction [36]. AC is a load-bearing material allowing the diarthrodial joints to sustain various types of movement (sliding, gliding, rotation) as well as compressive and shear stresses with minimal CoF and wear [63, 64, 69]. More specifically, during movements, AC is able to withstand 2.5-5 times the human body weight [73], compressive pressure up to 20 MPa, and compressive strain up to 40% [64, 74]. For example, tibiofemoral AC, one of the most commonly damaged articulations found in the knee, withstands compression amplitude up to 20% and sliding velocity up to 100 mm s^{-1} during normal activities [26].

Despite its unique mechanical properties, AC exhibits a limited capability of self-healing and repair because it has limited blood vessels, limited lymphatics nerves, poor replicative capacity of chondrocytes and consequently, it takes much longer than other tissues to be repaired [75].

1.4.3.2 Synovial fluid

SF is an aqueous-based mixture of surface-active macromolecules including proteins (albumins and globulins), glycoproteins (e.g. lubricin), phospholipids and HA [76]. HA, γ-globulin, Human Serum Albumin (HSA) and lubricin are the major SF constituents [31]. SF is vital in lubricating the sliding articulating interfaces and the other tissues in joints during loading. SF lubrication is attributed to the hydrodynamic lubrication mechanism, and the boundary lubrication mechanism via the adsorption of its constituents on AC surfaces [76]. Except for the lubrication, SF affects AC

mechanical function. For example, it provides AC with compressive resilience through the negative electrostatic repulsion forces that generate with proteoglycan aggregates [77]. Furthermore, depending on its protein concentration and its pH, it could prevent corrosion in the case of metallic implants [78]. In addition to the lubrication, SF transports nutritional substances as glucose to the AC [77]. SF function is so critical that even small alterations on its structure could lead to arthritis [26, 65].

1.4.4 Mechanical properties of joints

1.4.4.1 Lubrication regimes of joints

The properties of the contact surfaces in every tribosystem, including the diarthrodial joints, affect its lubrication properties [32]. However, those are not the only factors. The surrounding medium and the interactions occurring on it influence joints friction and wear [32]. The diarthrodial joints undergo a combination of lubrication modes, attributed to the lubricating properties of SF (hydrodynamic lubrication), the lubricating properties of the articular surfaces (boundary lubrication), and a combination of those (mixed lubrication) [35, 79].

When the articulating surfaces start moving perpendicular to each other, the viscosity of the SF creates pressure [80]. By pressurising the SF, the load is transmitted across the supported bearing surfaces, minimising the load to be backed up by them, preventing contact between them, and therefore, minimising the CoF and wear [35, 81]. The SF pressure carries 90-99% of the load applied at the beginning of the normal articulation [82]. This mechanism is called squeeze-film lubrication [80].

During the early stages of motion, when no load is applied to the joint, the fluid film /hydrodynamic lubrication is observed. A thick layer of SF separates the AC surfaces completely [81]. In the presence of relative speed between the AC surfaces, the hydrodynamic mechanism dominates. In that case, fluid forces are being generated either because of the AC surfaces or of the SF inserting between them [35, 81]. In both cases, the thickness of the SF film is approximately a micron and changes with the SF viscosity, the applied load, and the topography of the articulating surfaces [29, 81].

During joint's compression, when the velocity starts to decrease and load to be applied, the SF becomes thinner, reaches the edges of the articulating surfaces, and then the elastohydrodynamic lubrication dominates [35]. During the elastohydrodynamic lubrication, the porous articulating surfaces provide load support undergoing elastic deformation and maintaining the SF in place [35].

Under prolonged periods of motion, thin and low viscous SF, low sliding speeds, or increased contact load, the fluid film lubrication mechanism cannot separate the load-bearing AC surfaces effectively. Consequently, the AC surfaces come in direct contact, and the boundary lubrication dominates [29, 83]. The boundary lubricant molecules of the SF (surface active phospholipids (SAPLs), lubricin and HA) adsorbed over the rubbing AC surfaces, reduce the shear strength preventing that way the AC wear, and therefore, the premature joint degeneration [29, 83]. The existence and concentration of proteins like lubricin, albumin, and globulin determine AC lubrication [32, 84]. Moreover, it is thought that in conjunction with them, cytokines and proteases offer excellent joint lubrication [32]. It is evident then that the boundary lubrication mechanism is shaped by the chemical composition and the chemical interactions at

the articulating surfaces, while other parameters like the speed are not so relevant [78]. It is believed that hydration lubrication happens in the joints under boundary lubrication regime thanks to SF macromolecules [85]. Hydration lubrication occurs when water molecules surround the surface of charged macromolecules [86]. The water trapped in those layers sustains its fluidity and is not squeezing out under high load and shear [86]. As such, hydration layers formed between sliding surfaces offer exceptional lubrication properties and capability of withstanding high loads even though they are very thin [86].

1.4.4.2 Mechanical properties of articular cartilage

The healthy articulating surfaces demonstrate excellent lubrication under physiological conditions (CoF=0.001-0.03) [74, 87]. However, the lubrication of the joints is being affected during articulation [26]. At the beginning of the motion, the CoF is very low (<0.01) but increases with time [88, 89] because the SF is squeezed out and the load is transferred to the articulating surfaces [88]. The support from the SF is minimal under low-speed conditions when the fluid has been squeezed out [90]. Additionally, as the contact area increases, fluid pressurisation decreases, and the CoF increases [90]. Apart from the above, it has been reported that the CoF and the adhesion in load-bearing joints are lower than in non-load-bearing regions, possibly due to the existence of higher concentrations of boundary lubricants like lubricin [91]. Last, the stiffness of the healthy AC increases with increasing depth [92, 93].

1.4.4.3 Rheology of synovial fluid

The viscoelasticity of the SF affects joint's lubrication [65]. Although SF is an excellent lubricant, viscosity reduction occurs under dynamic loading of diarthrodial joints during physical activities [94]. The healthy SF is a viscous, stringy non-Newtonian fluid, exhibiting shear-thinning behaviour and no temperature dependence [26, 76]. The high viscosity of the SF is regulated by the HA and its aggregates with proteins [95]. The non-Newtonian behaviour of SF is mainly attributed to the 1.5 nm chain of the COO^- group of HA [26]. The different protein and HA content, the varying molecular weight of HA, and the different constituents found in the SF result in significant variability in the rheological properties [95]. Furthermore, the SF behaves different at low frequency activities like walking compared to high-frequency activities like running [95]. At low frequencies, SF behaves as viscous (molecules through rearrangements and disentanglements release stress), whereas at increasing strain amplitudes at higher frequencies as an elastic and shock absorber (molecules behave as temporary cross-linked networks) [96-99]. Indeed, it has been observed that at low frequencies, the viscous modulus, *G''* is elevated compared to the elastic modulus, *G'*, and their difference decreases as the cross-over is being approached [65].

1.4.4.4 Articular cartilage boundary lubrication

The exceptionally low CoF developed in the joints is attributed to a synergy of the ECM components. **Figure 1.5** is a schematic representation of the boundary lubrication on the AC surface. HA attaches to lubricin and creates complexes capable of remaining at the AC surface under high loading and speed conditions and lubricating it [100-102]. HA forms complexes with the saturated phosphatidylcholines (PCs) of the

SF at the AC surface, creating a protective film capable of withstanding high pressures and preventing CoF increase [103]. PCs expose their hydrophilic heads towards the opposing AC surface providing hydration lubrication [103]. Below the contribution of the individual components of AC and SF to joint boundary lubrication is described.

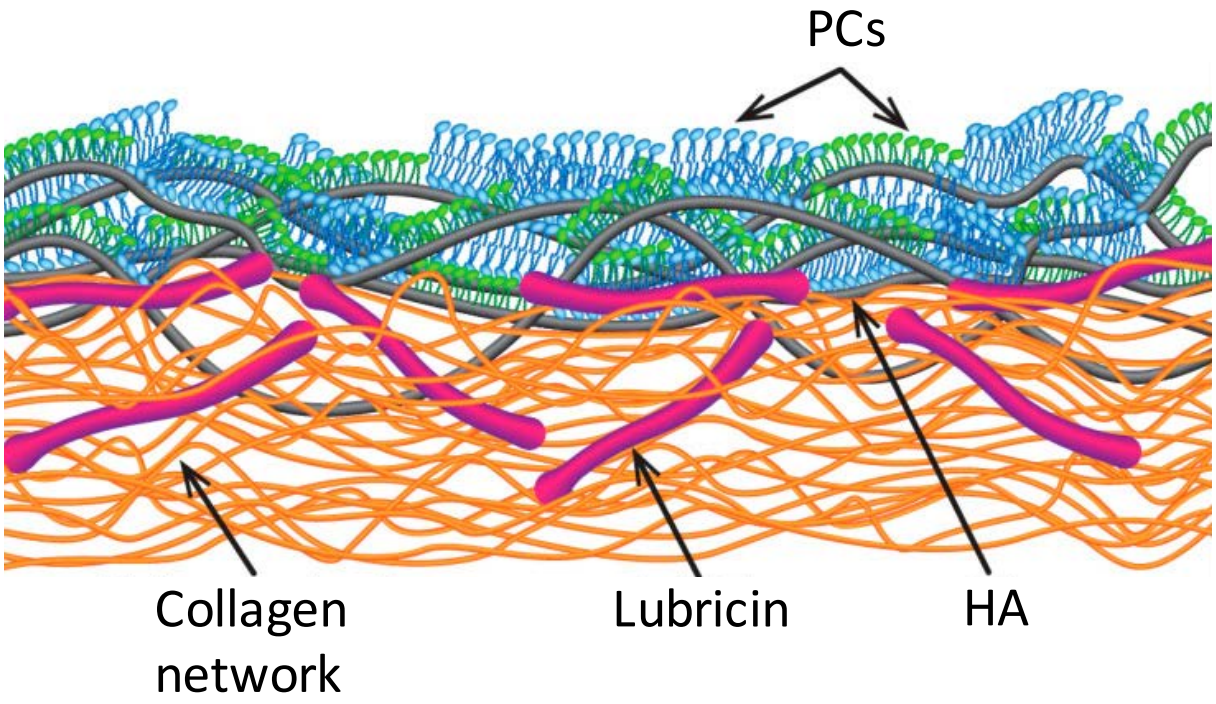


Figure 1.5: Schematic representation of boundary lubrication on the AC. Collagen network is represented with orange colour, lubricin with fuchsia, HA with grey and PCs with green and blue. Adopted from [104].

Hyaluronic acid

HA ($C_{28}H_{44}N_2O_{23}$) is the dominant constituent of the SF, which exists in AC as well. HA is the longest high molecular weight GAG consisting of numerous disaccharide units of D-glucuronic acid-N-acetyl-D-glucosamine proteoglycans [63,

76]. HA's molecular weight ranges from 27 kDa to 10 MDa (Da=1 g mol^{-1}) [105]. **Figure 1.6** displays the chemical structure of the HA.

HA has a bottlebrush structure (polymeric sidechains attached to a linear backbone), providing the SF with its typical viscosity and rheological behaviour [63, 76]. Shear viscosity increases with increasing HA molecular weight and concentration [96, 98], but there are some discrepancies among papers about the exact proportion [106]. The crossover angular frequency of HA decreases as the molecular weight increases because of the faster transition from the viscous to the elastic regime [96, 98]. In general, at short deformation times, the increased molecular weight of HA leads to lower viscosity, stiffness, and elastic response [96].

HA is also a load-bearing and anti-adhesion hydrophilic component, which reduces the CoF and the wear of AC by hydration lubrication [74, 105]. Single HA is not the component that provides AC with its remarkable low CoF because of its inability to remain at its surface under high load and speed conditions [100-102]. However, the HA combined with other biomolecules is a more efficient lubricant [100-102]. For example, HA-aggrecan aggregates reduce the CoF thanks to the powerful bond of the SF hydration sheath to the GAGs chains [107].

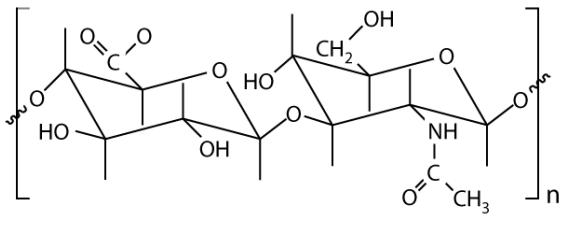


Figure 1.6: Chemical structure of HA. Adopted from [64].

Lubricin

Lubricin (Proteoglycan 4 (PRG4) or Superficial Zone Protein (SZP)) is a glycoprotein that can be found in the SF, the synovial lining of joint cavities, the meniscus, the tendon, and the surface of the AC [64, 108]. Most lubricin is secreted from the ECM tissue into the SF, where it has an average concentration of 200 μg ml^{-1}[109]. A schematic representation of lubricin's structure is displayed in **Figure 1.7**. Lubricin bound with HA are significant in providing boundary lubrication to the joint and preventing cell or protein adhesion [108, 109]. By inhibiting the collagen network damage, it can protect the joint [64, 108]. Additionally, when the joint withstands mechanical forces higher than the normal ones, lubricin synthesis is increased [32]. Tribological measurements on a broad spectrum of materials, have shown that the presence of lubricin could effectively reduce the CoF between two sliding surfaces, and not only between AC surfaces [110]. Lubricin's ability to act as boundary lubricant derives from its vast mucin-like regions, facilitating surface adsorption and consequently lubricin film formation [64, 108]. Steric repulsion between adsorbed lubricin films at the sliding interface is lubricin's action mechanism in reducing CoF and controlling AC frictional behaviour [109].

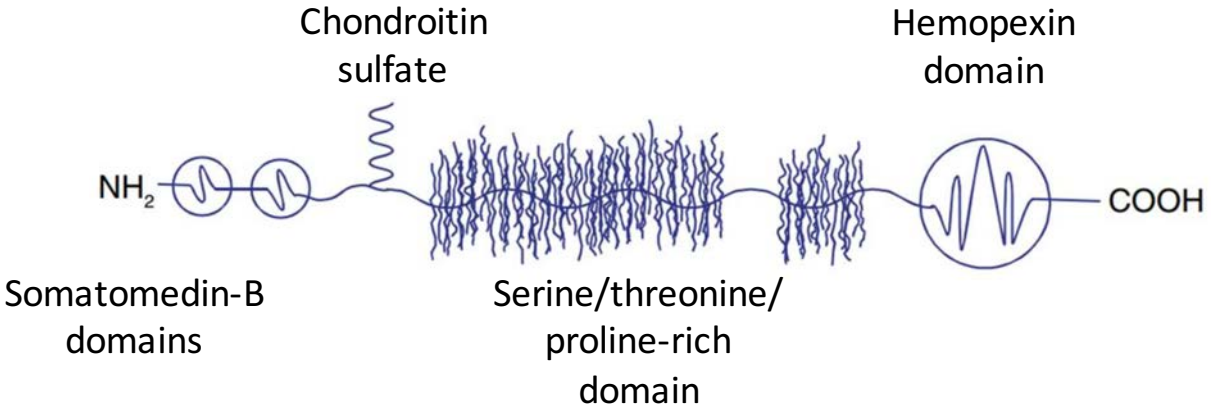


Figure 1.7: Schematic representation of lubricin structure. Adopted from [111].

Γ-globulin

Γ-globulin or Immunoglobulin ($C_8H_7N_2O_4$-HGG) is a major protein constituent, which can be found in the SF in the form of γ-globulin complexes [112]. **Figure 1.8** displays the chemical structure of γ-globulin. Γ-globulin decreases the CoF of the AC in a concentration-dependent manner, thanks to its high adsorption on rubbing surfaces and production of large cohesive forces [31]. The level of γ-globulin in the SF contributes to the increasing the film thickness in the boundary lubrication regime, and therefore, enhancing the joint's lubrication [78].

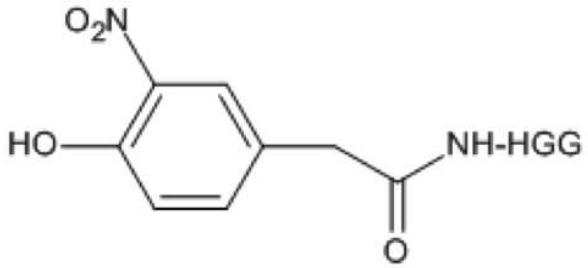


Figure 1.8: Chemical structure of γ-globulin. Adopted from [113].

Human serum albumin

Human serum albumin (HSA) ($C_{123}H_{193}N_{35}O_{37}$) is a dominant protein in the SF, with an approximate concentration of 8 mg ml^{-1} [8]. The chemical structure of HAS can be seen in **Figure 1.9**. HSA has a significant influence in the lubrication of the AC because it creates HA by aggregating at a state of rest [76, 114]. Furthermore, boundary lubrication can be affected by HSA unfolding, which can be occurred by an increase of temperature below the AC surface [8].

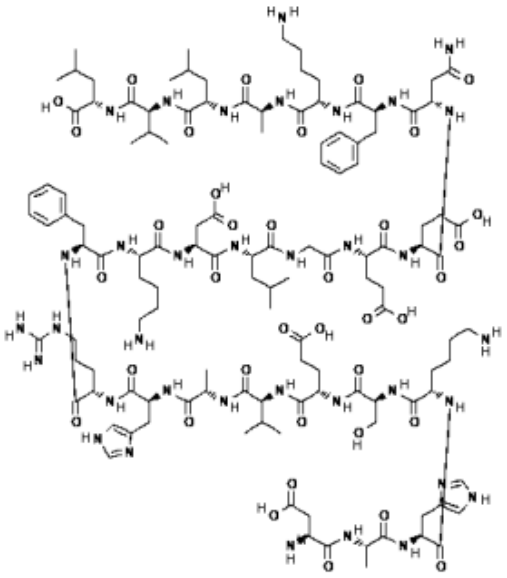


Figure 1.9: Chemical structure of HAS. Adopted from [115].

Surface-active phospholipids

SAPLs are lipids with highly hydrated phosphate head groups and hydrophobic hydrocarbon chains [74], which exist in the SF. The chemical structure of SF's major SAPLs Phosphatidylethanolamine ($C_9H_{18}NO_8P$), Phosphatidylcholine ($C_{44}H_{84}NO_8P$), and Phosphatidylserine (PS) $C_{42}H_{82}NO_{10}P$ are presented in **Figure 1.10**. The SAPLs

are categorized into the PCs, which dominate in SF, and the non-PCs [116]. PCs contribute to joints lubrication since they are less saturated than the non-PCs [105]. The SAPLs act as boundary lubricants; by forming load bearing liposomes with the other ECM components on the upper layer of the AC [117]. Moreover, by adsorbing onto the AC surface, reduce its wettability [29].

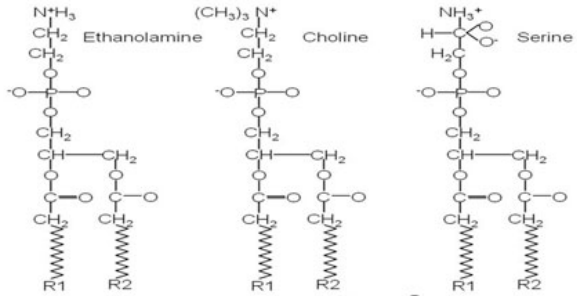


Figure 1.10: Chemical structure of Phosphatidylethanolamide, Phosphatidylcholine, and Phosphatidylserine. Adopted from [118].

1.4.5 Osteoarthritis and its effect on the joints

OA is a pathological condition of the joints and the dominant kind of arthritis. About 8.5 million people in the UK suffering from it [2]. The number of people affected by OA is likely to elevate in the next decades owing to population ageing and obesity [119]. By 2030 OA is anticipated to be the most frequent reason for disability [120]. OA usually occurs on the knee but can arise in any joint, such as the hip, elbow, wrist, ankle, shoulder, spine, hands, and feet joints [121]. Typical symptoms include pain, tenderness, stiffness, soreness, grinding sensation, and swelling [2]. Those symptoms usually worsen with time and prevent patients from doing their daily activities.

OA affects the structural and mechanical functions of the whole joint [121, 122]. Even at the early OA, the biomechanical properties of the joint change at the

nanoscopic scale. **Figure 1.11** illustrates the differences between a healthy and an osteoarthritic knee joint. Calcification of AC (replacement by bone tissue), subchondral bone sclerosis (increased hardness), osteophytes (bony lumps) formation, SF synovitis, ligaments rupture, meniscal extrusion, muscle weakness, and hypertrophy of the joint capsule cause joint degradation and lead to OA [123-125]. A loss and consequently break down of the AC leaves bones exposed [123, 124]. All those pathological changes disrupt the normal joint function, resulting in bones rubbing together, causing pain and consequently disability [126].

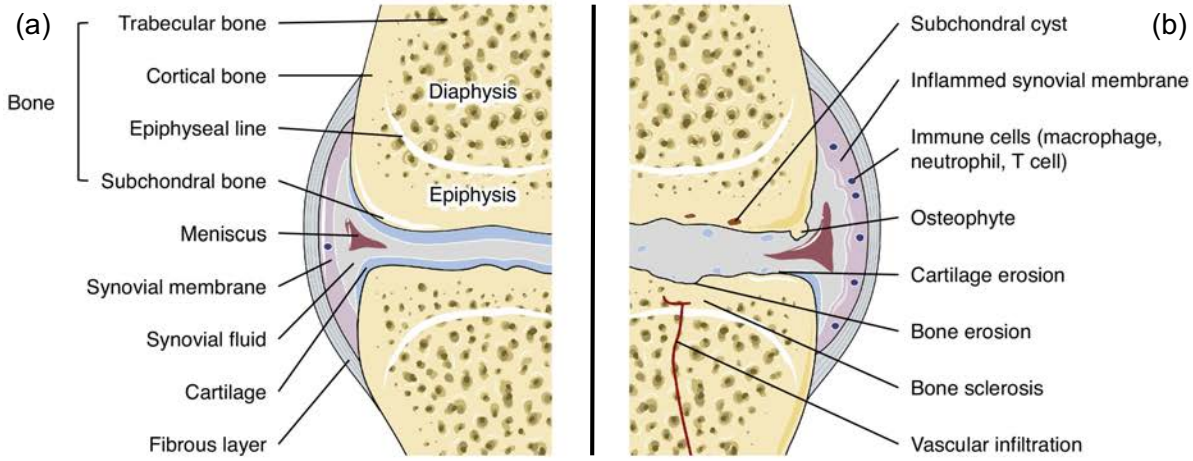


Figure 1.11: Differences between a (a) healthy and (b) osteoarthritic knee joint. Adopted from [127].

The mechanical deterioration of osteoarthritic joints could be attributed to changes in the individual components. For example, the decrease of Γ-globulin [128] and proteoglycan (aggrecan, lubricin) content [69] are related to diminished joints lubrication expressed via increased AC, wear, roughness and decreased stiffness [108, 129]. Likewise, the concentration and molecular weight of HA diminish in individuals with OA, possibly due to its abnormal biosynthesis or its chain free-radical

depolymerisation due to OA [105, 130, 131]. HA concentration ranges between 1 and 4 mg ml^{-1} in physiological SFs and between 0.7 and 1.1 mg ml^{-1} in osteoarthritic SFs [132, 133]. On the contrary, SAPLs increase with OA progression, likely as a natural reaction of the joints following the reduction of the other components [105].

Effect of osteoarthritis on acrticular catilage mechanical properties

A common characteristic of osteoarthritic joints is their poor lubrication demonstrated by increased CoF [134]. During OA progression, the superficial layer, is entirely taken away, disrupting AC's biphasic lubrication mechanism and increasing the CoF of the joint [128]. The decrease in the interstitial fluid pressurisation, and protein content contribute to the CoF increase [63]. The CoF increases with increasing AC degradation until it reaches an equilibrium [63]. The surface roughness of AC is positively associate to the CoF, and as it can be seen in **Figure 1.12**, increases significantly with OA progression [31, 63, 135].

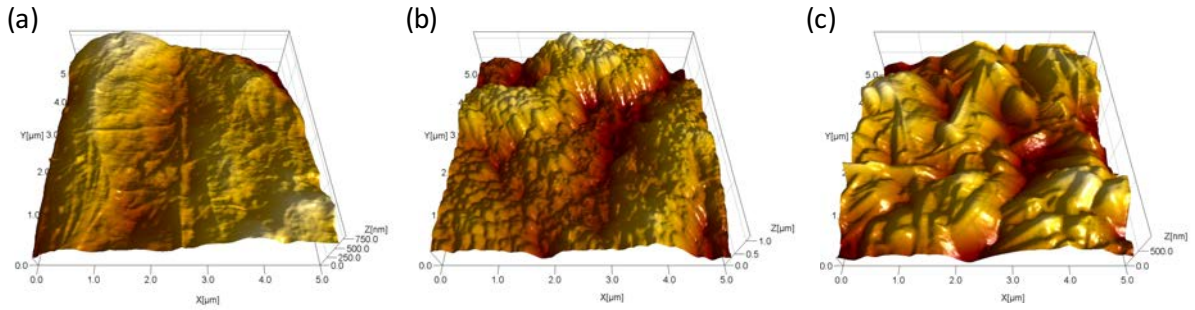


Figure 1.12: Topographies of human AC explants from (a) healthy, (b) mild osteoarthritic and (c) advanced osteoarthritic knee joint. Adopted from [135].

The adhesion between the ECM components at the opposing AC surfaces when they come in contact is an essential mechanical property for AC's physiological

operation and relates to the concentration of the ECM components at the AC surfaces [91]. Adhesion is the ability of a single cell/molecule to stick strongly to another cell/molecule [136]. The adhesion on the AC increases significantly under OA conditions. The collagen network is getting disrupted, and therefore, the adhesion between aggrecan and collagen network increases [137]. In addition to that, in inflammatory arthritis, there is an increase in cell adhesion (e.g. Polymorphonuclear leukocytes), which can be attributed to the breakdown of surface proteins [72]. It has to be mentioned that the level of adhesion molecules like the vascular cell adhesion molecule 1 is a proven indicator of severe OA in the knee and hip joints [138].

Even if the micro-stiffness of the AC remains stable, the nano-stiffness in the surface and the middle layers of AC decreases with OA progression because the fibrillar collagen network is getting destroyed [3, 6, 92, 130]. OA at the early stages affects only the AC surface, leaving the AC nano-stiffness from the middle and deep layers relatively the same as in a healthy AC [92]. Despite the decrease with OA stage, the nano-stiffness at early OA was higher than the nano stiffness of healthy cartilage, requiring further research [139].

Effect of osteoarthritis on synovial fluid rheology

The rheological properties of the osteoarthritic SF are affected by the concentration of SF components, the applied shear, the pH, the temperature, and any impurities [98, 140]. The average steady-shear viscosity ranges from 0.05 to 14.40 Pa s for osteoarthritic SFs [95], whereas for healthy SFs the range is 6-175 Pa s [141, 142]. The decrease in the viscosity is related to a decrease in HA concentration and molecular weight [143]. Similarly, the viscous and elastic modulus are lower in

osteoarthritic than in healthy joints [95]. The deterioration in SF elasticity is more severe than in viscosity, explaining why patients pain more during high-frequency activities, like running rather than walking [95]. Moreover, the cross-over frequency is increased in osteoarthritic SF because it is affected by the concentration and the molecular weight of HA [95]. However, the variability between the rheology of osteoarthritic SFs is wide, and therefore, it is difficult to make safe conclusions.

1.4.5.1 Factors affecting osteoarthritis

The breakdown of AC is a complex process with unknown aetiology. Various factors such as dietary habits, obesity, lifestyle conditions, previous joint injuries, age, gender, metabolism, physical activity, even genetics contribute to OA progression. Below the factors examined in the present thesis are analysed.

Age

The progression of OA with age is a fact. For instance, the number of patients with knee OA increases from 27.4% for those in the 60s to 34.1% for those in the 70s and 43.7% for those over 80 years old [144]. Chondrocytes apoptosis is a characteristic of ageing [145], attributed to increased levels of reactive oxygen species (ROS) [146, 147]. Additionally, the ageing chondrocytes stimulate catabolic activity due to increased expression of matrix metalloproteinases and cytokines [148]. Chondrocytes reduction limits the synthesis of the ECM components and contributes to AC degradation [149, 150]. For example, the decreased content of proteoglycans with age results in reduced dehydration of AC [3, 151] and CoF increase [152]. Moreover, SF composition and biomechanics change significantly with age. For

example, HA concentration decreases with ageing by 10.5% per decade [133], resulting in SF's viscosity reduction [153].

Obesity

Obese and overweight people are at severe risk to develop knee, hip, and hand OA [154, 155]. Body mass index (BMI) and waist-hip ratio (W: H) are commonly utilised criteria of obesity. BMI is not always a factor leading to OA because it considers the total body mass (lean muscle, body fat and bone) and not only the fat [156]. W: H represents truncal obesity [157]. People with BMI above 30 and W: H above 0.9 (for men) and 0.85 (for women) are considered obese [158]. W: H associations with OA independent from BMI were found only for women suffering from knee [159], hip [160], and lower-limb OA [161]. The differentiation from men could be because women' fat is accumulated below the hips, significantly affecting W: H compared to men whose fat is accumulated at the abdominal level [160].

Obesity affects the joints by overloading or destroying the metabolic processes [162, 163]. The quadriceps fail to absorb the applied abnormal load, and the AC is required to withstand greater loads [164]. AC compression activates chondrocytes mechanoreceptors, which initiate inflammatory mediators and, therefore, AC degradation [165]. However, obesity in women is also related to OA in hand, a non-weight-bearing joint [166]. In obesity, truncal adipokines (adiponectin, leptin, resistin, visfatin) are secreted into the systemic circulation at elevated levels and induce joint inflammation and degradation [167, 168]. For example, leptin controls the synthesis of ECM chondrocytes [169] and the production of inflammatory cytokines like IL-1b,

MMP-9, and MMP-13 [170]. The increase in inflammatory cytokines is also associated with alterations in metabolic activity related to OA [156].

Gender

The female gender is associated with elevated OA incidents [171]. Various hormonal and reproductive factors like pregnancy, oral contraceptive use, and hormone replacement therapy, induce OA in normal weight reproductive women [172]. For example, the miRNA content of SF extracellular vesicles in women with OA was lower than men, highlighting reduced estrogen responsivity and decreased ability to innate the immune system [173]. Especially after menopause, the percentage of women suffering from OA is double compared to men (18% vs 9.6%)[174]. The estrogens levels decrease due to ovary deficiency causing structural and functional deterioration on the AC, leading progressively to OA [175]. Moreover, sexual dimorphism might relate to the prevalence of OA in women [176]. For example, women demonstrated lower AC volume [176] and concentration of chondroitin sulphates than men, which provide resistance to AC compression [177]. Women are predominately associated with knee OA because their fat is accumulated below the hips compared to men, whose fat is at the abdominal level [176, 178]. Apart from knee OA, hip, hand and lower-limb OA are associated with obesity in females only [179, 180].

1.4.6 Treatment of osteoarthritis

OA is not treatable yet at its onset. The existing intervention approaches are neither competent enough to treat the damage of the joint entirely nor to decelerate its degeneration. At the early stages of OA, patients follow a pharmacological treatment,

which is focused on pain relief and is not always effective. It includes analgesics that suppress the pain, nonsteroidal anti-inflammatory drugs (NSAIDs) for the inflammatory types of OA and steroids for pain relief in emergencies [181]. The long-term treatment using the last two drug categories is associated with gastrointestinal and cardiovascular side effects [182]. Non-pharmacological approaches are a solution for patients with pre-existing diseases (heart disease, diabetes) who already take many NSAIDs [183]. Physiotherapy [184], hydrotherapy [185], physical activity [183], and vitamin supplements [186] reduce pain, improve joints mobility and increase patients' quality of life [187].

The most effective treatment at the last stage of OA progression is total/partial joint arthroplasty. Arthroplasty is a surgical intervention for patients, who do not benefit from pharmacological and complementary approaches [188]. During arthroplasty a part or the whole joint is being replaced by artificial implants. Even if arthroplasty lasts up to 15 years, clinical complications could occur, leading to bone resorption or mechanical loosening of the prosthetic component and the necessity for a cost-consuming revision arthroplasty [8]. Therefore, there is a need for more effective treatments at early-OA, which can delay or even prevent the need for arthroplasty.

1.4.6.1 Intra-articular injection therapy

IAI is an effective therapy used to recover the SF's viscoelasticity and prevent surgery at the early stage of OA when no other treatment has succeeded to improve the pain [189]. IAI is a minimally invasive targeted therapy, based on in-situ injections of therapeutic compounds in the diseased joint cavity [189]. Limited drug doses are required and, as such, the side effects to the other organs are minimised [190]. In

addition, intra-articular therapy is a solution to the low oral bioavailability and limited absorption nature of the NSAIDs and steroids [190, 191].

Corticosteroids and HA are widely used in the IAI therapy of OA [181]. Corticosteroids in the form of solutions or suspensions of crystals reduce joint inflammation and pain. However, they demonstrate a short retention time (1-4 weeks) and their prolonged use is associated with various side effects, including the destruction of AC [191]. HA injections restore SF's viscoelasticity [76] and load-bearing function [74]. IAI with HA reduces the inflammation and pain for up to six months, and slows down the progression of OA thanks to the chondroprotective abilities and the normalization of HA synthesis [181]. The recovery of the HA concentration in the SF needs up to three days after the injection and is subject to the polymerization and molecular weight of the existing HA [76]. The commercially available HA formulations are hydrogels of HA in water with a molecular weight ranging from 500 kDa (Hyalgan) to 6000 kDa (Hylan GF-20) [131]. Introducing IAI formulations containing the lost ECM components could help the osteoarthritic joint to restore its lubrication properties. Previous studies in animals demonstrated lubricin's excellent capability in enhancing boundary lubrication, inhibiting chondrocytes hypertrophy/inflammation and cell adhesion [192, 193]. Recently, IAI of blood and mesenchymal stem cells was suggested to enhance the natural healing and regeneration of the diseased AC [181].

The prominent drawback of IAI therapy is the short retention time of the therapeutic compounds in the joint caused by degradation [190]. The half-life of an IAI drug is constrained from its low molecular weight and can be from 6 minutes to 6 hours [194]. Small molecules diffuse from the joint via synovial capillaries (blood vessels

transporting nutrients) and macromolecules via the lymphatic system [127]. Prolonged retention time is vital in treating the OA because the drug should weather the surface and access the inner layers of AC prior to its rapid clearance from the SF [195]. The short residence time results in temporary pain relief, and therefore the need for an increased number of intra-articular injections, which are linked to pain, infection risk, and are cost-consuming [187].

Drug delivery systems like biocompatible microparticles/NPs, micro/nanogels, and liposomes increase the half-life of drugs by 10-30 times [14]. **Figure 1.13** illustrates the IAI injection of an osteoarthritic joint and highlights the retention time of the drug in the joints offered by those systems. Microparticles/NPs are the most promising systems because they provide a longer retention time than micro/nanogels [127]. This study is focused on the NPs because their size is within the range of the reported surface roughness of the human AC (137-533 nm) [63, 196]. As such, NPs will not increase the surface roughness of the AC and can smoothen it.

Various studies reported the potential uses of NPs as drug delivery systems in OA. Albumin NPs demonstrated a retention time of several weeks in IAI on diseased joints [63]. Superparamagnetic iron oxide NPs with Polyvinyl alcohol (PVA) coating taken up intracellularly were demonstrated increased retention time [197]. The Naja kaouthia cytotoxin 1 decreased inflammatory biomarkers and resulted in less bone degradation when conjugated with gold NPs [198]. NPs made from various materials can be utilised in the treatment of OA. However, sustained drug release is difficult to be achieved when the drugs demonstrate high affinity to the material of the NPs [199].

Polymer NPs are promising drug carriers for the fight against OA. They can encapsulate every type of drug, increase its solubility and protect it from degradation [195]. Furthermore, they have low levels of immunogenicity and can be biodegradable [195]. NPs made from naturally occurring polymers (e.g. polysaccharides, HA, SAPLs) are biocompatible to biological surfaces, demonstrate minimal CoF/wear and provide additional therapeutic actions [200, 201]. For example, sodium hyaluronate restores SF viscoelasticity, while chondroitin sulphate inhibits the breakdown of AC [15]. NPs made of chitosan, hyaluronic acid, pluronic have been used as delivery systems of anti-inflammatory drugs or genes and provided sustained drug release, increased retention and good solubility [195]. Synthetic polymers (e.g. poly(ethylene glycol), poly(vinyl alcohol), poly(DL-lactic-co-glycolic acid)) demonstrate improved mechanical properties in nanoscale formulations for the treatment of OA compared to the natural polymers [202]. For instance, poly(DL-lactic-co-glycolic acid) NPs improved osteoarthritic joints providing high retention time, sustained release and minimising inflammation [203, 204]. Particles made of Poly-ethyleneglycol increased drug bioavailability inhibited Reactive oxygen species (ROS) increase [205, 206]. Moreover, NPs made from natural polysaccharides like the Phytoglycogen could be utilised as friction modifiers for the joints [207]. Synthetic polymers could also improve lubrication by covalently grafting or physical adsorbing on NPs or other surfaces [201].

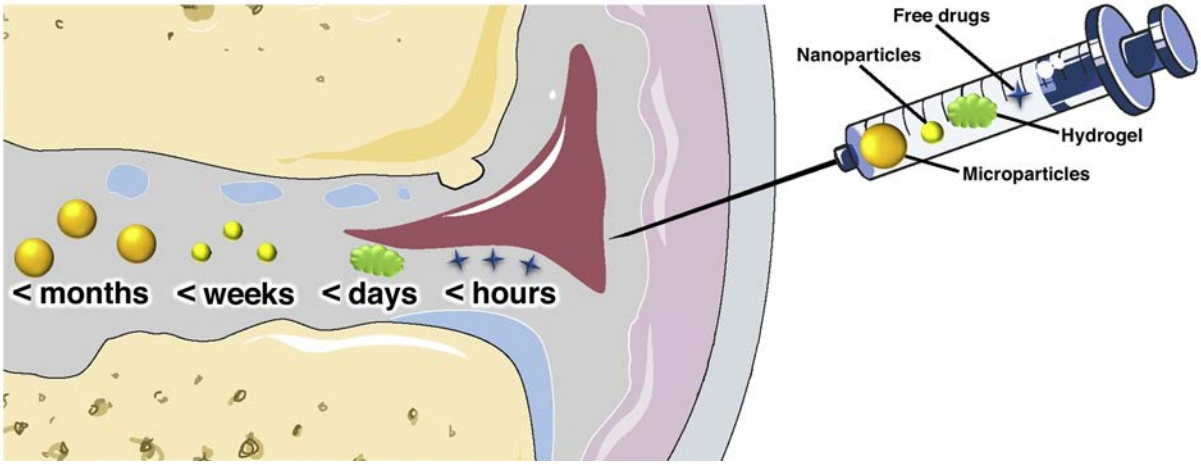


Figure 1.13: Schematic representation of drug retention time offered by various delivery systems to the joints via IAI therapy. Adopted from [127].

Hydrogels have also been used as drug delivery systems in IAI therapy of OA [195]. They are synthetic, or natural (extracellular polysaccharides, proteins) three-dimensional networks of cross-linked hydrophilic polymers [195, 208]. Hydrogels offer increased retention time, controlled drug release, and inhibition of inflammatory cytokines [195]. Moreover, they are excellent lubricants with good solubility and stability at a wide range of temperatures [56]. Hydrogels bind via electrostatic interactions to AC and form polymer brush-like gel layers at its surface, mimic the hydration lubrication happening with AC and SF macromolecules (lubricin, lipids) [209, 210]. They are capable of preventing wear, CoF and withstanding high loads [210, 211]. Hydrogels can even be optimised to remain longer at the AC surface by controlling their pore size, degradation kinetics, or density [212]. Micro-hydrogels have also been used for the development of synthetic SF [213]. Incorporating NPs in hydrogels improves their lubrication performance [214, 215]. Moreover, charged polymer brushes grafted onto drug-loaded mesoporous silica NPs have been tested in many studies as a potential treatment to OA and provided prolonged drug-release and

CoF reduction [216-219]. Grafted NPs with amino and alkyl chains combine the benefits of both groups and demonstrate excellent stability, compatibility with the lubricants, and absorbability to the contact surfaces [212]. For example, silica NPs grafted with amino and alkyl chains reduced the CoF by 40% and the wear scar diameter by 60%, comparing with pure Polyalphaolefin [59]. The polymer grafting principle has been applied to drug-loaded micro/nanogels and liposomes, and demonstrated good lubrication, sustained drug release, and the capability of stimulation with visible light temperature, magnetism, NIR irradiation, energy conversion from joint movement, and ROS [220, 221]. For instance, a mechanism of forming HA-poly(N-isopropyl acrylamide) NPs at body temperature has been developed, which demonstrated high stability, biocompatibility, drug retention time and anti-inflammatory action [222]. Nevertheless, it has to be mentioned that during the grafting processes (e.g. controlled radical polymerization), toxic metallic substances are introduced, which cannot be removed entirely and could be proved dangerous for biological systems [219].

The last years nanocarrier systems received considerable attention as potential therapeutic systems of OA because they can restore joints lubrication and offer pain relief simultaneously. **Table 1.1** summarises those studies. Most of them used mesoporous silica NPs as drug carriers because they are biocompatible, thermally stable and easily functionalised thanks to their large and porous surface area [219]. However, mesoporous silica NPs need a long time to degrade because of their stable structure resulting in long term bioaccumulation and, therefore, toxicity (inflammation, oxidation, organs fibrosis) in the human body [223, 224]. Another limitation of those studies is that the lubrication efficacy of the developed systems was examined on

implant materials (Ultra-high-molecular-weight polyethylene (PE), polytetrafluoroethylene (PTFE), silicon wafer, titanium), which do not mitigate the tribological behaviour of the complex AC surface properly. Only one study explored the lubrication effect of the nanocarrier on bovine AC [225] but not none on human AC. Likewise, the capacity of the drug to delay the progression of OA has only been tested limited times *in vivo* and only in rats [217].

Table 1.1: Summary of reported nanoparticle formulations for simultaneous pharmacological treatment and lubrication improvement of joints.

Nanocarrier	Drug type	Size (Avg)	Tribological testing method	Clinical testing method	References
Azobenzene/β-cyclodextrin-modified poly(2-methacryloyloxyethyl phosphor- ylcholine) - modified mesoporous silica nanoparticles	DS	150.0 nm	PTFE ball-silicon wafer disk	*In vitro*: MC3T3-E1 cells, mouse dermal tissue	[221]
Poly (2-methacryloyloxyethyl phosphor- ylcholine)-grafted mesoporous silica nanospheres	DS	260.0 nm	Tribopair: PE ball - Titanium disk Contact pressure: 26-41 MPa	*In vitro*: rat knee chondrocytes *In vivo*: rat knees	[217]
Chitosan- 1,3 propane sulfonate nanoparticles	Aspirin	171.8 nm	Tribopair: PDMS ball- Titanium disk & fresh bovine cartilage pair Normal load: 1 N	*In vitro*: C57BL/6 mouse mesenchymal stem cells	[225]
Poly(N-isopropylacryl-amide-2-methacryloyloxyethyl phosphorylcholine) nanospheres	DS	237.0 nm	Contact pressure: 12.2-33.2 MPa Tribopair: PTFE ball -silicon wafer	*In vitro*: murine cytokines-treated chondrocytes	[226]
D-glucosamine sulphate - loaded 1,2-distearoyl-sn-glycero-3-phosphocholine liposome mesoporous silica nanospheres	DGS	120.0 nm	Tribopair: polystyrene microsphere-silicon wafer	*In vitro*: mice knee chondrocytes	[227]
3-dimethyl-(2-(2-methylprop-2-enoyloxy)ethyl) azaniumyl) propane-1-sulfonate polymer (pSBMA) mesoporous silica naparticles	RhB	100.0 nm	Tribopair: PTFE ball and Titanium disc Contact pressure: 15.4-24.4 MPa	N/A	[228]

Nanocarrier	Drug type	Size (Avg)	Tribological testing method	Clinical testing method	References
Mesoporous silica naparticles grafted with poly (2-methacryloyloxyethyl phosphocholine)	RhB	590.3 nm	Tribopair: PTFE ball - Titanium disc Normal load: 1-4 N	N/A	[223]
Poly (3-sulfopropylmethacrylate potassium salt)-grafted mesoporous silica nanoparticles	DS	114.0 nm	Tribopair: PE ball – Titanium disk Contact pressure: 26.0-43.8 MPa	*In vitro*: rat knee chondrocytes *In vivo*: rat knee	[219]
Dopamine methacrylamide and 2-methacryloyloxyethyl phosphorylcholine coated methacrylate gelatin hydrogel microspheres	DS	150.0 μm	Tribopair: PTFE ball - silicon wafer disc Normal load:12 N	*In vitro*: rat chondrocytes *In vivo*: rat knee	[229]
Poly (dopamine methacrylamide-sulfobetaine methacrylate)- grafted gelatin methacrylate sphere	DS	100.0 μm	Tribopair: PTFE ball -Titanium disc Normal load: 5 - 10 N	*In vitro*: rat chondrocytes *In vivo*: rat knee	[230]
Distearoyl phosphatidylcholine coated mesoporous silica nanoparticles	RhB	384.0 nm	Tribopair: PE ball - Titanium disk Contact pressure: 26-41 MPa	*In vitro*: MC3T3-E1 cells	[231]
P-sulfonato-calix(4)arenes -capped betaine-modified mesoporous silica nanoparticles	RhB	100.0 nm	Tribopair: PTFE ball -Titanium disk Normal load:1-3 N	*In vitro*: rat chondrocytes *In vivo*: rat knee	[230]
Poly(3-sulfopropyl methacrylate potassium salt) hollow silica nanoparticles	Aspirin	422.0 nm	Tribopair: Steel ball - steel disc Contact pressure:1.66-2.64 GPa	*In vitro*: Hela cells	[231]
Poly(3-sulfopropyl methacrylate potassium salt) grafted poly(N-isopropylacrylamide) microgels	Aspirin	576.0 nm	Tribopair: PDMS ball - silicon wafer disk Normal load:1-10 N	*In vitro*: Hela cells	[220]
Poly (N-isopropylacry-lamide) nanogels	N/A	70.0 nm	Tribopair: PDMS ball - silicon wafer disk	N/A	[218]
Azobenzene/β-cyclodextrin-modified poly(2-methacryloyloxyethyl phosphorylcholine) -modified mesoporous silica nanoparticles	DS	150.0 nm	PTFE ball-silicon wafer disk	*In vitro*: MC3T3-E1 cells, mouse dermal tissue	[221]

DS: Diclofenac sodium, RhB: Rhodamine B, PDMS: Polydimethylsiloxane

1.5 Summary

OA is a pathological condition of the joint, which progresses with time, causing severe pain and disability. Osteoarthritic joints demonstrate poor tribological performance associated with pain. The CoF and the wear between the opposing AC surfaces elevate, while the viscosity of the SF reduces significantly. Alterations in SF and AC are happening in the nanoscale from the early OA. SF degeneration contributes to AC degradation [65], but limited research has been done on its nanomechanical properties apart from its rheological performance.

Various factors, including age, obesity, and gender, contribute to OA, but the exact degradation mechanism is unknown. Previous studies identified relationships between the stage of OA and the mechanical degeneration of the joints. However, the relationship between those is unclear because of the interelationship between the different ECM constituents and the differences arising from different patients and different joint regions.

Despite the severity of OA, there is no cure yet. Surgical replacement of the joints with implants is the only solution when the disease has progressed to its latest stage. Currently, the most effective treatment at the initial phase of OA is the IAI of the therapeutic compounds directly in the joints. The main drawback of this therapeutic approach is the limited retention time of the drugs in the joint cavity and the resulting temporary pain relief. Moreover, IAI supplements cannot treat the increased CoF of the joint during low-velocity movements like walking because they are squeezed out of the joint.

NPs are promising components for the improvement of the IAI formulations. They are known drug delivery carriers and could prolong the release of the therapeutic agents in the joint. A few recent studies proved their efficacy *in vitro* and *in-vivo* in rats. Additionally, there is evidence that NPs can reduce the CoF in the joints since they are excellent lubricant additives for other systems (e.g. industrial oils). NPs lubrication mechanism is not clear, although there are some theories. Their performance is governed by their physical properties (size, shape, concentration) and the mechanical properties of the contact surfaces (surface roughness, Young's modulus). Very limited NPs-based systems were reported offering both pharmacological treatment and improved lubrication, and those were mainly tested *in-vitro;* therefore, further development in this field is suggested.

2. METHODOLOGY

This chapter describes the fundamentals, operating procedures, and applications of the main analytical techniques employed in this thesis.

As described in section 1.4.4.1, joints undergo a combination of lubrication modes covering the whole span of the Stribeck curve [35]. **Figure 2.1** shows the experimental techniques used in this thesis to examine the lubrication regimes of the joints. In hydrodynamic lubrication, viscoelastic properties mainly affect the thickness of the synovial fluid (SF) and its ability to withstand load - those were studied with rheology. In boundary lubrication, properties like adhesion and stiffness were studied with the Atomic Force Microscope and friction with tribometers. In the mixed lubrication mode, there is a partial contribution of the articulating surfaces and SF on the support of the applied load. Therefore, articular cartilage (AC) and SF properties are essential in this mode, which were studied with all the above-mentioned techniques.

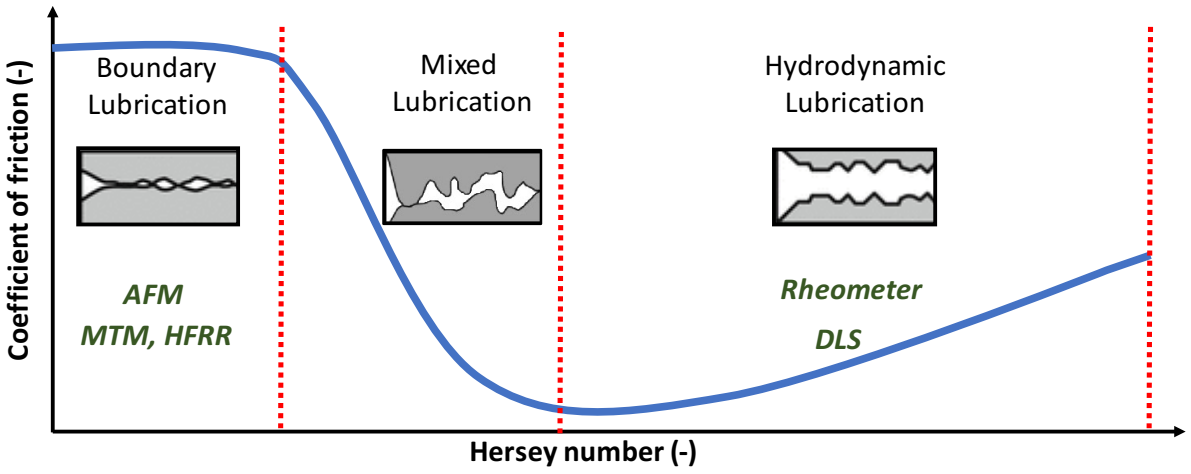


Figure 2.1: Experimental techniques used for the study of joints based on the Stribeck curve.

Another objective of the dissertation is to develop a NPs formulation to treat osteoarthritis (OA). This suspension needs to be effective under every lubrication regime. Its viscosity was designed to resemble that of the healthy SF so it can operate effectively under hydrodynamic conditions. Therefore, rheology was used to measure its viscosity. Dynamic Light Scattering (DLS) was also employed to ensure that the formulation is stable under hydrodynamic lubrication. Besides, the NPs were designed to adsorb to the AC surfaces and operate as friction modifiers under boundary conditions. Tribometers were employed to evaluate the performance of the NPs as friction modifiers.

2.1 Atomic Force Microscopy

2.1.1 Introduction to Atomic Force Microscopy

Atomic Force Microscopy (AFM) is part of a collection of microscopy techniques called Scanning Probe Microscopy (SPM). SPM includes also Scanning Near field Optical Microscope (SNOM), and Scanning Tunnelling Microscope (STM) [232]. SPM, which was first reported in 1986 [233] measures a range of properties, including structural surface features (morphology, roughness, cleanliness), and local mechanical properties (adhesion, adsorption, elasticity) [234]. SPM uses the localised interactions developed between a sharp probe and the sample's surface to create a signal that is translated to a map of a specific property e.g. topography of the sample with high resolution (nanoscale) [232, 234]. The main advantage of SPM compared to other characterisation techniques (e.g. Scanning Electron Microscopy (SEM)) is its capability of combining imaging surface topographies with localised mechanical/electrical measurements [234].

AFM enables simultaneous measurement of local mechanical properties (e.g. adhesion, stiffness) and quantitative structural surface features without perturbing the surfaces in contact [235]. As such, it enables the study of intermolecular interactions and even offers sample manipulation at the nano-scale level. AFM investigates samples with a wide range of surface roughness and not only atomically flat like other SPM techniques. AFM exhibits high spatial resolution, superior force sensitivity and versatility in various applications [236]. It achieves the unprecedented resolution of 1 nm in the lateral and 0.1 nm in the vertical direction [237] while being capable of measuring forces with pico-newton sensitivity [238]. For comparison, the optical microscopy has a resolution of 200 nm. Its most significant advantage is its capability of working under air, liquid, vacuum and at various temperatures [238], permitting the investigation of biological samples under their physiological conditions at high resolution [63]. That explains the widespread use of AFM in the investigation of proteins [239], DNA [240], and living cells [241]. AFM has also been used to evaluate the alterations in the structure, function and surface morphology and wear of joints' under OA [83, 107]. More specifically, AFM provided information about AC stiffness [242], adhesion [29, 91, 137], and coefficient of friction (CoF) [91, 243]. Finally, AFM has started getting used during arthroscopic procedures as a slightly invasive diagnosing tool, which can detect changes in AC nanomechanical properties at the early stages of OA [126].

2.1.2 Atomic Force Microscope cantilevers

Micro-fabricated cantilevers, acting as the probes for measuring interactions, are core elements for AFM. The cantilevers are V-shaped, or rectangular springs

mounted on micro-chips [232, 244]. They are approximately 100 μm long and usually made of silicon (Si) or silicon nitride (Si_3N_4), which possess suitable mechanical properties like high Young modulus and yield point and act as mirrors for the laser [232, 244]. The cantilevers have a coating of an anaclastic material (e.g. aluminium, gold), which makes them easily identifiable under the AFM camera [232]. Cantilevers carry a pointed tip of 5-50 nm at their free end, which could have various shapes, including pyramid and cylindrical cone [232]. A wide range of cantilevers is available in the market. Cantilevers are selected for specific applications primarily based on their spring constant, which defines their measurement quality [244]. **Figure 2.2** is an image of a representative AFM probe captured via SEM.

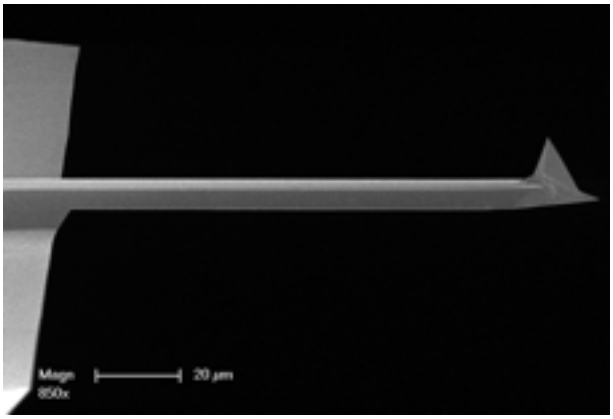


Figure 2.2: SEM image of an AFM probe.

The radius and the shape of the tip are of great importance because AFM measurements are solely based on the interactions between the tip and individual molecules. The smaller its radius and the higher its aspect ratio (width : height), the better the AFM resolution [232]. For example, if the radius of the tip is greater than the surface's asperities, then the asperities cannot be imaged. Following the same principle, AFM cantilevers should be as clean as possible. Impurities contaminate the

tip and increase its size resulting in a compromised magnitude of interaction, false force curves and reduced imaging resolution [232]. Even new cantilevers require cleaning because they are contaminated from the PDMS coated surface that keeps them fixed inside the plastic boxes [232] and they attract airborne contaminants as soon as they get in contact with the environmental air [232].

2.1.3 Atomic Force Microscope working principle

The working principle of the AFM is represented in **Figure 2.3**. The scanning is initiated when the cantilever's tip touches the surface of the sample, guided by a piezoelectric actuator (Z-piezo) [232]. The actuator triggers either the sample or the cantilever. The developed tip-sample forces deflect the cantilever towards or away from the surface accordingly [244]. A laser beam directs to the cantilever and detects its movement [232]. The cantilever shifts with force application and the reflection angle of the laser beam is shifted. That reflection is collected by one of the four quadrants of a photodetector [232, 245]. The left-right and top-bottom difference in the photodetector provide the lateral deflection and the vertical deflection values of the cantilever, respectively [232]. The cantilever's deflection is proportional to the detected signal. A small change in the bending angle corresponds to a significant deviation [245]. The cantilever's deflection is converted to an electrical signal, from which three-dimensional topographic images can be acquired, and the forces curves can be generated [238]. The controller adjusts the difference between the setpoint and the cantilever's actual height taking into account the sample's surface height differences.

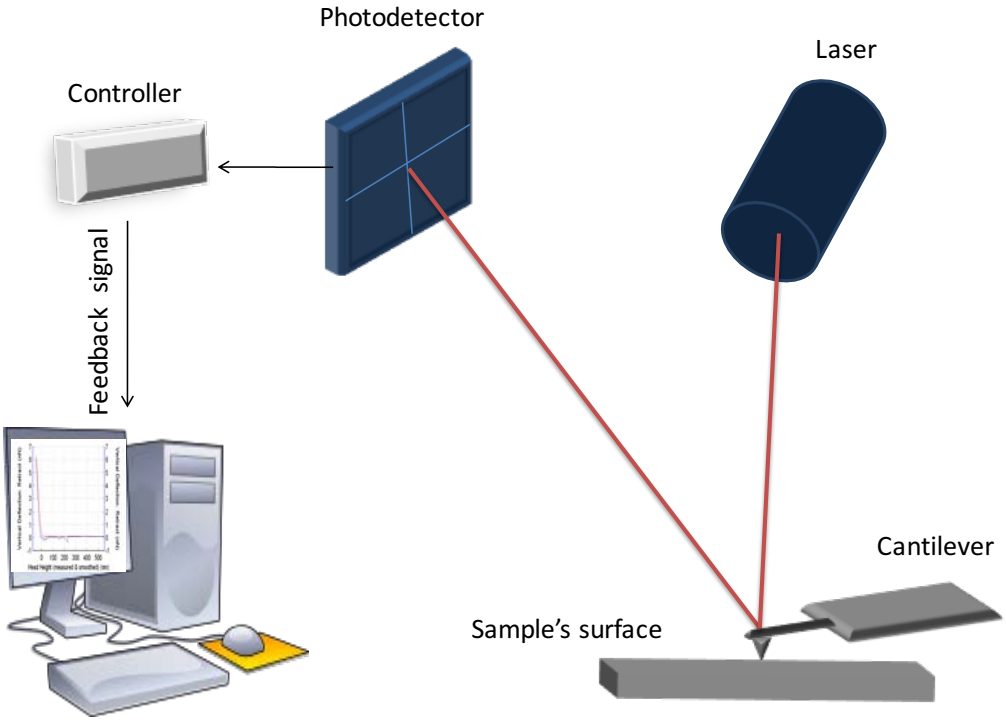


Figure 2.3: Schematic representation of AFM basic principle.

2.1.4 Imaging modes

AFM images represent the topography of an area ranging in size from less than 1 nm^2 to 10^4 μm^2 [246]. AFM imaging modes could be grouped into static or dynamic based on the cantilever's movement [238]. Contact, intermittent-contact, and non-contact are the most commonly used AFM imaging modes. **Figure 2.4** illustrates the way of working of those imaging modes.

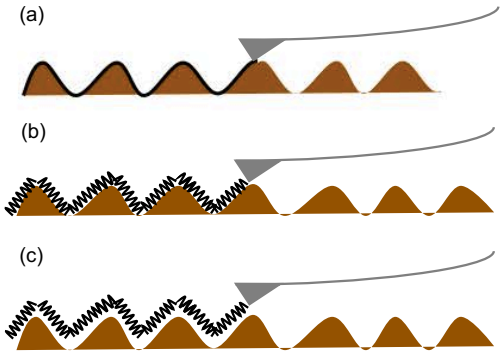


Figure 2.4: AFM imaging modes (a) contact mode, (b) intermittent-contact mode, and (c) non-contact mode.

The static/contact mode is considered the fastest AFM imaging mode [232]. It provides good resolution in ambient and liquid environments, but it is significantly affected by capillary forces in the ambient. Contact mode is mainly used on flat and hard surfaces because the high lateral forces developed can impair the sample's surface morphology [232, 234]. In that case, the tip touches the sample all the time (**Figure 2.4a**) [234]. Contact mode can be applied with fixed setpoint of force or height [232]. The applied force remains constant in the constant force mode by keeping the cantilever's vertical deflection fixed [232, 234]. During imaging, the controller monitors the deflection, and in case it is not the same as the given setpoint (vertical deflection of the cantilever), then the Z-piezo is adjusted (controls distance between cantilever and sample) [232]. During imaging, the setpoint can be controlled. A higher set point means higher forces are applied. On constant height mode, the Z-piezo position is fixed, and because of that, only atomically flat surfaces can be imaged without destroying the cantilever and produce higher resolution images than the constant force mode [232].

On dynamic modes (intermittent-contact, non-contact), the cantilever oscillates in a sinusoidal motion around its resonant frequency [232]. In addition to the topography, dynamic modes provide qualitative mechanical properties (e.g. stiffness, adhesion) for the samples via phase signal image (difference between actual cantilever's position and the tip-sample interactions signal) [232, 234].

Intermittent-contact mode is ideal for imaging soft and fragile samples (e.g. biological samples) or samples with weakly adsorbed molecules on their surface because the lateral forces are lower than the in contact mode [232, 238]. For intermittent-contact mode in ambient, a cantilever stiffer (20-75 N m^{-1}) than intermittent-contact in liquid or contact mode (0.01-2 N m^{-1}) is needed because when imaging in air, water is condensed on the surface of the cantilever and the substrate and develops strong capillary forces upon contact [232]. In intermittent-contact mode, cantilever-sample contact is only periodically (**Figure 2.4b**) [232, 234]. The setpoint is the oscillation amplitude, and so, higher setpoint results in lower applied forces. When the cantilever touches the surface during scanning, the amplitude changes and the Z-piezo adjusts the height to match it [232].

In non-contact mode, although the cantilever oscillates very close to the sample, there is no contact between them. Therefore, non-contact is the least destructive mode and often used on soft biological samples. However, it is not widely used because cantilever-sample attractive interactions when in close proximity make the imaging challenging [232, 234]. Additionally, the non-contact mode has a shorter oscillation amplitude compared to the intermittent-contact mode denoting that it is more difficult for the cantilever to pull off from the cantilever-sample contact, deteriorating image

quality [232]. The attractive forces between cantilever and sample create a phase shift between oscillatory and driving frequency, triggering the Z-piezo to read just the height by pulling away from the cantilever and retaining stable frequency [238].

2.1.5 Force spectroscopy

The most significant advantage of AFM compared to any other microscopy technique is its capability of measuring forces developing between the tip and the substrate with high sensitivity [238]. Those forces are in the range of pico to micro Newton [238]. Moreover, in force spectroscopy the lateral forces are minimum. The only disadvantage is the cantilever's slow movement compared to contact mode imaging [238].

With the aid of Z-piezo, the cantilever approaches the sample's surface vertically, and when those are in contact, it applies a given force (set point) to the sample before retracting away [232]. The cantilever's deflection during the tip-sample contact is monitored and displayed on the y-axis of a force curve against Z-piezo displacement on the x-axis [232]. **Figure 2.5a** represents a typical force curve for a hard substrate, while **Figure 2.5b** is a real force curve between a Silicon Nitride cantilever and a Cobalt-chromium (CoCr) alloy in Phosphate-buffered saline (PBS).

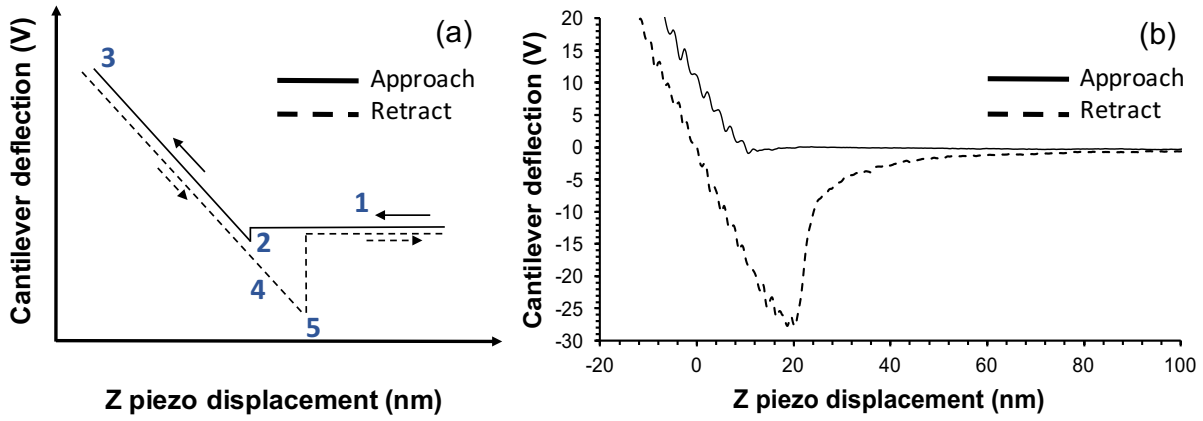


Figure 2.5: (a) Schematic representation of typical force curve for a hard surface, and (b) real force curve for PBS between a Silicon Nitride cantilever and a CoCr alloy substrate.

At position 1 ("free level"), the cantilever approaches the sample, but it is away from it, so no tip-surface interaction forces exist [232]. When the cantilever approaches the sample, attractive or repulsive interaction forces are developed between them, causing a downward or an upward movement of the cantilever, respectively [232]. Up to the point those forces are weaker than the cantilever's stiffness, the cantilever returns quickly to its "free level" position, and there is no tip-sample contact, but when they are stronger the cantilever jumps to contact with the sample (position 2-"jump-to-contact") [232]. The attractive interaction force at position 2 is illustrated with a negative peak on the force curves (**Figure 2.5**). When there are no interaction forces, the "jump-to-contact" point cannot be distinguished in the force curve [232]. During the tip-sample contact, repulsion forces start to develop between the electrons of the opposing materials, which are displayed as positive movement on the force curve (position 3) [232]. The cantilever's retraction follows the same path with the approach initially but stays in contact with the surface longer [232]. On hard, not easily deformable samples, an adhesion peak higher than the approach curve is usually observed. At that point

(position 4), adhesive forces hinder the cantilever's retraction from the sample's surface, creating a hysteresis between the approach and retraction curve [232]. When the cantilever's stiffness/spring constant becomes stronger than the adhesive forces (position 5), the cantilever comes off the sample's surface and returns to its free level position [232]. Cantilever's deflection at position 5 is used to calculate adhesive forces. The adhesion energy is the area the adhesion peak covers between the approach and the retract curve. However, each sample produces its unique characteristic curve that could be significantly different from the one described here.

For an accurate calculation of the detected forces the Z-piezo displacement needs to be converted to distance using the cantilever's sensitivity (slope). The sensitivity is measured on stiff non-deformable surfaces like mica at the tip-sample contact region [232]. Since AFM cantilevers resemble springs, Hooke's law models their motion [238]:

$$F = -k_c\, Q \qquad (2.1)$$

where F is the restoring force (N), k_c the spring constant and Q the deflection of the cantilever. Cantilever suppliers provide an approximate nominal spring constant but the exact spring constant value is found through calibration methods like the thermal tuning. Thermal tuning, correlates the spring constant to the cantilever's thermal/Brownian motion [247]. During that method, the cantilever driven by thermal noise oscillates close to its resonance frequency in a series of frequencies sweeps [248].

Force spectroscopy can also be applied with microspheres and other molecules (e.g. protein molecules) attached at the end of the cantilevers instead of the tip [232]. Those cantilevers are known as colloidal probes, and their usage is a common technique for measuring particle-particle or molecule-molecule interactions on the molecular level [232]. **Figure 2.6** depicts a colloidal probe with an attached borosilicate glass particle of 22 μm. Colloidal probes are used for AFM nanoindentation measurements and offer a high spatial resolution, which is especially important for heterogeneous biological samples like the AC [249, 250]. The force curves taken using colloidal probes are used to measure the elasticity of materials [251]. More specifically, the approach curves are used because they are free from interactions (e.g. adhesion) and enable the determination of the indenter-sample contact point [252]. The Z-piezo-vertical deflection slope is used to calculate the indentation depth [251, 252]. Then, the curve is fitted with a contact mechanics model (e.g. Hertz) [252]. The indenter's shape, size and Poisson ratio are provided to the JPK DP software to calculate elastic properties like Young's modulus [252].

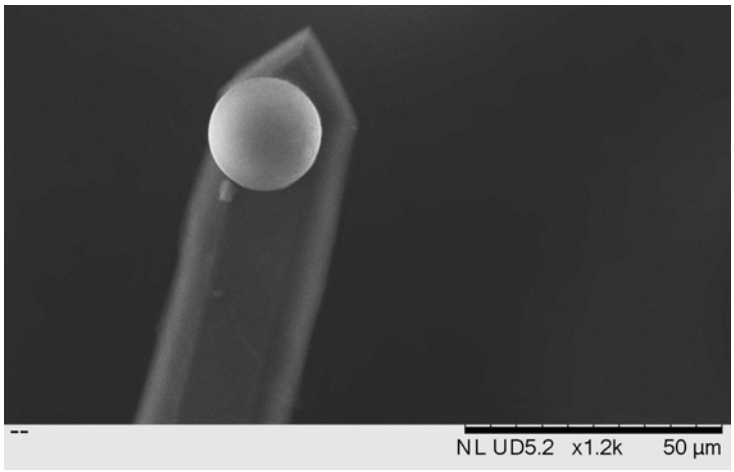


Figure 2.6: SEM picture of a typical colloidal probe with a borosilicate glass particle.

2.2 Tribological testing

2.2.1 Mini-Traction Machine

Mini-Traction Machine (MTM) (MTM2, PCS Instruments, UK) is a commercially available benchtop tribometer capable of measuring various materials tribological properties. It has been widely used for the study of engine oils [253], foods [254], and cosmetics [255]. The standard configuration consists of a disc and a ball with 46 mm and 19.05 mm diameter, accordingly. Instead of balls, pins can also be loaded. Pure sliding, pure rolling, or a combination of both conditions could be achieved thanks to the ball's and disc's motors capability to move independently. The Slide-Roll-Ratio (SRR) describes the sliding/rolling conditions and is calculated using the equation:

$$\mathrm{SRR} = \frac{u_\mathrm{s}}{U} = \frac{|u_\mathrm{b} - u_\mathrm{d}|}{0.5\ (u_\mathrm{b} + u_\mathrm{d})} \qquad (2.2)$$

where u_s: sliding speed (mm s^{-1}), U: entrainment speed (mm s^{-1}), u_b: ball speed (mm s^{-1}), and u_d: disc speed (mm s^{-1}). SRR ranges from zero (only ball moves) to two hundred percent (only disc moves).

MTM's working principle is similar to any other tribometer. **Figure 2.7a** is a schematic representation of MTM and Figure 2.7b an actual picture of the machine. A disc is placed in the sample holder and a ball is located at a small contact point with it. A lubricant is added between those surfaces in quantity enough to cover the disc's surface (minimum 12.5 ml). A volume reducing insert is used to cover the space between the end of the disc and the holder's wall, reduce the required sample's quantity and eliminate the dead zones, enabling homogenous measurements. The

sample holder is secured with two lids, which ensure that the lubricant's temperature remains stable, and evaporation is prohibited. A water bath attached to the MTM's pot jacket and controlled by the PC achieves the desired temperature. When the test starts, the lubricant warms up and only when it reaches the desired temperature, the friction test starts. As the surfaces move, a force is applied to the upper specimen, and a force perpendicular to the normal load (friction force) starts to develop. A force transducer captures the friction force, and the software automatically calculates the CoF . The measurement is repeated six times without unloading, and the acquired Stribeck curves are alternating between ascending and descending. In addition to the friction force, the MTM measures the applied normal load, wear, lubricant's temperature and electrical contact resistance (if available) using high sensitivity sensors.

The measurement profile is set on the software and includes the SRR%, the normal load, the lubricant's temperature, and specimens speed. Two types of tests can be applied in MTM. In the first one, the speed increases under fixed normal load and in the second one the normal load increases under fixed speed. The applied load in the MTM ranges from 1 to 7 N and the speed from 1 to 1000 mm s^{-1}.

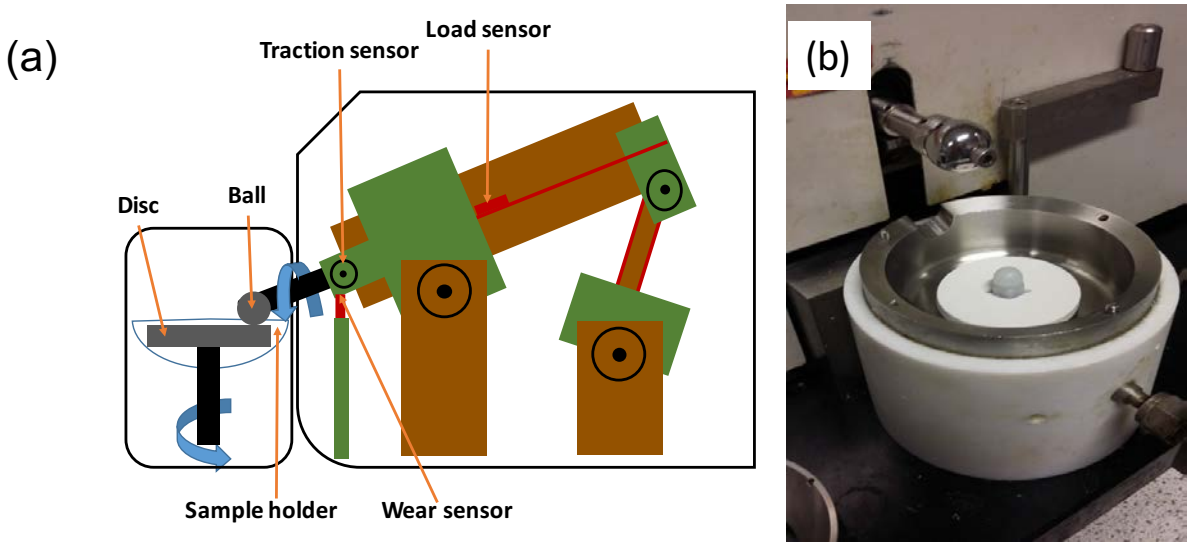


Figure 2.7: MTM basic principle (a) schematic representation, and (b) picture. The arrows show the direction of rotation of the shafts.

2.2.2 High Frequency Reciprocating Rig

High-Frequency Reciprocating Rig (HFRR) (PCS Instruments, UK) is a commercially available ball-on-disc tribometer, capable of measuring wear and CoF in sliding motion. The upper specimen is a ball of 6 mm diameter, and the lower specimen a disc with 10 mm diameter and 3 mm thickness. The ball and disc are smaller than MTM specimens, allowing smaller samples to be examined on a smaller scale. HFRR is the world's industry standard for the tribological evaluation of diesel fuels [256, 257] and has been used for the characterisation of biofuels [258], greases [259], gasoline [260], and marine lubricants [261]. HFRR was also used to study the tribological behaviour of AC under different lubrication regimes [262].

The standard HFRR consists of the central mechanical unit, a control unit with a microprocessor, and a PC. The mechanical unit is inside a hood enabling accurate temperature and humidity control. The working principle as well as the actual picture

of HFRR are illustrated in **Figure 2.8**. The sample holder is filled with 2 ml of lubricant. A fixed force load is provided from the ball to the disc utilising a dead weights mechanism. Afterwards, an electromagnetic vibrator oscillates the ball against the disc, which is fixed in the sample holder [262]. The CoF is calculated as the average of the entire stroke and displayed on the software. Apart from that, the software displays the lubricant's temperature and film thickness. The HFRR could also measure and image the wear scar when combined with an optical microscope.

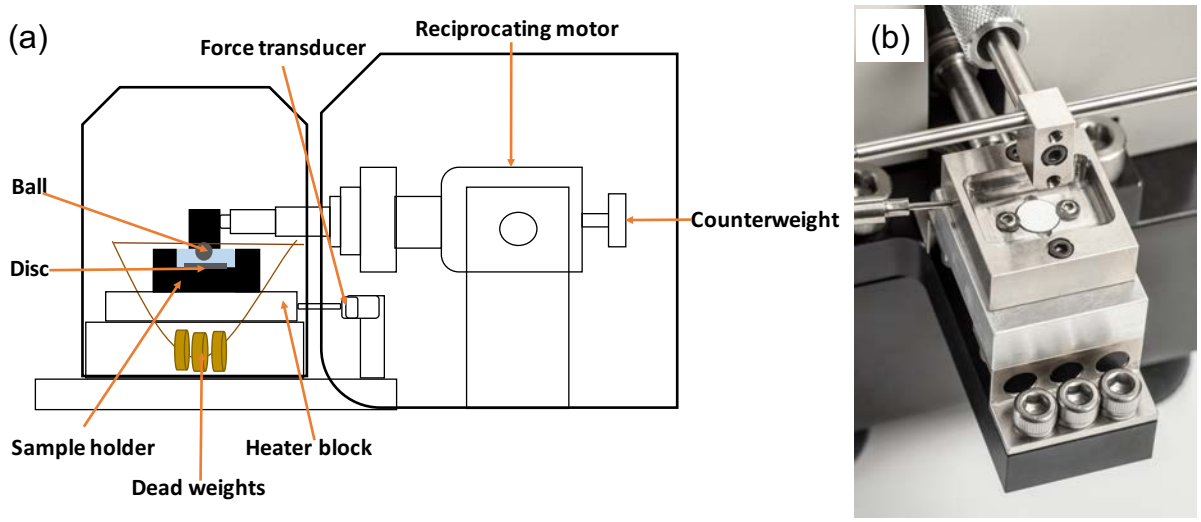


Figure 2.8: HFRR basic principle (a) schematic representation, and (b) picture adopted from [263].

The measurement cycle is undertaken under the conditions described in the measurement profile. The most notable difference of HFRR compared to MTM lies in the measurement profile. Instead of setting the speed directly (as in MTM), the HFRR measurement profile requires the setting of stroke length and frequency. The sliding velocity and, therefore, the lubrication regime is controlled by the combination of stroke length and frequency based on the equation:

$$u_s = x_s f \tag{2.3}$$

where u_s is the sliding speed (mm s^{-1}), x_s is stroke length (mm), and f is the frequency (Hz) [262]. However, the sliding speed changes during the loading cycle due to the reciprocal movement and as such, it is considered a measure of velocity [262]. HFRR also allows the investigation of different lubrication regimes at the same test by building up a measurement profile with a series of various stroke length/ frequency steps. The machine operates at stroke length 0.020-2 mm, frequency range 10-200 Hz, and temperatures up to 150^{o}C.

2.3 Contact mechanics

Hertz, Derjaguin–M$\ddot{u}$ller–Toporov (DMT), and Johnson–Kendall–Roberts (JKR) equations simulate the elastic deformation between surfaces in contact at the beginning of loading. The adhesion force *F* that develops in each system affects the relationship between the indenter load *W*, the sample deformation *δ*, the contact radius *α* and, as such, determines the selection of the most appropriate model. The effect of adhesion can be predicted from the dimensionless load parameter $\overline{P}$:

$$\overline{P} = \frac{W}{\pi \, \Delta\gamma \, r} \tag{2.4}$$

where *W* is the indenter load (N), *Δγ* the adhesion work (N m^{-1}), and *r* the spherical indenter radius (m) [264]. The work of adhesion is defined as:

$$\Delta\gamma = \gamma_1 + \gamma_2 - \gamma_{12} \tag{2.5}$$

where $\gamma_{1,2}$ is the surface energies of the interacting materials (N m^{-1}) and γ_{12} the interfacial energy (N m^{-1}) [264]. Hertz model is very accurate when describing the contact area of elastic materials under minimal surface interactions and especially zero adhesion force [265]. The other two models are advancements of the Hertz model and consider that adhesion is applied outside (DMT) or within (JKR) the contact area [264].Those models represent two extreme opposite conditions of the dimensionless Tabor number [266]. DMT model simulates the contact between a small sphere and a stiff low surface energy plane surface [264]. A small adhesion is developing in the area surrounding the surfaces described by the DMT model [264, 267]. JKR model simulates the contact between a large sphere and a malleable (low Young's modulus) plane surface with high surface energy [264]. A significant adhesion is developing only among the contact surfaces described by the JKR model [264, 267]. Lastly, DMT and JKR are suitable when small normal loads are applied, and adhesion determines the contact area between the opposing surfaces [264]. Hertz model is suitable when high normal loads are applied, and the surfaces behave as continuous elastic media (do not withstand plastic deformation) [238, 264]. **Figure 2.9** illustrates the differences between the three models, and **Table 2.1** presents their mathematic models. Symbol *a* represents the contact radius (m), *δ* the deformation (mm), *F* the adhesion force (N), *r* the radius of the sphere (m), *W* the indenter load (N), *A* the adhesion per unit area (N m^{-2}), and E_{tot} the reduced Young's modulus (N m^{-2}).

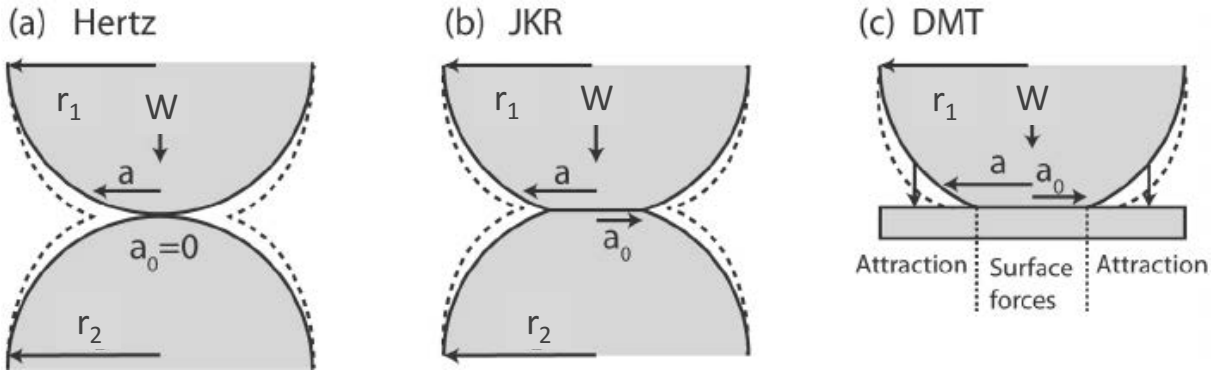


Figure 2.9: Schematic illustration of (a) Hertz, (b) JKR, and (c) DMT models in the case of a sphere in contact with another sphere or a planar surface [267]. Continuous lines represent the configuration under zero load and dotted lines under applied load.

Table 2.1: Contact radius, sample deformation, and adhesion force approximations based on Hertz, DMT and JKR models.

Models	Contact radius, a	Deformation, δ	Adhesion force, F
Hertz	$\sqrt[3]{\frac{r\,W}{E_{tot}}}$	$\frac{a^2}{r}=\left(\frac{W^2}{rE_{tot}^2}\right)^{1/3}$	0
DMT	$\sqrt[3]{\frac{r}{E_{tot}}(W+2\pi rA)}$	$\frac{a^2}{r}=\frac{(W+2\pi rA)^{2/3}}{\sqrt[3]{rE_{tot}^2}}$	$2\pi rA$
JKR	$\sqrt[3]{\frac{r}{E_{tot}}\left(W+3\pi rA+\sqrt{6\pi rAW+(3\pi rA)^2}\right)}$	$\frac{a^2}{r}-\frac{2}{3}\sqrt{\frac{6\pi A\alpha}{E_{tot}}}$	$\frac{3\pi rA}{2}$

For AFM measurements, neither Hertz nor JKR and DMT models are suitable. Under the low load developed in the micro/nanoscale, the surface-to-bulk ratio and adhesion contribution are significant and should be taken into account [264, 268]. MD (Maugis-Dugdale) covers the whole area that can be measured with AFM [269]. and is the most appropriate choice for most materials. MD model is accurate in most cases, whereas JKR and DMT models provide results on its limits, respectively [264].

For the study of contact mechanics in this thesis, the reduced Young's modulus is quantified based on the equation:

$$\frac{1}{E_{tot}} = \frac{3}{4}\left(\frac{1-v_1^2}{E_1} + \frac{1-v_2^2}{E_2}\right) \quad (2.6)$$

where $v_{1,2}$ Poisson ratio for the sphere and the surface (-), E_{tot} reduced Young's modulus, and $E_{1,2}$ Young's modulus for the sphere and the surface (N m^{-2}) [245]. The circular contact area C (m^2) in a sphere-plane surface contact is defined as:

$$C = 4\,\pi\,a^2 \quad (2.7)$$

Finally, the applied contact pressure, p (N m^{-2}) is calculated as:

$$p = \frac{F}{C} \quad (2.8)$$

2.4 Rheology

2.4.1 Introduction to rheology

Rheology studies fluid flow and deformation in time under the application of shear forces acting parallel to a surface [270, 271]. The study of the rheological properties of a system is called rheometry. Rheometry consists of two main testing categories the steady-state shear, which concerns mainly the viscosity and the dynamic/oscillatory, which studies structural information in relation to the time and temperature [272].

2.4.2 Steady-state shear rheometry

Shear flow is the motion between hypothetical layers within the fluid, with the upper one having the highest velocity and the bottom one being stationary [273]. The shear force is a force parallel to a plane surface that provokes shear flow in a fluid [274]. The shear force applied per unit area in a fluid is the shear stress, σ (Pa = N m^{-2}) [273]. The shear stress dislocates the upper layer leading to a velocity gradient in among the fluid layers (y-axis) called shear rate $\dot{\gamma}$ [271, 274]. The shear rate is meters/seconds/meters, which results in the unit s^{-1} [271]. Each type of movement is related to a specific range of shear rates that should be used during rheological measurements to achieve representative results. For example, the shear rate developed during chewing and swallowing ranges from 100-1000 s^{-1} [271]. Shear stress against shear rate provides the dynamic viscosity η (Pa s) [273]. Viscosity is the resistance of a fluid's movement; the more viscous a fluid, the more force needs to be applied to it to start flowing [274]. In the case of very low viscosities, the prefix m is used that demonstrates the 10^{-3}.

2.4.2.1 Types of shear viscosity

The most common categories of fluids based on their rheological behaviour are shown in **Figure 2.10**. Newtonian fluids demonstrate a constant viscosity independent of shear rate or time [270]. In **Figure 2.10**, the Newtonian fluid is illustrated as a straight line. Many common fluids are considered Newtonian, including water, corn syrup, and petrol [271]. Under extremely high shear rates (e.g. 10^{12} s^{-1} for water), all fluids become non-Newtonian [271].

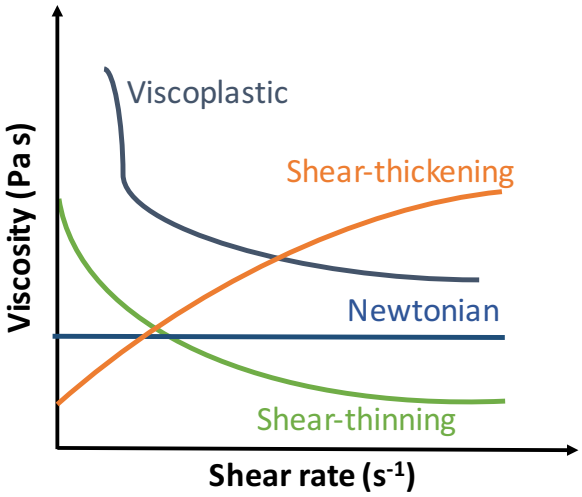


Figure 2.10: Types of shear viscosity fluids.

A viscoplastic fluid requires critical external shear stress (yield stress) to start moving [274]. A viscoplastic fluid behaves like a solid (deforms elastically) below the yield stress and flows like a liquid above it because the high applied stress induces structural collapse [270]. Ketchup is an example of a viscoplastic fluid [271]. The yield stress can be identified from various rheological tests, including steady shear, oscillatory amplitude sweep, and creep tests. The most appropriate is the shear stress ramp test, which identifies the peak of viscosity (yield stress) in relation to shear stress.

Shear-thinning/pseudoplastic is a fluid with a viscosity that reduces as shear rate elevates [274]. Such fluids usually demonstrate a constant viscosity at low and high shear rates called zero shear viscosity, η_o (Pa s), and infinite shear viscosity, η_∞(Pa s), accordingly [271]. The shear-thinning area can be modelled with the Power law model:

$$\eta = \mathrm{m}\,\dot{\gamma}^{n-1} \qquad (2.9)$$

where η: viscosity (Pa s), *m*: consistency (Pa s), *n*: Power-law index (-), and $\dot{\gamma}$: shear strain rate (s^{-1}). The Power-law index ranges from 0 (pure shear-thinning) to 1 (pure Newtonian) [271]. The entire viscosity curve of shear-thinning materials can be successfully modelled with the Cross model [271]. The shear-thinning behaviour is a result of molecular rearrangements owing to the of shear. At the initiation of shearing, the fluid's molecules are positioned in irregular order due to inter-particle forces [273]. In the case of yield stress, at low shear rates, the fluid molecules form a network and only when that network breaks the fluid start flowing [273]. Under high shear rate and stresses, the inter-particle interactions of the shear-thinning fluid decrease, the molecules rearrange to maximise the free space between them, and the viscosity decreases [273]. Examples of those rearrangements include stretching and disentangling polymer chains, breaking aggregated structures, deforming particles/emulsion droplets and aligning with the flow. A characteristic example of shear-thinning fluid is the SF [26].

Thixotropic is a shear-thinning fluid, which returns with time to its original viscosity in the absence of shear stress [273]. Rheopectic behaviour is the opposite of thixotropic. The more shear stress is applied to rheopectic fluids, the more their viscosity increases. A three-step shear test is used to measure the thixotropy/rheopexy of fluids [273]. A low shear rate/stress is applied during the first step to maintain equilibrium. Then, time-constrained high shear rate/stress is applied to breakdown the molecular structure of shear-thinning fluids. Finally, the same low shear of the first step is applied, and the restoration of the viscosity is recorded. The more the time needed, the higher the thixotropic nature of the fluid [273]. Paint is a characteristic example of

a thixotropic material, whereas the osteoarthritic SF is rheopectic under physiological conditions [275].

Shear thickening is a fluid with a viscosity that rises as shear rate/stress elevate [274]. Such behaviour could be a region of shear-thinning fluids under specific shear rates/stress. In those cases, the alignment of the molecules is disturbed, “jamming” occurs, and the material behaves temporarily like a solid - its viscosity increases [273]. Shear thickening has been observed in dispersions with high concentrations of solid particles and amphiphilic polymers, which stretch their chains and form temporal inter-particle interactions at high shear rates.

The viscosity of every fluid varies with pressure and temperature [273]. Viscosity increases with increasing pressure, but the increase is usually insignificant for most of the fluids [271]. The way pressure affects the viscosity depends significantly on the type of fluid [271]. The viscosity of water decreases initially with increasing pressure, and increases only above 1000 bar [271]. Temperature’s effect on viscosity is more critical than pressure. Based on Arrhenius law, viscosity diminishes as the temperature elevates because of the increasing Brownian motion of its molecules [271]:

$$log_{10}\,\eta = I + \frac{E_a}{R\,T} \qquad (2.10)$$

where I is the pre-exponential factor (s^{-1}), E_a is the activation energy (m N mol^{-1}), R is the universal gas constant 8.314 (m N K^{-1} mol^{-1}), and T is the temperature (K) [271].

2.4.3 Oscillatory rheometry

Viscoelastic materials combine properties from ideal liquids (viscous) and ideal solids (elastic) under deformation [273]. The elastic materials are defined by the elastic modulus *G*', which is analogous to the material's resistance to deformation and stiffness, and the viscous by the viscous modulus *G*" [273]. Time affects the stress-strain relationship of those materials [276]. Viscoelastic properties range significantly between various fluids [276]. When force is applied on viscoelastic materials, a deformation induces an immediate elastic response [271]. The resulting restoring force increases initially linearly, afterwards non-linearly until a phase during which the increasing rate decreases, and finally, at large deformations, the material ends up in a steady-state viscous response phase [271]. The restoring force induces microstructural alterations and makes the material anisotropic [271]. Besides elastic forces, viscous forces are present in all viscoelastic fluids. Most of the everyday materials like polymers, wood demonstrate viscoelastic behaviour under high temperature [276].

2.4.4 Rheometer working principle

The rheological properties of a fluid are usually studied with a rheometer. The rheometer measure the viscosity and the viscoelasticity of fluids [271]. **Figure 2.11** displays the rheometer used in this thesis. A rheometer's geometry is the upper surface that comes in contact with the fluid during testing. Different geometries are used for different types and viscosities of fluids. Parallel-plates, cone-plate, concentric cylinder, tubes are the most commonly used geometries. In general, parallel-plates and cone-plates geometries are preferable for high viscosity fluids, whereas concentric cylinders

and tubes for low viscosity fluids. A specific volume of fluid dictated by the geometry is loaded on the lower part of a geometry. For parallel-plate or cone-plate geometries, the lower part is a temperature-controlled stationary plate. For concentric cylinders and tubes, the lower part is a temperature-controlled cylinder. As the measurement starts, the upper part of the geometry is lowered, leaving a specific gap dictated by the lower's part geometry. During testing, force or velocity is applied in the lower part of the geometry [271]. The rheometers convert the applied force or velocity to shear stress or shear rate accordingly at a specific point of immediate contact between geometry and sample [271]. A point of contact could be the cone-plate geometry's outer edge, the inner cylinder of the concentric cylinders geometry or the tube wall [271].

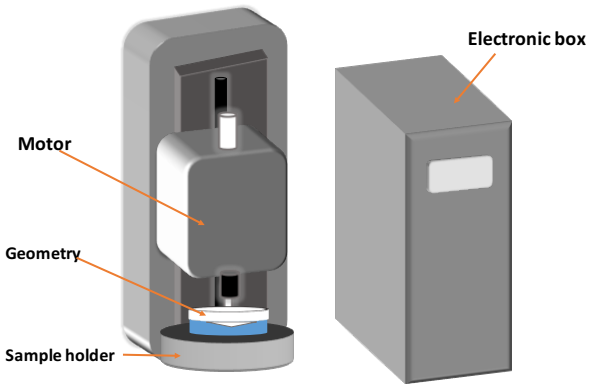


Figure 2.11: Schematic illustration of the ARES-G2 rheometer (TA Instruments, USA) and the 20 mm 2^{o} steel cone geometry used in this thesis.

The geometry selection is crucial because the smooth geometry's surface could interfere with the sample's microstructure and produce slip effects (decrease sample's concentration close to the wall compared to the bulk) [271]. Geometries should be carefully handled because bending their spindles provides unrealistic rheology results. Also, geometries should be made of stainless steel or plastic to avoid corrosion and prevent their ions from mixing with samples. A rheometer is common to produce zero

errors/drifts due to mechanical and electronic faults; therefore, zero settings (low-speed results) should be regularly checked [271]. Sample's evaporation is another issue, especially at the edges of cone-plate or parallel plate geometries [271]. That issue can either be solved with a sample trap or, by covering the sample's edges with an oil layer. Finally, recirculating the suspensions should be applied to reduce the expected sedimentation [271].

2.4.5 Types of rheological tests

2.4.5.1 Flow tests

There are four types of flow tests; constant shear stress/rate, steady-state flow, flow sweep, and flow temperature ramp. In the first category, fixed shear stress/rate are implemented for the whole duration of the measurement, and the performance of the fluid's viscosity with time is recorded. During steady-state flow tests, shear stress/rate are implemented until the fluid reaches the steady state. The resulting flow curve of viscosity is essential for evaluating the behaviour of non-Newtonian materials. The steady-shear viscosity of healthy and osteoarthritic SF has been extensively studied [95, 141, 142, 275]. Moreover, the effect of temperature in SF steady-shear viscosity has been investigated [95].

The flow sweep test is used for the identification of yield stress. There are two variations of that test: the steady stress and the steady rate sweep. The steady stress sweep is used for fluids of medium viscosity [277]. Stress is applied in increments from high to low until the fluid starts to flow [277]. Each stress step is applied to the fluid for a specific time. When the shear stress stabilises, the yield stress has been reached

[277]. The yield point is when a minor alteration in stress results in a significant decrease in viscosity [277]. The steady rate sweep test follows the same principle but is used for fluids of low viscosity [277].

During the flow temperature ramp tests, the shear rate/stress are fixed, while the temperature is ramping. As a result, the relationship of viscosity and temperature is acquired.

2.4.5.2 Viscoelasticity tests

Oscillatory shear tests study viscoelastic materials. Those tests involve applying stress/strain on a sample that is oscillated around its equilibrium state and monitoring the resulting oscillatory stress/strain over a range of frequencies [271]. Creep, stress relaxation, and start-up tests belong in viscoelasticity measurements.

Oscillatory shear tests identify the viscous and elastic part of each material and quantify their relative storage *G'* (N m^{-2}) and loss *G"* modulus (N m^{-2}) over angular frequency [271]. **Figure 2.12** illustrates the general behaviour of *G'* and *G"* for viscoelastic non-Newtonian fluids over angular frequency [271]. At low frequencies, all materials demonstrate a viscous/terminal region, in which the fluid's viscous nature dominate. The *G'* is quadric and *G"* linear at this part of the graph, but, common rheometers are not sensitive enough to detect it. The next region is called transition-to-flow because *G'* becomes significant, overcomes *G"*, and as such, elastic behaviour prevails. The crossover point of the moduli *G'* is essential for the calculation of various viscoelastic properties. The third region is the rubbery/plateau, in which the elastic nature of the material dominates (*G'* > *G"*). In that region, *G'* increases very slightly

(plateau). The following region is the leathery/transition. It is called transition because, towards the end of this region, the *G"* overcomes *G'* due to dissipation and relaxation mechanisms and crossover time can be calculated. The last region that is found at high frequencies is the glassy. At this region, *G"* and consequently, the material's viscous nature dominate [271]. The above-mentioned behaviour of the viscoelastic materials can be modelled using the Maxwell model at low frequencies and the Kelvin-Voigt models at high frequencies [271].

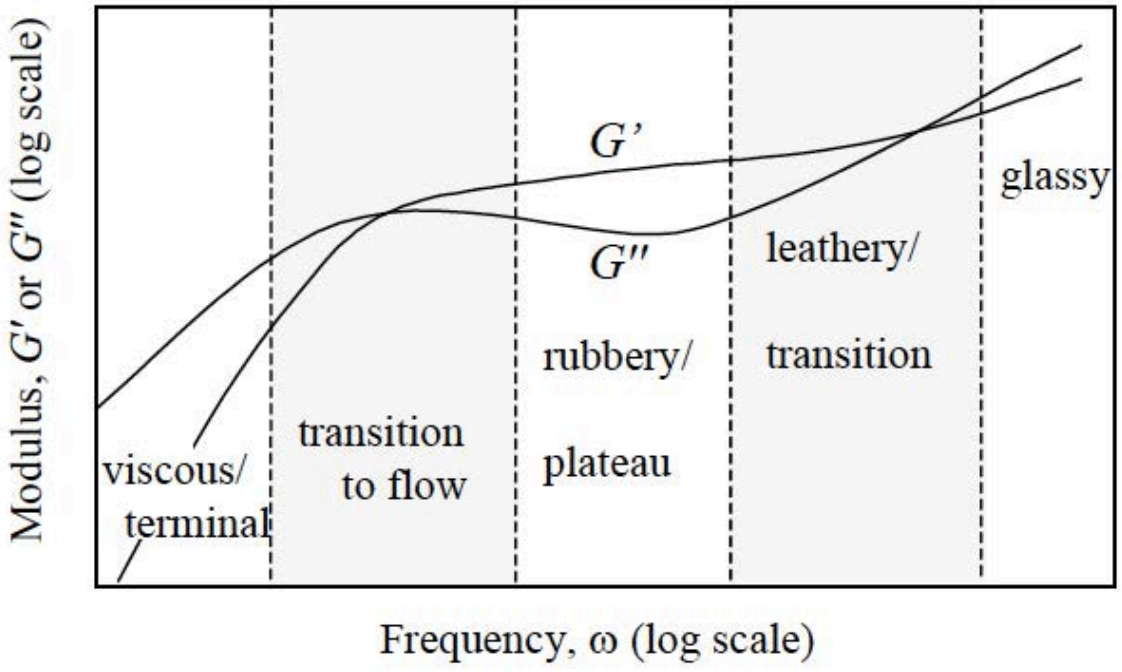


Figure 2.12: Viscoelasticity of non-Newtonian fluids against angular frequency. Adopted by [271].

It is rare to detect all the regions described above in a single measurement because of angular frequency restrictions. Most of the rheometers work on angular frequencies between 10^{-2} and 10^{2} rad s^{-1}, under which only the first two regions can be seen. The regions, which can be detected depend on the material's longest

relaxation time (τ_{max}) [271]. When $\omega\tau_{max}$ equals 1, then the first two regions can be seen. When $\omega\tau_{max}$ <1, then the viscous regions can be seen. When $\omega\tau_{max}$ >1, then the rubbery can be seen and often the glassy as well.

Only the linear region of the viscoelasticity graph is used for the oscillatory tests because in that *G'* and *G''* are independent of oscillation stress [271]. The oscillatory shear tests in the linear region enable the study of the material with no intervention to their microstructure thanks to the small applied amplitude (maximum applied strain). However, the linear region is found over a wide range of angular frequencies even for materials of the same type [271]. The viscoelasticity of osteoarthritic SF was studied and compared to healthy SF using oscillatory shear tests. The viscous modulus, elastic modulus and crossover angular frequency are among the studied properties [95].

2.5 Particles size and Zeta Potential measurements

2.5.1 Size measurements - Dynamic Light Scattering

DLS is used to measure the size of the particles. More specifically, DLS measures hydrodynamic quantities (translational and rotational diffusion coefficients) and translates them to size and PDI using mathematical models [278]. **Figure 2.13** illustrates the working principle of DLS. The particles in the suspension move randomly with a velocity depending to the size-, temperature, and solvent's viscosity, due to their interactions with the solvent molecules (Brownian motion) [279]. A laser light beam is directed to a colloid system placed in a quartz or glass tube [280]. A part of the laser beam is absorbed as energy, while another part is scattered from the particles through the medium according to particle size [280]. The particle size is negatively correlated

with the Brownian motion because smaller particles are turned away faster (smaller intensity fluctuations) than bigger ones (larger intensity fluctuations) when interacting with the molecules of the solvent [281]. The scattered light from the moving particles creates time-dependent intensity fluctuations, which are recorded by a photon detector [281]. The photon detector can only detect a specific range of light intensity; thus, an attenuator is used to modulate the laser source's intensity when needed [281]. DLS detectors could be positioned in two angles, either at 90^{o} or 180^{o} from the incident laser beam [280]. The second position is called backscatter detection and comes with the advantage of negligible rotational diffusion [280]. In that case, samples with high particle concentration can be tested since no multiple scattering is happening [280]. Afterwards, the scattering intensity is transmitted from the detector to the auto correlator [281]. A build-in algorithm correlates the scattering intensity fluctuations with the time decay *g(τ)* (s) in real-time and afterwards with the particle size [280]. The time decay relates to the translational diffusion coefficient, *D* (m^2 s^{-1}) of the scattering particles and the propagation vector length of density fluctuations, *q* (m^{-1}) based on the equation [282]:

$$g(\tau) = (e^{-2Dq\tau}) \qquad (2.11)$$

The propagation vector length can be calculated based on the equation below:

$$q = \frac{4\,\pi\,\tilde{n}}{\lambda_o}\sin\frac{\vartheta}{2} \qquad (2.12)$$

where $\tilde{n}$ is the solvent's refractive index (-), λ_o is the laser light's wavelength (m), and θ is the scattering angle (^{o}) [280]. The particles diffusivity depends on various

parameters, including their shape [282], surface chemistry, concentration, and medium's ionic strength [281]. The translational diffusion coefficient is utilised for the calculation of the hydrodynamic diameter *d(H)* (m). The hydrodynamic diameter has the size of a sphere hypothesised to diffuse as fast as the examined particle. For spherical particles, the hydrodynamic diameter *d(H)* is calculated based on the Stokes-Einstein equation:

$$d(H) = \frac{k\,T}{3\,\pi\,\eta\,D} \qquad (2.13)$$

where *k* is Boltzmann's constant (1.38 10^{-23} kg m^2 s^{-2} K^{-1}), *T* the absolute temperature (K), and *η* the solvent's viscosity (Pa s) [282]. Therefore, having a stable temperature during the measurements is critical. The size distribution is presented as a plot of the scattered light intensity or the number or the volume of particles versus various size classes in a software. In addition to the hydrodynamic diameter, the software calculates the mean particle size and the sample's PDI [281].

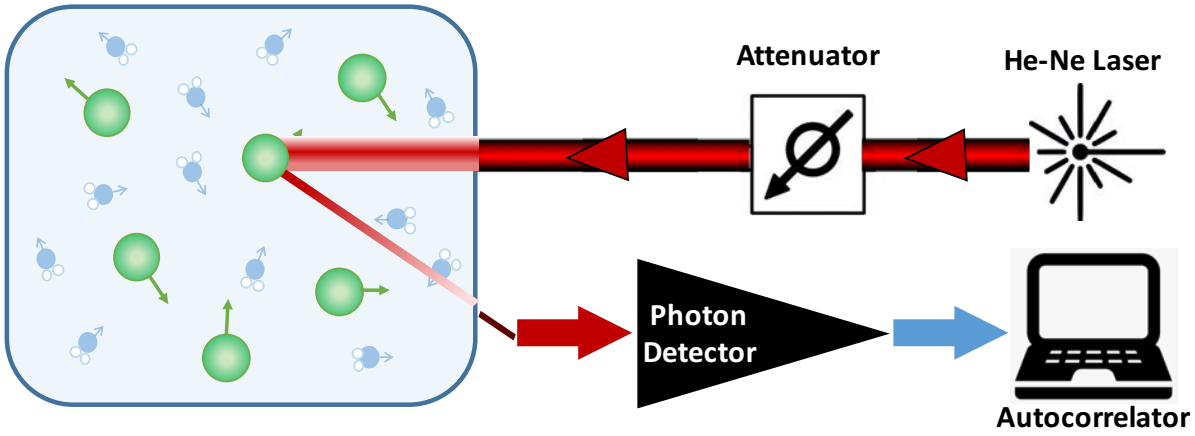


Figure 2.13 Schematic representation of the basic principle of DLS.

2.5.2 Benefits of Dynamic Light Scattering

DLS is a fast (each measurement is completed within minutes) highly reproducible technique, which requires only a few mL of the testing sample per measurement. Its main advantage is that it enables the characterisation of colloid systems or molecules in liquid in the micro scale [281, 283]. The standard technique for evaluating particle size in the absence of DLS is SEM [278]. Particles tested via SEM tend to aggregate because they are in a dry state, leading to incorrect interpretations of size if the nominal particle size is not known. However, aggregates can also be formed in liquid media. Therefore, DLS and SEM combined are expected to provide the most representative results. DLS is an essential tool for various colloid systems like lubricants, drugs, food, cosmetics, paints, ceramics, and personal care products [284]. It has even been deployed to characterise NPs suspensions for the therapy of OA [285, 286].

DLS assists in understanding the interactions between the particles of the suspensions by measuring the particle size, and polydispersity (PDI) [287, 288]. The NPs size is positively correlated with the sedimentation rate and, therefore, the dispersion stability [10]. Nano lubricants with poor stability, aggregation and sedimentation demonstrate diminished wear and friction reduction ability [289, 290]. In addition to that, the size of the NPs affects their mechanical properties (e.g. hardness) [291], hence, their lubrication performance. The NPs shape determines their load carrying capability [10] and, as such, their frictional properties. [278]. Polydispersity is very common on NPs suspensions [278]. In polydisperse suspensions there is a large variation in the size of the particles.

2.5.3 Zeta Potential measurements - Electrophoretic Light Scattering

The ZP is an indication of colloidal systems' stability and agglomeration tendency [10]. ZP ranges from -200 to +200 mV and, in general, a water-based NPs suspension with ZP higher than 30 mV is considered highly stable [292, 293]. It needs to be mentioned that the absolute value of ZP is important and not the positive or negative dimension, which depend on the movement of the particles towards the electrodes [294]. However, the ZP is not always representative of the stability because it accounts only for the electrostatic repulsive forces. The stability depends additionally on the attractive Van der Waals forces, the steric, and hydrophobic interactions based on the Derjaguin, Landau, Verwey, and Overbeek theory [295].

The ZP should not be confused with particles charge; it indicates the surface potential difference in the interface of the charged particles at the Electric Double Layer (EDL) and the suspension's medium [294]. EDL consists of the Stern and the diffuse layer [294]. **Figure 2.14** illustrates the EDL on a negatively charged particle. The first layer of the EDL is the Stern layer, which is a layer of oppositely charged ions surrounding the charged particles in the suspension [296]. The second layer of the EDL is a diffuse layer of negatively and positively ions that develops a few nm from the Stern layer because of the particles' weak surface charge [294]. The composition of the diffuse layer is related to the particles/ions concentration and the pH [294]. The hypothetic plane at the particles-medium interface is named the slipping plane [294], and its potential is the ZP [296].

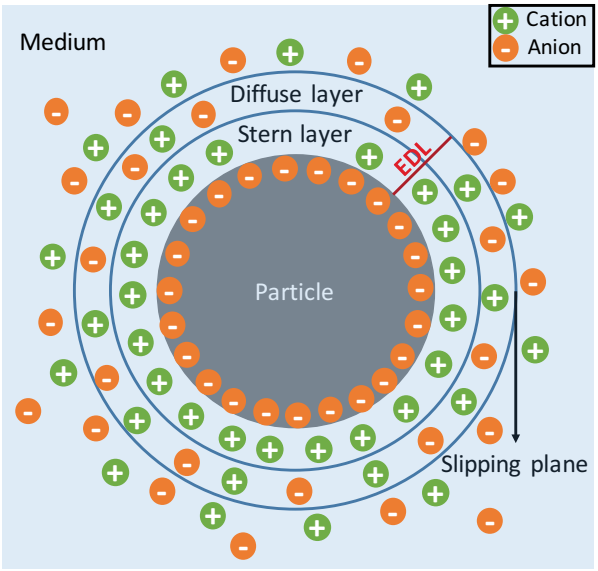


Figure 2.14: Schematic illustration of the EDL on a negatively charged particle. The EDL consists of the Stern layer and the diffuse layer. The ZP is the potential measured at the slipping plane.

Electrophoretic Light Scattering (ELS) is the most frequently employed method to measure the ZP [296]. During ELS, half of the laser beam is fired through the sample and a half through combines with the scattered beam [294]. The particles scatter the light to different frequencies than the incident laser beam inducing a frequency shift proportional to particles velocity known as Doppler shift [294]. The particles' velocity is subtracted from the Doppler shift to calculate the electrophoretic mobility [294]. The sample is placed on special cuvettes with inbuilt electrodes. Under electric field, The particles start moving towards the oppositely charged electrode and develop electrophoretic mobility [294]. The ZP can only be determined by experimental results based on Henry's equation:

$$\mu_e = \frac{2\,\varepsilon_0\,\varepsilon_r\,\zeta\,f(K\alpha)}{3\,\eta} \qquad (2.14)$$

where $\mu_e$is particles electrophoretic mobility (m^2 s^{-1} $Volt^{-1}$), ε_0 is the dielectric constant in vacuum (-), ε_r is the dielectric constant (-), *f(Kα)* is Henry's function (-), and *η* is medium's viscosity [294]. The electrophoretic mobility is defined as:

$$\mu_e = \frac{u}{S} \qquad (2.15)$$

where *u* is particles' velocity (m s^{-1}), and *S* is the strength of the electric field (Volt m^{-1}) [294].

Anoother measuring method of the ZP is the electroacoustic phenomenon. During the electroacoustic phenomenon, an electric field is applied that induces particles oscillatory mobility [294]. From the analysis of that oscillation, the ZP can be identified [294]. The electroacoustic method is mainly used for dense suspensions when properties like viscosity, thermal conductivity, density, and thermal expansion coefficient are available [296].

Although DLS and ELS are powerful techniques, they have some limitations. They are reliable only for particles smaller than the wavelength of the laser (usually 632.8 nm for He-Ne laser) [297] and larger than the solvent's molecules because the scattered laser beam correlates to the particle size and the laser wavelength *λ* [283]. DLS and ELS are also very sensitive to contaminants. For example, dust particles are large enough to deteriorate the results [280]. In addition to that, DLS and ELS work only for optically transparent samples because they are based on light scattering, making them automatically unsuitable for many samples [280]. Another disadvantage is that they cannot identify the material of the particles [278]. The operator should provide that information, combined with the reflective index and the medium's viscosity,

before initiating the measurements. Also, DLS and ELS are based on the principle that there are no interactions between the particles, and therefore, they only provide representative results for a specific range of particle concentrations [278]. Finally, in dilute solutions (< 0.01% w/v), the scattering intensity is weak, and only equipment with powerful laser sources can achieve good signal to noise ratios [278].

3. INVESTIGATION OF RHEOLOGICAL AND SURFACE PROPERTIES OF OSTEOARTHRITIC SYNOVIAL FLUIDS

3.1 Introduction

Osteoarthritis (OA) is a progressive abnormal condition of the joints afflicting millions worldwide [298]. Treating OA is not possible yet; current therapies target only at relieving its symptoms. Diagnosing OA using existing diagnostic tools like Magnetic resonance imaging (MRI) is only possible at its late stages when the morphology of the joints changes significantly [6]. Considering its severity and the lack of effective diagnostic tools and treatments, the need for further research on OA seems incumbent. Therapeutic methods capable of preventing the initiation and progression of OA need to be developed. Various factors including age, obesity, gender, traumatic incidents, and limited physical activity are deemed to induce OA [16], but the degeneration mechanisms are not well-defined. Investigating the effect of OA on the joints' mechanical properties will provide biomedical researchers with a better understanding of OA's onset and progression mechanisms, risk factors, and pathological ranges.

Healthy joints demonstrate excellent lubrication, maintaining a coefficient of friction (CoF) in the "superlubricity" regime (0.001 to 0.03) during everyday activities [74, 87]. The exceptional lubrication is assigned to a mixture of lubrication mechanisms suggested over the years, including the hydrodynamic, the elastohydrodynamic, the squeeze film, the boundary, and the hydration lubrication theory [81, 86, 299]. Based on those theories, both synovial fluid (SF) and articular cartilage (AC) properties contribute significantly to joints' lubrication. AC and SF molecules like Hyaluronic acid (HA), lubricin, albumin, and γ-globulin determine joints lubrication, especially in the

boundary regime when the lubrication is credited to the macromolecules adsorbed on the AC surface [32, 84]. The porosity, elasticity, geometry, and uneven thickness of the AC provide a uniform pressure distribution and load-bearing capacity to the joint [300]. Finally, the highly viscous SF forms thick protective films, which prevent direct contact between the AC surfaces [299].

SF properties protect joints over the whole spectrum of the lubrication regimes [35]. The high SF viscosity (up to 175 Pa s at low shear rates) [141, 142, 153, 301, 302] and its shear-thinning behaviour contribute to the exceptional lubrication of the joints [26, 95, 108, 109]. The high SF viscosity contributes to efficient lubrication via the formation of film thickness under the hydrodynamic regime. The shear-thinning characteristic has the additional advantage of increasing the film thickness under the boundary regime via squeeze film action [303, 304]. That capacity is vital for the joint, which withstands high pressures under boundary lubrication. The same behaviour has been seen in oil systems, in which shear-thinning fluids provide a CoF reduction of 50% even though their film thickness is lower than the isoviscous Newtonian under high shearing [305]. In addition, SF has an increased load-carrying capacity compared to Newtonian fluids of the same viscosity under physiological stresses thanks to SF high relaxation (squeeze film) time which decreases the normal stresses [306, 307].

SF's lubrication efficiency deteriorates significantly under OA. Rheological properties such as steady-shear viscosity and viscous/elastic modulus reduce under OA [95, 275]. SF deterioration is related to alterations in its composition, including HA and lubricin reduction [105, 108]. The effect of OA on SF's viscosity has been studied since 1959 [153]. **Table 3.1** summarises the reported studies on the steady-state flow

viscosity of healthy and osteoarthritic SF from humans after death. In general, healthy SF demonstrates higher viscosity than osteoarthritic SF. Both osteoarthritic and normal SFs cover a wide viscosity range between 0.008-25 Pa s and 0.06-175 Pa s, respectively [95, 141, 142, 153, 301, 302]. Direct comparison of those levels is not possible because they were acquired using different experimental methodologies (e.g. shear rates). For instance, some studies examined the broadest possible shear rate range (up to 1000 s^{-1}) [95, 141], whereas others explored smaller ranges [308, 309].

Table 3.1: Steady-state flow viscosity of osteoarthritic and healthy SF samples reported in the literature. Values annotated with (*) correspond to the average viscosity ± standard error.

Number of osteoarthritic synovial fluids (-)	Number of healthy synovial fluids (-)	Viscosity of osteoarthritic synovial fluids (Pa s)	Viscosity of healthy synovial fluids (Pa s)	Testing conditions	References
4	91	0.15 ± 0.05	0.06 – 1.4	t=100s	[153]
4	2	0.1 – 1	1 – 100	0.1 s^{-1}, 21°C	[141]
N/A	N/A	0.1 – 2	6 – 60	0.001 s^{-1}	[142]
N/A	N/A	0.1 – 1	6 – 12	0.001 s^{-1}, 25°C	[301]
35	0	0.087 – 25	-	0.001 s^{-1}	[310]
N/A	N/A	0.1 – 1	1 – 175	0.01 s^{-1}	[302]
12	0	0.1 – 10	-	0.1 s^{-1}, 25°C	[308]
44	0	Patients with flare: 0.214 ± 0.328* Patients without flare: 0.874 ± 0.89*	-	1 s^{-1}, 25°C	[309]
34	0	0.05 – 14.4	-	0.01 s^{-1}, 37°C	[95]
76	0	0.008 – 0.171	-	1mm amplitude, 37°C	[311]
15	0	0.040 ± 0.003		N/A, 37°C	[312]

*When viscosity range was not given, viscosity is displayed as the average value ± standard error.

The SF bulk rheological properties are essential for the joints' lubrication in the hydrodynamic regime. In the boundary regime, joints' lubrication relies mainly on the surface interactions of the SF components with the AC. The adhesion of synovial cells

and macromolecules to the AC creates a film that separates the AC surfaces. The adsorption of the SF components to the AC surface and their effect on lubrication is investigated in this study by adhesion measurements. Under OA, the adhesion increases either because the collagen network is disrupted [137] or the proteins are broken down [72].

This chapter studies the lubrication properties of human osteoarthritic SFs and correlates them with patient characteristics. The present study is based on 49 samples collected during arthroplasty. As shown in **Table 3.1**, this study and the one published by Galandakova et al. [311] investigated the largest number of osteoarthritic SF samples so far. In this work, rheological and surface interactions (adhesion) measurements were carried out. Adhesion measurements were carried out via Atomic Force Microscopy (AFM) in a few samples as a supplementary method to evaluate the effect of macromolecules adsorption on joints' lubrication. Comparing the results from those two techniques will shed light on the existence of correlations between bulk and surface properties in the osteoarthritic joints from various patient groups.

This chapter aims to expand the current understanding of OA's impact on the lubrication properties of the joints in order to identify the requirements of a new treatment for OA. The differences in the lubrication properties of the SF from various patient groups indicate the patient characteristics leading to poor joints lubrication and relate to the compositional changes in the osteoarthritic SF, which make people susceptible to OA. The composition of the new treatment, the target lubrication regime and the target patient group will be defined. The hypothesis is that OA acts differently on patients with different physical and anatomical characteristics (e.g. age, obesity,

fat), which are associated with the joints' mechanical properties. Although previous studies have already reported the composition of osteoarthritic SFs in various patient groups, very little is known about the effect of patient characteristics on SFs' lubrication properties. Identifying the different ways OA affects the lubrication of the joints in every person assists in establishing targeted treatments based on individual characteristics. In addition, the established pathological range of mechanical properties could be used to develop new biomarkers for the diagnosis of OA.

3.2 Materials and methods

3.2.1 Materials

SF samples were acquired from forty-nine patients suffering from OA who underwent total knee or hip replacement at The Royal Orthopedic Hospital in Birmingham. SF was removed from the patient's joint by the medical practitioner and placed into a sterile test tube during the operation. Debris and cells were removed by centrifugation, and the supernatants were frozen immediately at -80^{o}C. The ethical approval for examining those samples is in Appendix A1. Each SF was thawed at room temperature (18-20^{o}C) for thirty minutes before the testing. The samples were categorised according to gender, age, the body part of which they were acquired, the body weight, Body Mass Index (BMI), total fat levels, and Waist to Hip ratio (W: H) circumference of the patient. **Table 3.2** presents the range and average values of patient characteristics.

Table 3.2*:* Characteristics of patients / donors of synovial fluid suffering from OA.

Gender	Body part	Age (y)	Height (cm)	Weight (kg)	BMI (kg/m^2)	Fat (%)	W: H (-)
27 F	29 knee	49-82	149-181	53.2-119.5	19.4-41.4	3.0-46.0	0.7-1.1
22 M	19 hip	(70.9±1.1)	(166.5±1.2)	(80.9±2.4)	(29.1±0.8)	(32.1±1.7)	(0.9±0.0)

(average ± standard error)
F: female, M: male

Phosphate-buffered saline (PBS) (Fisher Scientific, USA) was used as a reference and solvent in the present work at a concentration of 0.01 M (1 x PBS). Its selection is attributed to its wide application in biologic research. PBS's osmolarity and ion concentration are at the same level as those of the human body [313]. Furthermore, it does not contain any SF components and, as such, it can be used as a reference solution.

Silicone oil (Sigma-Aldrich, USA) was utilised to obstruct SF's evaporation throughout the rheological testing at 37^{o}C. A small amount of silicone oil was placed around the sample as a sealant, a standard technique for rheological tests without a solvent trap [314]. It was confirmed experimentally that the silicone oil did not affect the rheological properties of SF.

3.2.2 Methods

3.2.2.1 Rheological measurements of synovial fluids

Steady-state flow tests of SF were conducted on an ARES-G2 rheometer (TA Instruments, USA). The sample and lower plate were heated at 37^{o}C using an advanced Peltier system, which transfers the heat through a non-contact mechanism. The geometry used was a 20 mm 2° standard steel cone with a gap of 53 μm, chosen

because it requires only 75 µl of the sample and provides good results for a wide range of viscosities. The rheometer was first calibrated with a mixture of polysaccharides with a known viscosity. SF samples were tested at least in duplicates. The results are presented with the standard error associated with those measurements.

Viscosity was measured versus shear rate. The physiological range of shear rates in the synovial joints is broad, starting from very low shear rates close to zero and reaching $10^{6\text{-}7}$ s^{-1} [315, 316]. However, a smaller shear rate range was explored here. The selected shear rate range was based on the rheometer's sensitivity, the chosen geometry, and the purpose of the study. In many SF samples, the rheometer demonstrated the common issue of zero errors/drifts at shear rates below 2 s^{-1}. That fault is attributed to mechanical/electronic faults of the machine [271]. Therefore, 2 s^{-1} was the lowest shear rate explored here. The highest shear rate explored was 100 s^{-1}. SF is shear-thinning and, as such, with increasing shear rate, its viscosity becomes very low and resembles Newtonian fluids [315]. At such high shear rates, there is no differentiation between the SF samples. The study aims to compare the rheological behaviour of the SFs and not to acquire the exact value of viscosities. A short shear rate range across which the SFs maintain their rheological properties and the rheometer works well was deemed appropriate. For completion, it needs to be mentioned that twenty viscosity points were taken per decade.

The Power-law model was employed to calculate the Power-law/shear-thinning index of the SFs (*n*). The definition of the model can be found in section 2.4.2.1 of the methodology section.

3.2.2.2 Surface interactions measurements of synovial fluids

Adhesion energy measurements were conducted on the Force Spectroscopy-Contact mode of the AFM (JPK Instruments, Germany) using the SPM Control Software (JPK Instruments, Germany). The measurements were carried out in PBS between a Si_3N_4 cantilever with a spring constant of 0.27 N m^{-1} and a resonance frequency of 30 kHz (Windsor Scientific Ltd, UK) and the adsorbed SF layer on a titanium substrate. The titanium substrate has been selected as one of the materials currently used for joint implants [317]. The measurements were done at ambient temperature (18-20^{o}C) to prevent the evaporation associated with higher temperatures of SF in an open environment. The applied normal load during the measurements was 6 nN. One hundred and fifty force curves were conducted for every sample. Each force curve was acquired at a different surface point to ensure the surface was intact. The adhesion energy was calculated from the adhesion peak area on the JPK Data Processing Software (JPK Instruments, Germany). The measurement of SF's adhesion on AFM was challenging even with high spring constant cantilevers because of its high viscosity. Therefore, the SF samples were tested 10, 100, 800 and 1500 times diluted in 1 x PBS solution. By diluting the SF samples multiple times, the amount of the SF molecules adsorbed to the surface could be identified and differentiated. Before the AFM measurements, 80 µL of diluted SF sample was placed on a clean, dry titanium substrate and left to be absorbed for two hours at room temperature. Two hours is the maximum time required for the SF adsorption to reach equilibrium on a titanium substrate. That time has been found through Quartz crystal microbalance (QCM) tests. The adhesion energy was measured for ten SF samples. PBS was used

as a reference. Surfaces interaction measurements were contacted in PBS following the same experimental conditions.

3.2.2.3 Statistical analysis

A basic statistical analysis of the data was implemented in Microsoft Excel. The patients were split into six categories based on age, gender, BMI, fat %, W: H, and the sample's origin. For each category, two or three subcategories were formed (e.g. males and females for gender). The average, minimum, maximum, standard deviation and standard error values of each subcategory were calculated. Results were plotted against patient characteristics (e.g. age) and fitted with the linear regression model. The coefficient of determination (R^2) and the probability value (P) were calculated. The R^2 demonstrates the percentage of data fitted to the linear regression model. The higher the R^2, the better the fitting. The P is an indication of a significant statistical difference between the data. When the P is less than 0.05, there is a significant statistical difference. Following the regression analysis, two-sample assuming unequal variances t-Tests were applied to find significant differences in the subcategories (e.g. age 49-59 years, and age 60-69 years). Those tests provided the P between two subcategories.

The high number of rheological data allowed advanced statistical analysis to be performed. The viscosity and shear-thinning index data were further analysed using a six-way Analysis of Variance (ANOVA) in the SPSS software package (IBM SPSS Statistics, US). Six-way ANOVA provides the advantage of simultaneously comparing all six variables (age, gender, BMI, fat %, W: H, and origin of the sample) and evaluating their effect on the rheological properties. Another advantage is that it

controls better than the t-Tests the type 1 error Rheological data from 31 patients were analysed because there were missing information from some patient characteristics. Viscosity data at 2, 10, 100 s^{-1} and the shear-thinning index were used. Bonferroni Post Hoc test was performed to investigate the influence of specific patient characteristics on the SF rheological properties. ANOVA provided also the Partial Eta Squared (η_p^2), which indicates the percentage of the variance explained by a given independent variable (small effect: η_p^2 < 0.06, medium effect: η_p^2 < 0.14, large effect: $\eta_p^2 \geq 0.14$).

3.3 Results and discussion

3.3.1 Rheological characterisation of synovial fluids

The SF samples presented a shear-thinning behaviour, confirming the previous publications [76, 95, 141]. The decrease in the viscosity variation as shear increases highlights the shear-thinning trend [95]. For example, the viscosity at 100 s^{-1} ranges from 0.006 to 0.076, a difference of only 0.07 Pa s, whereas at 2 s^{-1}, there is a variation of 0.55 Pa s. The shear-thinning index of the examined SF samples varies widely from 0.43 to 1. **Table 3.3** presents the range and the averaged values of the shear-thinning index for all the patient groups. All the samples are considered shear-thinning apart from one corresponding to a female 76 years old overweight patient with hip OA. The progression of OA is associated with the reduced shear-thinning extent in the SFs [141, 301, 318]; as such, that sample could have seriously degenerated. Three SFs showed an almost Newtonian behaviour (n > 0.9), of which the common characteristics are the high W: H ratio (W: H > 0.9) and the elevated age (over 70s). In contrast to the Newtonian samples, no clear correlation was found among the patients whose samples demonstrated the strongest shear-thinning behaviour (n: 0.4 - 0.5). **Figure**

3.1 illustrates the viscosity of four indicative SF samples and the reference PBS. One of those is very shear-thinning (*n*=0.475), one almost Newtonian (*n*=0.903) and two moderate shear-thinning (*n*=0.772, 0.753).

Table 3.3: Shear-thinning index (**n**) of SF samples from various groups of patients suffering from OA.

Groups of patients	***n* (-)** Min-Max (Average ± standard error)
Male	0.43 - 0.90 (0.71 ± 0.03)
Female	0.45 -1.00 (0.73 ± 0.03)
Knee OA	0.43 - 0.92 (0.72 ± 0.03)
Hip OA	0.45 - 1.00 (0.72 ± 0.04)
Age: 49-59 y	0.42 - 0.85 (0.57 ± 0.08)
Age: 60-69 y	0.50 - 0.89 (0.80 ± 0.03)
Age: over 70 y	0.45 - 1.00 (0.72 0.02)
Normal weight	0.45 - 0.93 (0.69 ± 0.05)
Overweight	0.43 - 1.00 (0.72 ± 0.04)
Obese	0.50 - 0.92 (0.74 ± 0.03)
Fat 21-31%	0.43 - 0.93 (0.72 ± 0.04)
Fat over 31%	0.45 - 0.92 (0.68 ± 0.04)
W: H 0.70-079	0.45 - 0.89 (0.71 ± 0.10)
W: H 0.80-0-89	0.50 - 0.89 (0.72 ± 0.04)
W: H 0.90-1.10	0.43 - 0.92 (0.69 ± 0.03)

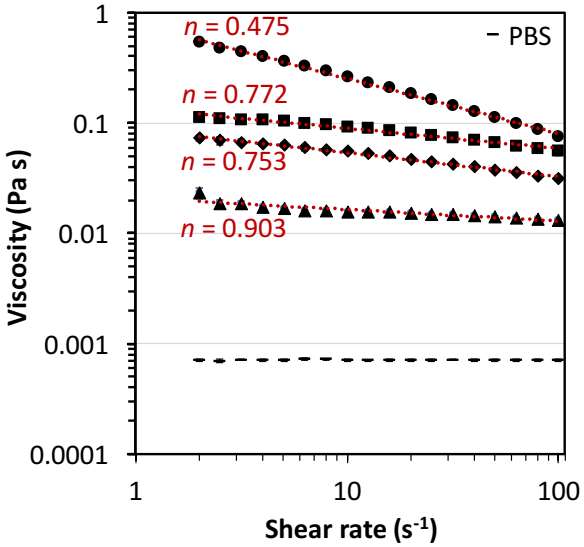


Figure 3.1: Viscosity of four indicative SF samples from patients suffering from OA and the reference PBS in relation to the shear rate. Circle: 57 yr, overweight, male, knee OA, fat 28.3%, W: H 1.12. Square: 74 yr, overweight, female, knee OA, W: H 0.97. Rhombus: 71 yr, overweight, female, knee OA, fat 37.8%, W: H 0.91. Triangle: 76 yr, overweight, male, knee OA, fat 24.8%, W: H 0.93. The data are fitted with the Power-law model. For every SF sample, the shear-thinning index (n) is presented. Each data point is the average viscosity value of three repetitions of the same sample. The error bars represent their standard error.

The Power-law model fitted well with the rheological behaviour of the present samples (average R^2: 0.941 ± 0.096). The model provided the shear-thinning indices and a consistency equals to 0.206 ± 0.03 Pa s. The Power-law is a commonly used model for shear-thinning fluids, especially when there is a shear-thinning behaviour across all tested shear rates [319]. The viscosity of the SF samples is modelled most of the time using the Power-law model or modifications of it in the literature [320-322]. The Cross model has also been used for modelling the viscosity of SFs [302, 310]. However, it is not appropriate in this case because, in addition to the shear-thinning, it considers a Newtonian element at zero and high shear rates [323], which have not been observed in the present data. The use of the Carreau-Yasuda model has also been suggested for SFs [324]. This model is used for viscosity behaviour similar to the

Cross model but incorporates an additional exponent for the transient area from Newtonian to shear-thinning.

The interactions between the HA and the SF proteins explain the SF shear-thinning behaviour on the molecular level. At low shear rates, there are strong inter-particle interactions between the anionic HA and the cationic proteins of SF, forming a highly entangled network that causes resistance to flow and, as such high viscosity [314]. More specifically, hydrogen bonds stabilise their interactions and strengthen the rheological performance of the SF [308]. At high shear rates, those interactions decrease due to molecular disentanglements like breakage of HA chains and HA-protein aggregates [314], and the molecules align with the direction of the flow [275, 308]. As a result, the free space between the molecules increases and the viscosity decreases [273].

The SFs in the present study cover a broad range of viscosity indicating a high level of heterogeneity and suggesting OA acts in various ways in the population. For example at 2 s^{-1}, the viscosity covered an area from 0.012 to 0.562 Pa s. The variation in SF viscosity could be attributed to the different SF composition, such as the HA and protein content or the different characteristics like the HA molecular weight [95]. SFs viscosities are within the reported range for osteoarthritic samples 0.085-25 Pa s [95, 141, 153, 275]. However, a direct comparison with previous studies is not possible due to the different instruments and methodologies used (**Table 3.1**). Mathieu *et* al. for instance, reported a viscosity range 3.5 times smaller than the range found in this study [308]. Since the variability of the SFs viscosity is significant, the more the tested samples (49 samples versus 12), the wider the viscosity range. The higher temperature

is probably another reason for the lower average viscosity of the SFs in the present study. As reported, the viscosity of osteoarthritic SFs declines with temperature rise [95]. 37^{o}C was used during the measurements to simulate the human body temperature instead of 25^{o}C used by Mathieu *et* al. [308]. Although there is an overlap between the reported ranges for non-osteoarthritic and osteoarthritic SFs, it has to be pointed out that none of the tested SFs exceeded the 1 Pa s, which was found in multiple studies as the lowest viscosity limit for non-osteoarthritic SFs (**Table 3.1**). Therefore, it is likely that the SFs in the present study have degenerated. Based on the literature, the reduced viscosity of the osteoarthritic SFs in consequence of the decreased concentration and molecular weight of HA [105] or the increased content and molecular weight of proteins [325, 326].

The effect of patients' physical and anatomical characteristics on the viscosity and the shear-thinning of their SFs is presented below. Although some statistically significant correlations have been revealed, most of the correlations are weak, and many outliers can be seen. The weak correlations could be attributed to the heterogeneity of human samples and other unknown patient characteristics. The samples were analysed based on the known characteristics of age, gender, BMI, fat %, W: H, and sample's origin. However, according to the literature, there are many other factors inducing OA, like the duration of having OA, joint injuries, physical activity, occupation, diet, metabolism and genetics, which might have affected the rheological properties of the SFs [176].

3.3.1.1 Effect of age

Age demonstrated the strongest correlation (P=0.039) with the rheological properties of the SFs. A decreasing trend of viscosity with increasing age is shown in **Figure 3.2a**. The SF viscosity of the young patients (49-59 yr) was the highest for all the tested shear rates, suggesting that osteoarthritic SF loses its exceptional high viscosity with age progression. More specifically, the average SF viscosity of the patients in their sixties is 58% lower than the SF viscosity of the young patients. The difference between the young patients and those in their sixties and the young patients and those in their seventies is significant (P=0.034 and P=0.048 accordingly), in contrast to the difference between patients in their sixties and seventies (P=0.12). With the shear rate increase, the viscosity correlation with age is less important (P=0.058 at 10 s^{-1} and P=0.067 at 100 s^{-1}). That is an expectable result given the shear-thinning nature of the SF. Similar to the viscosity, the shear-thinning extent of the SFs reduces with age progression. Even if the correlation is statistically weak (P=0.546), the shear-thinning index increases with age by 40%, as shown in **Figure 3.2b**. The 66.1% of the shear-thinning index data are explained based on the age. The average shear-thinning index for patients 60-69 years old is 29% higher than the patients 49-59 years old, and a significant difference between those groups was found (P=0.024). The R^2 of the regression line is low for the viscosity and shear-thinning data. This was expected because of the high variability of the SF rheological data. Linear regression was used to identify correlations and not to model the data. Significant trends (P<0.05) between the rheological properties and the patient characteristics can still be identified reliably.

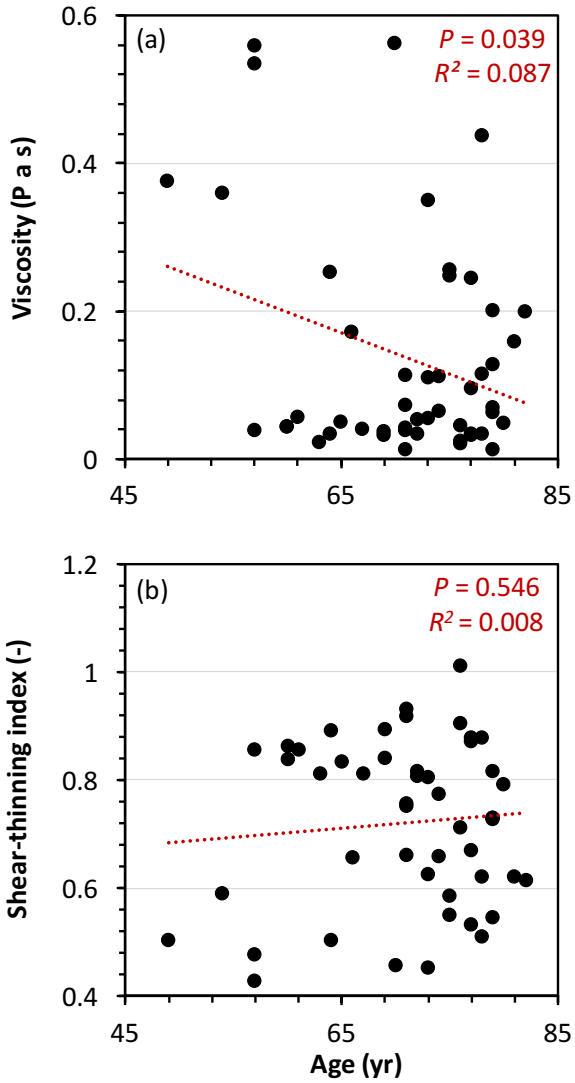


Figure 3.2: SF (a) viscosity at 2 s^{-1} and (b) shear-thinning index in relation to the age of patients with OA. Each viscosity data point is the average of three repetitions of the same sample. Each shear-thinning index data point was found using the Power-law model on three repetitions of the same sample. The error bars were omitted for presentation purposes. The R^2, P and the trendline were calculated using linear regression analysis in Microsoft Excel.

3.3.1.1.1 Effect of Hyaluronic acid

Figure 3.2 indicates that SF loses its exceptional high viscosity and shear-thinning properties with age progression. The diminished rheological attributes might relate to the age-related reduction of HA concentration in the SF [133]. HA is critical because it provides SF with its characteristic high viscosity and shear-thinning

behaviour [26]. A similar negative trend with age has been found for the viscosity of the healthy SF as well [153]. It is essential to note that all human tissues deteriorate with ageing [327]. Alterations in the musculoskeletal system of older adults result in the breakdown of AC, enhancing susceptibility to OA [328]. For example, the subchondral bone develops bone marrow lesions [329], ligaments lose their capacity to absorb compression load [330], and meniscus tears become ordinary with age progression [331].

3.3.1.2 Effect of fat levels and Waist: Hip

It is crucial to consider the effect of fat levels and their distribution on the human body on the rheology of the SF. The total fat percentage of the SF samples demonstrated a similar but weaker correlation (P=0.613) with the viscosity (**Figure 3.3a**). The averaged SF viscosity from patients with fat 21-31% was at the same level as the SF viscosity from those with fat more than 31% (0.17 ± 0.06 and 0.17 ± 0.04 Pa s accordingly). SFs from patients with shallow fat levels (less than 15%) demonstrated very low viscosity, possibly because the body does not operate physiologically under such low abnormal fat levels. The fat-free muscle mass is unable to protect joints against OA [332]. Deficient fat levels could induce OA similarly to high-fat levels. Studies relate deficient fat levels to health issues like reduced muscular strength and increased risk of death [333].

The W: H, associated with the risk of developing OA, is commonly used by medical professionals as a measure of fat distribution. **Figure 3.3c** illustrates the viscosity of the SFs regarding the W: H of the patients at 2 s^{-1}. Even if the correlation of viscosity with W:H is weak (P=0.245), an increasing trend can be observed. The

average SF viscosity of patients with W: H 0.7-0.79, 0-8-0.89, and 0.9-1.1 was found 0.12 ± 0.07, 013 ± 0.03, and 0.17 ± 0.03 Pa s respectively. In other words, the more fat is distributed around the waist, the higher the viscosity of the SF. It could be that the waist withstands more mechanical stresses than the hips/knees because of the fat accumulation around it, and therefore the hip/ knee SFs retain their viscosity.

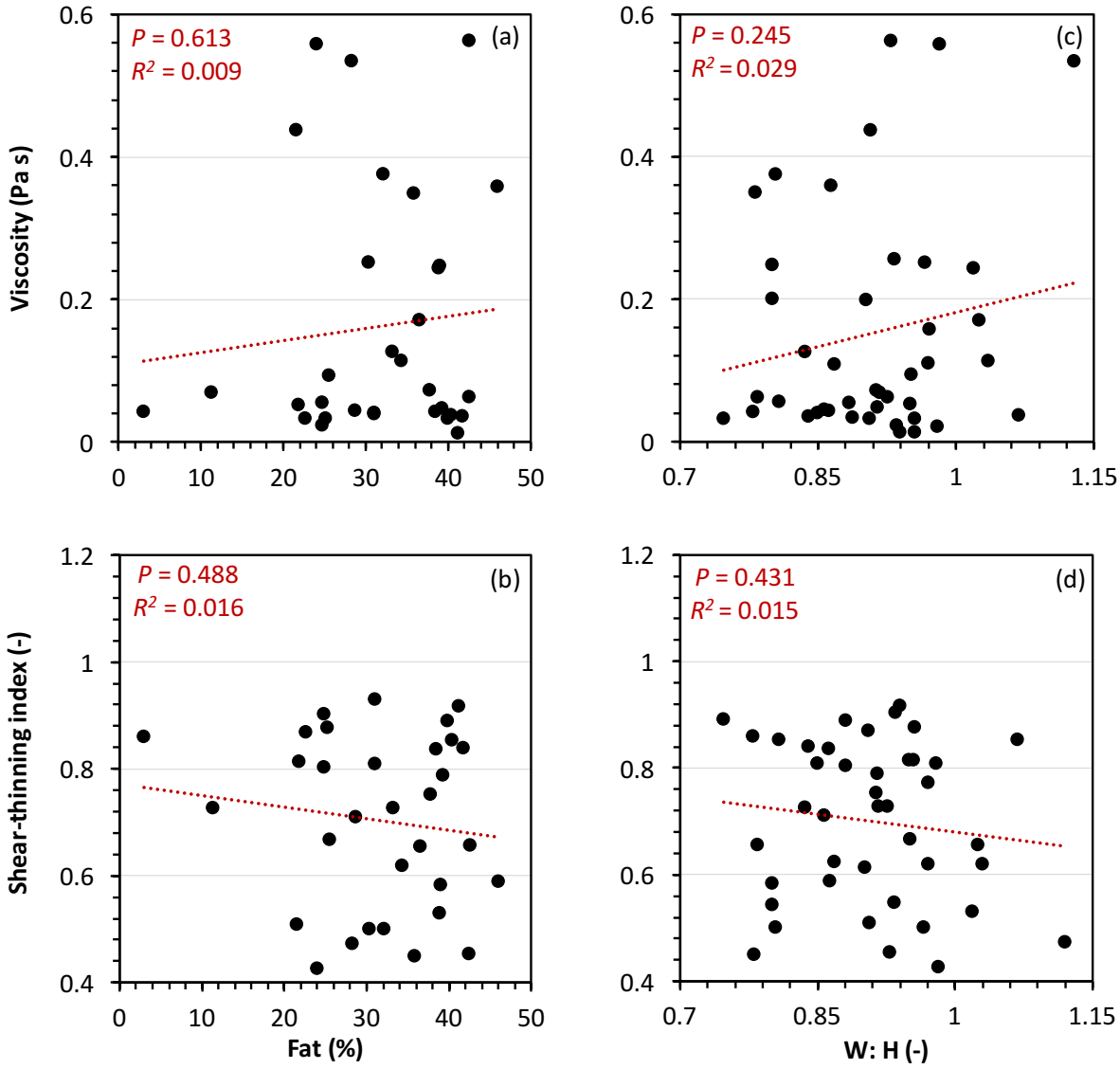


Figure 3.3: SF viscosity at 2 s^{-1} and shear-thinning index in relation to the (a,b) fat and the (c,d) W: H for patients with OA. Each viscosity data point is the average of three repetitions of the same sample. Each shear-thinning index data point was found using the Power-law model on three repetitions of the same sample. The error bars were

omitted for presentation purposes. The R^2, P and the trendline were calculated using linear regression analysis in Microsoft Excel.

The shear-thinning index of the SFs from patients with fat levels over 31% is 5.9% lower than those with 21-31% fat (**Figure 3.3b**). Alike that, the shear-thinning of patients with W: H 0.90-1.1 was found to decrease by 3.6% compared to those with W: H 0.7-0.79 (**Figure 3.3d**). Despite statistically insignificant, those trends indicate that elevated fat levels distributed around the waist (high W: H) induce inter-particle interactions between the SF molecules, providing SF with shear-thinning behaviour.

3.3.1.3 Effect of obesity

Although no significant statistical difference was identified between viscosity and obesity (BMI), the average SF viscosity from obese patients at 2 s^{-1} was 38% lower than the normal-weight and overweight patients' viscosity, which were at the same levels (0.15 ± 0.04 and 0.16 ± 0.04) (**Figure 3.4a**). In addition to the viscosity, obesity correlates with a statistical difference (P=0.026) to the shear-thinning index, explaining 70.2% of the data (**Figure 3.4b**). The average shear-thinning index of the SFs was found to increase for the obese patients compared to the normal weight patients by 7%. As such, the shear-thinning behaviour of the SFs decreases with increasing BMI, suggesting that the increased body weight weakens SF's viscosity. It can be observed that the BMI affects SF viscosity different than the fat (**Figure 3.3**), highlighting the need to evaluate the effect of body fat distribution in combination with the BMI [159, 180, 334]. BMI is considered more representative than the total fat because it incorporates the total fat, lean muscle, and bone mass [335].

The above-mentioned results confirm clinical data suggesting that obesity contributes to OA [165, 336]. Obesity causes mechanical overloading and alters joints composition, structure and mechanics leading progressively to degeneration [337, 338]. The high levels of truncal adipokines measured in SF from obese patients confirm the adverse effect of obesity on the SF [156, 167]. Adipokines contribute to the development of diseases associated with obesity like OA [339].

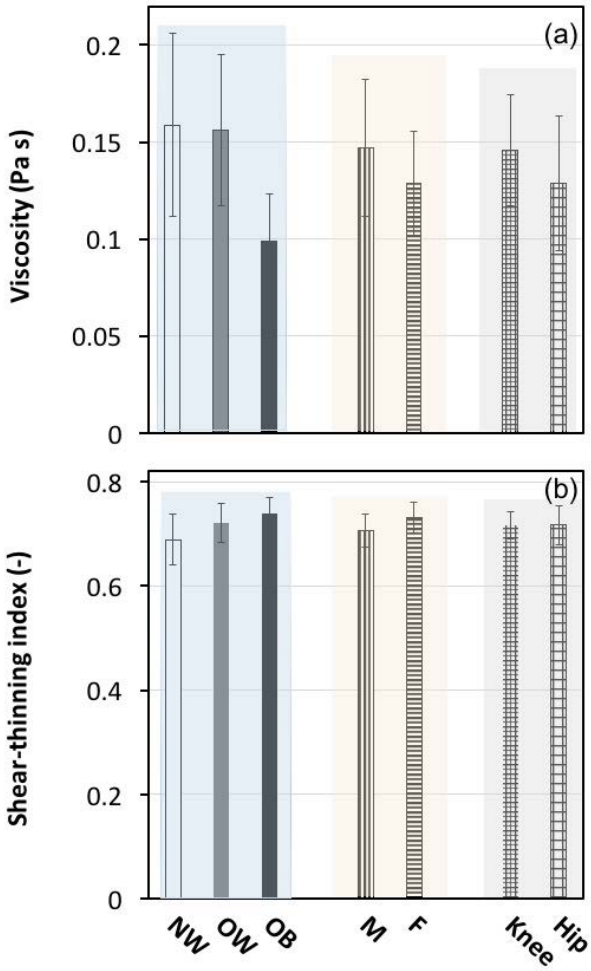


Figure 3.4: SF (a) viscosity at 2 s^{-1} and (b) shear-thinning index as a function of the weight status, the gender, and the origin of the sample of patients with OA. Each bar represents the average value of all the patients of the group (Normal weight (NW) N=11, Overweight (OW) N=21, Obese (OB) N=17, Male (M) N=22, Female (F) N=27, Knee N=29, Hip N=19). The error bars represent the standard error of the viscosity of the different SF samples within each group.

3.3.1.4 Effect of gender

The average viscosity of SFs from female patients (0.13 ± 0.03 Pa s) was found lower than the male patients (0.15 ± 0.03 Pa s) by 14% (**Figure 3.4a**). Nonetheless, the difference between them is not statistically significant (*P*=0.68). Similar to the viscosity, the shear-thinning index was not statistically significant between genders (**Figure 3.4b**). Women exhibited an average shear-thinning index 3.3% higher than men (0.73 versus 0.71). The above data suggest that women SF is less viscous, less shear-thinning, and therefore, less efficient lubricant than men's SF. Although there is no previous evidence about gender differences in the SF rheology, diminished SF lubrication in women was expected because OA affects women more than men [340, 341]. Some compositional differences render women SF prone to OA. For example, the miRNA content of extracellular vesicles in women SF is lower than in men, highlighting reduced ability to innate the immune system [173]. Furthermore, chondroitin sulphates, which provide resistance to AC compression, are decreased in women than men SF [177].

3.3.1.5 Effect of sample origin

The last patient category is based on the origin of the SF sample. The tested SFs were acquired either from a knee or a hip joint of a patient. Although there was no statistical difference, the average SF viscosity from knees was higher than the hips for all tested shear rates (**Figure 3.4a**). At 2 s^{-1} the average viscosity of the SF samples from the knees was 11% higher than hips. The higher viscosity of knee SFs could be associated with the reported higher concentration of GAGs in knee joints [342]. HA is the most important GAG of the SF, and its concentration is positively correlated to SF

viscosity [105]. Furthermore, the mechanical stresses applied on the hips during daily activities are higher (5.3-11.9 MPa [343]) than those applied on the knees (1-6 MPa [344]) and, as such, hip SFs might degenerate. The SF shear-thinning indices from patients suffering from knee OA and hip OA were at the same levels (0.72), indicating no difference between the different types of joints (**Figure 3.4b**).

3.3.1.6 Further statistical analysis

ANOVA confirmed the above correlations of patient characteristics with SF viscosity and shear-thinning. Levene's Test of Equality of Error Variances revealed a significant effect of P=0 on the viscosity and P=0.003 on the shear-thinning of the independent variables (age, gender, BMI, fat levels, W: H, sample's origin). The relationship between viscosity/shear-thinning and the six variables was strong since they explained 94.2% of the viscosity and 94.9% of the shear-thinning index data (R^2: 0.942, R^2: 0.949). **Table 3.4** presents the statistically significant interactions of the rheological properties with the patient groups at 2, 10 and 100 s^{-1}. The same patient groups (age, BMI) demonstrated statistically significant interactions across all tested shear rates. Nevertheless, there is a small reduction in those interactions with increasing shear rate, highlighted by the increase in the P and the decrease in the η_p^2. Fewer correlations were expected at high shear because of the SFs are shear-thinning. An additional interaction with the sample origin was revealed in the case of the highest shear rate of 100 $s^{-1.}$ That differentiation between the viscosity of knee and hip joints could be related to the actual behaviour of the joints under high shear rates activities like running. Higher mechanical stresses are applied on the hips [343] than the knees [344], and, as such, hip SFs viscosity might degenerate more. Bonferroni post hoc

tests revealed that the age group of 49-59 years old patients demonstrated a significantly different viscosity than the age group of the 60s and 70s. However, the BMI subgroups demonstrating a significant difference in the viscosity and the shear-thinning were not identified.

Table 3.4: Significant interactions of viscosity (η) and shear-thinning index ($\mathbf{n}$) with patient groups acquired by ANOVA. The probability (P) and the Partial Eta Squared (η_p^2) are provided for each interaction.

Rheological properties	Age	BMI	Sample origin
η at 2 s^{-1}	*P*=0.012, η_p^2=0.77 (*P*=0.008 49-59 yr-patients 60s, *P*=0.011 49-59 yr-patients 70s)	*P*=0.021, η_p^2=0.73	-
η at 10 s^{-1}	*P*=0.02, η_p^2=0.73 (*P*=0.01 49-59 yr-patients 60s, *P*=0.013 49-59 yr-patients 70s)	*P*=0.026 η_p^2=0.70	-
η at 100 s^{-1}	P=0.041, η_p^2=0.66 (*P*=0.014 49-59 yr-patients 60s, *P*=0.014 49-59 yr-patients 70s)	*P*=0.032, η_p^2=0.68	*P*=0.039, η_p^2=0.53
n	*P*=0.039, η_p^2=0.66 (*P*=0.024 49-59 yr-patients 60s)	*P*=0.026, η_p^2=0.70	

Similar SF rheological properties were identified between subgroups. At the shear rate of 2 s^{-1}, male patients and knee OA patients demonstrated an average viscosity of 0.147 ± 0.027 Pa s and 0.146 ± 0.029 Pa s accordingly. Female patients (0.129 ± 0.027 Pa s), patients with hip OA (0.129 ± 0.035 Pa s), and those with W: H 0.7-0.79 (0.122 ± 0.076 Pa s) can be grouped concerning their viscosity levels. Another group could be the normal-weight OA patients (0.159 ± 0.047 Pa s), the overweight patients (0.156 ± 0.039), and those with fat up to 31% (0.154 ± 0.050 Pa s). Similar SF viscosity suggests a similar level of deterioration for those patients. In those cases, clinicians could provide them with a common treatment strategy to alleviate OA symptoms.

3.3.2 Surface interactions of synovial fluids

Other than its rheological characteristics, surface interaction of SF at the articulating interface is believed to play a major role towards its exceptional lubrication. Adhesion energy measurements were carried out in a few samples as a supplementary method to evaluate the effect of SF's macromolecules adsorption on joints' lubrication. The hypothesis is that the higher the SF viscosity, the more molecules adsorb to the substrate and, as such, the lower the adhesion energy.

Even though AFM force curves cannot indicate the specific SF molecules adsorbed onto the titanium surface, they can reveal the lubrication performance of the tested SF samples. Understanding the competitive adsorption mechanism of SF components is complex because any SF component may adsorb to the AC/implant's surface, and SF composition varies from person to person. Human serum albumin (HSA), glycoproteins (lubricin, alpha-1-acid glycoprotein, alpha-1-antitrypsin), γ-globulin and HA-phospholipids (SAPLs) mixture adsorb onto joint's implants materials and create a protective film [345-347]. Γ-globulin, HSA and lubricin are the most dominant boundary lubricants. Under competitive adsorption, HSA blocks lubricin, while γ-globulin displaces pre-adsorbed HSA and HA molecules [347].

SF samples were diluted to different magnitudes by PBS buffer to reduce their viscosity, meeting the requirements for AFM experiments. The adhesion energy required to withdraw the AFM cantilever tip from the titanium surface contained in SF was calculated from the adhesion peak area of the AFM force curves as described in section 2.1.6 of chapter 2. The protocol for investigating the surface adhesion energy of SFs is a new method for studying SFs' lubrication properties, which was developed

during this study. Ten random SF samples were analysed and established a negative correlation with viscosity as hypothesised. The limited number of tested SF samples is related to the limited availability of samples provided by OA patients who underwent total knee or hip replacement at The Royal Orthopedic Hospital in Birmingham.

The force curves demonstrated multiple detachment points (**Figure 3.5b**), possibly due to the various adsorbed SF molecules. The detachment points and, as such, the adhesion energy decreased with increasing dilution for all samples (**Figure 3.5a**). Upon dilution, the concentration of the SF components decreases proportionally, and as a result, less adsorption occurs on the titanium surface. The adhesion energy was found to decrease with an increasing dilution ratio for all samples, confirming that fewer and fewer molecules adsorbed on the solid substrate. Similar to viscosity, wide variability was identified in the adhesion energy. The average adhesion energy of the ten-times diluted SFs varied from 7.7 to 105.6 10^{-18} J, whereas the reference PBS demonstrated adhesion energy between 0.3 to 16.3 10^{-18} J under the same experimental conditions. Moreover, every sample followed a different trend upon further dilution, highlighting once more the heterogeneity of the SFs. In the following sections, the behaviour of the adhesion energy is analysed based on the patient characteristics.

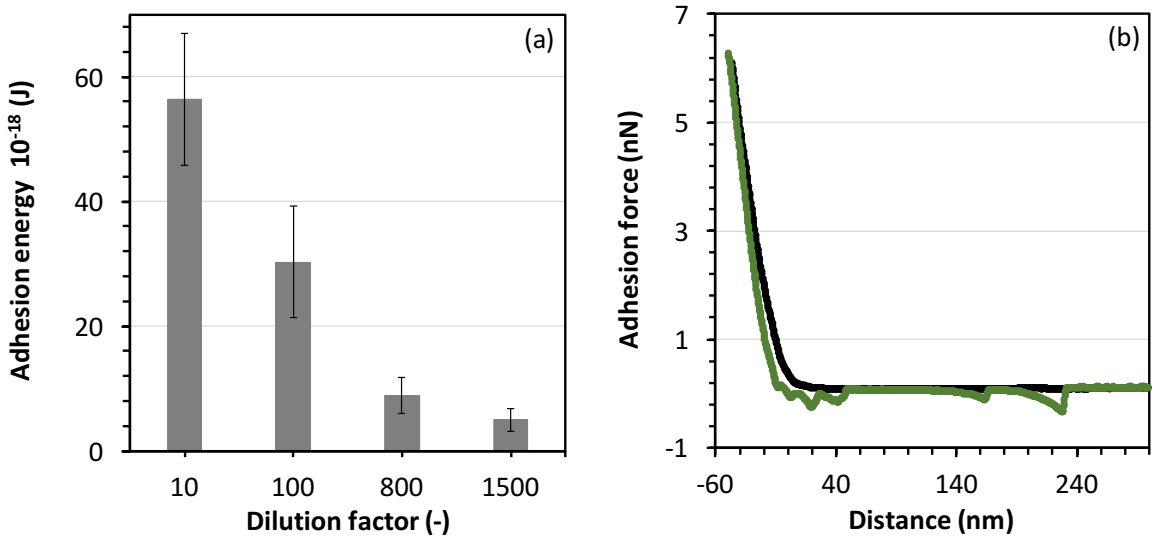


Figure 3.5: (a) Average adhesion energy of ten osteoarthritic SF samples as a function of the dilution factor. Each bar represents the average value of ten SF samples at the same dilution factor. The error bars represent their standard error. (b) Representative force curve of a human osteoarthritic SF (green). The black curve is the force curve of PBS. The measurements were performed between a silicon nitride cantilever and a titanium substrate.

3.3.2.1 Effect of age

Figure 3.6 indicates that the adhesion energy elevates with patients' age, demonstrating a statistical significance of *P*=0.035, which is also correlated with the viscosity results. In the older adults (above 80 yr), the adhesion energy increased by 172% compared to the young patients (49-59 yr) under 10-times dilution. That outcome, combined with the fact that adhesion increases with OA progression [137], highlights the degeneration of osteoarthritic SFs with increasing age. The increase in adhesion could be attributed to the decreased adsorption of boundary lubricants. For instance, lubricin forms a film on the AC, enhancing joints lubrication [345], but it decreases with age progression [348]. Therefore, it is hypothesised that the tested osteoarthritic SFs from older adults lack lubricin, resulting in decreased adsorption and

consequently diminished lubricating properties (increased adhesion energy and CoF) [105, 108]. The increase of cell-adhesion genes with advanced age has already been seen in mices' meniscus [349].

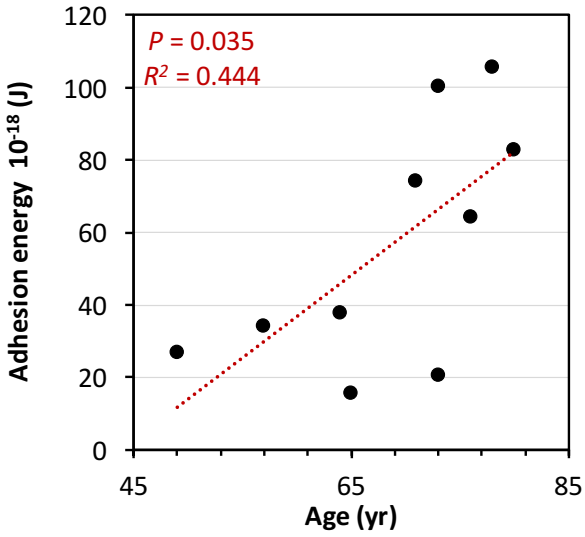


Figure 3.6: Adhesion energy of ten SFs samples diluted ten times in PBS as a function of the age for patients with OA. Each adhesion energy point is the average from one hundred and fifty force curves made with the same sample. The error bars were omitted for presentation purposes. The R^2, P and the trendline were calculated using linear regression analysis in Microsoft Excel.

3.3.2.2 Effect of obesity and Waist: Hip

Figure 3.7 and **Figure 3.8** illustrate a significant correlation (P=0.052) of SF adhesion energy with BMI. An increasing trend has been observed across all dilutions. The average SF adhesion energy from obese patients was 234-673% higher than normal-weight patients. Compositional changes in osteoarthritic SFs, like the reduced presence of SAPLs on the AC surface, may account for alterations in lubrication performance. The shorter hydrophobic chain length of surface-active SAPLs in osteoarthritic SFs [350, 351] diminishes lubrication due to the reduced adsorption on

the AC surface [352]. Moreover, obesity creates an inflammatory environment in the joints [156], impelling an increase in cell-adhesion molecules like the E-selectin and the Intercellular Adhesion Molecule 1 [353, 354]. Similar to BMI, the adhesion energy increases as W: H increases. However, in that case, the correlation is not statistically significant (P=0.315).

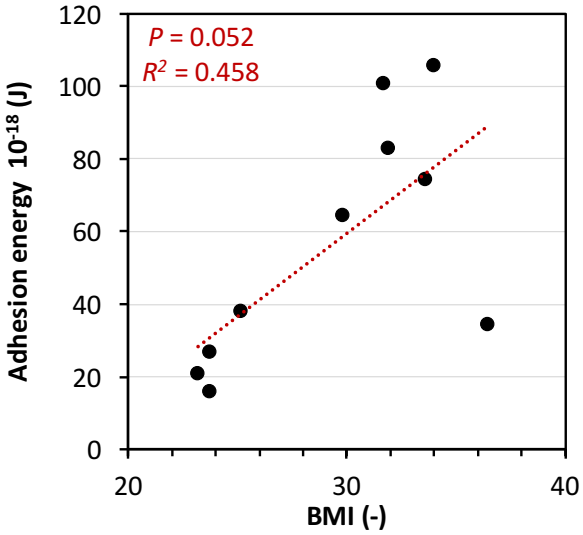


Figure 3.7: Adhesion energy of ten SFs samples diluted ten times in PBS as a function of patients' BMI. Each adhesion energy point is the average from one hundred and fifty force curves made with the same sample. The error bars were omitted for presentation purposes. The R^2, P and the trendline were calculated using linear regression analysis in Microsoft Excel.

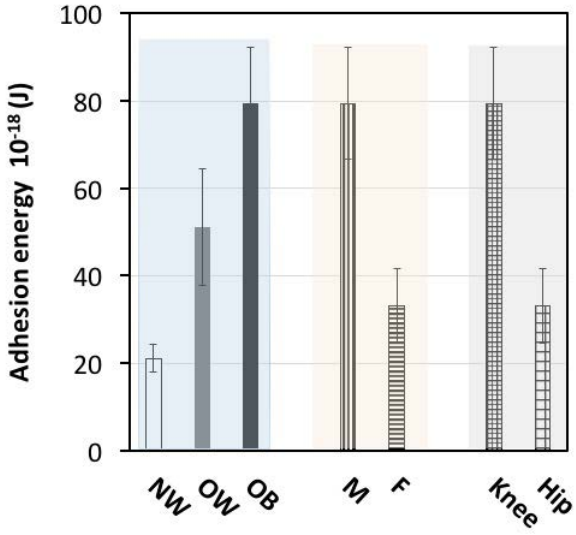


Figure 3.8: Average adhesion energy for ten-times diluted osteoarthritic SF samples as a function of the weight status, the gender and the origin of the sample. Each bar represents the average adhesion energy of all the patients of each group (Normal weight (NW) N=3, Overweight (OW) N=2, Obese (OB) N=5, Male (M) N=3, Female (F) N=7, Knee OA N=5, Hip OA N=5). The error bars represent the standard error of the adhesion energy of the different SF samples within each group.

3.3.2.3 Effect of gender

Women demonstrated 8-67% higher average adhesion energy than men across all dilutions (**Figure 3.8**). As stated above, that result was anticipated, given that females are more prone to OA than males [176], and high adhesion is associated with increased degeneration [137]. It needs to be stressed out, though, that the number of female samples (seven) was significantly higher than male samples (three), and therefore, it is not safe to make any definitive conclusions.

3.3.2.4 Effect of sample origin

The average adhesion energy of knee SFs was higher than hip SFs by 55-75% across all examined dilutions (**Figure 3.8**). For ten-times dilution, the adhesion energy

of knee SFs was higher than hips by 58%. The *P*, in that case, was 0.02. The increased mechanical stresses on the hips [343] compared to the knees [344] could explain that result. Previous studies reported increased adhesion in low-load bearing joints compared to high-load bearing joints [91]. AC from high-load bearing joints demonstrates significantly lower adhesion than AC from low-load bearing joints, possibly due to the increased surface concentration of boundary lubricants which protect the joints from adhesion [91]. Indeed, lubricin, HA, and aggrecan concentration is higher in high-load than low-load bearing joints [355, 356]. Furthermore, AC from high-load bearing joints withstand increased compressive stiffness and decreased permeability [357]. It needs to be mentioned that the same number of knee and hip SF samples was examined here.

3.3.3 Correlations between rheological and surface properties of synovial fluids

The results presented above demonstrate that SF bulk (viscosity, shear-thinning) and surface (adhesion energy) properties degenerate under OA compared to healthy [137]. Although viscosity was measured on neat SF samples and adhesion energy on ten-times diluted samples, a negative correlation was identified between them. The patient groups, which demonstrated a reduction in viscosity demonstrated a raise in the adhesion energy and vice versa. **Figure 3.9** highlights that correlation by comparing the adhesion energy from ten-times diluted samples and the viscosity of the same neat SF samples. Despite the small number of samples presented here, they strengthen the reliability of the overall results of this study. That comparison is only meant to be used qualitatively because samples analysed at the different experimental

conditions. Ideally, the testing should have been done using the same sample, this was not feasible because of the different methodology requirements.

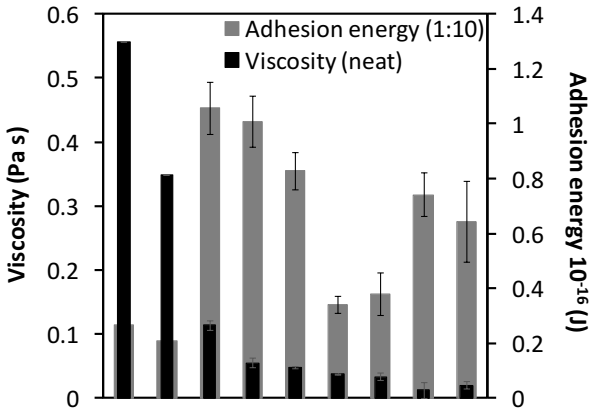


Figure 3.9: Adhesion energy and viscosity of the same nine osteoarthritic SF samples. Viscosity was measured on neat SF samples, whereas adhesion energy on ten-times diluted samples. Each bar represents one SF sample. The error bars represent the standard error of three repetitions for the viscosity and one hundred and fifty for the adhesion energy of the same sample.

The adhesion energy could be associated with the CoF in the joints. In general, adhesion affects the applied normal load and is positively correlated to the CoF [91, 358]. That correlation has been confirmed experimentally in the AC surface [91, 347, 359]. Adhesion affects the CoF of the AC significantly especially following long equilibration times [360]. The exact level of CoF cannot be estimated here because the adhesion energy was measured on diluted samples. However, the present data could give an indication about the joints' CoF behaviour without testing it. For example, higher CoF is expected in knee rather than hip joints because knee samples exhibited higher average adhesion. Additionally, the increase in adhesion could be related to compositional alterations of the Extracellular matrix (ECM) and indicate a decrease in "good" boundary lubricants like lubricin [63, 64] and γ-globulin [128] or an increase in

“bad” boundary lubricants like the HSA. Alpha-1-acid glycoprotein, alpha-1-antitrypsin, lubricin, and γ-globulin decrease the CoF thanks to the soft protective film they form [345], whereas HSA increases the CoF due to its denaturation (orientation and configuration) on the AC surface [345] and the blocking of lubricin adsorption [347].

3.4 Conclusions

This study confirmed the diminished lubrication in osteoarthritic joints under boundary and hydrodynamic regimes and identified strong correlations of the SF lubrication properties with patient characteristics. Bulk (rheology, shear-thinning index) and surface (adhesion energy) lubrication properties were examined to cover all lubrication conditions in the everyday operation of joints. Age is identified as the most influential factor leading to SF degeneration and possibly inducing OA development. SF’s viscosity decreases with age progression, while the Newtonian behaviour and adhesion energy increase significantly. The reduced SF lubrication efficiency with advanced age could be attributed to compositional changes such as the reduced concentration of HA and the increased cell-adhesion genes. In addition to age, BMI demonstrated a statistically significant interaction with SF’s lubrication properties. SF viscosity from obese patients was significantly lower and less shear-thinning than the normal-weight and overweight patients. Moreover, SF adhesion energy was found significantly increased with BMI. The adverse effect of increased BMI on SF lubrication properties could be explained by the compositional alterations induced by increased mechanical stresses applied to obese joints, as stated in the literature [337, 338] and the inflammatory environment, which promotes cell adhesion [353, 354]. The adhesion energy results revealed an additional significant correlation with the sample origin. The

adhesion energy of knee SFs was 58% higher than the hips. That observation could be related to the increased concentration of boundary lubricants at low-bearing joints like the knee [91].

Patients were sorted into three broad categories depending on their rheological properties. Moreover, the pathological ranges of those properties were established for each category. The first category includes males and patients with knee OA. The second category consists of females, patients with hip OA and W: H 0.7-0.79. The third category comprises normal-weight, overweight, and patients with fat levels up to 31%. The SFs of those patients demonstrate a similar level of deterioration and, therefore, a similar disease progression rate. Clinicians could utilise that data and provide the patients with specific treatment approaches tailored to the lubrication requirements of each patient group. Based on the established pathological ranges and the identified correlations between the lubrication properties, clinicians could estimate other lubrication properties without testing them, leading to faster and more efficient diagnosis. For example, adhesion is positively correlated to CoF, which is the primary source of pain for OA patients. SF's lubrication properties could also be used in the diagnosis of OA. SF's viscosity has already been recognised as an accurate and sensitive marker for detecting Periprosthetic Joint Infection [312].

No strong trends were established with the other physical characteristics despite age and BMI. That outcome could be associated with the limitations of studying human SF samples' properties. Such samples can only be collected post-mortem or during arthroplasty. The SF samples used in this study were collected during arthroplasty of patients suffering from OA. There was no control over the number of

patients who needed to undergo surgery during the span of this study. The donors were at the last stage of OA, and therefore, the results are relevant to the late OA, and generalising them for the early stages of the disease requires additional research. Furthermore, the minimal quantity of the SF samples restricted the number of measurement repetitions. Having the same number of samples for each patient category was not feasible because the donors were a live population. Female, obese, elderly are more prone to OA, and as such, the number of donors for those groups was higher than the rest. Finally, to achieve solid statistical correlations, all patients within a group should have the same fixed characteristics and differ only at one variable at a time. However, this is not possible with humans. For example, older people are, at the same time, females or males. Finally, no healthy SF samples were available for this project, and instead, literature data was used. The only possible source of healthy SFs is from post mortem individuals, but such samples were unavailable for this study.

In summary, the present study confirmed the diminished lubrication in osteoarthritic joints under boundary and hydrodynamic regimes. Advanced age (above 60 yr) and elevated BMI (above 30) were the dominant risk factors for OA progression. Combining the experimental results with the literature suggests that the lack of HA in osteoarthritic SFs is associated with reduced lubrication. As such, the requirements for a new treatment for OA were identified. This study also categorised the patients into groups based on their lubrication properties and provided the pathological ranges of those properties. That knowledge enables clinicians to detect OA early and provide patients with treatment tailored to their needs. Furthermore, a new method for analysing the lubrication properties of diluted SFs using AFM has been developed, which could be a promising approach for the future investigation of human SFs.

4. NANOPARTICLES AS FRICTION MODIFIERS FOR OSTEOARTHRITIC JOINTS

4.1 Introduction

Poor lubrication characterises the osteoarthritic joints under all lubrication regimes, as reported in chapter 3 and in the literature [134]. Although the contact between the articular cartilage (AC) surfaces in healthy joints demonstrates the lowest coefficient of friction (CoF) in nature (CoF=0.001-0.03), the CoF increases significantly under osteoarthritis (OA), resulting in joint damage and pain during physical movements [134]. It has been proved that an increased CoF further accelerates the AC degradation, which associates with OA progression [134]. Since there is no cure for OA yet and the natural healing of the joints is insufficient [75], it is essential to develop effective treatments for maintaining the lubrication of the joints [361].

Lubrication of the joints could be improved by direct injection of lubricants into the diseased joints, a process called intra-articular injection (IAI) [189]. The current formulations used in the IAI treatment of OA aim primarily to restore the viscoelasticity of the synovial fluid (SF) in the joints [181]. Nonetheless, thanks to their high viscosity, they maintain simultaneously low CoF under high-velocity activities like running when the AC surfaces are insulated by the formulation (hydrodynamic regime) [35]. However, the IAI formulations cannot minimise the CoF in low-velocity conditions like walking (boundary regime) because the formulations are squeezed out of the joint, and the AC surfaces come in direct contact [35]. Another drawback of IAI therapy is the temporary pain relief caused by the diffusion of the small therapeutic compounds from the joint via synovial capillaries [7, 190]. Hence, the therapeutic action cannot be

sustained for long, requiring an increased number of IAIs [191]. IAI therapy needs to be improved to ensure the CoF in the joints remains low under all physiological movements, and its therapeutic benefits last long [29, 63].

Unlike classic therapeutic compounds, which diffuse away, nanoparticles (NPs) could adsorb on the AC surfaces and offer prolonged lubrication characteristics in the joints. In the past twenty years, NPs have been successfully used as lubricant additives for various applications like engine oils [56]. Research has recently focused on the core-shell NPs, which demonstrate advanced lubrication performance owing to the improved dispersibility/stability provided by the reinforcing fillers and enhanced surface adsorption [362, 363]. NPs acting in combination with other systems like ionic liquids and hydrogels demonstrate significant advantages [364, 365]. Hydrogels are promising systems for minimising the CoF in the joints because they could replicate the hydration lubrication offered to AC by SF macromolecules [85] and can be optimised to remain longer at the AC surface [212]. The addition of NPs in hydrogels improves even more, the lubrication. Several hydrogels made from charged polymer brushes grafted onto silica NPs have been investigated and provided significant CoF reduction [216-218].

The present work is based on the hypothesis that NPs reduce the CoF in the joints. Although there are some proposed lubrication mechanisms for the NPs [9, 10], the way they work under different tribosystems is not clear yet. To that end, the lubrication efficiency of formulations with various viscosities and NPs types was tested between material combinations, replicating the natural and the artificial joints. Although the previous chapter identified the need to enhance HA in the osteoarthritic joints,

simple low and high viscous solvents were used to understand NPs mechanisms better. The selection of the contacting surfaces was based on the hypothesis that the CoF of the tested tribosystems is affected by Young's modulus. Therefore, substrates with low (silicone elastomer (SE)), medium (Glass), and high (CoCr) Young's modulus were tested as opposed to elastic ultra-high molecular weight polyethylene (PE) balls and stiff stainless steel balls. Each material combination corresponds to a different stage of OA. The aim was to establish the effect NPs formulations have on the CoF of materials resembling the joints and determine the conditions and, as such, the stage of OA under which they work effectively. Silica and latex NPs were used as model NPs. Their selection was based on the availability of NPs with the same particle size and the fact that their mechanical properties represent extreme cases (**Table 4.1**). The size of 200 nm was chosen for the NPs because it is within the range of the reported surface roughness of the human AC (137-533 nm) [63, 196]. As such, those NPs will not increase the surface roughness of the AC; instead, they can smoothen it.

4.2 Materials and methods

4.2.1 Materials

Silica (Sigma-Aldrich, UK) and latex (Agar Scientific, UK) were used as model NPs (average size: 200 nm) because they were commercially available in many sizes and covered a wide range of mechanical properties. **Table 4.1** lists some mechanical and physical properties used in the interpretation of the results. The differences in Young's modulus and the hardness between silica and latex NPs are substantial. The low Young's modulus of the latex NPs is expected to increase the contact area of the tribopairs more than the silica NPs and, therefore, increase the CoF, based on the

literature [366]. According to the literature, the hard silica NPs are expected to scratch the tribopairs and increase the CoF compared to the soft latex NPs [367, 368]. The NPs were diluted in two types of solvents; Phosphate-buffered saline (PBS) and a mixture of polysaccharides. The mixture of polysaccharides was made from sodium alginate and gellan gum based on the literature [369]. It is considered an alternative artificial SF because its viscosity is at the same level as the actual SF; therefore, it will be called artificial SF (ASF) [369]. The PBS (Fisher Scientific, USA) in a concentration 1 x PBS has comparable ion concentration and osmolarity to human body fluids [313].

Table 4.1: Mechanical and physical properties of silica and latex NPs.

Nanoparticles	Young's modulus (GPa)	Density (Kg m^{-3})	Hardness (MPa)	References
Silica	66.3-85.0	2600	4500-9600	[370-373]
Latex	3.0-3.5	980-1040	143	[374-376]

4.2.2 Preparation of nanoparticle formulations

Formulations with four NPs concentrations (0.01%, 0.1%, 0.5%, 1% w/w) were prepared each time. The exact amount of NPs was weighing in a scale for the silica (powder form) or in a volumetric cylinder for the latex NPs (10% water suspension). A summary of the tested formulations is given in **Table 4.2**. The next stage was the magnetic stirring of the formulations until NPs were well dispersed, followed by sonication for three hours, the addition of Sodium Dodecyl Sulfate (SDS) (Fisher Scientific, USA) as a surfactant in a concentration of 0.5% w/v, and magnetic stirring overnight. This procedure yielded a size of nanoparticles very similar to the nominal size. All concentrations are expressed as % w/v.

Table 4.2: Summary of tested nanoparticle formulations.

Formulations' abbreviations	NPs* (0.01-1 % w/v)	SDS (0.5 % w/v)	PBS/ASF (balanced to 100 ml)
NPs	√		√
NPs/SDS	√	√	√

* NPs: Silica, Latex

4.2.3 Surface morphology of substrates

The discs used for the friction tests (CoCr, SE, Glass) were imaged on the Imaging-Intermittent Contact mode of the Atomic Force Microscope (AFM) (JPK Instruments, Germany). The measurements were performed in ambient with an Antimony doped Si cantilever with spring constant 42 N m^{-1} and resonance frequency 320 kHz (Bruker Ltd, UK). The AFM cantilevers were cleaned before each test. Cleaning with Ultraviolet light for ten minutes was the first step used to remove organic contaminants. A ten-minute immersion of the cantilevers in 99% ethanol solution followed, then a ten-minute immersion in High Performance Liquid Chromatography (HPLC) water, and drying with Nitrogen. The AFM images of the specimens were analysed, and their surface roughness was calculated using Gwyddion software.

4.2.4 Size and Zeta Potential measurements of nanoparticle formulations

A Zetasizer Nano ZS (Malvern Instruments, UK) consisting of a He-Ne laser (633 nm) and an MPT-2 Titrator was used to characterise silica and latex NPs formulations. All measurements were performed at 25^{o}C. The refractive index and absorption rate of silica and latex NPs was 1.45-0.01 and 1.59-0.01, respectively. HPLC water (Fisher Scientific, USA) with a refractive index of 1.33 and viscosity of 0.8872 cP was used as the aqueous medium. A few millilitres of each aqueous

suspension at 0.1% w/v were placed in a disposable polystyrene cuvette and fitted in the Zetasizer. The particle size of the NPs formulations was expressed as Z-average and their width distribution as polydispersity index (PDI). Each time a new sample cell was used for the particle size and PDI measurements. Zeta Potential (ZP) measurements were performed with the same machine. The cuvette for the ZP measurements was rinsed with distilled water between the measurements and was changed only when there was visible deterioration. All samples were tested in triplicates.

4.2.5 Viscosity measurements of nanoparticle formulations

The rheometer ARES-G2 Rheometer (TA Instruments, USA) used in this study. The rheometer was calibrated with a material of published viscosity [369]. The measurement test was a steady-state shear flow between 2-100 s^{-1} shear rates (for consistency with Chapter 3) at a temperature of 37^{o}C (physiological human body temperature) [369]. The geometry used was selected based on the viscosity of the suspension. When the formulation medium was the viscous ASF, a 20 mm 2° standard steel cone geometry with 53 mm gap (TA Instruments, USA) was used, but when the solvent was the low-viscosity PBS, a standard double concentric cylinder made from aluminium with a gap of 500 μm (TA Instruments, USA) was used. Concentric cylinders geometries are suitable for the analysis of NPs formulations. Three repetitions of each sample were carried out and the resulting standard error was calculated. The geometry and the sample plate were rinsed between every measurement with SDS, ethanol, and distilled water.

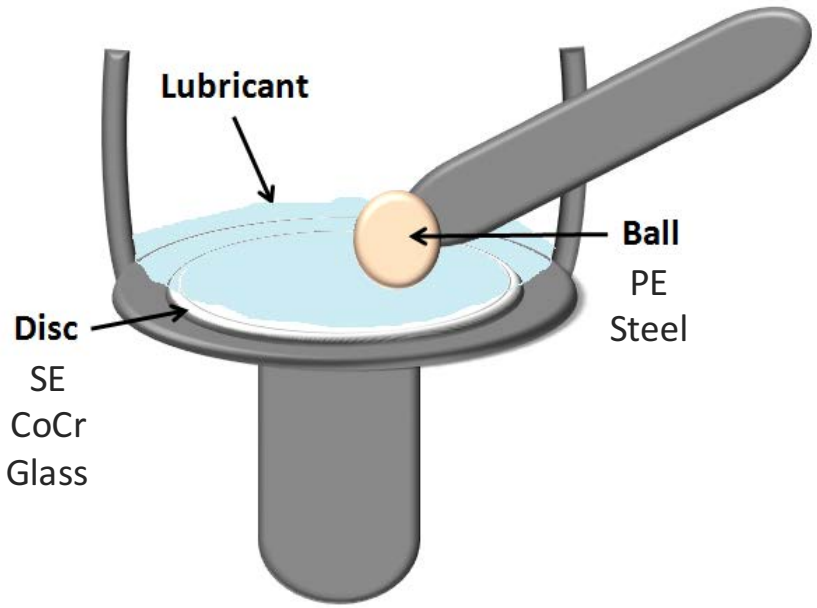
4.2.6 Contact angle measurements of nanoparticle formulations

Contact angle measurements of the NPs formulations and the reference solutions were performed using a Contact Angle Goniometer (Ossila, UK). Contact angle measurements were conducted on the substrates (CoCr, SE, Glass). The contact angle value presented below is the average of six separate areas of each substrate. Ossila contact angle software was used for the video recording of the drops and the data analysis. Three repetitions of each sample were carried out and the resulting standard error was calculated.

4.2.7 Tribological measurements of nanoparticle formulations

Tribological measurements of silica and latex NPs formulations in PBS solution or ASF were performed using the MTM (PCS Instruments, UK). MTM was chosen because it provides automatic and accurate control of load and temperature, providing repeatable and accurate results. Moreover, MTM enables a detailed examination of all three lubrication regimes by producing continuous Stribeck curves. Various combinations of specimens (configurations) were tested. The balls were either made of steel or PE (PCS Instruments, UK). The discs were made of CoCr, Glass (PCS Instruments, UK) or SE (Samco Silicone Products, UK). The specimens were chosen because they enabled the screening of a wide range of Young's modulus and were also available to be bought off the shelf. **Figure 4.1** is a graphical abstract of the tested ball-disc tribopairs. The measurements were conducted at 37^{o}C. Pure sliding conditions were applied (Slide-Roll-Ratio (SRR) = 200%) with the ball being stationary and the disc sliding between 1 and 100 mm s^{-1}. The maximum available by the MTM force of 7 N was implemented from the ball to the disc to bring the lubrication regime

as close as possible to the boundary, which is the target lubrication regime for the therapeutic formulation under investigation. However, the type of the regime depends primarily on the mechanical properties of the contacting materials and their initial contact pressure. The initial contact pressure of the configurations (**Table 4.4**) suggests that Steel-Glass and Steel-CoCr were expected to work mainly in the boundary regime, whereas the rest under mixed lubrication. The Hersey number was used in the results section to identify the lubrication regimes. The CoF was captured against velocity increase in six continuous testing cycles. The average CoF of those cycles and the associated standard error are presented against the sliding velocity.



Ball - Disc tribopairs
Steel - SE
Steel - CoCr
Steel - Glass
PE - SE
PE - CoCr
PE - Glass

Figure 4.1*:* Graphical abstract of ball-disc tribopairs.

A new SE substrate was employed for each measurement, but all the other specimens were reusable until significantly worn. The effect of specimens' wear on the CoF was monitored daily with a reference test, and when a statistical difference in the CoF was seen, the substrates were changed. More specifically, the wear loss was

acceptable until the reference (PBS) provided an average CoF of more than 10%, different from the specimens' first usage. Additionally, imaging of the substrates via AFM was performed regularly to inspect them for wear loss. The potential contribution of specimens' wear has been mentioned in the conclusions. The cleaning process of the specimens before each test includes Ultraviolet (UV) light treatment, 10 min of sonication in ethanol and 10 min of sonication in distilled water. After the cleaning, the specimens were dried with liquid Nitrogen.

4.2.8 Statistical analysis

The CoF results were studied using a Machine Learning Analysis (MLA) tool developed specifically for this project in collaboration with the School of Computer Science. MLA uses advanced algorithms not used by other statistical analysis tools like ANOVA, enabling a more thorough and accurate analysis. The developed MLA tool uses linear regression, support vector regression, random forest regression, multi Linear Regression, Multi Lasso Regression, and Multi Polynomial Regression algorithms, whereas ANOVA uses only linear regression. Additionally, MLA determines the most impactful parameters by providing their statistical significance and calculates correlation coefficients between them, whereas ANOVA only tests the existence of a significant difference between the means of the parameters. Finally, ANOVA cannot be used to analyse dynamic data because that would violate its independence assumption (data isn't connected in any way). In this case, it is essential to study the effect of the increasing sliding speed because the CoF does not always follow the same pattern and is affected by other parameters.

To determine the quality and, therefore, the reliability of each model, the coefficient of determination (R^2), the mean absolute error, and the root mean squared error of each were displayed by the MLA tool. The closer the R^2 score is to 1, the closer the predictive data were to the actual data. The error values indicate if the R^2 score can be trusted. The lower the error values, the better the performance of the algorithm. Also, the mean squared error of the CoF must be below the suggested error limit (suggested error limit: 15% of the average CoF value). Correlation coefficients (CC) were generated by the tool to identify the statistical importance of each parameter and the correlations between them. The higher the CC, the more significant its impact. A positive coefficient denotes a positive correlation and vice versa. In addition to the MLA tool, factorial regression analysis was applied to the data in Mini Tab. The probability value (P) was used to identify the statistically significant parameters. When the P is less than 0.05, the parameter is considered statistically important.

4.3 Results and discussion

The choice of specimen used for the tribological investigation was mainly based on Young's modulus. The primary aim was to understand Young's modulus effect on the CoF when NP formulations are used as lubricants. Therefore, specimens covering a wide range of Young's modulus were chosen. The selected specimens were also made of materials for joint implants, so their tribological performance could relate to the natural and artificial joints. The specimens were made of stainless steel, CoCr, PE, SE, and glass, all materials used in joint implants [377-380].

The specimen combinations that relate to the natural joint conditions are described below. The PE ball - SE disc combination replicates the AC-AC contact in a

healthy joint. PE and SE are materials with low Young's modulus like the healthy AC (**Table 4.3**). SE is rough and porous and simulates, even more, the AC surface [381-384]. It has even been used as a filler for the damaged AC in rat joints [377]. PE was selected because of its high wear resistance and wide use in joint implants [378]. As OA progresses, the AC in the joint starts to break down, and gaps are created, resulting in AC-bone contact. A steel ball replaced the PE ball to replicate that condition. Although the Young's modulus of the steel ball is not at the same level as the bone (**Table 4.3**), steel is closer to the bone than the PE in terms of hardness. At the final stages of OA, AC is almost gone, resulting in bone-bone contact. In that case, the PE ball has been replaced by a steel ball and the SE surface by a CoCr disc.

Table 4.3: Mechanical and morphological properties of specimen and real joint contacts.

Contact surfaces	Young's modulus 10^{-3} (GPa)	Surface roughness (nm)	Poisson ratio (-)	References
AC	2.6-5.6	72.0 - 114.4	0.40	[381-385]
Bone	11.1-15.3	-	0.30	[386, 387]
SE disc	6.9	94.3 ± 21.0	0.50	[388]
Glass disc	75,000	15.0 ± 6.0	0.24	[389]
CoCr disc	225,000	18.0 ± 6.0	0.30	[390]
Steel ball	207,000	10.0	0.29	[388, 391]
PE ball	940	-	0.40	[390, 392]

The tribological conditions in the artificial joints were also investigated. One of the most commonly used combinations of materials for joint implants is metal on metal, thanks to their exceptional mechanical properties (high stiffness, high wear-resistant) and low cost. Steel and CoCr were used for that scenario. Titanium could have also been used, but CoCr was chosen because it is more wear-resistant [378]. In older adults who are less active, ceramic on metal combinations are mainly used for the implants. Ceramics offer the lowest possible wear combined with high strength,

stiffness, and durability but are more fragile [393]. Glass was used to mitigate the ceramic joint implants because MTM specimens made of ceramics were not available to buy. Similar to ceramics, glass demonstrates high Young's modulus and high hardness [394]. Metal on metal joint implants is not always the best choice due to clinical complications reported in the literature [395]. Metals/ceramics on PE are other commonly used combinations of implant materials that are preferable for older adults. Those were examined using a PE ball against CoCr and Glass disc.

1.5.1 4.3.1 Substrates characterisation

Figure 4.2 presents the topography of the three substrates used for the tribological tests. The images of the substrates included in the thesis were taken when those substrates were deemed no longer acceptable for usage. Therefore, the CoCr and Glass discs, which were used multiple times, were worn. The averaged mean roughness (R_a), extracted based on AFM images of 100 x 100 μm size, is 18 ± 6 nm for the CoCr, 15 ± 6 for the Glass, and 156 ± 39 nm for the SE. SE is significantly (88.5-90.4%) rougher and more porous than the other two surfaces. The difference in the surface roughness of CoCr and Glass is not clear because it depends on the selected area and their wear (existence of scratches).

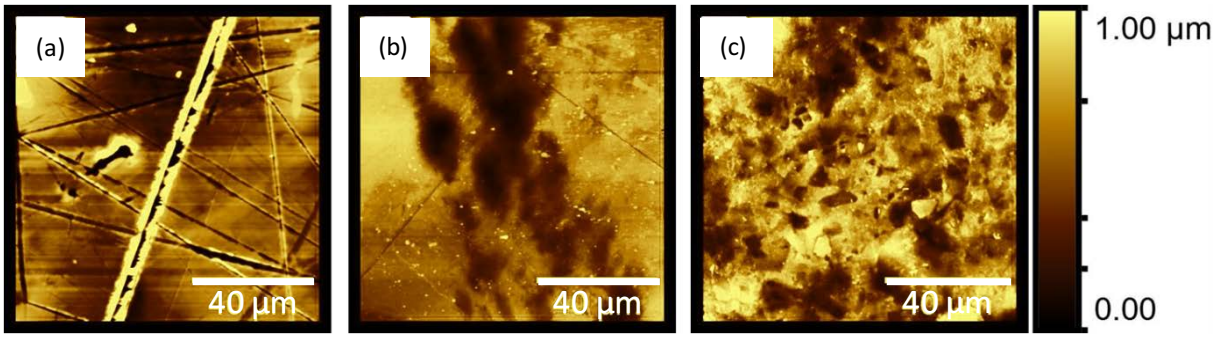


Figure 4.2: Topography of MTM substrates. (a) CoCr, (b) Glass, and (c) SE. Images acquired by JPK AFM and analysed with Gwyddion software.

Contact angle measurements revealed that Glass and CoCr substrates are hydrophilic, whereas SE is hydrophobic (**Figure 4.3**). Also, glass is more hydrophilic than CoCr. The SDS increased the hydrophilicity of all substrates but had a prominent effect only on the SE. SDS would adsorb on the SE with its hydrocarbon tail on the surface, exposing the polar head towards the water, rendering the substrate more hydrophilic [396]. It needs to be mentioned that the UV treatment used to clean the specimens has the additional advantage of increasing the hydrophilicity [397].

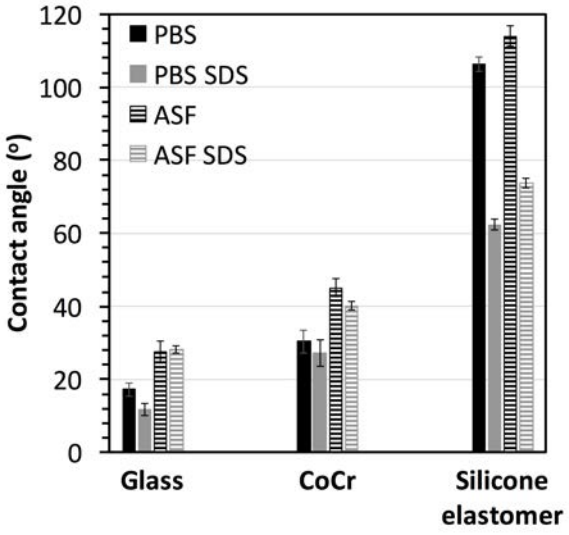


Figure 4.3: Contact angle of pure PBS, pure ASF, and PBS/ASF in the presence of SDS (0.5%) on the Glass, CoCr, and SE substrates. Each bar represents the average

of three different samples tested on six different areas of each substrate. The error bars represent their standard error.

4.3.2 Nanoparticle formulations characterisation

Figure 4.4 does not revealed any significant difference for the contact angle of silica and latex NPs. Only in the case of ASF formulations on CoCr, silica NPs were found more hydrophilic than latex.

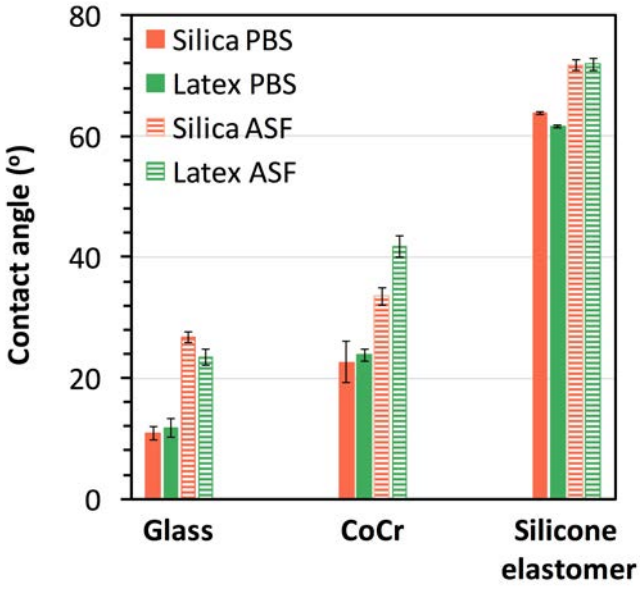


Figure 4.4: Contact angle of latex and silica NPs formulations on the Glass, CoCr, and SE substrates. The formulations consisted of NPs (0.5%) and SDS (0.5%) in PBS and ASF. Each bar represents the average of three different samples tested on six different areas of each substrate. The error bars represent their standard error.

The averaged particle size of NPs in water was 197.6 nm for the latex and 371.3 nm for the silica (**Figure 4.5a**), suggesting there is aggregation in silica formulations. The SDS reduced the particle size of silica to 290 nm but did not eliminate the aggregation (nominal size 200 nm). **Figure 4.5b** indicates that latex NPs distributed better than silica in any medium, with or without SDS. Latex provided only one peak

with narrow distribution close to their expected size, whereas silica provided two narrow peaks; one close to their expected size and the other at 3.7 nm, which is the size of the free SDS molecules [398]. The agglomeration and polydispersity of the silica formulations are possibly related to the powdery form of silica NPs. An important increase in the particle size was noticed in ASF formulations (**Figure 4.5a**). The agglomeration in ASF formulations could be attributed to the elevated viscosity of the medium. The diffusion kinetics of the particles is hindered due to the high viscosity, according to Stokes-Einstein equation [399]. The agglomeration in the suspension could also result from the mechanical energy being insufficient to separate the NPs because of the high viscosity. Although SDS decreased the average particle size of the NPs significantly, it could not separate them to their nominal size. The final particle size of latex and silica formulations in AS with SDS was 453.2 nm and 811.07 nm, respectively. Moreover, all formulations were stable based on the high |ZP| (|ZP| > 25 mV) (**Figure 4.5c**). SDS increased the stability of the latex formulations because it prevented NPs aggregation. Another observation is that ASF formulations demonstrated higher ZP and, therefore, higher stability than the water formulations. The elevated ZP could be due to the negatively charged polysaccharides ASF is made [400, 401]. However, the formulations examined were made with PBS, not water. Water was only used to conduct ZP measurements because PBS would affect the ZP due to its ionic strength. PBS as a buffer demonstrates a pH of 7.4, whereas ASF is expected to exhibit a pH lower than 7. ASF comprises sodium alginate gel with natural pH 3-3.5 [402], gellan gum with natural pH 5.3 [403], and HPLC water with pH 7. In negatively charged silica NPs when the pH increases, the absolute value of the ZP

increases [404]. Similar but weaker behaviour has been reported for negatively charged latex NPs [405].

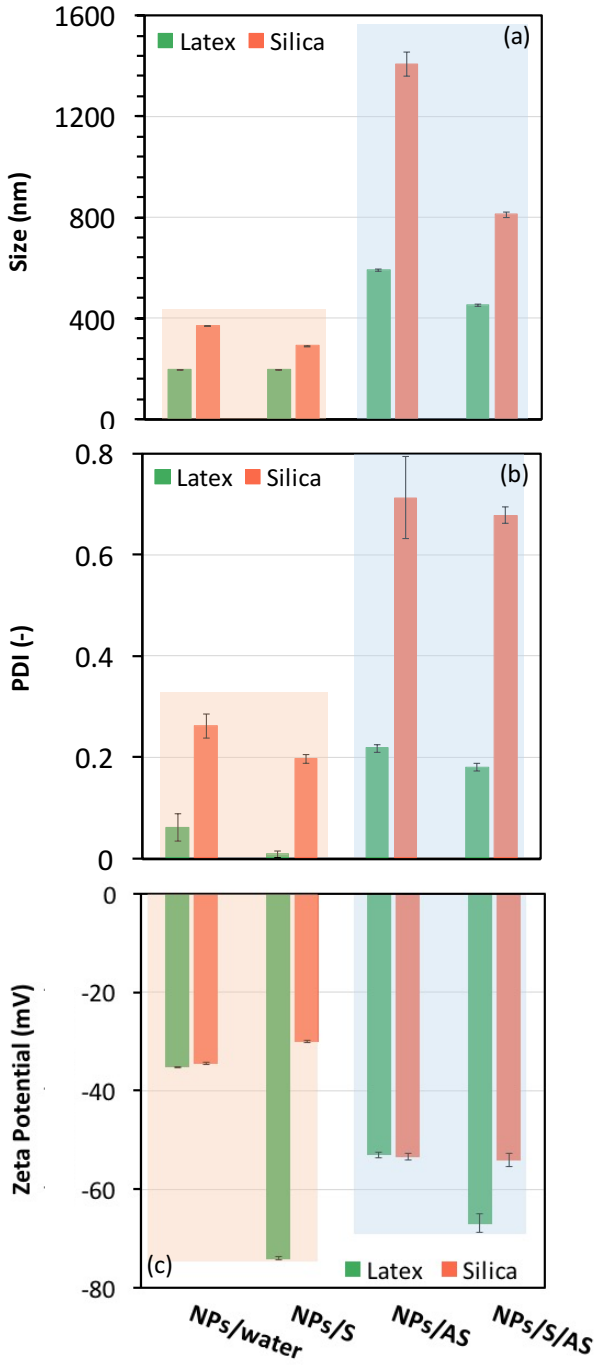


Figure 4.5: (a) Size, (b) PDI, and (c) Zeta Potential of formulations with latex and silica NPs in water and ASF(AS). The concentration of NPs and SDS (S) was 0.5%. Each bar represents the average of five repetitions of three different samples. The error bars represent their standard error.

The viscosity of the NPs formulations is attributed mainly to the viscosity of the solvent (**Figure 4.6**). ASF viscosity is approximately 100 times higher than the PBS (**Figure 4.6**). An additional increase with NPs concentration has been identified. The viscosity increase is more evident in ASF rather than PBS formulations. Silica NPs induced a greater increase in viscosity than latex. For instance, 1% of silica NPs increased the viscosity of the ASF suspension by 174-838% across all the shear rates. That increase could be attributed to silica aggregation (**Figure 4.5a**) and creation of structures more resistant to flow than the individual NPs [406-408]. In contrast to silica, latex ASF formulations behaved differently. The viscosity of ASF formulations increased with latex concentrations up to 0.1% but decreased with concentrations above that. Latex formulations contained additional water in their original formulation (0.1% w/v) that inevitably reduced the viscosity, especially at high NPs concentrations. Furthermore, latex NPs do not aggregate, and even if they were in powder form, they were expected to provide viscosity lower than the silica. It needs to be mentioned that before testing the samples, the viscosity of a reference was tested as a baseline. Therefore, there is a small difference in references tested on a different day, like the PBS in **Figure 4.6**.

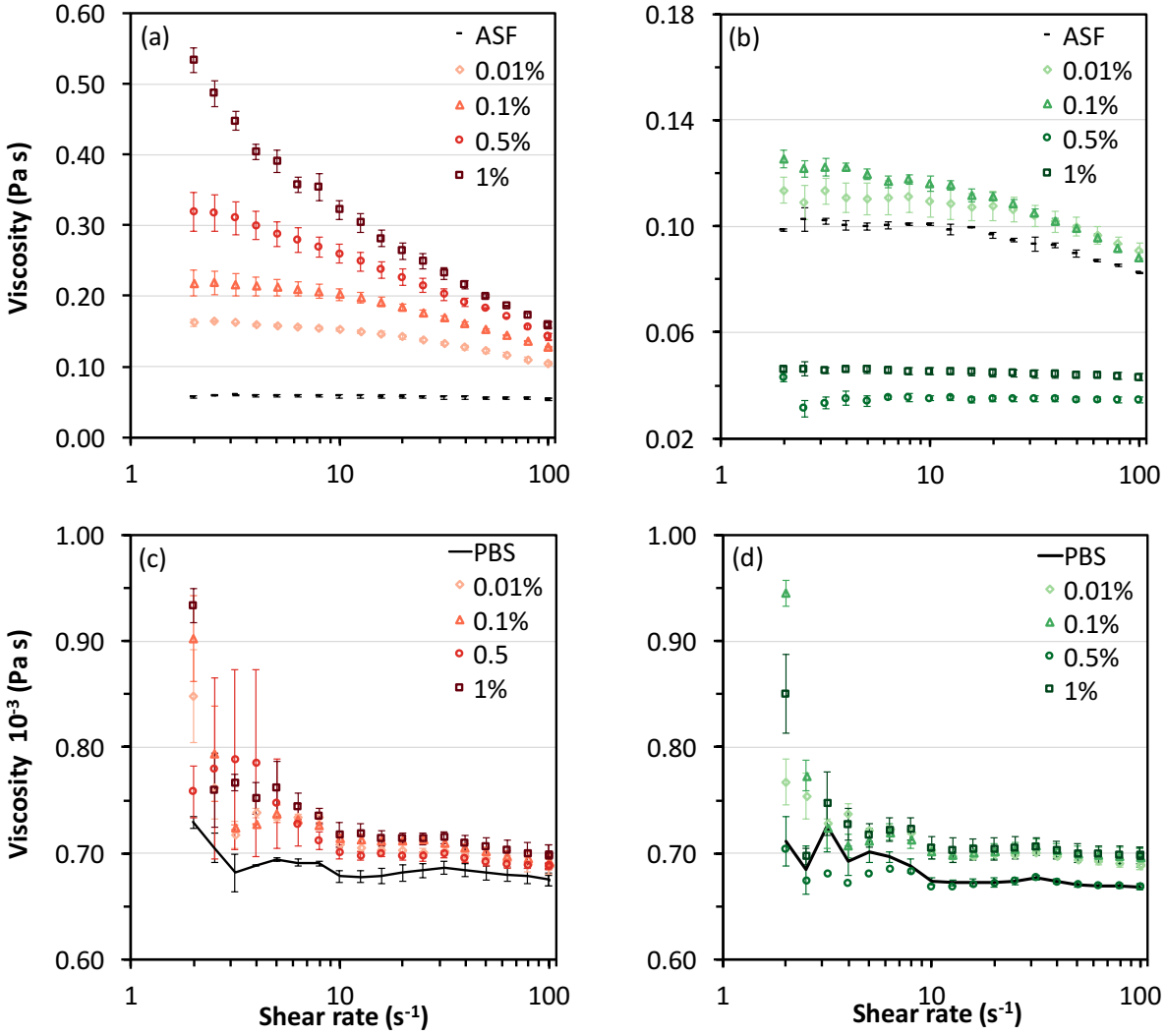


Figure 4.6: Viscosity of silica NPs in (a) ASF, (c) PBS, and latex NPs in (b) ASF, (d) PBS. The concentration of NPs was 0.01%, 0.1%, 0.5%, and 1%. Formulations contained NPs and SDS (0.5%). Each data point is the average viscosity of three repetitions of the same sample. The error bars represent their standard error.

4.3.3 Coefficient of friction of nanoparticle formulations

4.3.3.1 Effect of pressure on the coefficient of friction

CoF behaviour depends primarily on the lubrication regime. Based on the Hersey number equation (1.2), the lubrication regime, in that case, is only affected by

the contact pressure because the same NPs formulations were tested under the same velocities, and the contact pressure is the only parameter that differs. **Table 4.4** lists the initial contact pressure applied in each configuration, calculated using the Hertz model [245]. The equations describing Hertz model can be found in section 2.3 of Chapter 2.

Table 4.4: Initial contact area and pressure for six materials' configurations based on the Hertz model.

Configuration	Contact area 10^{-8} (m^2)	Contact pressure (MPa)
Steel-SE	4710	0.15
Steel-CoCr	7.82	89.56
Steel-Glass	13.05	53.63
PE-SE	4730	0.15
PE-CoCr	158	4.42
PE-Glass	159	4.38

Statistical analysis demonstrated that the Hersey number was the first or the second most important parameter determining the CoF on all configurations. **Figure 4.7** illustrates the CoF in relation to the Hersey number for the formulation consisting of latex (0.1%) and SDS (0.5%) in PBS. That formulation was chosen as an example because it has a medium concentration of NPs and its NPs do not aggregate. The viscosity of that suspension is almost Newtonian (n=0.96); therefore, the same viscosity of 7.1 10^{-4} Pa s was used to calculate the Hersey numbers.

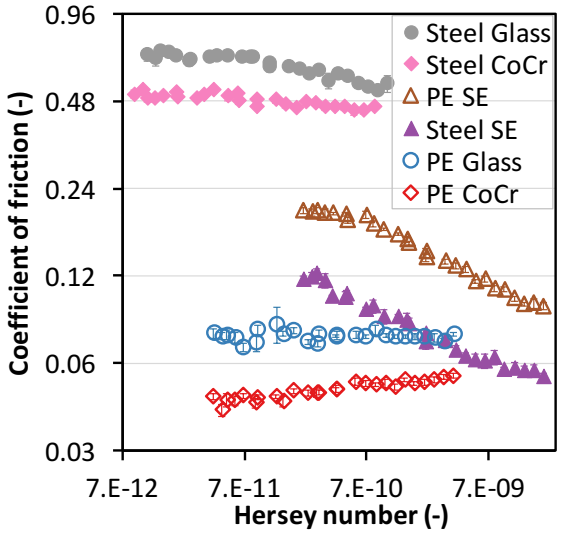


Figure 4.7: CoF against Hersey number for six material configurations using a formulation of latex NPs (0.1%) and SDS (0.5%) in PBS. The coefficient of friction for configurations with a steel ball is illustrated with filled symbols, whereas with a PE ball with unfilled symbols. The same shape of symbols is used for configurations with the same substrate. Each data point is the average CoF of six repetitions of the same sample. The error bars represent their standard error.

The average CoF developed on the six configurations between 1 and 100 mm s^{-1} ranges from 0.05 to 0.59 for the six configurations (**Table 4.5**). The Steel-Glass, Steel-CoCr configurations demonstrated the highest CoF. Those configurations developed the highest pressures (53.63, 89.56 MPa), and hence, were operating mainly in the boundary lubrication regime (**Figure 4.7**). Although their $CC_{cof\text{-}vel}$ is negative (**Table 4.5**), many formulations, especially at low velocities (1-7 mm s^{-1}), were operating in the boundary lubrication, in which the CoF remains stable.

Table 4.5: Coefficient of friction and its correlation coefficient with sliding velocity for six materials' configurations.

Configuration	Avg CoF (-)	$CC_{cof\text{-}vel}$ (-10^{-2})
PE-CoCr	5.30 ± 0.80	0.26
PE-Glass	6.20 ± 2.20	-0.08
PE-SE	12.20 ± 1.50	-8.57
Steel-SE	7.10 ± 1.10	-4.03
Steel-CoCr	36.80 ± 3.50	-7.26
Steel-Glass	59.10 ± 4.70	-19.2

The lowest CoF developed on the PE-CoCr and PE-Glass configurations (**Table 4.5**). Some formulations of the PE-Glass were in the mixed lubrication, whereas most had entered the hydrodynamic regime, as highlighted by the weak negative correlation of CoF with sliding velocity ($CC_{cof\text{-}vel}$: -0.08). PE-CoCr is the only configuration demonstrating a positive $CC_{cof\text{-}vel}$, highlighting that the dominant regime was the hydrodynamic, which is characterised by a gradual increase in the CoF with increasing velocity. The contact pressure of PE-CoCr and PE-Glass was 4.38 and 4.42 MPa accordingly. Contact pressures were significantly lower than the configurations operating in the boundary regime as expected.

The Steel-SE and PE-SE configurations developed the lowest pressure between the tested configurations (0.15 MPa), and therefore, were expected to be more progressed in the Stribeck curve (closer to the hydrodynamic regime) than the PE-CoCr and PE-Glass. However, this did not happen (**Figure 4.7**), and most formulations were operating in the mixed lubrication regime as suggested by their negative $CC_{cof\text{-}vel}$ (**Table 4.5**). Only some formulations had entered the hydrodynamic

lubrication at high velocities (over 33 mm s^{-1}), possibly because of the surface properties of the contact materials, as discussed in the following section.

4.3.3.2 Effect of surface characteristics on the coefficient of friction

In the boundary and mixed regimes, surface characteristics affect the transition from one regime to the other and, as such, the CoF. For example, the hydrophilicity of the substrates has been proved essential. **Figure 4.7** shows that the PE-CoCr and PE-Glass configurations entered the hydrodynamic regime at lower velocities than the Steel-SE and PE-SE despite the higher contact pressures. The greater hydrophilicity of the Glass and CoCr substrates compared to the hydrophobic SE accelerated their transition to the hydrodynamic regime because it promoted entrainment of the lubricant [409].

The Young's modulus of the specimen was also found to be an important contributor to the CoF development. The PE-SE configuration demonstrated higher CoF than the Steel-SE (**Figure 4.7**), which likely relates to the low Young's modulus of the PE ball compared to the Steel ball (**Table 4.3**). The elastic PE ball compresses on the substrate, increases the contact area of the system (**Table 4.4**), and therefore, the CoF, based on the literature [366]. Following the same principle [366], the lower Young's modulus of Glass compared to the CoCr could be responsible for the higher CoF developed in configurations in which it was used (e.g. CoF: Steel-Glass > Steel-CoCr, PE-Glass > PE-CoCr) because the Glass asperities compress on the balls and increase the contact area (**Table 4.4**).

Another influential surface property is surface roughness. The higher CoF of Steel-CoCr and Steel-Glass configurations compared to the Steel-SE could be explained by the high surface roughness of the SE. NPs in materials with high surface roughness decrease the contact area (contact made by peaks rather than the whole surface) and, as such, the CoF of the system [409].

The configurations can be categorised into two groups regarding their average CoF. The first group consists of PE-CoCr, PE-Glass, and Steel-SE configurations, which provided CoF less than 0.1. The common characteristic of those configurations is that they consist of a stiff (high Young's modulus) and an elastic (low Young's modulus) surface material. The second group consists of the combinations PE-SE, Steel-CoCr, and Steel-Glass, which consist of materials with similar Young's modulus; either two elastic materials (PE & SE) or two stiff surface materials (Glass & Steel, Steel & CoCr). The CoF of the configurations in the second group lies above 0.1. The combinations of stiff-elastic surfaces are associated with low CoF, which is unexpected because it contradicts the literature [366]. Therefore, it is suggested that the lubricant with its additives (NPs) is the dominant factor of those systems and not the Young's modulus of the specimens. The developed film thickness could assist in understanding the tribological behaviour of those systems. Nevertheless, MTM did not have the capability to measure it, and no theoretical equation exists that can be used to calculate the film thickness under pure sliding conditions.

4.3.3.3 Effect of nanoparticle formulations on the coefficient of friction

The NPs formulations in this study provided a CoF reduction between 4.0% and 50.8% (**Figure 4.8**), a result consistent with the literature, suggesting an average CoF

reduction of 40% [28]. The formulation provided the maximum CoF reduction (difference from the PBS/ASF) is different for each configuration (**Table 4.6**). Different NPs types, NPs concentrations and solvent viscosity were found optimum every time.

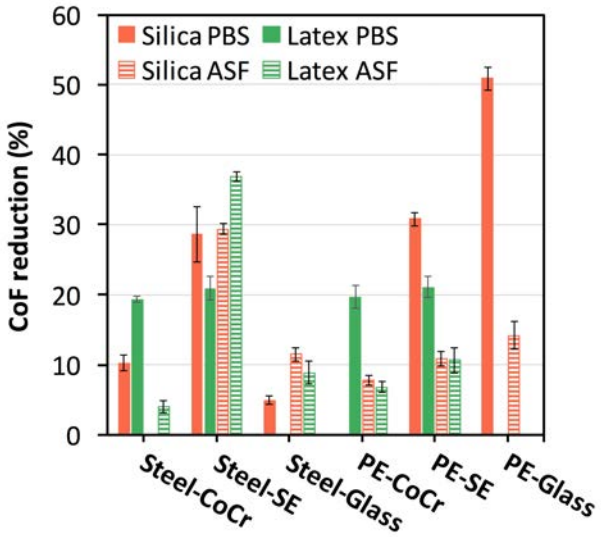


Figure 4.8: Maximum reduction of the CoF achieved with silica and latex NPs formulations in PBS and ASF for six contact material configurations. The missing bars represent the cases when there was no reduction in the CoF. Each bar represents the average CoF reduction of six repetitions of the same sample. The error bars represent their standard error between the sliding velocities 1-100 mm s^{-1}.

Table 4.6: Optimum lubricant for various materials configurations.

Surface combination	PE-CoCr	PE-Glass	Steel-SE	PE-SE	Steel-CoCr	Steel-Glass
Optimum lubricant	0.5% latex ASF	0.01% silica PBS	0.1% silica ASF	0.1% silica ASF	ASF	1% silica ASF

PE-SE and Steel-SE were the only configurations in which CoF reduction was achieved with all NPs formulations (**Figure 4.8**). That effect is attributed to the elevated roughness of the SE compared to the other discs. As illustrated in **Figure 4.9**, NPs smoothen the rough SE surface by filling up its valleys according to the polishing effect

theory [10]. Those results confirm the hypothesis that NPs can be used as friction modifiers in the joints because the SE has comparable surface roughness and Young's modulus to the AC (**Table 4.3**). Representative graphs of the effect of NPs formulations to the CoF of the other four configurations can be seen in **Figure A1**-Appendix.



Figure 4.9: Suggested lubrication mechanism of NPs formulations on the surface of the rough SE.

Figure 4.10 shows in more detail the CoF behaviour of the PE-SE and Steel-SE configurations against sliding velocity. As described above, the Steel-SE demonstrated a lower average CoF than the PE-SE. The solvent type was the most significant parameter for the CoF of both configurations (Steel-SE: P=0.006-0.012, PE-SE: P=0-0.01), with ASF providing the lowest CoF. Higher CoF reduction was achieved with the PBS formulations on the PE-SE, whereas on the Steel-SE with the ASF formulations. The CoF on the Steel-SE was not reducing at high velocities, but it was stabilising, denoting that the system had entered the electrohydrodynamic regime, in which the high viscosity of the ASF formulations is preferable. That behaviour is not observed in the PE-SE configuration, in which the CoF was reducing with increasing velocity (mixed lubrication regime). The $CC_{cof\text{-}vel}$ confirm the above since it is more negative in the PE-SE than the Steel-SE (**Table 4.5**).

The effect of NPs type on the CoF reduction is significantly different only on the PE-SE configuration. The correlation coefficient of CoF with silica is negative ($CC_{cof\text{-}silica}$: -8.21 10^{-3}), highlighting their contribution to CoF reduction, whereas it is positive

for latex ($CC_{cof\text{-}latex}$: 2.60 10^{-4}). That behaviour was seen on both solvents but is more evident in the PBS. PBS formulations with silica NPs reduced the CoF by 17.6%-30.7% and with latex NPs by 12.6%-21.1%. Silica and latex efficiency was not statistically different ($CC_{cof\text{-}silica}$: -4.53 10^{-3}, $CC_{cof\text{-}latex}$: -8.37 10^{-3}) on the Steel-SE configuration. Silica were more effective in PBS formulations (CoF reduction: silica 17.0-28.6 %, latex 7.7-20.9%), whereas latex were more effective in ASF formulations (CoF reduction: silica 11.6-29.3%, Latex 16.8-36.8%). That result could be related to the fact that the ZP of silica NPs increases significantly with an increase in the pH of the solvent [404] in contrast to latex NPs, which demonstrate a weak correlation with the ZP [405]. As described earlier, PBS exhibits higher pH than the ASF, and therefore, silica NPs probably developed a higher ZP in PBS and were more effective as additives. Lastly, NPs concentration was a significant parameter only in the Steel-SE configuration (P=0.034), in which high concentration resulted in high CoF reduction. In the PE-SE configuration, the CoF reduction was not significantly different for the different concentrations (P=0.098-0.261).

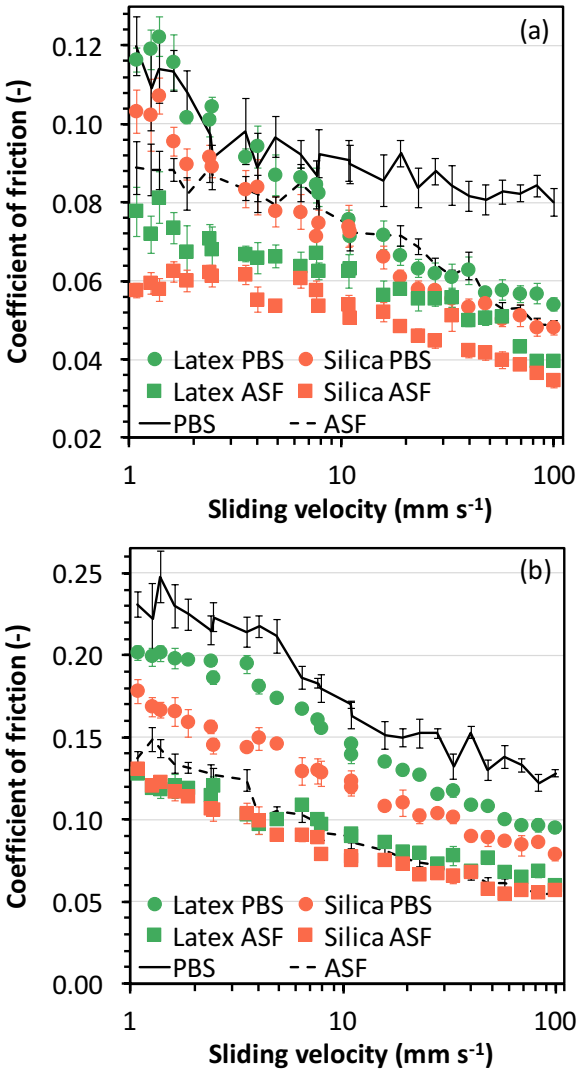


Figure 4.10: CoF against sliding velocity of the formulations 0.1% silica/latex NPs in PBS/ASF between (a) a steel ball and a SE disc and (b) a PE ball and a SE disc. Each data point is the average CoF of six repetitions of the same sample. The error bars represent their standard error.

Effect of nanoparticle type on the coefficient of friction

The type of NPs is statistically significant in determining the CoF of every configuration apart from the Steel-SE (**Figure 4.8**). Silica formulations demonstrated lower CoF values (**Table 4.6**) and higher reduction rates (**Figure 4.8**) than the latex in most configurations. The maximum CoF reduction silica formulations achieved was

50.8%, while latex formulations achieved only 36.8%. Silica formulations were successful in the PE-Glass, PE-SE, and Steel-Glass configurations. It is speculated that their efficiency could be attributed to their high viscosity (**Figure 4.6**). The PE-Glass configuration was operating in the hydrodynamic regime, in which viscosity dominates. The PE-SE configuration was operating in the mixed lubrication regime, and therefore, the fact that silica formulations were more efficient than latex suggests that the CoF was mainly affected by the lubricant's bulk properties (viscosity) and not the surface's properties. Nevertheless, silica formulations are also preferable in the Steel-Glass, a configuration operating in the boundary regime. In that case, silica's excellent efficiency could be related to their large particle size, which speeds up the separation of the contact surfaces and the transition to the following regime. Latex formulations were successful in the PE-CoCr and Steel-CoCr configurations. In the Steel-CoCr, which operates in the boundary regime, the efficiency of latex NPs could be associated with their low hardness compared to the silica NPs (**Table 4.1**). NPs of low hardness protect the opposing surfaces from scratches and reduce the CoF [367, 368]. However, latex is the optimum NPs type in the case of PE-CoCr as well, which might relate to its excellent dispersion.

Effect of solvent viscosity on the coefficient of friction

The solvent's viscosity is statistically significant in determining CoF level in almost all configurations apart from the PE-Glass. Especially on the Steel-SE, Steel-CoCr, and PE-SE configurations, solvent type is the most influential parameter. On those configurations, the blank ASF and its formulations provided lower CoF than the PBS and its formulations, respectively. ASF provided lower CoF than the PBS on those

configurations probably because its high viscosity accelerated the transition to the following regimes (Steel-CoCr: mixed, Steel/PE-SE: hydrodynamic), which are characterised by lower CoF values.

Figure 4.8 shows that PBS formulations were more effective in reducing the CoF than the ASF formulations in the PE-Glass, PE-SE and Steel-CoCr configurations. The higher CoF reduction provided by the PBS formulations is likely attributed to better NPs dispersion (**Figure 4.5**). It is suggested that NPs in PBS created a uniform protective film, which reduced the CoF [10], whereas, in ASF, NPs aggregated, increased the surface roughness, and therefore, the CoF [410, 411]. The significant influence of NPs dispersion in the CoF of the Steel-CoCr and PE-SE configurations was expectable because they were operating in the boundary and mixed regime, which are affected by the surface characteristics. The improved performance of PBS formulations could also be related to their increased pH compared to the ASF. As mentioned earlier, in negatively charged silica and latex NPs when the pH increases, the absolute value of the ZP increases [404, 405], providing a more stable formulation.

ASF formulations were more effective in reducing the CoF than the PBS formulations in the Steel-SE, Steel-Glass, and PE-CoCr configurations. In Steel-SE and Steel-Glass, the significant decrease in the CoF could be explained by the large size of the NPs in the ASF. The large size might have contributed to the separation of the contact surfaces and the faster transition to the following regime. In the Steel-SE, PBS formulations were also effective in reducing the CoF but mainly under high sliding velocities (**Figure 4.10a**). The efficiency of PBS formulations in high velocities could be attributed to more efficient convective mass transfer of NPs. The CoF reduction in

the PE-CoCr configuration could be associated with the high viscosity of the ASF formulations compared to the PBS formulations (**Figure 4.6**). As mentioned above, the PE-CoCr configuration operates in the beginning of the hydrodynamic regime, in which a lubricant of high viscosity is required for separating the opposing surfaces [412].

Effect of nanoparticles concentration on the coefficient of friction

The maximum CoF reduction was given by NPs concentration of 0.5% in most configurations. It is hypothesized that above 0.5%, NPs form an uneven tribofilm, which induces the roughness of the substrates, and as such, the CoF [410, 411]. In the PE-CoCr and PE-Glass configurations, low NPs concentrations (0.01%, 0.1%) were efficient, whereas concentrations above 0.1% increased the CoF. Possibly aggregates larger than the surface roughness of the substrate created an uneven tribofilm, which roughened the surface and increased the CoF [410, 411]. That effect was more evident with silica NPs. Indeed, based on **Figure 4.5**, the average particle size of silica formulations (ASF: 811.10 $\pm$ 9.77 nm, water: 290.83 $\pm$ 2.02 nm) is considerably larger than the surface roughness of the substrates (CoCr: 18 ± 6 nm, Glass: 15 ± 6). Steel-Glass was the only configuration in which the concentration of 1% provided the highest CoF reduction. That outcome could be related to Steel-Glass operating under the highest contact pressure and requires higher NPs concentrations to separate the contact surfaces compared to the other configurations. The effect of NPs concentration observed here is consistent with the literature suggesting that NPs concentrations less than 1-2% w/w are considered effective in reducing the CoF [28, 368].

The concentration of NPs is statistically significant for all configurations apart from the PE-SE (P=0.098-0.261) and Steel-CoCr (P=0.205-0.595). In those cases,

there is no significant differentiation on the CoF provided from the different NPs concentrations. All formulations apart from the 0.01% and 1% latex in ASF in the PE-SE reduced the CoF. A possible explanation for the CoF increase in the case of 0.01% is that NPs were not enough to cover the rough SE surface adequately to prevent asperity contact, whereas the high concentration of 1% induced NPs aggregation and resulted in increased surface roughness [410, 411]. In the Steel-SE and PE-glass configurations, NPs concentration is statistically significant only at high velocities (10-100 mm s^{-1}). That result could be attributed to the decreased viscosity caused by the increased temperature in high velocities. Steel-SE entered the hydrodynamic and PE-glass the hydrodynamic regime at high velocities, which are governed by viscosity.

4.3.3.4 Future usage of Machine Learning Analysis tool

The CCs provided by the MLA tool were used to explain the effect of the NPs formulations on the behaviour of the CoF on the different tribopairs. The $CC_{cof\text{-}vel}$ (Table 4.4) were used to identify the dominant lubrication regime, the $CC_{cof\text{-}silica/latex}$ (Section 4.3.3.3), to understand the effect of the type of NPs in the CoF and the correlations of CoF with the type of solvent to understand the effect of viscosity to the CoF reduction (Section 4.3.3.3). Additionally, the MLA tool identified the optimum fitting of the CoF data. **Table 4.7** displays the algorithm that demonstrates the best fitting for each of the six tribopairs, the algorithm's R^2 score, and the algorithm's mean squared error. The CoF developed in Steel-SE and PE-SE configurations fitted best (highest R^2, errors lower than the suggested error limits) with the random forest algorithm, suggesting that it fits well with the CoF in the mixed lubrication regime. The support vector regression algorithm was the best fit for the PE-CoCr, and Steel-Glass configurations, whereas

the linear regression algorithm performed best for the Steel-CoCr. Despite the best fit, Steel-Glass and Steel-CoCr fitted well with all three algorithms. As such, the CoF in the boundary lubrication could be fitted with any of those. The MLA tool could be used in the future to predict and analyse the behaviour of similar tribosystems without the need of performing actual lab experiments. For example, the CoF behaviour of tribopairs operating in the mixed lubrication regime and demonstrating high surface roughness can be predicted with the random forest algorithm of the MLA tool. The users could amend the values of the parameters they wish to predict (e.g. concentration of NPs), and the program will use the developed model to calculate the expected CoF. This feature is advantageous for making predictions and determining how well the algorithms fit the data. The MLA tool is user-friendly and does not require any prior knowledge in MLA. It runs on Windows, does not require any program to be installed and allows the import/export of data in Microsoft Excel. More details about the MLA tool can be found in Gan's dissertation [413].

Table 4.7: Fitting parameters of the tribological behaviour of six contact surfaces configurations (MLA).

Configurations	Mean squared error (10^{-1})	Algorithm	R^2	Suggested error limit (10^{-1})
PE-CoCr	0.53 ± 0.08	Support Vector Regression	0.80	0.07
PE-Glass	0.62 ± 0.22	No fitting	-	-
PE-SE	1.22 ± 0.15	Random Forest	0.86	0.18
Steel-SE	0.71 ± 0.11	Random Forest	0.64	0.11
Steel-CoCr	3.68 ± 0.35	Linear Regression	0.86	0.55
Steel-Glass	5.91 ± 0.47	Support Vector Regression	0.82	0.89

4.4 Conclusions

NPs could be used to counterbalance the insufficient lubrication of the osteoarthritic joints and meliorate patients' pain. NPs formulations reduced the CoF of systems, which resemble the contact surfaces of natural and artificial joints. Even though reduction has been seen in various tested systems, those incorporating a rough SE substrate demonstrated CoF reduction with all NPs formulations. On those configurations, the CoF reduction is attributed to the polishing of the rough SE by inserting NPs into its valleys, rendering the surface smoother and preventing direct contact of the opposing surfaces. The SE has comparable surface roughness and Young's modulus to the AC. As such, those results highlight the potential of NPs formulations to minimise the CoF in real joints. A treatment utilising NPs formulations could be beneficial at the beginning of the OA when there is AC-AC contact (PE-SE) and at the early-OA when the AC starts to break down, and there is partial bone-AC contact (Steel-SE). That is the ideal scenario because the delivery of those nano lubricants to the joints could happen via IAI, a treatment method used only at the early stages of OA. However, no correlation was found in the material configurations, which exhibited increased CoF. The weak correlations might relate to the fact that the specimens were reused multiple times. The wear loss of the specimens could have affected the behaviour of the CoF.

The effect of NPs formulations on the average CoF and CoF reduction is significant. NPs are capable of reducing the CoF when added to low and high viscosity mediums. That result highlights their capacity to be used in viscous formulations and enhance the diminished viscosity of osteoarthritic SFs found in chapter 3. PBS

formulations achieved higher CoF reduction than ASF formulations, likely due to better dispersion in PBS than ASF. However, ASF formulations displayed an average CoF lower than the PBS formulations in most configurations, highlighting the prevalence of high viscosity on the average CoF. Silica formulations demonstrated lower CoF values and higher reduction rates than the latex in most configurations. The superiority of silica formulations could be attributed to the high Young's modulus, viscosity, and ZP relative to latex. Last but equally important, a concentration of NPs of 0.5% was the most efficient in most configurations.

Apart from the NPs formulations, the CoF is controlled by the mechanical and surface properties of the tribopair. The level of CoF and its trend with increasing velocity are primarily affected by the lubrication regime in which each system operates. For example, ASF formulations achieved a higher CoF reduction percentage than the PBS formulations on the Steel-SE and Steel-Glass configurations b probably because its high viscosity accelerated the transition to the following regimes. In general, the contact pressure was positively related to the CoF on the examined configurations. In addition to the pressure, the CoF depends on the properties of the tribopair in the boundary and mixed lubrication regimes. Young's modulus and surface roughness were negatively correlated to the CoF, confirming the literature.

In a few words, this work highlights the potential of NPs incorporated in IAI formulations to ameliorate the tribological characteristics of natural and artificial joints and minimise the patients' pain. Although CoF reduction was demonstrated in various combinations of contact materials, it was more evident on rough substrates like the

AC. Therefore, this approach could effectively treat the increased CoF in osteoarthritic joints in early OA when AC is still present.

5. NANOPARTICLE FORMULATION FOR INTRA-ARTICULAR TREATMENT OF OSTEOARTHRITIC JOINTS

5.1 Introduction

Loss of lubrication capacity is one of the most severe pathological changes in osteoarthritic joints [63, 128]. Even from the early stages of osteoarthritis (OA), the articular cartilage (AC) degrades, and the SF loses its viscoelasticity [6], disrupting the lubrication mechanism of the joints and leading to an increased CoF [63, 128]. Joint pain, stiffness, and eventually loss of mobility are the consequences of poor lubrication [414]. Despite the severe symptoms, there are no therapeutic approaches competent enough to treat the damage of the AC entirely or mitigate its degeneration. In the early stages of OA, patients follow a pharmacological treatment, which is not always effective [181] and is accompanied by gastrointestinal and cardiovascular side effects [182, 191]. Replacement of the joints by artificial implants at the final stage of the disease is currently the only effective therapeutic option [188].

Intra-articular injection (IAI) is an alternative treatment of early OA [189], in which the delivery of the therapeutic compounds takes place directly into the diseased joint via in-situ injections [190, 197]. IAI treatment is more successful than the standard pharmacological treatment [190, 197] because it limits the side effects [190, 191, 197] and increases drugs' bioavailability [190, 191, 197]. However, current IAI formulations offer short-term pain relief (maximum of six months) because the small drug molecules diffuse away from the joint quickly [190]. Furthermore, current IAI supplements with elevated viscosity like Hyaluronic acid (HA) restore SF's viscoelasticity but cannot counteract the increase of CoF in the boundary regime [29, 63], in which osteoarthritic

joints have lost their lubrication capacity as revealed in Chapter 3. This chapter is centred on the tribological improvement of the IAI formulations, and chapter 6 on the simultaneous pharmacological and tribological advancement.

In the previous chapter, silica and latex NPs of 200 nm size were used as model NPs to establish the proof of principle that NPs covering a wide range of mechanical properties reduce the CoF of materials replicating the rough natural AC like the silicone elastomer SE. This chapter is based on the hypothesis that biocompatible polymer NPs of the same size (200 nm) exhibit the same lubrication effect. Polymer NPs are promising systems for minimising joints damage and inflammation in many types of arthritis [190, 415, 416]. A few studies have already demonstrated their capacity to improve joints' lubrication [201]. In this chapter, NPs manufactured from the polymers Polymethylmethacrylate (PMMA), Polycaprolactone (PCL), and Polylactic acid (PLA) were used. The selection of those polymers was based on their biocompatibility. In addition, PCL and PLA are biodegradable and do not accumulate in the human body [417, 418]. Their approval for use in IAI therapy is feasible since they have already been approved for biomedical applications. The US Food and Drug Administration (FDA) has authorised the use of PMMA in bone cement implants [419]. FDA has also approved PLA as a filler for the repair of meniscus and bone implants and as a material for artificial scaffolds, sutures and screws [417, 420]. PCL has been certified as FDA approved for use in various medical applications, including sutures and scaffolds for regeneration of AC [421, 422]. The mechanical and physical properties of the PMMA, PCL, and PLA NPs are given in **Table 5.1**.

Table 5.1: Mechanical/physical properties of PMMA, PCL, and PLA NPs.

Nanoparticles	Young's modulus (GPa)	Contact angle (°)	Density (Kg m^{-3})	Hardness (Shore D)	References
PMMA	2.03-3.01	77	1190	96	[423-427]
PCL	0.33-0.38	80 ± 7	1145	55	[428-432]
PLA	1.28-7.00	79 ± 2	1252	76 ± 0.5	[433-437]

In Chapter 4, it has been shown that model NPs reduce the CoF of SE when added to high (artificial SF (ASF)) and low (PBS) viscosity mediums. Moving forward, PBS was chosen as the solvent medium because it has a pH similar to SF [313], and HA was added to enhance the viscosity of the osteoarthritic SF, which decreases with OA progression, as concluded in chapter 3. The formulation under investigation aims to improve the joints' CoF at the early OA when bone-AC contact occurs. To that end, the CoF was evaluated between two surfaces that replicate the bone-AC contact.

5.2 Materials and methods

5.2.1 Synthesis of polymer nanoparticles

The polymer NPs were prepared at the Guangzhou University of Chinese Medicine in China. PMMA (Shanghai Macklin Biochemical Co., Ltd., China), PCL (Shanghai Yuanye Bio-Technology Co., Ltd., China), and PLA (Shandong Academy of Pharmaceutical Sciences, China) were dissolved in Dichloromethane then added in 2% Polyvinyl alcohol (PVA) (Shanghai Aladdin Bio-Chem Technology Co., Ltd., China). The particle suspension was first homogenised (ATS Engineering Inc., China). Solvent evaporation was followed by magnetic stirring the suspension to remove the dichloromethane and centrifugation to remove the PVA. The remaining NPs were resuspended in water by ultrasonic agitation and washed twice with water. The

washings were centrifuged, and the NPs were resuspended in water. The suspensions were freeze-dried, and the NPs in powder form were stored at 4^{o}C until used.

5.2.2 Preparation of nanoparticle formulations

The required amount of NPs was weighed on a scale and added in Phosphate-buffered saline (PBS) solution (Fisher Scientific, USA) with 0.1% w/v HA (Bloomage Freda Biopharm Co., Ltd., China) and 0.5% w/v SDS (Fisher Scientific, USA). Formulations of 0.01, 0.1, 0.5, and 1% w/v of NPs were made. NPs were made of PMMA, PCL, and PLA. A summary of the formulations tested in this chapter is presented in **Table 5.2**. The next stage was the magnetic stirring of the suspensions until the NPs were visually dispersed, followed by three hours of ultrasonic agitation. All concentrations are expressed as % w/v.

Table 5.2: Summary of tested nanoparticle formulations.

Formulations' abbreviations	NPs* (0.5 % w/v)	SDS (0.5 % w/v)	HA (0.1 % w/v)	PBS (balanced to 100 ml)
NPs	√			√
NPs/SDS	√	√		√
NPs/HA	√		√	√
NPs/HA/SDS	√	√	√	√

* NPs: PCL, PLA, PMMA

5.2.3 Tribological measurements of nanoparticle formulations

The CoF tests of the NPs formulations were performed with the tribometer MTM (MTM2, PCS Instruments, UK) between a stainless steel ball of 19.05 mm diameter (PCS Instruments, UK) and a silicone elastomer (SE) disc of 46 mm diameter (Samco

Silicone Products, UK). The measurements were conducted for sliding velocities 1-100 mm s^{-1} at 37^{o}C. Conditions of pure sliding were applied (Slide-Roll-Ratio (SRR) = 200%). A new SE substrate was used for each measurement, whereas steel balls were reusable. All specimens were cleaned before the friction tests following an Ultraviolet light treatment and sonication in ethanol and distilled water.

5.2.4 Size and Zeta Potential measurements of nanoparticle formulations

Size and Zeta Potential (ZP) measurements were performed by a Zetasizer consisting of a He-Ne laser (633 nm) (Nano ZS, Malvern Instruments, UK). All tests were performed at 25^{o}C. The refractive indices of PMMA, PCL, and PLA NPs were 1.49 [426], 1.50 [438], and 1.47 [439], respectively. The aqueous medium in which the NPs were diluted was High Performance Liquid Chromatography (HPLC) water (Fisher Scientific, USA) and had a refractive index of 1.33 and viscosity of 0.8872 cP. The measurements were done in pure HPLC water, HPLC water with 0.01% HA, HPLC water with 0.5% SDS and HPLC water with 0.01% HA and 0.05% SDS. A few millilitres of 0.5% w/v suspension of NPs were placed in disposable polystyrene cuvette/zeta cell and fitted in the Zetasizer. The size of the NPs formulations was expressed as Z-average and their width distribution as polydispersity index (PDI). Each time a new sample cell was used for the particle size and PDI measurements, whereas the cuvette for the ZP measurements was reusable. The average values were calculated as the average of three measurement circles.

5.2.5 Imaging of substrates morphology

The SE discs used for the friction tests were imaged via Atomic Force Microscope (AFM) on the Imaging-Intermittent Contact mode (Multimode AFM, Bruker Ltd, UK). The measurements were conducted in the ambient with an Antimony doped Si cantilever with spring constant: 42 N m^{-1} and resonance frequency: 320 kHz (Bruker Ltd, UK). Gwyddion software was used for the analysis of the images and the calculation of their corresponding surface roughness. The ImageJ software was used for the calculation of the surface coverage of the NPs.

5.2.6 Viscosity measurements of nanoparticle formulations

Steady-state flow tests of the nano lubricants were conducted on a rheometer (HR-1 Discovery Hybrid Rheometer, TA Instruments, USA). The geometry was a standard double concentric cylinder made from aluminium with a gap of 500 μm (TA Instruments, USA). The viscosity of the samples was evaluated at shear rates 2-100 s^{-1} at a temperature of 37^{o}C. All samples were tested in triplicates.

5.3 Results and discussion

5.3.1 Characterisation of nanoparticle formulations

The formulations consisted of NPs, SDS and HA. NPs had a target size of 200 nm, which has been proved in Chapter 4 successful. Their actual size was 200 ± 2 nm for PMMA, 224.8 ± 0.8 nm for PLA and 244.1 ± 0.4 nm for PCL (**Figure 5.1a**). ZP measurements revealed that the NPs were not charged (**Figure 5.1c**).

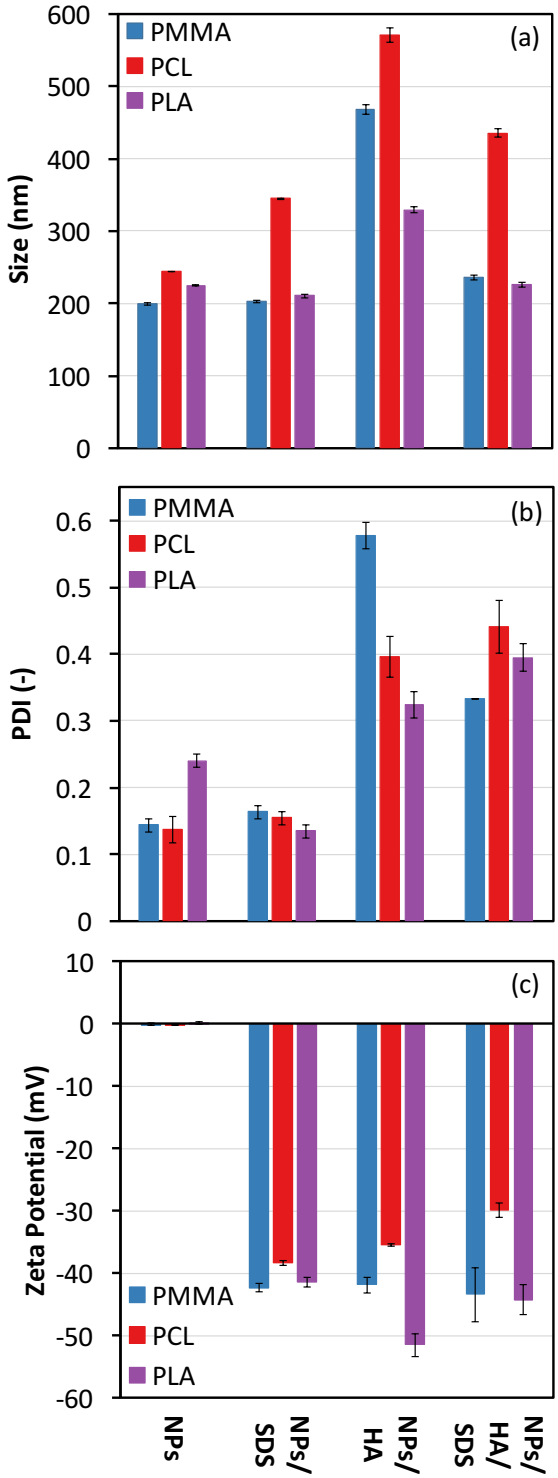


Figure 5.1: (a) Size, (b) PDI, and (c) Zeta Potential of PMMA, PCL, and PLA NPs (0.5%) in water, water/SDS (0.5%), water/HA (0.01%), and water/HA (0.01%)/SDS (0.05%). Each bar represents the average of four repetitions of the same sample. The error bars represent their standard error.

SDS was added to the formulation in a concentration of 0.5% to reduce aggregation and improve NPs stability [9]. A concentration of 0.5% is a commonly used concentration for surfactants in all NPs-based formulations [440]. That concentration was sufficient to create a protective layer for all NPs (Appendix A.3). Indeed, in some cases like the pure PLA NPs in water, the addition of SDS decreased the average particle size from 224.8 ± 0.8 nm to 196.4 ± 0.4 nm (**Figure 5.1a**), and the PDI from 0.24 to 0.13 (**Figure 5.1b**). Furthermore, SDS reduced the size of the particles to the initial levels in the NPs/ HA formulation (**Figure 5.1a**).

HA was added to the formulation to improve SF's viscoelasticity. HA has a concentration of 0.1-0.4% [133] in the healthy SF, which decreases significantly with OA progression. Four HA concentrations (0.01%, 0.05%, 0.1%, and 0.22%) were tested in a PBS formulation consisting of 0.5% NPs (PLA) and 0.5% SDS. The concentration of 0.5% for the NPs was the optimum for CoF reduction (Chapter 4). The highest HA concentration examined (0.22%) represents the average concentration in the SF of healthy human knee joints [133]. The formulation with 0.01% HA achieved the greatest CoF reduction (19.99 ± 1.28%). However, the concentration of 0.1% HA was chosen because it resulted in the lowest average CoF (0.08 ± 0.00) and had a good CoF reduction rate (12.46 ± 0.96%). Another reason for excluding the 0.01% is that it was lower than the physiological concentration of HA in healthy SFs [133].

The synergistic action of HA and SDS resulted in a stable formulation. The ZP of the final formulation was higher than 25 mV for all kinds of NPs (**Figure 5.1c**), indicating a low tendency of agglomeration and consequently high stability. The HA alone led NPs to aggregation (increased size) (**Figure 5.1a**) and increased PDI

(**Figure 5.1b**). It is believed that NPs were trapped within HA's bottlebrush structure [441] and created NPs-HA conjugates because of the attractive depletion effect [442]. The hydrophobic domains of the HA (CH groups) [443] could have adsorbed at the surface of the hydrophobic polymer NPs and turned the ZP of the system negative (**Figure 5.1c**) because HA is negatively charged [443]. In that case, the size of the NPs was approximately two times higher than their original size (**Figure 5.1a**), indicating that aggregates were formed from two HA-conjugated NPs. It is suggested that when SDS and HA were added to the formulation, SDS coated the NPs first because it is more surface active than the HA [444]. The hydrophobic tail of the SDS likely adsorbed at the surface of the hydrophobic polymer NPs [445, 446] and the anionic head of SDS was positioned towards the aqueous phase, charging the whole complex negatively (**Figure 5.1c**). It is also possible that the SDS formed complexes with the HA in the bulk solution by hydrophobic bonding (SDS tail bonded with CH groups of HA) [447]. As a result, it is expected that the SDS-coated NPs (**Figure 5.1c**) and the HA-SDS complexes repelled each other since both were negatively charged. **Figure 5.2** is a schematic representation of the suggested interactions within the formulation.

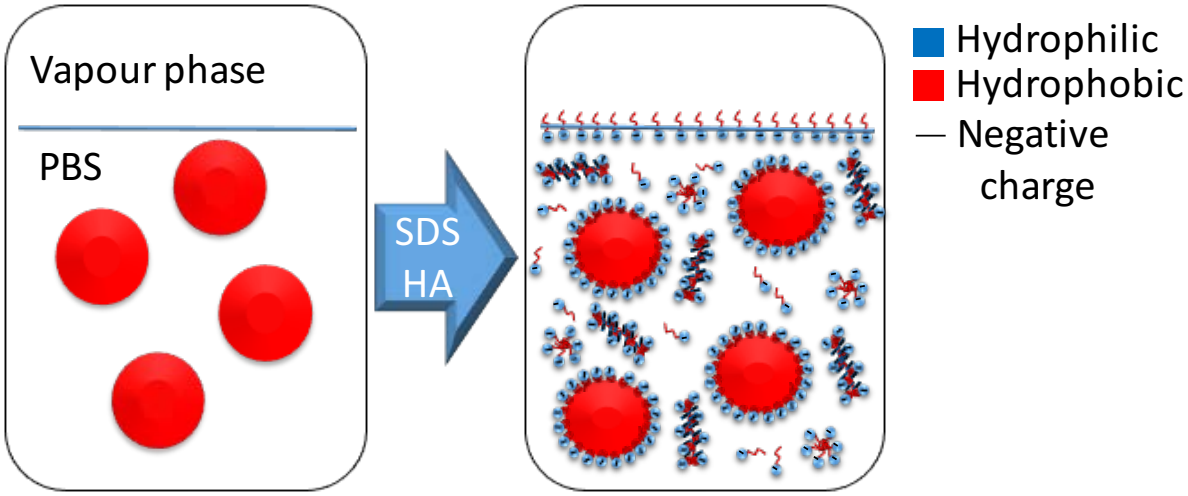


Figure 5.2: Schematic representation of the microstructure and the interactions between polymer NPs (red circles), HA, and SDS in the formulation.

The PCL/HA/SDS formulation was not as stable as the other suspensions. Its average size and PDI remained high (**Figure 5.1a and Figure 5.1b)** even in the presence of the SDS. Furthermore, it demonstrated the lowest ZP (**Figure 5.1c**). In that case, the attractive depletion forces between the NPs should have been strong for SDS to separate them. The stronger depletion interactions of PCL compared to PLA and PMMA are attributed to its larger particle size that strengthens the depletion interactions [448].

5.3.2 Effect of nanoparticle formulations on viscosity

The viscosity of the formulations was examined between 2 and 100 s^{-1} under 37^{o}C. **Figure 5.3** illustrates that all samples, including the reference, behaved as Newtonian. The viscosity of the formulations was fitted with the Power-law model (Eq. 2.14), and the Power-law indices (n) were above 0.97 (**Table 5.3**), confirming their Newtonian nature. The viscosity of other polymer NPs formulations at low concentrations and shear rates has been found Newtonian in the literature [449-451].

The NPs formulations were semi-dilute (volume fraction: 0.004), which, based on the literature, are Newtonian [408]. The detailed calculation of the volume fraction is in Appendix A.3. The viscosity level of the formulations is mainly provided by the HA, a component known for its high viscosity [441]. In fact, it was found that HA increased the viscosity of the pure PBS by 522% (**Figure A.2**-Appendix). The shear-thinning behaviour of the HA does not affect these formulations because at low concentrations (0.1%) and low shear rates (2-100 s^{-1}), the base fluid (the Newtonian PBS) dominates the rheological behaviour of HA solutions [452].

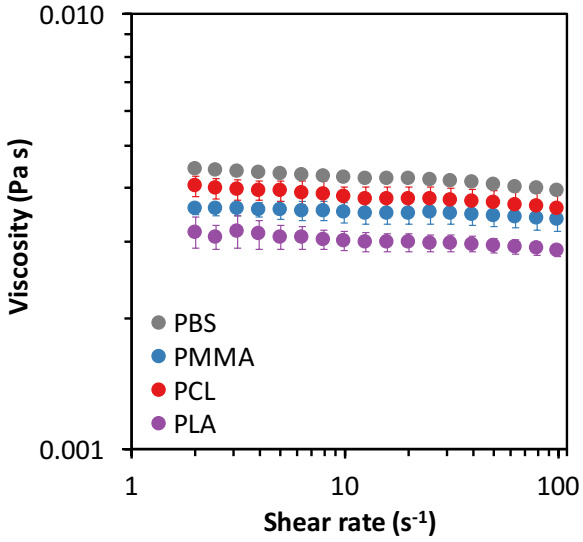


Figure 5.3: Viscosity of PMMA, PCL, and PLA NPs formulations at 37°C. The formulations consisted of NPs (0.5%)/HA (0.1%)/SDS (0.5%) in PBS. Each data point represents the average viscosity of three repetitions of the same sample. The error bars represent their standard error.

Table 5.3: Viscosity (η), consistency (m), Power-law index (n), and coefficient of determination (R^2) of nanoparticle formulations and PBS.

Formulations	*η* (mPa s)	*m* (mPa s)	*n* (-)	R^2 (-)
PBS	4.19 ± 0.03	4.50	0.97	0.97
PMMA	3.50 ± 0.01	3.60	0.99	0.92
PCL	3.80 ± 0.03	4.10	0.97	0.98
PLA	3.01 ± 0.20	3.20	0.98	0.93

All NPs/HA/SDS formulations demonstrated lower viscosity than the PBS alone (**Table 5.3**). Although the difference between the NPs formulations and the PBS is minimal (3.4-12.9 10^{-1} mPa s), it was still unexpected. The viscosity reduction could be attributed to the SDS. It was shown experimentally that 0.5% SDS reduced the viscosity of the 0.1% HA/PBS solution up to 7.47%. It is hypothesised that the SDS interacted with HA by hydrophobic bonding (SDS tail bonds with CH groups of HA) [447] and made hydrophilic complexes. Those complexes enhanced the wettability of the system by enabling the flow of PBS molecules and reduced the viscosity [447]. Additionally, such hydrophobic interactions between surfactants and polymers result in conformational rearrangement, and therefore, size reduction of the polymer chain, which leads to viscosity reduction [453]. Another reason for the reduced viscosity could be the dispersion methods (magnetic stirring, sonication) used to reduce the PDI, which inevitably increased the temperature of the samples and could have decreased the viscosity. High temperatures break the attractive interparticle (between the NPs) and intermolecular (between the NPs and the molecules of SDS) interactions irreversibly, enabling the flow of the PBS molecules and decreasing the viscosity [454].

The viscosity of the different NPs suspensions were slightly different and followed the row PCL > PMMA > PLA. That trend could be explained by the different tendencies of the NPs to aggerate. NPs aggregates increase the active volume fraction of NPs in a suspension and create structures more resistant to flow than the individual NPs, increasing the viscosity consequently [406-408]. Indeed, the particle size of the NPs suspensions in the final formulation (**Figure 5.1a**) follows the same row as the viscosity (**Figure 5.3**). PCL with the largest average particle size of 435.6 $\pm$ 6.25 resulted in a formulation with the highest viscosity, and PLA with the smallest average

particle size of 226.7 ± 3.39 provided a formulation with the lowest viscosity. However, the differences are at the level of mPa and are considered minor.

5.3.3 Effect of nanoparticle formulations on the coefficient of friction

The CoF was studied between a stainless steel ball and a SE disc. Those materials replicate the natural bone-AC contact in a joint at the early stage of OA when the AC starts to break down and the bone is revealed. The steel ball simulates the bone due to its comparable hardness and the SE disc the elastic and rough AC. Those properties can be found in **Table 4.3** of chapter 4. The contact pressure between those two specimens during the friction tests was 0.15 MPa, and their contact area 4710 10^{-8} m^2 based on the Hertz model [245]. The tests were conducted between 1-100 mm s^{-1}(typical joint velocities during normal activities [26]) at 37^{o}C (physiological body temperature).

SDS acted also as a friction modifier, confirming the literature [10]. The CoF of the system decreased for all tested velocities up to 28% with the addition of 0.5% SDS in PBS (**Figure 5.4a**). Thanks to its amphiphilic nature, the SDS forms micelles [455], which adsorb at the solid interfaces (electrostatic interactions with steel or hydrophobic interactions with SE) and act as boundary lubricants [10]. The ability of SDS to adsorb to steel surfaces and enhance lubrication has been already reported [456].

The addition of NPs on top of SDS, further decreased the CoF. A formulation of 0.5% PMMA NPs/0.5% SDS/PBS decreased the CoF up to 34% (**Figure 5.4a**). The additional lubrication is attributed to the presence of NPs. Based on the polishing lubrication mechanism, it is believed that NPs deposited at the valleys of the rough SE

rendered the surface smoother, reduced its surface roughness, and moderated the CoF [10]. However, the CoF increased for velocities higher than 10 mm s^{-1}(**Figure 5.4a**). It is probable that at high speeds under the extreme conditions of pure sliding, the NPs initially placed at the valleys of the SE were removed, resulting in direct contact of the specimens and increased CoF [457].

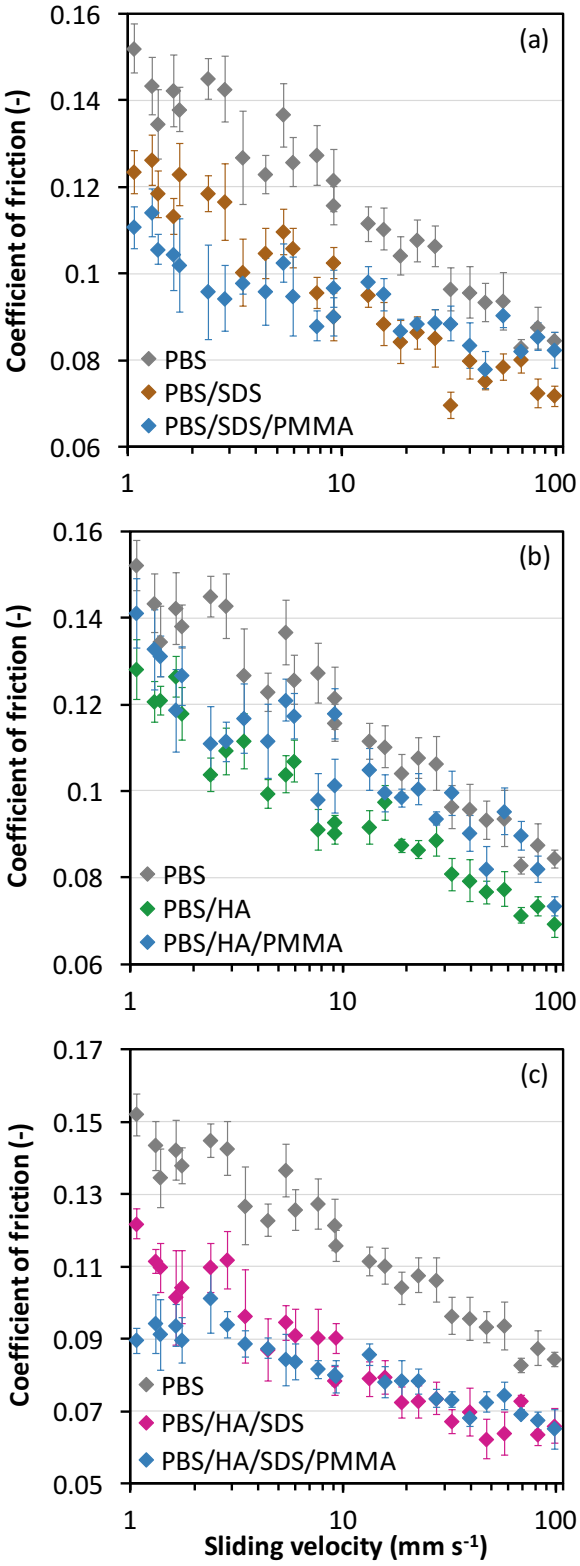


Figure 5.4: Effect of (a) SDS, (b) HA, (c) SDS and HA on the CoF between a steel ball and a SE substrate as a function of sliding velocity. The concentration of NPs and SDS was 0.5% w/v, whereas the concentration of HA 0.1% w/v. Each data point represents

the average CoF of six repetitions of the same sample. The error bars represent their standard error.

Even if HA induced aggregation and increased the PDI (Figure 5.1), it reduced the CoF up to 28% compared to the reference (Figure 5.4b). That reduction could be attributed to HA's capability to increase viscoelasticity and shear-thinning extend [441]. As those increase, the film thickness of the fluid increases, resulting in less direct contact of the asperities and lower CoF [391]. However, when NPs were added to the HA solution, the CoF increased (Figure 5.4b). This could be a consequence of NPs aggregation (Figure 5.1). Aggregates were larger than the valleys of the SE (Table 4.3) and probably acted as contaminants. They induced abrasive wear, increased the surface roughness of the SE and, as a result, increased the CoF [411].

SDS and HA in PBS acted synergistically and achieved a higher reduction than each component separately (35% versus 28%) (**Figure 5.4c**). The high CoF decrease is linked to the adsorption of the SDS micelles at the surface of the SE, and the increased viscosity provided by the HA. Adding 0.5% PMMA NPs in the HA/SDS/PBS solution provided the highest CoF reduction percentage of 41% (**Figure 5.4c**). The NPs formulation was more effective at low velocities (up to 8 mm s^{-1}), presumably because the NPs were removed from the substrate at high velocities, and the contact area between the steel and the SE was increased.

5.3.4 Effect of nanoparticle formulations on substrates' morphology

AFM verified the polishing effect as the main lubrication mechanism provided by the developed formulation. The intact SE is a rough material (R_a: 94.35 ± 21 nm –

Figure 5.5a). The spherical SDS micelles can be seen on the left corner of the SE surface after a friction test with SDS (0.5%)/PBS (**Figure 5.5b**). Even if SDS increased the surface roughness slightly (R_a: 105 ± 37 nm-**Figure 5.5b**), it reduced the CoF by 28% (**Figure 5.4a**) by adsorbing at the surfaces and acting as boundary lubricants [458]. NPs were adsorbed to the SE surface after a friction test with 0.5% PLA NPs in PBS (**Figure 5.5c**) and reduced the surface roughness slightly (89.79 ± 38), confirming the polishing effect mechanism [10]. NPs covered 15.41 ± 2.65% of the surface of the SE on that image. The HA in the formulation (0.5% PLA/0.1% HA/0.5% SDS) covered the largest part of the SE surface (**Figure 5.5d**) and made it significantly smoother (R_a: 65.16 ± 27). The crystals of the dry HA covered most of the area (**Figure 5.5d**), suggesting that HA created a film on the surface of the SE, which reduced the CoF. However, other parts of the SE were not entirely covered with HA after a test with the final formulation, and in those areas, the NPs adsorbed to the SE surface can be seen (**Figure 5.5e**). In summary, the worn SE images in **Figure 5.5** confirm the contribution of the formulation components to its lubrication performance. The SDS micelles adsorbed on the surface of SE and minimised the contact of the opposing surfaces, the NPs turned the surface smoother by filling its valleys, and the HA created an additional protective film, which covered the surface and reduced its roughness significantly. Last but not least, it has to be mentioned that no wear track has been observed on the surface of the used SE surfaces, additional proof of the lubricating performance of the proposed formulation.

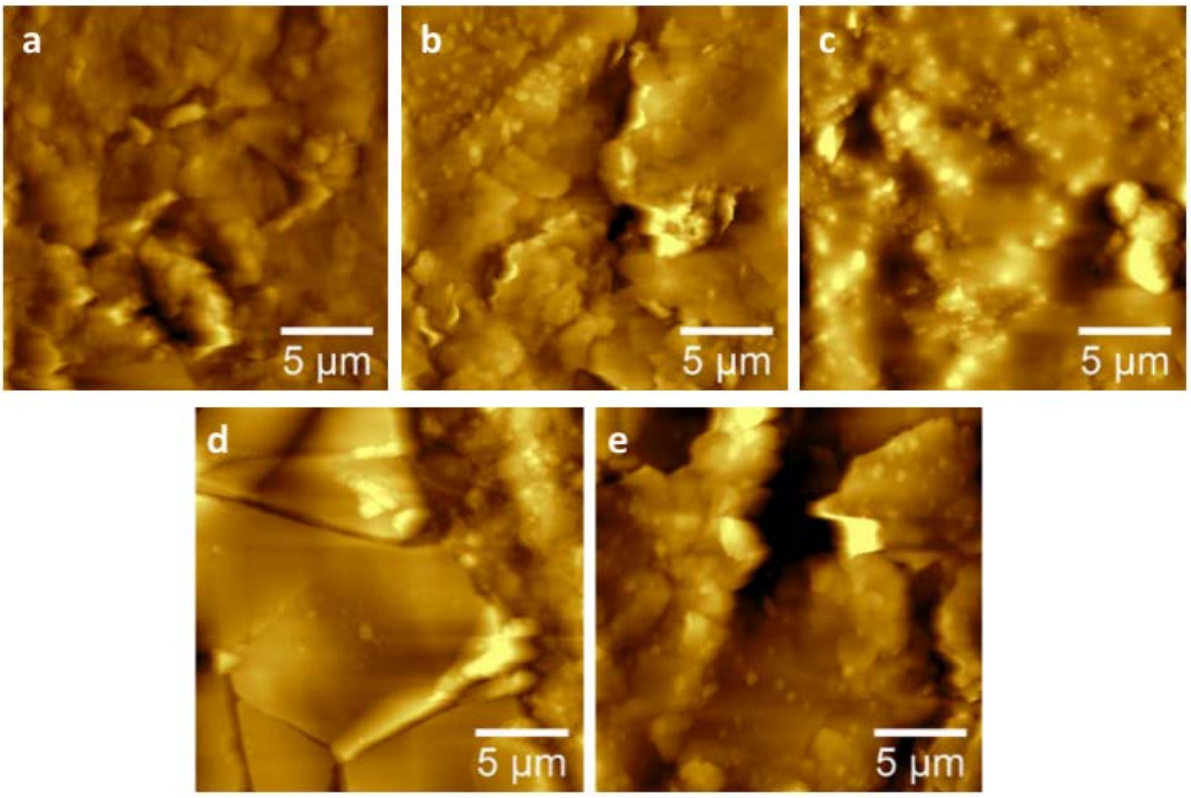


Figure 5.5: AFM images of SE (a) clean, (b) used with SDS (c) used with PLA NPs, (d) and (e) used with PLA NPs/HA/SDS. The concentration of NPs and SDS was 0.5%, whereas the concentration of HA 0.1%. All formulations were based on PBS. The size of the images is 400 μm^2.

5.3.5 Effect of nanoparticles concentration on the coefficient of friction

Friction tests with three NPs concentrations of 0.1%, 0.5%, and 1% were carried out at the same configuration (steel ball-SE). NPs were added in the HA (0.1%)/SDS (0.5%) PBS formulation. PMMA, PCL, and PLA NPs, which had a similar particle size (approximately 200 nm) and comparable densities (**Table 5.1**), demonstrated similar behaviour. The effect of PLA concentration on the CoF is presented below as a representative example (**Figure 5.6a**). The formulation with NPs in a concentration of 0.1% provided a weak CoF reduction (8.5%) and demonstrated similar behaviour to

the PBS. Both PBS and the 0.1% NPs formulation exhibited a steep reduction indicative of the mixed lubrication regime. The formulations with NPs concentration 0.5% and 1% decreased the CoF significantly by 22.5% and 26.6%, respectively. The difference between their CoF behaviour is not significant at low velocities (below 10 mm s^{-1}). The proposed lubrication mechanism is represented in **Figure 5.6b**. It is believed that a concentration of 0.5% NPs was sufficient to fill the valleys of the rough SE and decrease the CoF. At a concentration of 1% NPs, the excessive NPs deposited on the top of the previously deposited NPs and created an additional protective film. At high velocities, NPs are removed from the surface, and therefore, the highest concentration of 1% is preferable. The CoF of formulations with NPs concentrations 0.5% and 1% decreased very slowly, highlighting that the system was operating at the beggining of the hydrodynamic regime. The thick film of NPs might have pushed apart the contact surfaces and resulted in faster progression to the hydrodynamic regime.

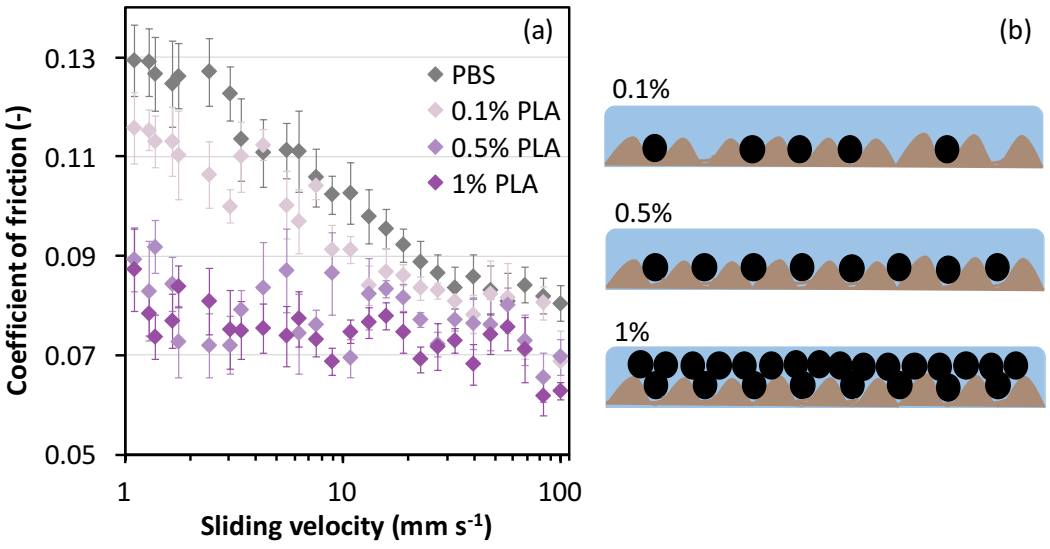


Figure 5.6: (a) Effect of NPs concentration (0.1%, 0.5%, 1%) on the CoF developed between a steel ball and a SE substrate. Each data point is the average CoF of six repetitions of the same sample. The error bars represent their standard error. (b) Schematic representation of the suggested lubrication mechanism. The formulations were consisted of PLA NPs/HA (0.1%)/ SDS (0.5%) in PBS.

5.3.6 Effect of nanoparticle type on the coefficient of friction

The optimum composition of the formulation in terms of the CoF reduction performance is NPs (1%)/HA (0.1%)/SDS (0.5%) in PBS. However, because of the limited availability of the NPs, a concentration of 0.5% was used in the following tests instead of 1%. Formulations with PMMA, PCL, and PLA NPs were used as lubricants for the friction tests between a steel ball and a SE substrate. **Figure 5.7** presents the frictional behaviour of the PMMA, PCL, and PLA NPs formulations as a function of the Hersey number. Hersey numbers were calculated incorporating the viscosity (η) from **Table 5.3** on the equation (1.2).

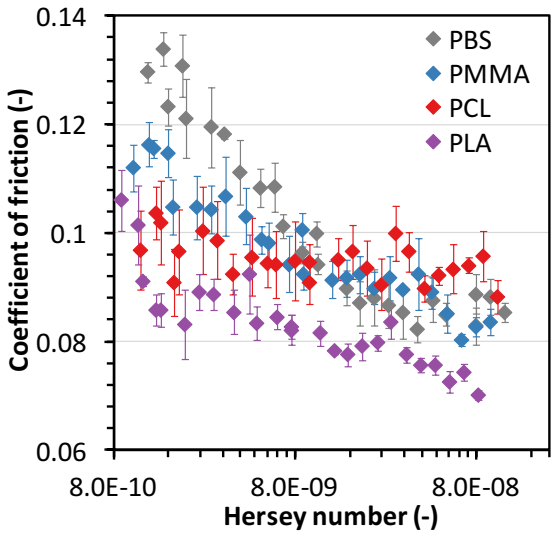


Figure 5.7: CoF of PMMA, PCL, and PLA NPs formulations between a steel ball and a SE substrate as a function of Hersey number. The formulations were consisted of NPs (0.5%)/HA (0.1%) /SDS (0.5%) in PBS. Each data point is the average CoF of six repetitions of the same sample. The error bars represent their standard error.

All NPs formulations reduced the CoF up to 8 mm s^{-1} (Hersey number: 6.4-8.9 10^{-9}) compared to PBS alone (**Figure 5.7**). The CoF reduction denotes the entrainment of the lubricants and the development of a protective film between the ball and the disc

[450]. At high velocities (above 8 mm s^{-1}), the CoF of PMMA and PCL formulations was higher or at the same levels with PBS (**Figure 5.7**), probably because NPs were removed from the surface because of the high speeds [457]. Another possibility is that the viscosity, and therefore, the film thickness was getting decreased because of the high shear rates/increased temperatures; hence the CoF was increased [459].

Based on the Stribeck curve, it is suggested that PMMA and PLA formulations were on the mixed lubrication regime because their CoF was decreasing with increasing Hersey number (**Figure 5.7**). It is speculated that PCL formulation was operating at the beginning of the hydrodynamic regime because it demonstrated an almost constant CoF as a function of Hersey number. Since PCL formulation demonstrated slightly higher viscosity than the other NPs suspensions, the speed that it needs to float is less; hence the opposing surfaces were pushed apart earlier, and it reached first the hydrodynamic regime [388]. Apart from the PCL suspension, the reference solution (PBS) also entered the hydrodynamic regime at the tested velocities (**Figure 5.7**). In that case, the absence of NPs resulted in a quicker separation of the opposing surfaces and hence quicker initiation of the hydrodynamic regime compared to the NPs suspensions.

Figure 5.8 presents the average reduction in the CoF provided by the different NPs formulations. The reduction rate is given for four selected sliding velocities up to 8 mm s^{-1}. Up to that point, all formulations demonstrated a CoF lower than the PBS. The CoF reduction rate decreased with increasing velocity for all formulations probably because the formulations were transitioning from the mixed to the hydrodynamic regime. That outcome highlights the effectiveness of the developed formulation to

reduce the CoF at the beginning of joints motion (low sliding speed). Different NPs formulations provided different CoF reduction rates. The average decrease was 10.67 ± 1.38 % for PMMA, 14.22 ± 1.61% for PCL, and 15.17 ± 2.06% for PLA. The PLA formulation was the most effective, especially at low speeds, providing a maximum reduction of 24.29%. In addition to that, the PLA suspension provided the lowest CoF compared to the other formulations for the whole range of velocities (**Figure 5.7**). It is believed that the lowest decrease in the CoF provided by the PCL formulation is attributed to the fact that it entered the hydrodynamic region, in which the CoF is stable (**Figure 5.7**) and that it exhibited high aggregation of NPs. PLA and PMMA formulations were operating in the mixed lubrication regime, in which the surface characteristics and rheology of the lubricant shape the tribological profile [391]. PLA's hardness, which is 21% smaller than PMMA (**Table 5.1**), could be the reason for the higher CoF reduction rate. Hard NPs scratch the opposing surface, induce abrasive wear and increase the CoF [367, 368]. The fact that the PLA formulation with the lowest viscosity demonstrated the lowest CoF indicates that the CoF was mainly affected by the characteristics of the opposing surfaces in this system.

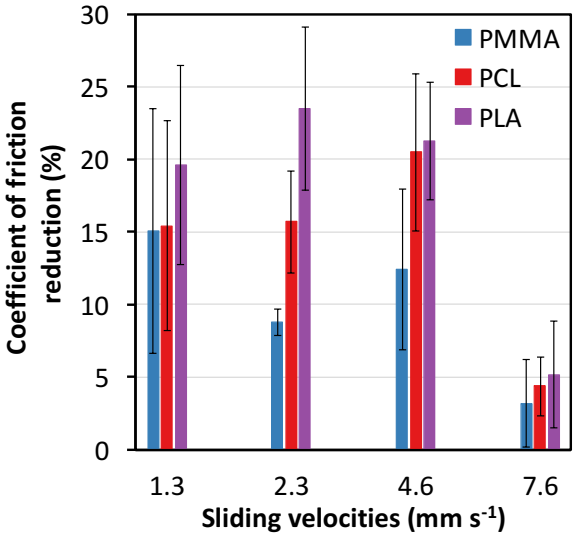


Figure 5.8: Reduction of the CoF caused by PMMA, PCL, and PLA NPs formulations against sliding velocity between a steel ball and a SE substrate. The formulations were made of NPs (0.5%)/HA (0.1%)/SDS (0.5%) in PBS. Each bar represents the average CoF reduction of six repetitions of the same sample. The error bars represent their standard error.

5.4 Conclusions

OA is untreatable at the early stages and IAI therapy is currently the most effective treatment. In this chapter, a NPs formulation for the IAI treatment of the poor tribological performance of osteoarthritic joints was developed. The formulation consisted of polymer NPs, HA, and SDS dispersed in PBS. The NPs incorporated in the formulation were made of PMMA, PCL, and PLA polymers. Those materials were chosen thanks to their biocompatibility and their wide application in medicine. The composition of the formulation was optimised to provide the joints with desirable CoF, viscosity, and stability for their normal operation under all lubrication regimes. The CoF was measured between a steel ball and a SE disc, which replicate the bone-AC contact at the early OA when the AC is partially removed.

The NPs formulations reduced the CoF under conditions that replicate the sliding of the joints at the beginning of their movement (low sliding velocities) when the other IAI formulations are not effective. NPs proved excellent lubricant additives, thanks to their capacity to adsorb on rough surfaces and polish them. HA provided the desired viscosity for restorating SF's lost viscoelasticity, and SDS enhanced the stability of the formulation. All three polymer NPs were proved capable to reduce the CoF. PLA provided the highest CoF reduction rate, suggesting that soft (low hardness) NPs are the most efficient frictional additives. Polymer NPs like those used in this study could also be used as drug delivery systems and provide the joints with additional therapeutic action (e.g. pain and inflammation suppression), as shown in the following chapter.

6. DUAL FUNCTIONAL FORMULATION FOR INTRA-ARTICULAR TREATMENT IN EARLY OSTEOARTHRITIS

6.1 Introduction

Intra-articular injection (IAI) treatment is commonly used at the early stage of osteoarthritis (OA) to alleviate pain in patients with minimal radiographic signs of articular cartilage (AC) damage [460]. IAI is more effective than conventional drug treatments because it increases drug absorption and limits side effects [181, 191]. Despite those benefits, the ability of the current IAI formulations to mitigate the progression of OA is minimal [461] because of the diffusion of the drugs via synovial capillaries [7], resulting in short retention times (1-4 h) in the joint cavity [462] and also their inability to address the increased CoF developed in the osteoarthritic joints [29, 63]. Even though viscous IAI formulations like Hyaluronic acid (HA) hydrogels improve joint's lubrication in the hydrodynamic and mixed lubrication regimes, they are ineffective in the boundary lubrication regime because HA alone is not a boundary lubricant and squeezes out of the joint under loading [29].

New IAI formulations are required to improve joints' lubrication and prolong drugs release. Various systems have been proposed to ameliorate the tribology of the articulating surfaces. For instance, Polyvinylpyrrolidone in bovine serum or deionized water is an excellent boundary lubricant with demonstrated capacity to reduce the CoF up to 50% [463]. Similarly, lubricin, a natural boundary lubricant of the joint [108], reduced the CoF of explants under inflammatory conditions by 33% [464]. In this work, colloidal systems are employed, which are excellent lubricant additives capable of reducing the CoF and wear of AC surfaces [9, 10, 56]. For example, nanodiamonds in

a simulated body fluid reduced the CoF three times by developing a carbon film on the surface of an implant [465]. NPs could also increase the retention time of the drugs from hours to weeks and control their release [190]. Several studies have demonstrated increased retention time of drugs delivered by NPs under OA conditions, attributed to NPs capacity to adsorb on the AC surfaces and prevent diffusion [190, 198, 203, 466, 467]. Polymer NPs specifically are excellent candidates because, in addition to the increased retention time, they exhibit low levels of immunogenicity [235], have successfully treated pain, inflammation [195, 468], and the elevated CoF of osteoarthritic joints [201].

In the last decade, a few NPs-based systems demonstrating both prolonged drug release and improved tribological characteristics for osteoarthritic joints have been developed (**Table 1.1**). Most of them consisted of cytotoxic drug-loaded (DL) mesoporous silica NPs grafted with charged polymer brushes [216, 218, 219] or DL-micro/nano gels grafted with polymer brushes [220, 469]. The biocompatible Polymethylmethacrylate (PMMA), Polycaprolactone (PCL), and Polylactic acid (PLA) [418-421] were used to make the NPs in the present study. PCL especially is characterised by a slow degradation rate (2-3 years) and could achieve the desirable long-term delivery of drugs in the intra-articular cavity [421, 422]. Celecoxib was incorporated into the NPs as a model drug: it is an approved therapeutic agent for OA, which relieves pain and reduces inflammation [470]. Celecoxib demonstrates disease-modifying effects thanks to its chondroprotective function and the inhibition of bone destruction [471]. It is also associated with low gastrointestinal incidents compared to other nonsteroidal anti-inflammatory drugs (NSAIDs) [470].

The aim of this chapter is to evaluate the feasibility of the NPs formulation regarding its lubrication capacity, drug release, and biocompatibility. The developed NPs-based formulation reduced the CoF of interfaces replicating the bone-AC contact in previous chapters. The hypothesis of the present chapter is that the NPs formulation loaded with a drug exhibits similar lubrication benefits on natural AC tissue and prolonged drug release. Previously reported systems were evaluated mainly on implant materials, which do not adequately replicate the complex AC surface, but the effectiveness of the present formulation was tested on osteoarthritic human and healthy animal AC explants. In addition, the cytotoxicity and the drug-release profile of the formulation were tested *in-vitro*.

6.2 Methodology

6.2.1 Synthesis of polymer nanoparticles

The NPs were synthesised by Piaopiao Pan at the Guangzhou University of Chinese Medicine in China. A modified combined homogenization/ solvent evaporation method was used. The polymers used were PMMA (Shanghai Macklin Biochemical Co., Ltd., China), PCL (Shanghai Yuanye Bio-Technology Co., Ltd., China), and PLA (Shandong Academy of Pharmaceutical Sciences, China). Polymer (50 mg) was dissolved in dichloromethane (10 ml) and added in 2% Polyvinyl alcohol (PVA) (Shanghai Aladdin Bio-Chem Technology Co., Ltd., China). For the synthesis of the DL-NPs, the drug Celecoxib (5 mg) was dissolved to an organic phase added and to the PVA solution. The suspension was first homogenised (ATS Engineering Inc., China). Solvent evaporation was followed by magnetic stirring to remove the dichloromethane and centrifugation to remove the PVA (13,000 rpm for 25 minutes,

4°C). The remaining NPs were re-suspended in water by ultrasonic agitation for 60 s and washed twice with water. The washings were centrifuged at 13,000 rpm for 20 minutes at 4°C and the pellet was re-suspended in water by 2 hours sonication. The NPs suspensions were freeze-dried for 37 hours, and the NPs in powder form were stored at 4°C until used.

6.2.2 Preparation of nanoparticle formulations

The preparation of the formulations started with weighing the exact amount of NPs (dry powder form), Sodium Dodecyl Sulphate (SDS) (Fisher Scientific, USA) and HA (Bloomage Freda Biopharm Co., Ltd., China) on a scale and adding them in a Phosphate Buffered Saline (PBS) solution (Fisher Scientific, USA). The formulations prepared in this chapter were NPs (0.5% w/v)/SDS (0.5% w/v)/HA (0.1% w/v). A summary of the tested formulations is given in **Table 6.1**.The next stage was the magnetic agitation of the formulations until the HA was dissolved, followed by three-hour ultrasonic agitation for the dispersion of the NPs. All concentrations are expressed as % w/v.

Table 6.1: Summary of tested nanoparticle formulations.

Formulations' abbreviations	NPs* (0.5 % w/v)	SDS (0.5 % w/v)	HA (0.1 % w/v)	PBS (balanced to 100 ml)
NPs	√			√
NPs/SDS	√	√		√
NPs/HA	√		√	√
NPs/HA/SDS	√	√	√	√

* NPs: PCL, PLA, PMMA, DL-PCL, DL-PLA, DL-PMMA

6.2.3 Size and Zeta Potential measurements of nanoparticle formulations

Size and Zeta Potential (ZP) of the formulations were measured by a Zetasizer consisting of a He-Ne laser (633 nm) (Nano ZS, Malvern Instruments, UK) at 25^{o}C. The refractive indices of PMMA, PCL, and PLA NPs were 1.49 [426], 1.50 [438], and 1.47 [439], respectively. High-Performance Liquid Chromatography (HPLC) water (Fisher Scientific, USA) with a refractive index of 1.33 and viscosity of 0.8872 cP was used as the aqueous medium. The formulations were diluted ten times to enable the conduction of Dynamic Light Scattering (DLS) measurements. The final composition was NPs (0.05%)/HA (0.01%)/SDS (0.05%). A few millilitres of the NPs formulation were placed in disposable polystyrene cuvette/zeta cell and fitted in the Zetasizer. The average values were calculated as the average of three measurement circles.

6.2.4 Generation of animal cartilage explants

AC explants were collected from healthy porcine knee joints grown at a farm of the University of Nottingham. The pigs were slaughtered at the University of Nottingham by a professional slaughter. The AC explants were removed and transported to the University of Birmingham, where they were immediately tested.

6.2.5 Generation of human cartilage explants and primary cells

AC explants were removed from patients who underdid total knee or hip replacement surgery due to OA at the Royal Orthopaedic Hospital, Birmingham. Femoral condyles and tibial plateau from osteoarthritic knees and femoral neck from osteoarthritic hips were collected peri-operatively and transported to the University of Birmingham. The AC was scraped from the subchondral bone utilising a scalpel and

immediately froze in liquid Nitrogen before being stored at -80^{o}C. Each sample was defrosted 30 min before its examination for subsequent analysis, and AC explant discs (10 mm diameter) were generated using a cork borer. The AC explant discs were then immediately tested or placed in PBS to prevent dehydration. Consent was obtained from all patients. The ethical approval for examining those samples is in Appendix A1.

Fawzeyah Alnajjar conducted primary cells isolation at the Institute of Inflammation and Ageing at the University of Birmingham. A portion of AC tissue was kept unfrozen and was digested in filter-sterilised collagenase IIA (2 mg/ml; Sigma Aldrich, Gillingham, UK) for 5 hours at 37^{o}C. Afterwards, the AC was filtered by weathering a 40 µm cell strainer (BD Biosciences, Oxford, UK). Primary chondrocytes were collected from the filtrate after centrifugation and were suspended in growth media (DMEM supplemented with 10% FCS, penicillin (100 U/ml), streptomycin (100 µg/ml), L-glutamine (2 mM), non-essential amino acids (5%v/v; all Life Technologies, Paisley, UK) and amphotericin (2µg/ml; Sigma Aldrich, Gillingham, UK) under 37^{o}C and 5% CO_2 to grow to 70-80% confluence before being utilised in subsequent studies.

6.2.6 Tribological measurements of nanoparticle formulations

The tribological tests of the AC explants were performed with the High-Frequency Reciprocating Rig (HFRR) (PCS Instruments, UK), a ball-on-disc tribometer. The HFRR was used instead of the Mini-Traction Machine (MTM) because the size of the AC explants is significantly smaller than the size of the disc required by the MTM. MTM works only with 46 mm diameter and 3 mm thickness circular discs. Instead, in HFRR, the CoF was measured between an AC explant of 10 mm diameter thickness less than 3 mm and a 6 mm stainless steel ball (PCS Instruments, UK). The

explant was glued to a steel disc to meet the required thickness. The AC explant then was placed in the sample holder and fixed via screws. The setup used is shown in **Figure 6.1**. The sample holder was filled with 2 ml of PBS (reference solution) or a NPs formulation. The steel balls and discs were reusable; they were cleaned before each test following a UV-Ozone treatment and sonication in ethanol and distilled water. The measurements were conducted at 37^{o}C (normal human body temperature), under the constant normal load of 1.96 N. That load was chosen to protect the AC explant from irreversible damage even though it resulted in lower pressure than the normal pressure in joints (0.14 MPa versus 1-6 MPa [472]). The sliding velocity was chosen to be 2.5 mm s^{-1} because it represents the boundary lubrication in joints [262]. The velocity was achieved with a stroke length of 0.25 mm, and a frequency of 10 Hz. The CoF was calculated as the average of the whole stroke for 30 min.

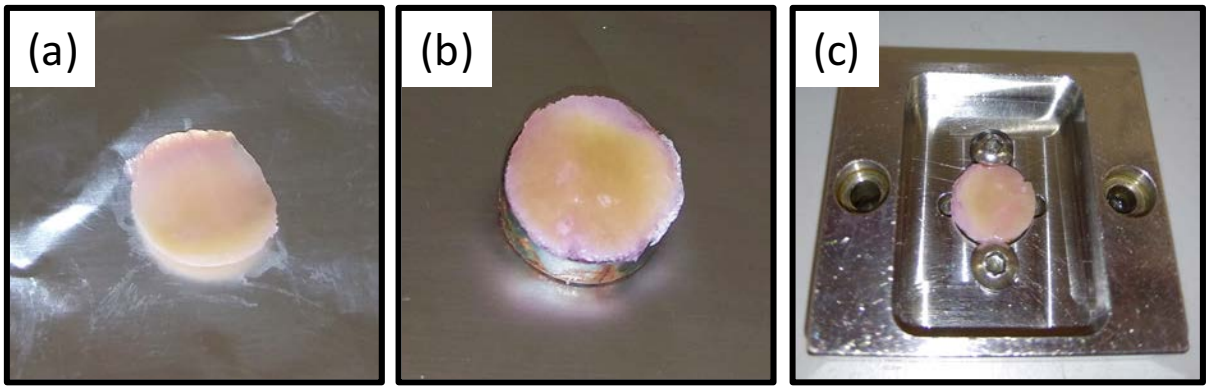


Figure 6.1: HFRR setup for testing human and animal AC explants. (a) AC disc generated using a cork borer, (b) AC disc fixed on a steel disc, (c) AC fixed in the sample holder.

6.2.7 Surface adsorption of nanoparticle formulations

The surface adsorption of the NPs was evaluated on a self-assembled monolayer (SAM) of (3-Mercaptopropyl) trimethoxysilane (Merck, Germany) using a

QCM (openQCM, Novaetech, Italy). The trimethoxysilane monolayer was used to replicate the chemistry of the silicone elastomer (SE), which mimics the mechanical properties of the AC [391]. The SAM was prepared by David Burgess on a gold-coated QCM crystal (Novaetech, Italy) operating at 10 MHz. The crystal was immersed in an ethanolic solution of the thiol (1 mM) for 24 hours. It was subsequently placed in a clean petri dish and backfilled with dry nitrogen until used (within 24 hours). The crystal was cleaned with UV-Ozone treatment before the formation of the SAM. Additional Information about the SAM can be found in Appendix A4.

The SAM-coated QCM sensor was placed in the QCM holder. The system was first rinsed with PBS and then with a formulation of 0.1% DL-NPs in PBS. When the dynamic adsorption had reached equilibrium (stable frequency), it was rinsed again with PBS. A peristaltic pump (Ismatec, Germany) connected with the QCM controlled the flow at 0.35 ml/min. The total adsorbed mass was evaluated based on Sauerbrey's equation for rigid and thin films [473]:

$$\Delta M = -J\,\Delta f \qquad (6.1)$$

where ΔM is mass change (g cm^{-2}), Δf is frequency change (Hz), and J is the nominal sensitivity constant of the crystal, which was equal to 4.42 x10^{-9} g Hz^{-1} cm^{-2} for the specific crystal [474]. The nominal area of the used crystal was 0.2043 $\pm$ 0.009 cm^2 [474]. The rigid layer developed by NPs in PBS was studied via QCM to understand NPs adsorption kinetics. The viscoelastic film developed by the complete formulation was evaluated via AFM to understand its effect on the surface roughness of the AC.

6.2.8 Imaging of sensors and cartilage explants

The adsorption of the NPs onto the QCM sensors and the topography of human osteoarthritic AC explants was investigated via Atomic Force Microscope (AFM) imaging. The samples (QCM sensors, AC explants) were imaged on the AFM Imaging-Intermittent Contact mode using a NanoWizard II (JPK Instruments Ltd, Germany) at a controlled temperature environment (17^{o}C). The QCM sensors were imaged in ambient, whereas the AC explants in PBS. The measurements were carried out with Si_3N_4 cantilevers with a spring constant of 42 N m^{-1} and a resonance frequency of 320 kHz (Bruker Ltd, UK). The Gwyddion 2.59 software was used to process the acquired images and calculate their corresponding surface roughness.

The topography of the AC explants was also examined via interferometry (MicroXAM, KLA Tencor, UK). Three areas of approximately 10^4 μm^2 were imaged before and after 30 min treatment with the NPs formulations at a magnification of 20x. Mapvue AE ver 2.27 software was used for imaging and calculating the surface roughness of those areas.

6.2.9 Surface properties of nanoparticle film

The surface properties of the NPs films were investigated using the Force Spectroscopy Contact mode of a JPK AFM (Nanowizard II, Germany). The experiments were conducted at controlled temperature (17°C) in liquid (PBS or NPs formulations). Force measurements were performed with stainless steel colloidal probes, which were prepared by attaching individual stainless steel particles of 27-31 μm size (Micro technology, UK) using a two-part epoxy glue (Araldite) onto tipless AFM

cantilevers (All-in-One-Al-Tipless, Budget Sensors, UK) with a spring constant of 7.4 N m^{-1} and a resonance frequency of 150 kHz. Force curves were collected at six different regions of each sample, applying forces between 40 and 280 nN. The velocity of the cantilever was 2 μm s^{-1}. The adhesion energy and Young's modulus were calculated by the JPK Data Processing 4.2 software incorporating the Hertz model and the stainless steel particle's actual diameter acquired by SEM imaging.

6.2.10 *In-vitro* cytotoxicity evaluation of nanoparticle formulations

A standard Microtubules (MTS) array was used to evaluate the *in-vitro* cytotoxicity of the NPs formulations on primary human osteoarthritic chondrocytes and fibroblasts. The cells were seeded into 96-well plates at a density of 6,000 cells per well for 24 hours. Cells were then exposed to various formulations and were incubated under 37^{o}C and 5% CO_2 for either one or five days. On the day of the test, 20 μl of the MTS reagent Thaw Cell Titer 96AQ (Promega, USA) was added per well, and the cells were incubated for two hours. Afterwards, their absorbance at 490 nm was examined with a microplate reader (Synergy HT, BioTek Instruments, USA). The number of cells was quantified from the absorbance values based on a reference curve.

6.3 Results and discussion

6.3.1 Surface roughness of human cartilage explants

Figure 6.2 illustrates the topography of one human AC explant at different area sizes, captured by AFM. The AC was rough as expected based on the literature. The average surface roughness of the AC explant is 42, 64, 291, and 350 nm for an area of 4, 25, 2.5 10^3, and 10^4 μm^2, respectively. The increase in the surface roughness with

increasing testing area, attributed to the increasing presence of surface features, has been reported for the AC [384]. The AC surface roughness found here is comparable with other AFM studies on the AC. For instance, the surface roughness over an area of 2.5 10^3 μm^2 was 291 nm, which falls within the reported range (137-533 nm) [63, 196]. The surface roughness of the AC depends on the measurement technique [384]. As such, the roughness of human AC explants was also tested with interferometry and found 1.19 $\pm$ 0.11 μm, confirming previous investigations of AC with interferometry [475]. Nevertheless, comparing the surface roughness of disparate joint specimens is not recommended because they demonstrate significant heterogeneity (Chapter 3). Moreover, the explants used here were affected during their removal from the joint. Features created by the medical blade are shown on their surface in **Figure 6.2c** and **Figure 6.2d.** The damage of the surface of the explants increased the surface roughness and might have increased the effectiveness of the NPs formulations in decreasing the CoF. NPs formulations were also tested on intact AC explants from pigs to confirm their effectiveness and were proven effective.

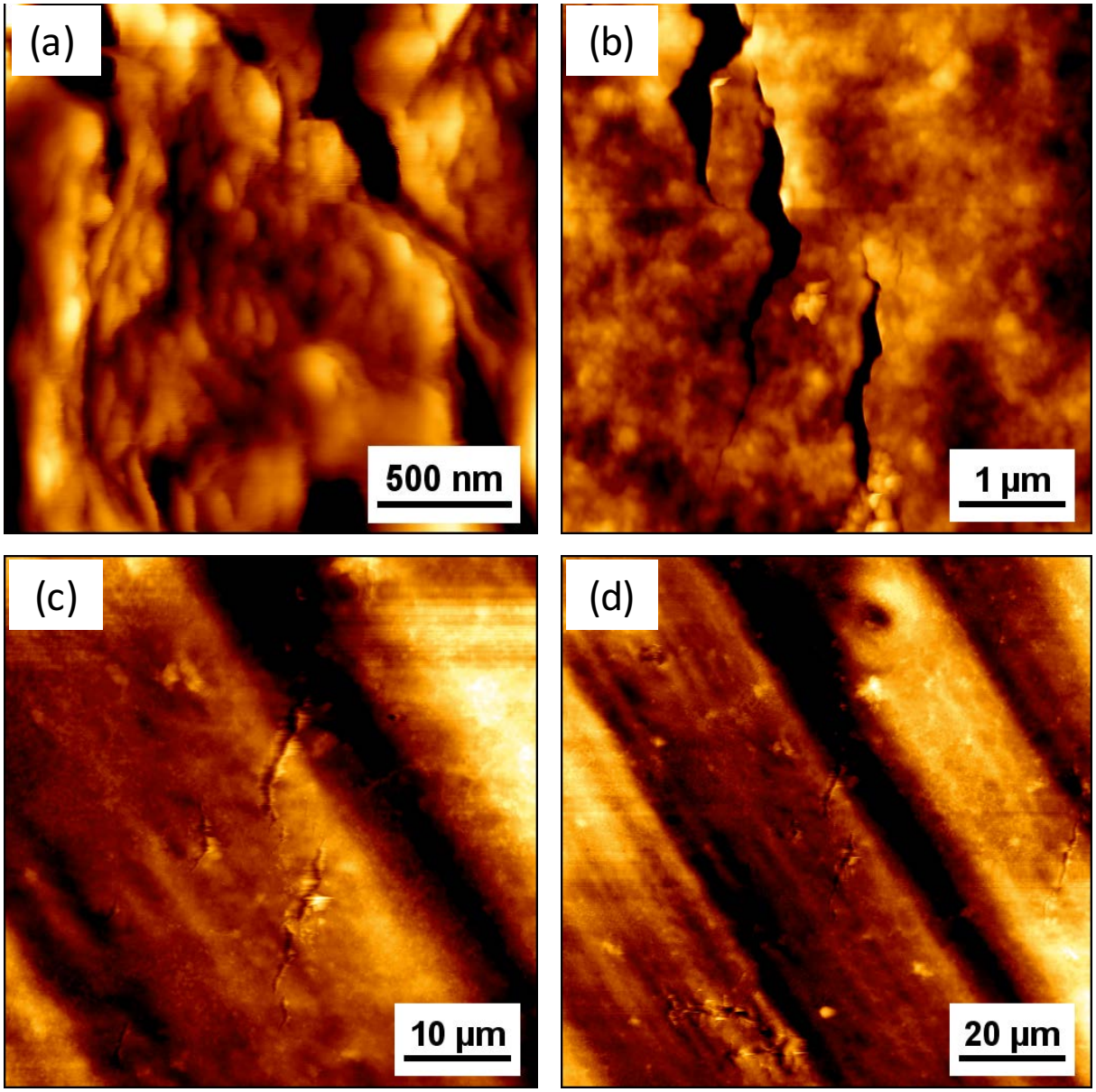


Figure 6.2*:* AFM topographies of the same human osteoarthritic AC explant at various sizes. (a) 4, (b) 25, (c) 2.5 10^3, and (d) 10^4 μm^2.

6.3.2 Effect of formulation on the stability

The formulation used in this chapter was NPs (0.5%)/HA (0.1%)/SDS (0.5%) in PBS. The formulation was investigated and optimised in Chapter 5 to provide the highest CoF reduction capacity, physiological viscosity for the normal operation of the

joints, and good stability. NPs were either blank or loaded with the drug Celecoxib and had a similar size (about 200 nm). They were expected to smoothen the rough AC surface as they did with the SE (Chapter 5) because their size of 200 nm was within the surface roughness of the AC (42.09-350.5 nm), as shown in **Figure 6.2**.

The size, polydispersity (PDI), and ZP of the blank and DL-NPs formulations exhibited similar results as presented in **Figure 6.3**. Their particle size was similar to their size in the water (Chapter 5), indicating no significant aggregation. The lack of aggregation and the low PDI (lower than 0.5) denote good dispersion of NPs and stability. The ZP of the formulations ranged from 29.9-54.6 mV, an additional indication of their excellent stability. Based on the literature, ZP higher than 25-30 mV for water-based NPs suspensions highlights a low tendency of agglomeration [292, 293]. It is worth noting that PCL formulations were not as stable as the others. Their average size and PDI were higher than the PMMA and PLA suspensions, and their ZP was the lowest. As discussed in Chapter 5, this is probably attributed to the larger particle size of PCL, which strengthens the depletion interactions.

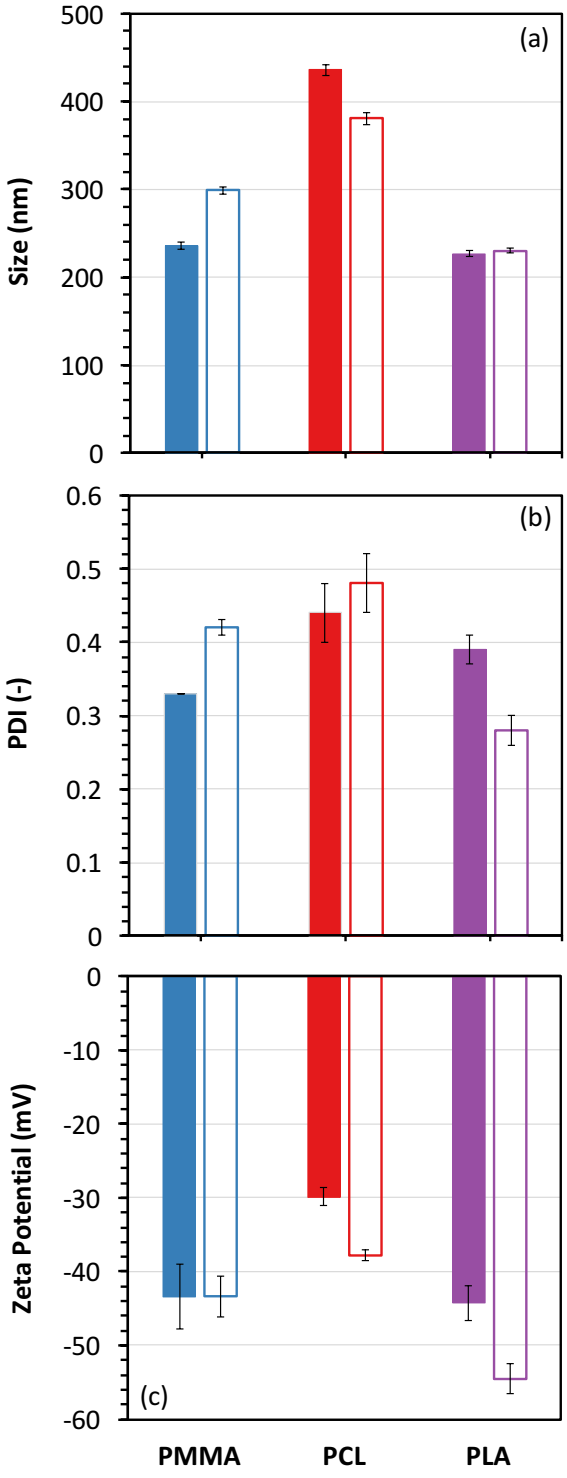


Figure 6.3: (a) Size, (b) PDI, and (c) Zeta Potential of formulations with blank and drug-loaded PMMA, PCL, and PLA NPs. The filled bars represent the blank and the non-filled bars the DL-NPs. Each bar represents the average of five repetitions of three different samples. The error bars represent their standard error.

6.3.3 Effect of nanoparticle formulation on the coefficient of friction of cartilage

Evaluating the effect of the formulation's components on the AC achieved via tribological tests on porcine AC against a steel ball. The tested formulations consisted of NPs only, NPs with SDS (0.5%), NPs with HA (0.1%), and NPs with HA (0.1%) and SDS (0.5%). On all of them, blank PLA NPs were used at a concentration of 0.5%. Alike in the SE, all formulations apart from the PLA/HA reduced the CoF (**Figure 6.4**). In the case of PLA/HA, the absence of SDS caused NPs aggregation (Chapter 5), which increased the surface roughness and consequently the CoF [411]. Although the HA slightly diminished the formulation's lubrication efficiency (CoF reduction: PLA/SDS: 17%, PLA/HA/SDS: 12%), it was included in the final formulation because of its capacity to improve SF's viscoelasticity.

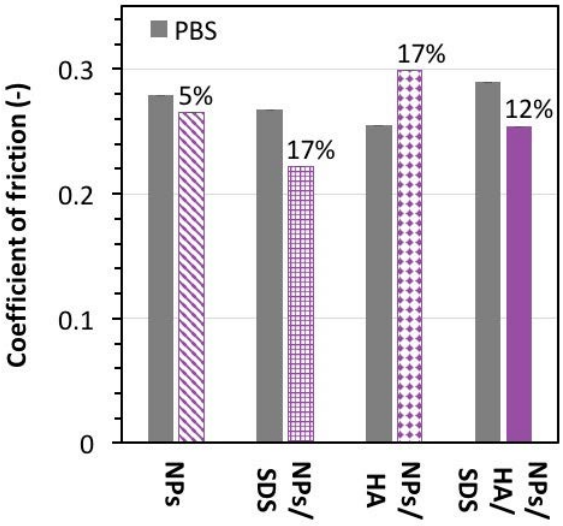


Figure 6.4*:* Effect of formulation's components on the CoF of porcine AC against a stainless steel ball. The formulations investigated consisted of PLA NPs (0.5%), PLA NPs (0.5%)/SDS (0.5%), PLA NPs (0.5%)/HA (0.1%), and PLA NPs (0.5%)/HA (0.1%)/ SDS (0.5%) in PBS. The percentages on the top of the bars represent the reduction of the CoF. Each bar represents the average CoF of a single sample at different time points within 30 minutes. The error bars symbolise their standard error.

The influence of blank NPs and DL-NPs on the CoF of human osteoarthritic AC was evaluated with a formulation of NPs (0.5%)/HA (0.1%)/SDS (0.5%) in PBS with three kinds of polymer NPs (PMMA, PCL, PLA). The reduction in the CoF when PBS was replaced by the formulations is shown in **Figure 6.5**. The average CoF of human osteoarthritic AC explants with PBS as a lubricant was 0.31 ± 0.01, a value consistent with the literature [262]. A significant reduction of 12-46% in the CoF can be seen upon introducing the formulations (**Figure 6.5**). It can be concluded that loading the NPs with the drug did not affect their CoF since both blank and DL-formulations reduced the CoF to a similar extent. The exceptional lubrication demonstrated by the NPs formulations exceeds the performance of most of the systems developed so far to treat OA [216, 464, 469]. The excellent tribological performance is mainly attributed to the NPs, which are known lubricant additives [9, 10, 56]. It is believed that NPs lubrication mechanism is the polishing effect [10], as discussed in Chapter 5.

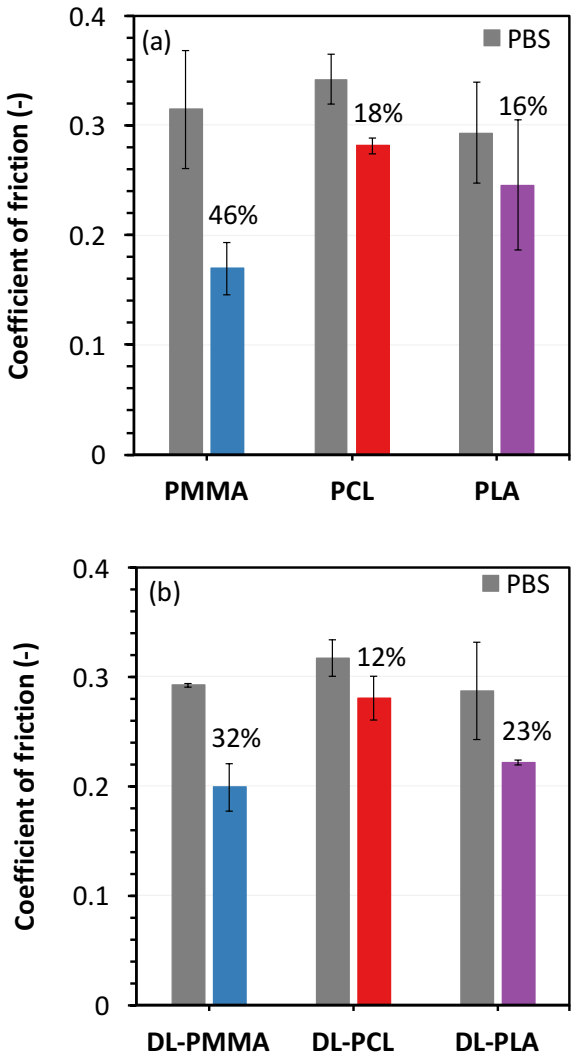


Figure 6.5: CoF of human osteoarthritic AC against a stainless steel ball with (a) blank and (b) DL-PMMA, DL-PCL, and DL-PLA NPs formulations as lubricants. The formulations consisted of NPs (0.5%) /HA (0.1%)/SDS (0.5%) in PBS. The percentages on the top of the bars represent the reduction rate of the CoF. Each bar represents the average CoF of a single sample at different time points within 30 minutes. The error bars symbolise their standard error.

Formulations with different polymer NPs provided different reduction rates to the CoF of the AC despite their identical composition (**Figure 6.5**). PMMA formulations were the most effective, providing a CoF reduction of 46% (blank NPs) and 32% (drug-loaded). PLA suspensions followed, providing a CoF reduction of 16% with blank NPs

and 23% with DL-NPs. PCL formulations were the least effective, likely because of the PCL NPs aggregation (**Figure 6.3**). The particle size of the aggregated PCL NPs (Blank: 435.60 ± 6.25 nm, DL: 380.4 ± 6.44 nm) was larger than the AC surface roughness (350 nm), resulting in a non-uniform film, which probably increased AC's surface roughness and consequently the CoF [410]. PMMA superiority in CoF reduction is probably attributed to its highest surface adsorption, as discussed in the following section.

6.3.4 Surface adsorption characteristics of nanoparticle formulations

QCM results indicated that NPs not only adsorbed on the trimethoxysilane-functionalised crystal but also remained on it after rinsing with PBS, as shown in a representative QCM curve (**Figure 6.6**). As such, the lubrication performance of the formulations is highly likely associated with the quantity of NPs adsorbed on the AC surface. NPs form strong lubricious films with lower resistance to shear than the substrates and reduce the CoF [476]. Therefore, NPs probably adhered to the AC surface and were not cleared from it as it happens with the current IAI analgesics [7]. That is a significant advantage compared to other reported systems for OA treatment, which incorporate functionalised NPs with polymer brushes [216, 218, 219]. Polymer brushes-coated NPs are expected to demonstrate low adsorption at the AC surface due to steric repulsion between them and prevent the formation of a thick protective film capable of reducing AC's surface roughness. Polymer brush-coated surfaces are known for their resistance to adsorption [477, 478].

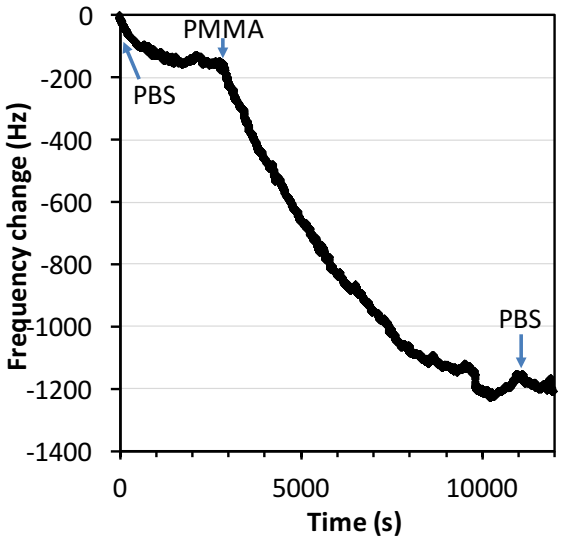


Figure 6.6*:* Representative QCM adsorption curve of a formulation consisting of 0.1% PMMA NPs in PBS on a (3-Mercaptopropyl) trimethoxysilane-functionalised QCM sensor. The force curve of a single measurement is presented here for presentation purposes.

The adsorbed mass of the DL-PMMA, DL-PCL, and DL-PLA formulations on the trimethoxysilane-functionalised QCM crystals is presented in **Table 6.2** and compared with the reduction those formulations provided to the CoF. The surface adsorption of the DL-NPs follows the same order with the CoF reduction. DL-PMMA NPs adsorbed in the highest amount on the SAM-functionalised QCM crystal and demonstrated the highest CoF reduction, followed by PLA and then PCL. The more the adsorption of NPs on the QCM electrode, the better their lubrication efficiency [476, 479, 480]. Furthermore, high adsorption might relate to uniformity, which results in suppressed adhesive forces, smoother sliding motion and higher CoF reduction [479].

Table 6.2: Adsorbed mass of DL-PCL, DL-PLA, and DL-PMMA NPs formulations on a (3-Mercaptopropyl) trimethoxysilane-functionalised QCM sensor and CoF reduction on human osteoarthritic AC explants.

Nanoparticles	DL-PCL	DL-PLA	DL-PMMA
Adsorbed mass (ng)	200 ± 2	650 ± 10	939 ± 20
CoF reduction (%)	12	23	32

AFM images confirmed the adsorption of NPs on the QCM sensors. **Figure 6.7** shows representative images of a clean SAM-coated sensor and sensors used with DL-PLA, DL-PCL and DL-PMMA**.** NPs can be seen on the surface of the used QCM crystals, suggesting strong NPs adsorption. The amount of the adsorbed NPs presented in **Figure 6.7** is consistent with the QCM results (**Table 6.2**). PMMA NPs adsorbed in the highest amount on the SAM-coated QCM sensors followed by PLA and PCL. Moreover, PMMA NPs, which provided the best lubrication performance, were the most uniform distributed NPs on the QCM sensor. Incomplete surface coverage results in increased surface roughness and increased CoF reduction [479]. Therefore, there is a strong correlation between CoF reduction, the quantity of adsorbed NPs, and homogenous NPs adsorption, which should be considered during the development of the formulations.

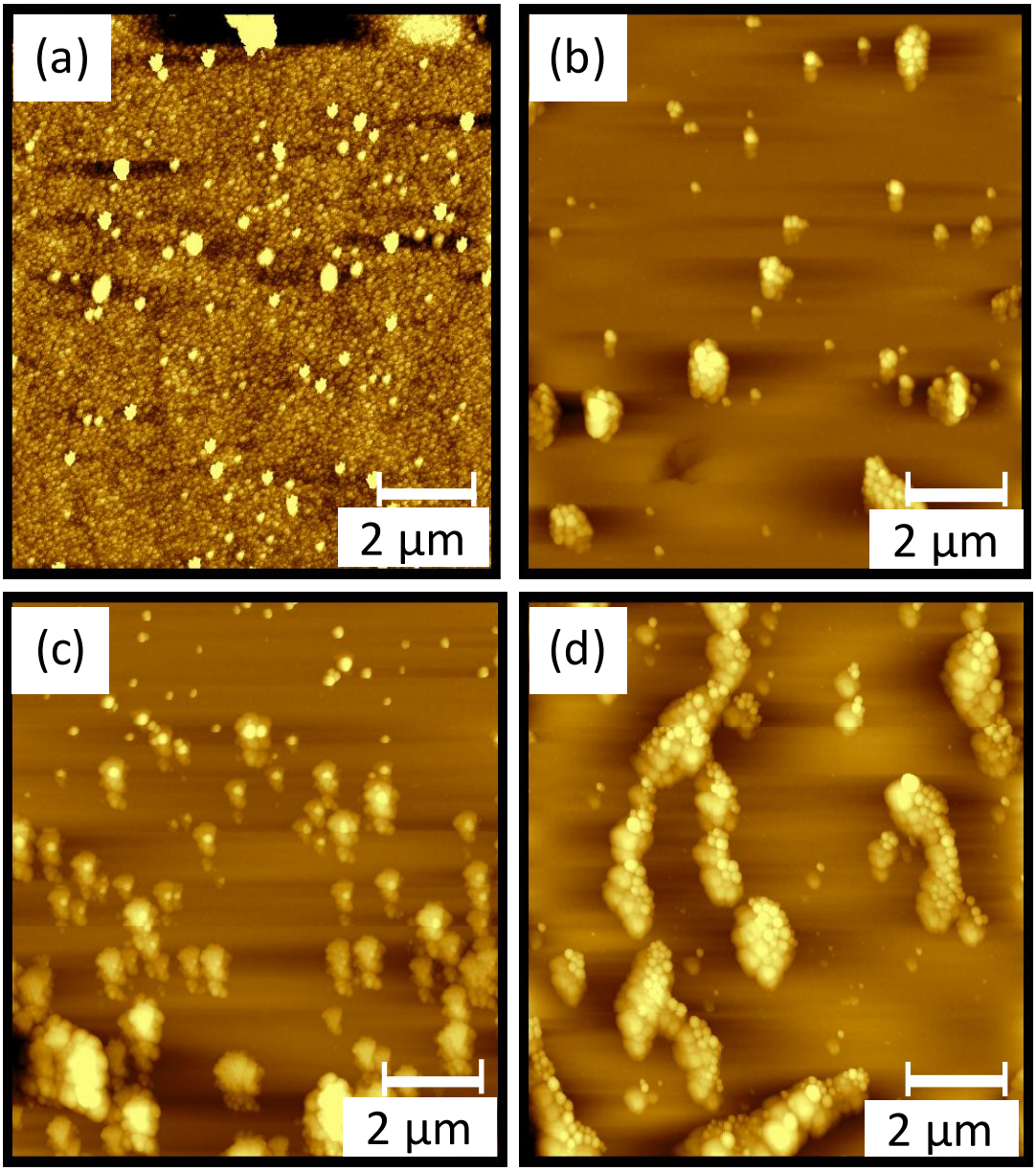


Figure 6.7*:* AFM images of (3-Mercaptopropyl) trimethoxysilane-functionalised QCM sensors (a) clean, (b) used with a DL-PCL NPs formulation (c) used with a DL-PLA NOs formulation, and (d) used with a DL-PMMA NPs formulation. The size of the images is 100 μm^2.

6.3.5 Effect of nanoparticle formulation on cartilage's surface characteristics

The NPs formulations reduced the average surface roughness of AC explants from 1.05 ± 0.20 µm to 0.64 ± 0.16 µm, a reduction of 39%. **Figure 6.8** compares the

roughness of the same AC explant before (**Figure 6.8a**) and after (**Figure 6.8b**) the treatment with a PCL NPs formulation. In that representative case, the surface roughness decreased from 1.25 μm to 0.45 μm. The surface roughness reduction provided by the NPs formulations is consistent with other studies [481-483] and strengthens the hypothesis of the polishing lubrication mechanism.

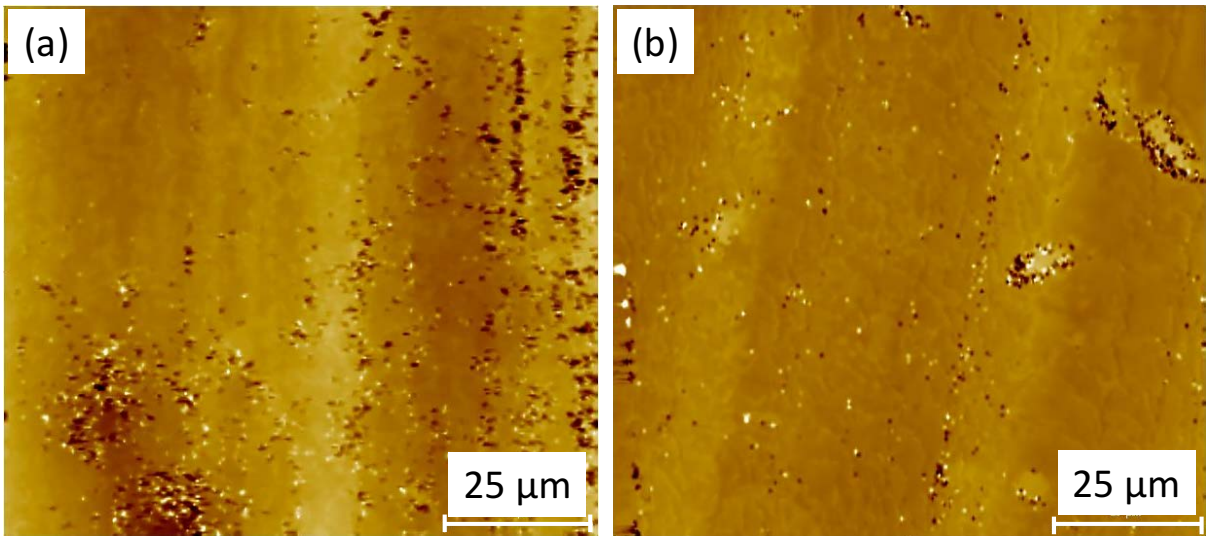


Figure 6.8*:* Interferometer images of human osteoarthritic ACs (a) intact with surface roughness 1.25 μm, and (b) treated with a NPs formulation with surface roughness 0.45 μm. The NPs formulation consisted of PCL NPs (0.5%)/SDS (0.5%)//HA (0.1%) in PBS. The size of both images is 10^4 μm.

The NPs formulations minimised the adhesion and reduced the stiffness of the AC surface. The AFM force curves of AC in PBS were sharp with a small adhesion peak, whereas in NPs formulations were smooth with no adhesion peak. **Figure 6.9** presents a characteristic force curve of an AC explant in PBS and NPs formulation. The absence of adhesion is associated with a uniform layer of NPs [479, 484]. The adhesion reduction is additional evidence of CoF reduction because adhesion and CoF are positively correlated [479, 485]. Furthermore, the AC explants demonstrated a suppressed Young's modulus (stiffness) over a range of indentation loads when

treated with NPs formulations. The reduced Young's modulus is attributed to the protective film made by NPs on the AC surface [486]. NPs have probably been incorporated into the elastic and porous AC's surface, making it more elastic and facilitating lubrication. The more elastic the surface, the higher the deformation and the fluid entrapment resulting in higher CoF reduction [487]. An increase of the Young's modulus was seen on measurements conducted on a flat surface (silicon wafer), confirming that the polishing lubrication mechanism only works on rough substrates. **Table 6.3** shows the decrease of AC Young's modulus after treatment with blank and DL-NPs formulations. PMMA NPs provided the highest reduction on Young's modulus, followed by PLA and PCL. Overall, PMMA NPs formed the most elastic and uniform film, as suggested by their surface adsorption characteristics (paragraph 6.3.4).

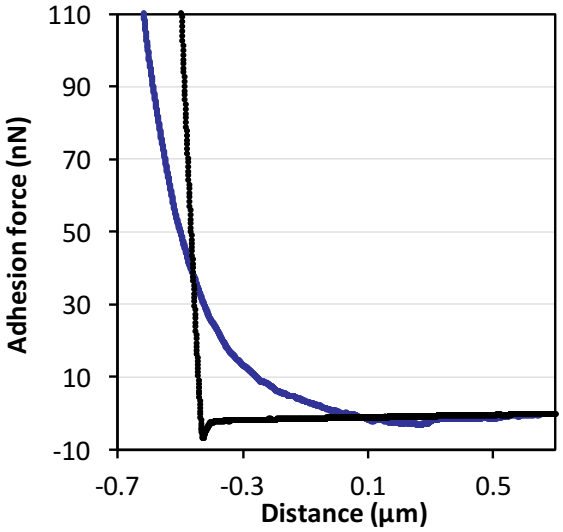


Figure 6.9: Representative force curve of a human osteoarthritic AC explant in PBS (black) and NPs formulation (blue). The force curves were created with a stainless steel colloidal probe. The force curve of a single measurement is presented here for presentation purposes.

Table 6.3: Reduction of human osteoarthritic AC explants Young's modulus with blank and drug-loaded (DL) PCL, PLA, and PMMA NPs formulations. Formulations consisted of NPs (0.5%)/HA (0.1%)/0.5% SDS (0.5%) in PBS.

Young's modulus reduction (%)	PCL	PLA	PMMA
Blank NPs	24	78	84
DL-NPs	50	58	61

6.3.6 Cytotoxicity of nanoparticle formulations

The toxicity of each component of the formulation (**Figure 6.10a**), as well as the toxicity of the formulation with different DL-NPs (PCL, PLA, and PMMA) (**Figure 6.10b**), were tested on primary human osteoarthritic synovial chondrocytes. As illustrated in **Figure 6.10a,** the number of cells increased with time from the first day of incubation when there was no SDS in the system (pure PBS, NPs/PBS, and NPs/HA/PBS), indicating cell proliferation. Cell proliferation relates to physiological conditions [219, 472, 488] and highlights the safety of the NPs and the HA for the cells. Moreover, cells number was not significantly different from the first to the fifth day of incubation, highlighting stable formulation toxicity. Nevertheless, chondrocytes reduced in the presence of the surfactant SDS. The SDS was toxic for the cells, inducing a reduction of 32-54% on their number within five days. Surfactants are known for their adverse health effects, including cell death, cell membrane damage, and local irritations [489]. The SDS alters the biomechanical characteristics of the extracellular matrix (ECM) (reduces Glycosaminoglycans (GAGs), increases collagen, degradation rate), resulting in decreased cell viability [490, 491]. The HA was compatible with the chondrocytes (**Figure 6.10a**) as expected because HA is a natural component of the joints. The polymer NPs were proved biocompatible. The addition of the PLA NPs in PBS increased the number of cells by 27-80% after one day and 18-61% after five

days (**Figure 6.10a**), confirming their biocompatibility. Several studies proved *in vitro* and *in vivo* the safety of PLA [417, 492], PCL [493], and PMMA .[494, 495].

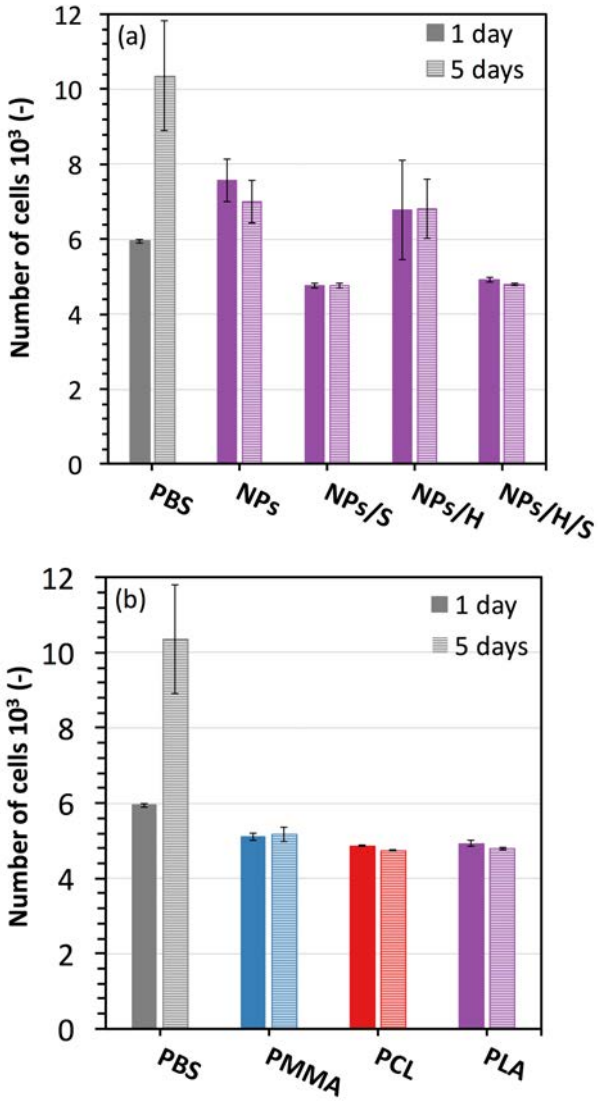


Figure 6.10: Cytotoxicity of chondrocytes after one and five days of incubation with (a) different components of the formulation, and (b) NPs formulations with different types of DL-NPs. The filled bars represent the average number of cells after one day and the stripped patterned bars after five days of incubation. The formulation on (b) consisted of DL-NPs (0.5%)/HA(H) (0.1%)/SDS(S) (0.5%) in PBS. DL- PCL, DL-PLA, and DL-PMMA NPs were used. The error bars represent the standard error from three wells seeded with the same sample.

The complete NPs formulation exhibited excellent biocompatibility (**Figure 6.10b**). After one day of incubation, a reduction of 13-18% on the number of the cells was observed, and there was no additional reduction with time (reduction after five days 11-18%). PMMA formulations were proved the most biocompatible, providing average cell viability of 88%, whereas PLA and PCL provided viability of 83% and 82% accordingly. PMMA incomplete drug release profile could explain their excellent biocompatibility. As shown in **Figure A.3**-Appendix, only 47% of Celecoxib was released from PMMA after five days, in contrast to PLA and PCL, which provided a drug release of 84% and 82% accordingly. Celecoxib is a cytotoxic drug [496-498], therefore, its increased release is related to increased cytotoxicity. Other than that, the three DL-NPs formulations did not provide significantly different cytotoxicity behaviour because they had similar size and surface charge, which influence cytotoxicity [499]. The low cytotoxicity of the formulations was also confirmed in fibroblasts (**Figure A.4**-Appendix).

6.3.7 *In-vitro* drug release from the nanoparticle formulations

Celecoxib-loaded-NPs demonstrated a sustained drug release compared to the free Celecoxib (**Figure A.3**-Appendix). PLA and PCL NPs released 80.4% and 83.6% of Celecoxib within 9 days. PMMA NPs demonstrated the lowest release rate (48%) because they are more hydrophilic than the others and exhibit low diffusivity (because of their low mobility) [418, 500, 501]. The sustained drug release is attributed to the polymer NPs, which are effective drug delivery systems [195, 468] and the HA, which may have acted as a physical barrier entrapping the drug inside the SDS-coated NPs.

The capacity of HA to extend the retention time of drugs has been previously reported [285, 502, 503].

Compared to previous studies, a significant improvement in the drug release has been reached by formulations with the DL-NPs PCL, PLA, and PMMA, indicating their suitability for OA treatment. NPs coated with polymer brushes achieved a 74.5%-87.5% release of aspirin [218, 220] and 59.8% release of diclofenac sodium [219] within 72 h. Chitosan microspheres loaded with brucine demonstrated 80% release within 5 days [504]. *In-vitro* release of Celecoxib from a liposome/solid lipid NPs formulation demonstrated a drug release of 87.5% within 72 h [285] and 95% within 7 days [505]. The NPs formulation developed in this study achieved 83.6% release of Celecoxib within 9 days. However, other carriers developed to treat OA reported a better drug release profile. For example, a click-cross-linked small intestine submucosa drug delivery system released 95% of methotrexate in 40 days [488]. Moreover, a scaffold of poly(lactic-co-glycolic acid) NPs with HA hydrogel delivered 65% of kartogenin in 60 days, and its release was kept increasing [467]. More information about the *in-vitro* drug release profile and the methodology used can be found in the Appendix A4. Piaopiao Pan has carried out the experimental work at the Guangzhou University of Chinese Medicine in China.

6.4 Conclusions

In the present chapter, the dual capacity of the developed drug-loaded nanoparticles formulation to improve the joint's tribological characteristics and prolong the release of anti-inflammatory drugs has been successfully demonstrated. The formulation consisted of the biocompatible polymer nanoparticles (PMMA, PCL, PLA)

loaded with the drug Celecoxib, which reduces pain and inflammation, the surfactant SDS, which stabilizes the formulation, and HA, which enhanced the lost viscosity of the osteoarthritic SF.

The formulation reduced the CoF of osteoarthritic human and healthy animal AC tissue, highlighting its capacity to be used at any stage of OA. The effect of such a NPs formulation on human AC has not been demonstrated so far. The improved lubrication performance is correlated to the adsorption of NPs on the AC. NPs adsorbed at the valleys of the AC and formed elastic protective films at its surface, which reduced the surface roughness and eventually minimised the adhesion and the CoF. The more NPs were deposited to the surface and the more uniform their distribution, the better the lubrication, suggesting that fine control on the attraction between the NPs and the target surface could be an essential designing parameter for any future work.

Besides the improved lubrication performance, the developed formulation demonstrated a sustained release profile of Celecoxib up to 9 days, attributed to the use of the NPs as drug delivery systems and the additional barrier provided by the HA. Last but not least, the formulation was found to possess excellent biocompatibility, providing 82-86% viability to synovial chondrocytes after five days of incubation, highlighting a vast potential for clinical application. Additionally, the formulation possessed excellent biocompatibility with synovial chondrocytes, highlighting a considerable potential for clinical application. The SDS is the only toxic component of the formulation, but biopolymers can replace it in the future.

The developed formulation is a promising system for any future design for the IAI treatment of OA. The lubrication improvement in the healthy and osteoarthritic AC explants demonstrates its capacity to be used at any stage of OA. It could be an alternative to the conventional HA formulations for IAI treatment of osteoarthritic joints at the early OA and offer additional lubrication improvement. In any case, it is anticipated to have long-lasting therapeutic effects, improve the quality of patients' life, and delay surgical interventions.

7. CONCLUSIONS AND FUTURE PERSPECTIVES

7.1 Conclusions

A series of formulations based on biocompatible nanoparticles (NPs) were developed to treat lubrication loss in joints under osteoarthritis (OA). First, the requirements for the new treatment were identified by studying the impact of OA on joints' lubrication. To that end, Synovial fluid (SF) lubrication of patients with OA was studied via rheological (viscosity, shear-thinning index) and surface interaction measurements (adhesion energy) to cover all lubrication conditions in the everyday operation of joints. SF's diminished lubrication in osteoarthritic joints under all lubrication regimes was confirmed. Patients were categorised into groups based on their physical/anatomical characteristics. Age and obesity were the most critical factors leading to SF degeneration. As age and BMI (Body Mass Index) increase, SF viscosity and shear-thinning decrease, while adhesion energy increases. The rheological degeneration of the osteoarthritic SF was associated with compositional alterations such as the reduced concentration of Hyaluronic acid (HA), while the increase in adhesion could be attributed to the inflammatory environment caused by OA.

Nanoparticle (NPs) formulations made of the model NPs silica and latex were explored as a potential treatment for the coefficient of friction (CoF) rise in osteoarthritic joints. Various contact surfaces covering a wide range of mechanical properties were investigated to determine how NPs work to reduce the CoF of the joints. The contact surfaces were made of implant materials, resembling natural and artificial joints. The different combinations of the contact surfaces corresponded to different stages of OA and indicated at which stage of the disease this treatment could be successful. The

lubrication regime in which each contact surface operates determines the influence of NPs size, solvent's viscosity, and surface properties (e.g. Young's modulus, surface roughness) in the CoF reduction. For instance, high viscosity is preferential in the hydrodynamic regime, whereas surface properties are dominant in boundary and mixed lubrication regimes. The surface roughness of the materials in contact was identified as the most critical factor. NPs formulations were always found effective in reducing the CoF of the rough silicone elastomer (SE). In that case, NPs lubrication mechanism is the polishing effect. More specifically, NPs smoothen SE by inserting into its valleys. Since SE resembles the rough and porous articular cartilage (AC), a treatment utilising NPs formulations could be beneficial when AC is still present in the joint at the beginning of the OA.

The delivery of NPs formulations to the joints could take place via intra-articular injection (IAI), the most effective treatment at the early stages of OA. NPs formulations aimed to substitute the available IAI supplements, which do not improve the CoF under low-velocity movements of the joints. NPs formulations were developed and tested between the rough SE and a steel ball, which replicate the AC-bone contact at the initial phase of OA when the AC is partially removed. The formulation consisted of biocompatible NPs, HA, and Sodium Dodecyl Sulphate (SDS) in Phosphate Buffer Saline (PBS). Biocompatible NPs made of Polymethylmethacrylate (PMMA), Polycaprolactone (PCL), and Polylactic acid (PLA) were chosen thanks to their biocompatibility and wide application in medicine (e.g. effective drug delivery systems). The decrease of HA's physiological concentration has been associated with SF's viscosity loss from the analysis of osteoarthritic SFs lubrication properties. Therefore, HA was added to the formulation to restore SF's viscosity. SDS was used to enhance

the stability of the formulation. The concentration of the formulation's components was optimised to provide maximum CoF reduction. All three biocompatible NPs reduced the CoF, thanks to their capacity to adsorb on the rough SE surfaces and polish them. The softest NPs (PLA) provided the highest CoF reduction rate in the uniform SE surface, highlighting the significant impact of hardness on the CoF.

Apart from being excellent lubricant additives, NPs also prolonged the retention time of drugs provided via IAI to the joints. The dual capacity of formulations made of polymer NPs loaded with an anti-inflammatory painkiller (Celecoxib) has been successfully demonstrated. Alike blank NPs, drug-loaded (DL) NPs confirmed their capacity to reduce the CoF. This time the lubrication was evaluated on osteoarthritic human and healthy animal AC explants, demonstrating the suitability of this approach for any stage of OA progression (any stage of AC degeneration). The CoF reduction is mainly associated with the quantity of the adsorbed NPs on the AC surface and the development of an elastic protective layer of NPs, which reduces the surface roughness and eventually the CoF. Moreover, the DL-NPs acted as delivery systems for the non-soluble drug and prolonged its release from a couple of hours to at least nine days. The sustained drug release profile is assigned to the improved stability/solubility of the drug provided by the NPs and the physical barrier provided to the NPs by their coating with HA. Furthermore, DL-NPs formulations provided excellent biocompatibility to human synovial chondrocytes.

In summary, an innovative approach was used for developing a treatment for the diminished lubrication of osteoarthritic joints. Developing an NPs-based treatment that offers simultaneous pharmacological and lubrication benefits is a new approach

introduced in 2014 and reported only by a few publications. NPs-based formulations were developed, which could replace the current IAI supplements for the early-OA treatment. The formulations provided high CoF reduction on human AC, cell viability and prolonged drug release, highlighting a considerable potential for clinical application. The NPs formulation is a platform ready to be used; its proof of principle has already been established in human AC. It is the first time the effectiveness of such a system has been established on natural human osteoarthritic AC. Similar NPs-based systems have only been tested on implant materials, which do not adequately mitigate the complex tribological behaviour of the AC. The advantages of the developed formulation compared to other reported systems like the polymer-brush-coated NPs are the prolonged drug release and the long-lasting lubrication attributed to the capacity of the NPs to adsorb to the AC surface and remain there even after the physiological squeezing of the solvent out of the joint. In addition to that, this study employed biocompatible and biodegradable polymer NPs instead of the toxic polymer-brush coated silica NPs used in most of the previously reported studies.

Besides the treatment for OA, this study developed a new method for analysing the lubrication properties of diluted SFs using Atomic Force Microscopy (AFM), which could be a promising approach for the future investigation of human SFs. Last but not least, new knowledge on the lubrication mechanism of NPs has been gained by conducting a comprehensive study on various contact materials and formulations. Based on that knowledge, a Machine Learning Analysis tool has been developed, which could be used in the future to predict and analyse the tribological behaviour of similar tribosystems lubricated by NPs without the need of performing actual lab experiments.

7.2 Recommendations for future work

This part of the thesis provides suggestions for the continuation of the present work. The suggestions aim to improve the experimental methodology used in this thesis and advance the developed formulation for animal and clinical testing.

Understanding further the lubrication in osteoarthritic joints by analysing more SF and AC tissues could be proved helpful. For instance, understanding better the range of AC surface roughness is essential for selecting the appropriate size of NPs. Also, testing the effect of the NPs formulation on the whole boundary lubrication region would provide a comprehensive understanding of the formulation's efficacy. In this thesis, because of the limited availability of the AC samples, tribological measurements were conducted only at one velocity. Moreover, samples from patients with early OA need to be tested, considering that the developed formulation is suggested as a treatment for them. This project used samples from patients with late OA, and therefore, those were deteriorated and not representative of the joints at the beginning of the disease.

In case natural tissues are not available, a careful selection of specimens for further tribological testing is essential to simulate the joints reliably. The first experimental chapters of this thesis were mainly focused on establishing NPs' proof of principle as lubricant additives by investigating the effect of mechanical properties (e.g. Young's modulus, surface roughness) on the CoF. Although contacting surfaces made of implant materials were chosen, their surface and mechanical properties were not identical to the human joints. For future investigations, selecting contact surfaces with properties identical to the joints is highly recommended to ensure the outcome of the

testing is indicative of the natural joints' behaviour. Moreover, it is important that the specimens are only used once to ensure their surface has not been affected and the results can be trusted. Selecting a tribometer capable of measuring the developed film thickness is also suggested because it will assist in better understanding the effect of the NPs formulations on the tribological behaviour of those systems.

Further optimisation of the formulation is also suggested. Cytotoxicity tests revealed the toxicity of the SDS to the cells. Therefore, the substitution of SDS with a non-toxic surfactant is necessary. Biopolymers like proteins or polysaccharides could be a good alternative. Polysaccharides could also be used to improve the viscoelasticity of the formulation. Although the stability of the NPs formulations was tested via size and Zeta Potential (ZP) measurements, it has not been observed over time, which is essential for the formulation's efficacy, especially in the case of commercialisation. Therefore, stability tests over time are recommended. Furthermore, modification of NPs surfaces needs to be considered to maximise their adsorption to the AC. Charging NPs surfaces would manipulate particle-AC interactions, increase NPs' adsorption, and, as shown in this thesis, increase CoF reduction.

The next step of this work could be the *in-vivo* evaluation of the therapeutic effect of the formulation. Tests could be applied on animals (e.g. rats) with an induced OA model. Following IAI treatment with the NPs formulation, an imaging technique like the X-Ray radiography can be employed to evaluate alterations in joint morphology (e.g. joint space width, osteophytes volume). Furthermore, histological evaluations could be utilised to identify signs of OA like erosions, and surface discontinuity, while immunohistochemical evaluations can quantify inflammation and Glycosaminoglycans

(GAGs) levels. Moreover, evaluating the drug release profile *in-vivo* is necessary to confirm the benefits of the NPs to the retention time. Those results will provide a good understanding of the formulation's therapeutic effect against OA and bring it closer to testing on humans.

Finally, developing measurement protocols for the mechanical properties of biological samples is challenging. Biological samples demonstrate wide variability in their properties, and as a result, measurement methods may work for some but not for all. The small quantity of the biological samples in combination with the large quantities required by conventional techniques limits the possible number of repetitions, and therefore, the reliability of the measurements. Therefore, the selection of specific methods, which require a small sample quantity and demonstrate high measurement sensitivity like the Atomic Force Microscopy (AFM), is suggested.

APPENDIX

This chapter provides data and calculations to help the reader understand further the claims made in the experimental chapters. Additionally, in A1 the ethical approval for examining human samples can be found.

A.1 Ethical declaration

The East of Scotland Research Ethics Service REC 2 has approved the examination of synovial fluid and articular cartilage samples from patients who underwent total arthroplasty for research purposes. The study took place at The Royal Orthopedic Hospital in Birmingham, UK. Each human sample was given a code to protect patients' identities. The ethical approval can be found below.

EoSRES

NHS SCOTLAND
Research Ethics Service

East of Scotland Research Ethics Service (EoSRES) REC 2
Tayside Medical Sciences Centre (TASC)
Residency Block C, Level 3
Ninewells Hospital & Medical School
George Pirie Way
Dundee DD1 9SY

Dr Simon W Jones
Senior Lecturer
University of Birmingham
School of Immunity and Infection, MRC-ARUK
Musculoskeletal Ageing Research
New Queen Elizabeth Hospital Research Laboratories
Mindelsohn Way
Edgbaston, Birmingham
B15 2TT

Date: 12 August 2014
Your Ref:
Our Ref: LR/**14/ES/1044**
Enquiries to: Mrs Lorraine Reilly
Direct Line: 01382 383878
Email: eosres.tayside@nhs.net

Dear Dr Jones

Study Title:	**Metabolic Mediators of Inflammation and their role in patholgical Joint Tissue Cross-Talk that Drives Osteoarthritis**
REC reference:	**14/ES/1044**
IRAS project ID:	**158458**

Thank you for your email of 08 August 2014, responding to the Committee's request for further information on the above research and submitting revised documentation.

The further information has been considered on behalf of the Committee by the Vice-Chair and Committee member.

We plan to publish your research summary wording for the above study on the HRA website, together with your contact details. Publication will be no earlier than three months from the date of this opinion letter. Should you wish to provide a substitute contact point, require further information, or wish to make a request to postpone publication, please contact the REC Manager, Mrs Lorraine Reilly, eosres.tayside@nhs.net.

Confirmation of ethical opinion

On behalf of the Committee, I am pleased to confirm a favourable ethical opinion for the above research on the basis described in the application form, protocol and supporting documentation as revised, subject to the conditions specified below.

Conditions of the favourable opinion

The favourable opinion is subject to the following conditions being met prior to the start of the study.

You should notify the REC in writing once all conditions have been met (except for site approvals from host organisations) and provide copies of any revised documentation with

POSITIVE ABOUT DISABLED PEOPLE

A.2 Supplementary data to Chapter 4

Effect of nanoparticle formulations on various contacting surfaces

Figure A.1 demonstrates that when contacting surfaces with low surface roughness were used (Glass, CoCr), nanoparticle (NPs) formulations were not always reducing the coefficient of friction (CoF). The formulations were either based on artificial synovial fluid (ASF) or phosphate-buffered saline (PBS).

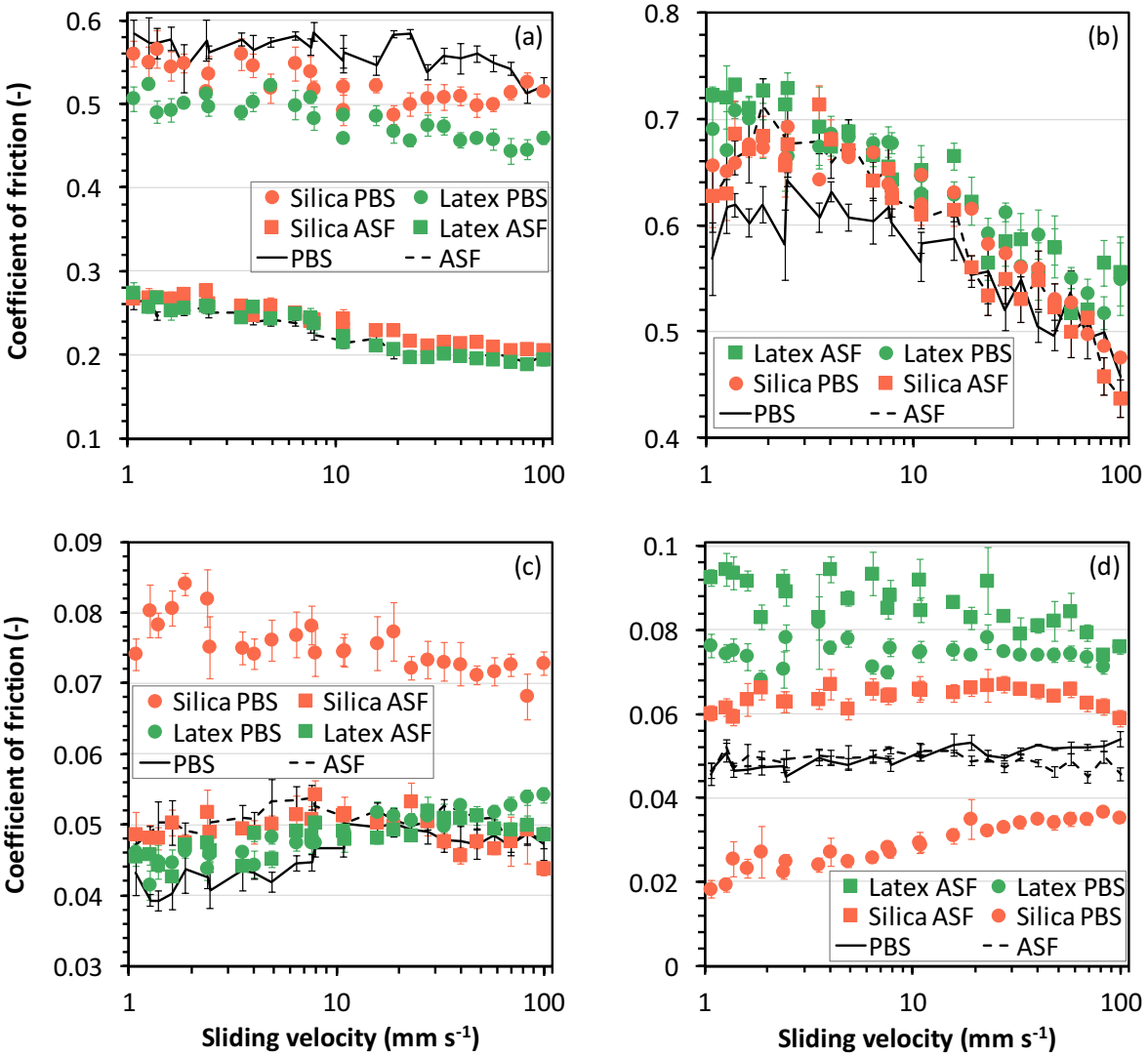


Figure A.1: CoF against sliding velocity of 0.1% silica/latex NPs formulations in PBS/ASF between (a) a steel ball and a CoCr disc, (b) a steel ball and a glass disc,

(c) a polyethylene (PE) ball and a CoCr disc, and (d). (c) a PE ball and a glass disc. Each data point is the average CoF of six repetitions of the same sample. The error bars represent their standard error.

A.3 Supplementary data to Chapter 5

Coverage of the nanoparticles from surfactant molecules

The coverage of NPs from SDS (Sodium dodecyl sulphate) molecules was calculated for the highest tested concentration of NPs (1% w/v) and the largest type of NPs, the Polycaprolactone (PCL). The assumptions made for the calculations are:

- Packing fraction of SDS heads is 100% because of their small size
- SDS molecules form a monolayer film around the NPs because they repel each other due to their anionic heads
- All NPs are equally covered with SDS
- NPs and SDS molecules are considered spherical
- The size of the SDS heads is the size of a micelle (e.g. average diameter: 3.75 nm)
- NPs size significantly larger (244 nm) than the size of SDS (3.75 nm)
- 15 ml of sample

The equations used to calculate NPs coverage by SDS are presented below. The volume occupied by one spherical particle/molecule is defined as:

$$V = \frac{4}{3}\,\pi\, r^3 \qquad \text{(A.1)}$$

where $\pi = 3.14$, and *r*: radius of the molecules (m). The surface area occupied by one particle/molecule is defined as:

$$A = 4\,\pi\,r^2 \tag{A.2}$$

where $\pi = 3.14$, and *r*: radius of the molecules (m). The number of a species (NPs, SDS molecule) in the suspension can be calculated as:

$$N = \frac{M}{\rho\,V} \tag{A.3}$$

where *M*: total mass of a species (g), ρ: density of a species (kg m^{-3}), and *V*: volume of one particle or molecule (m^3).

The total mass of the PCL (M_{PCL}) in 15ml of suspension with 1% w/v PCL is 0.15 g. The volume of one PCL NP was found 7.61 10^{-15} cm^3 using the equation (A.1) and its radius r_{PCL}=122 nm.

The number of PCL NPs in 15ml suspension was found N_{PCL}= 1.72 10^{13} using the equation (A.3), the total mass of PCL M_{PCL}=0.15 g, the density of ρ_{PCL}= 1.145 g cm^{-3}, and the volume of one PCL NP V_{PCL}=.7.61 10^{-15} cm^3.

The surface area covered by all the PCL NPs was found A_{PCL}= 32170.51 cm^2 by multiplying the equation (A.2) with the number of the PCL NPs N_{PCL}= 1.72 10^1 and utilising the radius of PCL NPs r_{PCL}=122 nm.

The surface area covered by one SDS molecule was found A_{SDS}= 4.42 10^{-13} cm^2 using the equation (A.2) and the radius of SDS r_{SDS}= 1.875 nm.

The number of the SDS molecules needed to cover the surface of all PCL NPs was evaluated by dividing the surface area covered by all the PCL NPs A_{PCL}= 32170.51 cm^2 with the surface area covered by one SDS molecule A_{SDS}= 4.42 10^{-13} cm^2. The SDS molecules needed to be were found 7.28 10^{16}.

The total mass of SDS (M_{SDS}) in 15ml of suspension with 0.5% w/v SDS is 0.075 g.

The volume of one SDS molecule was found 2.76 10^{-20} cm^3 using the equation (A.1) and the radius of the PCL r_{SDS}= 1.875 nm.

The number of SDS molecules that exist in the suspension was found 2.70 10^{18} using the equation (A.3), the total mass of SDS M_{SDS}= 0.075 g, the density of ρ_{SDS}= 1.0051 g cm^{-3} [506], and the volume of one SDS molecule V_{SDS}=.2.76 10^{-20} cm^3.

The number of the SDS molecules exist in the suspension (2.70 10^{18}) was found larger than the number of the SDS molecules needed to cover the surface of all PCL NPs (7.28 10^{16}). Therefore, 0.5% w/v of SDS is sufficient and, as such, all other kinds and concentrations of NPs.

Volume fraction of nanoparticles in formulation

The volume fraction (φ) is the percentage of the volume concentration (ϕ), which is defined as:

$$\phi = \frac{w\,\rho_w}{\left(1-\frac{w}{100}\right)\rho_p + \left(\frac{w}{100}\,\rho_w\right)} \qquad \text{(A.4)}$$

where w: weight concentration (0.5%), and $\rho_{w,p}$: density of water, particles (kg m^{-3}) [507]. The volume fraction of the NPs formulations was calculated using the density of

the NPs in **Table 5.1** and the density of the water (ρ_w=1190 kg m^{-3}). The volume fractions of the NPs formulations are presented in **Table A.1**.

Table A.1: Volume fraction of Polymethylmethacrylate (PMMA), Polycaprolactone (PCL), and Polylactic acid (PLA) nanoparticle suspensions.

NPs formulations	PMMA	PCL	PLA
φ 10^{-3} (%)	4.2	4.4	4.0

Effect of formulation's components on viscosity

Figure A.2 shows that hyaluronic acid (HA) significantly increased the viscosity of the Phosphate-buffered saline (PBS) formulations by approximately 522%, whereas the SDS effect on viscosity is minimal.

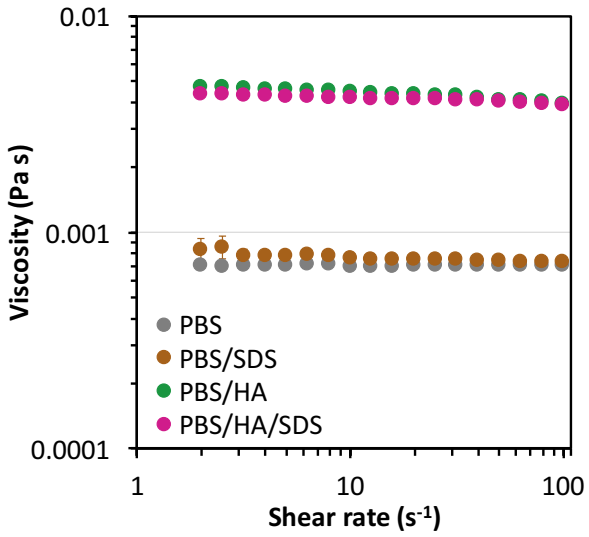


Figure A.2: Effect of SDS (0.5%) and HA (0.1%) on the viscosity of PBS at 37°C. Each data point is the average viscosity value of three repetitions of the same sample. The error bars represent their standard error.

Fitting of nanoparticle formulations frictional behaviour

The frictional behaviour of the NPs formulations in the Steel-SE tribopair fitted well (R^2: 0.90-0.96) with the random forest algorithm. As described in chapter 4, the random forest algorithm fits well the frictional behaviour of the Steel-SE configuration. The R^2 and the Correlation Coefficients between the CoF and the sliding velocity ($CC_{cof\text{-}vel}$) for each formulation are presented in **Table A.2**. The negative $CC_{cof\text{-}vel}$ values represent the slope of the curves and denote the negative correlation of the CoF with the sliding velocity. The more negative the $CC_{cof\text{-}vel}$, the steeper the decrease of CoF. As such, PBS demonstrated the steepest decrease in CoF, followed by PLA, PMMA and PCL formulations. The CoF in the PCL formulation was almost stable with the sliding velocity, as confirmed by the weak $CC_{cof\text{-}vel}$. The small CoF reduction provided by the PCL formulation could be ascribed to its aggregation within the suspension (**Figure 5.1a** and **5.1b).** The size of the PCL NPs (435.60 ± 6.25 nm) was notably larger than the surface roughness of the SE (94.35 ± 21 nm), and when those deposited to the surface, they could have increased its surface roughness and inhibited the flow of the lubricant [410].

Table A.2: Fitting of the tribological performance of the PMMA, PCL, and PLA nanoparticle formulations with the random forest algorithm.

Formulation	R^2 (-)	$CC_{cof\text{-}vel}$ 10^{-2} (-)
PBS	0.96	-1.5
PMMA	0.90	-0.7
PCL	0.90	-0.6
PLA	0.95	-0.8

A.4 Supplementary data to Chapter 6

SAM characterisation

David Burgess carried out SAM characterisation. The SAM was characterised using ellipsometry (alpha-SE, J.A. Woollam, USA) and a goniometer (Contact Angle Goniometer, Ossila, UK). The SAM was tested fresh after its preparation, after Hydrochloric acid treatment, and after cleaning. The Hydrochloric acid treatment included ten minutes' immersion of the SAM in HCl (0.5 M) to hydrolyse the methoxide groups leaving the surface more hydrophilic. Cleaning of the SAM was done with UV-Ozone treatment. The characterisation of the SAM is summarised in **Table A.3**.

Table A.3: Contact angle and thickness of the self-assembled monolayer.

Treatment	Contact angle (°)	Ellipsometric layer thickness (nm)
Fresh	66 ± 1	0.28 ± 0.11
Hydrochloric acid treated	56 ± 3	-
Cleaned	-	0.82 ± 0.09

The fresh SAM was hydrophobic (66 ± 1°) as expected because of the presence of ester and methyl groups. The layer thickness of 0.28 ± 0.11 nm was in the expected range because the alkyl chains/ molecules were most likely not in an organised 'stood up' arrangement due to the short-chain length [508]. Following the treatment with HCl, the surface of SAM became more hydrophilic (56 ± 3°) because of the presence of hydroxyl groups. Although only a small proportion of the ester groups were expected to be hydrolysed due to the short reaction time (reaction requires a few hours), the increased hydrophilicity is evidence of the existance of the silane monolayer. Finally, according to the ellipsometry data, the cleaning procedure failed to remove the silane

layer. The layer became thicker (0.82 ± 0.09 nm versus 0.28 ± 0.11 nm), probably due to a cross-linking reaction.

In-vitro drug release evaluation

Piaopiao Pan (Guangzhou University of Chinese Medicine in China) performed the *in-vitro* drug release evaluation of the NPs in a shaker (60 rpm, 37ºC). Free Celecoxib and drug-loaded (DL) NPs were placed into a dialysis bag (molecular weight cutoff, 8000-14000), which contained 1 mL 0.1% w/v HA. Afterwards, the dialysis bag was placed into a 15 ml tube containing 10 ml PBS with 0.5% w/v SDS release medium at 37^{o}C. After a fixed time, medium (0.5 ml) was removed and substituted by PBS solution (0.5 ml). The quantity of the Celecoxib, which was released was measured by High Performance Liquid Chromatography (HPLC) (Thermo Scientific, America).

Figure A.3 displays the release profiles of the free Celecoxib and Celecoxib-loaded NPs. The accumulated Celecoxib without a carrier demonstrated a rapid and almost complete release (94.6%) within 2 h, confirming the literature [505]. The burst release is typical for the active compounds administrated in the joint cavity with no delivery system [462]. Celecoxib-loaded-NPs exhibited a rapid release within 24 h, and a slower and more stable release was followed. The biphasic drug release behaviour is related to the release of the drug from the surface (burst effect) and the core (slower release) of the NPs, respectively and is common when NPs are the drug delivery system [418]. The Celecoxib-loaded-NPs demonstrated sustained-release compared to the free Celecoxib (**Figure A.1**). It is believed that the HA acts as a physical barrier entrapping the drug inside the SDS-coated NPs. HA conjugates extend the retention time for NPs delivery systems as reported multiple times before [285, 502, 503]. When

PLA and PCL were used as nanocarriers, 76.8% and 78.1% of Celecoxib was released within 24 h and 80.4% and 83.6% within 9 days, respectively, demonstrated a sustained-release effect. However, when PMMA NPs were employed, only 48% of Celecoxib was released in 9 days, indicating a low drug-release rate. The incomplete drug-release of the PMMA has been previously reported and related to its high hydrophobicity and low diffusivity [418]. PMMA hydrophilicity diminishes its swollen capacity and induces its dissolution/degradation in the presence of water [500]. Besides, the low mobility chains limit the available for the diffusion volume of the drug within the PMMA and thus, resulting in low drug diffusivity [501].

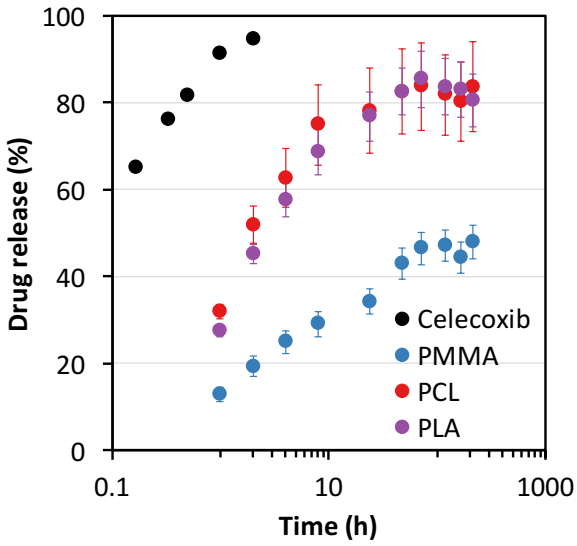


Figure A.3: Cumulative release profile of free Celecoxib, Celecoxib-loaded PCL, PLA, and PMMA NPs. Each data point represents the average drug release of three different samples taken from the same dialysis bag. The error bars represent their standard error.

Cytotoxicity of nanoparticle formulations on fibroblasts

The cytotoxicity of nanoparticles was tested on fibroblasts (**Figure A.4)** and demonstrated similar results to the synovial chondrocytes (**Figure 6.10**).

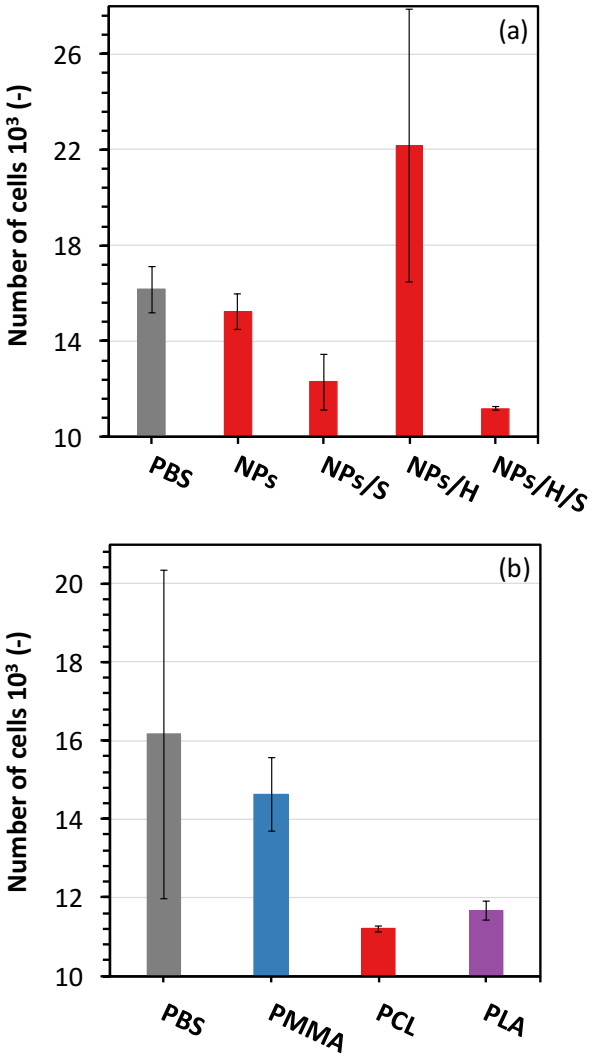


Figure A.4: Cytotoxicity of fibroblasts after five days of incubation with (a) different components of the formulation, and (b) formulations with different types of DL-NPs. The formulations in (b) consisted of DL-NPs (0.5%)/HA(H) (0.1%)/SDS(S) (0.5%) in PBS. DL-PCL, DL-PLA, and DL-PMMA NPs were used. Each bar represents the average number of live cells from three wells seeded with the same sample. The error bars represent their standard error.

LIST OF REFERENCES

1. *Osteoarthritis - level 3 cause*, in *Global Burden of Disease study*. 2019, Institute for Health Metrics and Evaluation: Washington, USA.
2. *What is Arthritis?*, ed. A.R. UK. 2012, Scotland: Arthritis Research UK.
3. Stolz, M., et al., *Erratum: Early detection of aging cartilage and osteoarthritis in mice and patient samples using atomic force microscopy.* Nat. Nanotechnol., 2010. **5**: p. 821.
4. Hani, A., et al., *Non-invasive and in vivo assessment of osteoarthritic articular cartilage: a review on mri investigations.* Rheumatol. Int., 2015. **35**(1): p. 1-16.
5. Nikahval, B., et al., *Comparison of radiographic and magnetic resonance imaging findings of early osteoarthritis of the rabbit knees: an experimental study.* Comp. Clin. Pathol., 2012. **21**(6): p. 1451-1456.
6. Knecht, S., B. Vanwanseele, and E. Stüssi, *A review on the mechanical quality of articular cartilage – Implications for the diagnosis of osteoarthritis.* Clin. Biomech., 2006. **21**(10): p. 999-1012.
7. Evans, C., V. Kraus, and L. Setton, *Progress in intra-articular therapy.* Nat. Rev. Rheumatol., 2014. **10**(1): p. 11-22.
8. Heuberger, M., et al., *Protein-mediated boundary lubrication in arthroplasty.* Biomaterials, 2005. **26**(10): p. 1165-1173.
9. Zhang, Z., D. Simionesie, and C. Schaschke, *Graphite and hybrid nanomaterials as lubricant additives.* Lubricants, 2014. **2**(2): p. 44-65.
10. Gulzar, M., et al., *Tribological performance of nanoparticles as lubricating oil additives.* J. Nanopart. Res., 2016. **18**(8): p. 1-25.
11. Waqas, M., et al., *A review of friction performance of lubricants with nano additives.* Materials, 2021. **14**(21): p. 6310.
12. Sui, T., et al., *Study on lubrication and friction reduction properties of ZIF-8 nanoparticles as Si3N4 ceramic water lubrication additives.* Front. Chem., 2021. **9**.
13. Cui, Y., et al., *Role of nanoparticle materials as water-based lubricant additives for ceramics.* Tribol. Int., 2020. **142**: p. 105978.
14. Evangelou, E., et al., *A meta-analysis of genome-wide association studies identifies novel variants associated with osteoarthritis of the hip.* Ann. Rheum. Dis., 2014. **73**(12): p. 2130-6.
15. Jain, A., et al., *Targeting of diacerein loaded lipid nanoparticles to intra-articular cartilage using chondroitin sulfate as homing carrier for treatment of osteoarthritis in rats.* Nanomedicine, 2014. **10**(5).
16. Fernández-Moreno, M., et al., *Genetics in osteoarthritis.* Curr. Genomics, 2008. **9**(8): p. 542-547.
17. Fernández-Puente, P., et al., *Multiplexed mass spectrometry monitoring of biomarker candidates for osteoarthritis.* J. Proteomics, 2017. **152**: p. 216-225.
18. Marjanovic, N., et al., *Design of modern concept tribometer with circular and reciprocating movement.* Tribol. Ind., 2006. **28**(3-4): p. 3-8.
19. Jackson, M. and J. Morrell, *5 - Tribology in manufacturing*, in *Tribology for Engineers*, J.P. Davim, Editor. 2011, Woodhead Publishing. p. 161-241.
20. Podgornik, B. and J. Vižintin, *Tribology of thin films and their use in the field of machine elements.* Vacuum, 2002. **68**(1): p. 39-47.

21. Holmberg, K. and A. Erdemir, *Influence of tribology on global energy consumption, costs and emissions.* Friction, 2017. **5**(3): p. 263-284.
22. Katiyar, J., et al., *Automotive tribology*. 2019: Springer.
23. Blau, P.J., *Elevated-temperature tribology of metallic materials.* Tribol. Int., 2010. **43**(7): p. 1203-1208.
24. Affatato, S. and F. Traina, *6 - Bio and medical tribology*, in *Tribology for Engineers*, J.P. Davim, Editor. 2011, Woodhead Publishing. p. 243-286.
25. Dowson, D., *Bio-tribology.* Faraday Discuss., 2012. **156**(1): p. 9-30.
26. Wong, B., et al., *Cartilage shear dynamics during tibio-femoral articulation: effect of acute joint injury and tribosupplementation on synovial fluid lubrication.* Osteoarthr. Cartil., 2010. **18**(3): p. 464-471.
27. Jiménez, A. and M. Bermúdez, *2 - Friction and wear*, in *Tribology for Engineers*, J.P. Davim, Editor. 2011, Woodhead Publishing. p. 33-63.
28. Jason, Y., et al., *A study on the tribological performance of nanolubricants.* Processes, 2020. **8**(11): p. 1372-1405.
29. Chan, S., et al., *Atomic force microscope investigation of the boundary-lubricant layer in articular cartilage.* Osteoarthr. Cartil., 2010. **18**(7): p. 956-63.
30. Burstein, L., I. Technion, and I. Haifa, *Lubrication and roughness*, in *Tribology for Engineers*, J.P. Davim, Editor. 2011, Elsevier: Tribology for engineers: A practical guide. .
31. Park, J., et al., *Effects of hyaluronic acid and γ–globulin concentrations on the frictional response of human osteoarthritic articular cartilage.* PLoS ONE, 2014. **9**(11).
32. Wimmer, M., T. Schmid, and J. Jacobs, *Tribology: a portal to understand joint failure?* Arthritis Rheum., 2007. **56**(11): p. 3511-3.
33. Niu, H.-j., et al., *Ultrasonic reflection coefficient and surface roughness index of osteoarthritic articular cartilage: relation to pathological assessment.* BMC Musculoskeletal Disord., 2012. **13**: p. 34-34.
34. Maerz, T., et al., *Surface roughness and thickness analysis of contrast-enhanced articular cartilage using mesh parameterization.* Osteoarthr. Cartil., 2016. **24**(2): p. 290-298.
35. McNary, S., K. Athanasiou, and A. Reddi, *Engineering lubrication in articular cartilage.* Tissue Eng., Part B, 2012. **18**(2): p. 88-100.
36. Kienle, S., et al., *Comparison of friction and wear of articular cartilage on different length scales.* J. Biomech., 2015. **48**(12): p. 3052-3058.
37. Pavkovič, D., N. Kranjčevič, and M. Kostelac, *Design of normal force control system for a pin-on-disk tribometer including active and passive suppression of vertical vibrations.* Automatika, 2013. **54** (3): p. 364-375.
38. Soltani, M., et al., *A comparative investigation on the tribological performance and physicochemical properties of biolubricants of various sources, a petroleum-based lubricant, and blends of the petroleum-based lubricant and crambe oil.* Tribol. Trans., 2020. **63**(6): p. 1121-1134.
39. Maru, M. and D. Tanaka, *Consideration of stribeck diagram parameters in the investigation on wear and friction behavior in lubricated sliding.* J. Braz. Soc. Mech. Sci. Eng., 2007. **29**(1): p. 55-62.
40. Deepika, *Nanotechnology implications for high performance lubricants.* SN Appl. Sci., 2020. **2**(6): p. 1128.

41. Minami, I., *Molecular science of lubricant additives.* Appl. Sci., 2017. **7**(5): p. 445.
42. Stachowiak, G. and A. Batchelor, *Engineering tribology*. 2013: Butterworth-heinemann.
43. Dorinson, A. and K. Ludema, *Mechanics and chemistry in lubrication*. Vol. 9. 1985, Amsterdam, The Netherlands: Elsevier.
44. Michael, J., *Covitch viscosity index additives* in *Encyclopedia of Tribology*, Q. Wang, Chung, YW, Eds, Editor. 2013, Springer: New York, USA.
45. Chan, C., et al., *Tribological behavior of biolubricant base stocks and additives.* Renewable Sustainable Energy Rev., 2018. **93**: p. 145-157.
46. Papay, A., *Antiwear and extreme-pressure additives in lubricants.* Lubr. Sci., 1998. **10**(3): p. 209-224.
47. Rizwan, M., et al., *Chapter 3 - Types and classification of nanomaterials*, in *Nanomaterials: synthesis, characterization, hazards and safety*, M. Tahir, M. Sagir, and A. Asiri, Editors. 2021, Elsevier. p. 31-54.
48. Saleh, T., *Nanomaterials: classification, properties, and environmental toxicities.* Environ. Technol. Innovation, 2020. **20**: p. 101067.
49. Buzea, C., I. Pacheco, and K. Robbie, *Nanomaterials and nanoparticles: sources and toxicity.* Biointerphases, 2007. **2**(4).
50. Rasheed, A., et al., *Graphene based nanofluids and nanolubricants–review of recent developments.* Renewable Sustainable Energy Rev., 2016. **63**: p. 346-362.
51. Bowden, F. and D. Tabor, *The friction and lubrication of solids*. Vol. 1. 2001: Oxford university press.
52. Huang, H., et al., *An investigation on tribological properties of graphite nanosheets as oil additive.* Wear, 2006. **261**(2): p. 140-144.
53. Joly-Pottuz, L., et al., *Ultralow-friction and wear properties of if-ws 2 under boundary lubrication.* Tribol. Lett., 2005. **18**(4): p. 477-485.
54. Spikes, H.A., *Friction modifier additives.* Tribol. Lett., 2015. **60**(1): p. 5.
55. Martin, J. and N. Ohmae, *Nanolubricants*. Vol. 13. 2008: John Wiley & Sons.
56. Wright, R., et al., *Oil-soluble polymer brush grafted nanoparticles as effective lubricant additives for friction and wear reduction.* Angew. Chem., 2016. **128**(30): p. 8798-8802.
57. Gulzar, M., et al., *Tribological performance of nanoparticles as lubricating oil additives.* J. Nanopart. Res., 2016. **18**(8): p. 223.
58. Sui, T., et al., *Effect of particle size and ligand on the tribological properties of amino functionalized hairy silica nanoparticles as an additive to polyalphaolefin.* Journal of nanomaterials, 2015. **2015**: p. 1-9.
59. Sui, T., et al., *Bifunctional hairy silica nanoparticles as high-performance additives for lubricant.* Sci. Rep., 2016. **6**(1): p. 1-9.
60. Chen, Y., et al., *Preparation of nickel-based nanolubricants via a facile in situ one-step route and investigation of their tribological properties.* Tribol. Lett., 2013. **51**(1): p. 73-83.
61. Dai, W., et al., *Roles of nanoparticles in oil lubrication.* Tribol. Int., 2016. **102**: p. 88-98.
62. Stachowiak, G. and A. Batchelor, *Experimental methods in tribology*. Vol. 44. 2004, Amsterdam, The Netherlands: Elsevier.

63. Lee, S., et al., *Frictional response of normal and osteoarthritic articular cartilage in human femoral head.* Proc. Inst. Mech. Eng., Part H, 2012. **227**(2): p. 129-137.
64. Han, L., A. Grodzinsky, and C. Ortiz, *Nanomechanics of the cartilage extracellular matrix.* Annu. Rev. Mater. Res., 2011. **41**: p. 133-168.
65. Chen, Y., et al., *Microrheology of human synovial fluid of arthritis patients studied by diffusing wave spectroscopy.* J. Biophotonics, 2012. **5**(10): p. 777-84.
66. Li, G., et al., *Subchondral bone in osteoarthritis: insight into risk factors and microstructural changes.* Arthritis Res. Ther., 2013. **15**(6): p. 223.
67. Donell, S., *Subchondral bone remodelling in osteoarthritis.* Efort Open Rev., 2019. **4**(6): p. 221-229.
68. Michaeli, D. *Does running actually cause knee osteoarthritis?* 2017 [cited 2022 14/03]; Available from: https://thedoctorweighsin.com/does-running-actually-cause-knee-osteoarthritis/.
69. Lu, X. and V. Mow, *Biomechanics of articular cartilage and determination of material properties.* Med. Sci. Sports Exercise, 2008. **40**(2): p. 193-9.
70. Fox, S., A. Bedi, and S.A. Rodeo, *The basic science of articular cartilage: structure, composition, and function.* Sports Health, 2009. **1**(6): p. 461-8.
71. Bhosale, A. and J. Richardson, *Articular cartilage: structure, injuries and review of management.* Br. Med. Bull., 2008. **87**(1): p. 77-95.
72. Mitani, Y., A. Honda, and H. Jasin, *Polymorphonuclear leukocyte adhesion to articular cartilage is inhibited by cartilage surface macromolecules.* Rheumatol. Int., 2001. **20**(5): p. 180-5.
73. Wang, M. and Z. Peng, *Wear in human knees.* Biosurf. Biotribol., 2015. **1**(2): p. 98-112.
74. Duan, Y., et al., *Insight into the tribological behavior of liposomes in artificial joints.* Langmuir, 2016. **32**(42): p. 10957-10966.
75. Aae, T.F., et al., *Norwegican cartilage project - a study protocol for a double-blinded randomized controlled trial comparing arthroscopic microfracture with arthroscopic debridement in focal cartilage defects in the knee.* BMC Musculoskelet. Disord., 2016. **17**: p. 292.
76. Goudoulas, T., et al., *Rheological study of synovial fluid obtained from dogs: healthy, pathological, and post-surgery, after spontaneous rupture of cranial cruciate ligament.* Ann. Biomed. Eng., 2010. **38**(1): p. 57-65.
77. Fox, S., A. Bedi, and S. Rodeo, *The basic science of articular cartilage: structure, composition, and function.* Sports Health, 2009. **1**(6): p. 461-8.
78. Fan, J., et al., *Synovial fluid lubrication of artificial joints: protein film formation and composition.* Faraday Discuss., 2012. **156**(0): p. 69-85.
79. Dintenfass, L., *Lubrication in Synovial Joints.* Nature, 1963. **197**(4866): p. 496-497.
80. Singh, N., *Synovial joints and lubrication mechanisms.* Int. J. Comput. Appl. Math., 2017. **12**(1): p. 23-33.
81. Ateshian, G., *The role of interstitial fluid pressurization in articular cartilage lubrication.* J. Biomech., 2009. **42**(9): p. 1163-76.
82. Park, S., et al., *Cartilage interstitial fluid load support in unconfined compression.* J. Biomech., 2003. **36**(12): p. 1785-1796.

83. Mirea, D., et al., *Role of the biomolecular interactions in the structure and tribological properties of synovial fluid.* Tribol. Int., 2013. **59**: p. 302-311.
84. Mavraki, A. and P. Cann, *Friction and lubricant film thickness measurements on simulated synovial fluids.* Proc. Inst. Mech. Eng., Part J, 2009. **223**(3): p. 325-335.
85. Chen, M., et al., *Lubrication at physiological pressures by polyzwitterionic brushes.* Science, 2009. **323**(5922): p. 1698-1701.
86. Jahn, S. and J. Klein, *Hydration lubrication: the macromolecular domain.* Macromolecules, 2015. **48**(15): p. 5059-5075.
87. Parkes, M., et al., *Tribology-optimised silk protein hydrogels for articular cartilage repair.* Tribol. Int., 2015. **89**: p. 9-18.
88. Krishnan, R., M. Kopacz, and G. Ateshian, *Experimental verification of the role of interstitial fluid pressurization in cartilage lubrication.* J. Orthop. Res., 2004. **22**(3): p. 565-570.
89. Caligaris, M. and G. Ateshian, *Effects of sustained interstitial fluid pressurization under migrating contact area, and boundary lubrication by synovial fluid, on cartilage friction.* Osteoarthr. Cartil., 2008. **16**(10): p. 1220-1227.
90. Ateshian, G. and H. Wang, *Rolling resistance of articular cartilage due to interstitial fluid flow.* Proc. Inst. Mech. Eng., Part H, 1997. **211**(5): p. 419-424.
91. Chan, S., et al., *Dependence of nanoscale friction and adhesion properties of articular cartilage on contact load.* J. Biomech., 2011. **44**(7): p. 1340-1345.
92. Niu, H., et al., *Relationship between triphasic mechanical properties of articular cartilage and osteoarthritic grade.* Sci. China: Life Sci., 2012. **55**(5): p. 444-451.
93. Wu, C., *Micro/nano-mechanics of cartilage with osteoarthritis*, in *HKU Theses Online (HKUTO)*. 2011, The University of Hong Kong (Pokfulam, Hong Kong).
94. Guidolin, D. and F. Franceschi, *Viscosupplementation with high molecular weight native hyaluronan. Focus on a 1500-2000 KDa fraction (Hyalubrix(R)).* Eur. Rev. Med. Pharmacol. Sci. , 2014. **18**(21): p. 3326-38.
95. Madkhali, A., et al., *Osteoarthritic synovial fluid and correlations with protein concentration.* Biorheology, 2016. **53**(3-4): p. 123-136.
96. Falcone, S., D. Palmeri, and R. Berg, *Rheological and cohesive properties of hyaluronic acid.* J. Biomed. Mater. Res., Part A, 2006. **76**(4): p. 721-8.
97. Zhang, Z. and G. Christopher, *The nonlinear viscoelasticity of hyaluronic acid and its role in joint lubrication.* Soft Matter, 2015. **11**(13): p. 2596-603.
98. Guillaumie, F., et al., *Comparative studies of various hyaluronic acids produced by microbial fermentation for potential topical ophthalmic applications.* J. Biomed. Mater. Res., Part A, 2010. **92**(4): p. 1421-30.
99. Madkhali, A., et al., *Osteoarthritic synovial fluid rheology and correlations with protein concentration.* Biorheology, 2016. **53**(3-4): p. 111-122.
100. Tadmor, R., N. Chen, and J. Israelachvili, *Thin film rheology and lubricity of hyaluronic acid solutions at a normal physiological concentration.* J. Biomed. Mater. Res., 2002. **61**(4): p. 514-523.
101. Tadmor, R., N. Chen, and J. Israelachvili, *Normal and shear forces between mica and model membrane surfaces with adsorbed hyaluronan.* Macromolecules, 2003. **36**(25): p. 9519-9526.
102. Benz, M., N. Chen, and J. Israelachvili, *Lubrication and wear properties of grafted polyelectrolytes, hyaluronan and hylan, measured in the surface forces apparatus.* J. Biomed. Mater. Res., Part A, 2004. **71**(1): p. 6-15.

103. Seror, J., et al., *Supramolecular synergy in the boundary lubrication of synovial joints.* Nat. Commun., 2015. **6**(1): p. 6497-6497.
104. Lin, W., et al., *The role of hyaluronic acid in cartilage boundary lubrication.* Cells, 2020. **9**(7): p. 1606.
105. Kosinska, M., et al., *Articular joint lubricants during osteoarthritis and rheumatoid arthritis display altered levels and molecular species.* Plos One, 2015. **10**(5).
106. Bothner, H. and O. Wik, *Rheology of Hyaluronate.* Acta Oto-Laryngol., 1987. **104**(sup442): p. 25-30.
107. Seror, J., et al., *Articular cartilage proteoglycans as boundary lubricants: structure and frictional interaction of surface-attached hyaluronan and hyaluronan–aggrecan complexes.* Biomacromolecules, 2011. **12**(10): p. 3432-3443.
108. Jay, G. and K. Waller, *The biology of lubricin: near frictionless joint motion.* Matrix Biol., 2014. **39**: p. 17-24.
109. Jay, G., et al., *The role of lubricin in the mechanical behavior of synovial fluid.* Proc. Natl. Acad. Sci. U. S. A., 2007. **104**(15): p. 6194-9.
110. Zappone, B., et al., *Adsorption, lubrication, and wear of lubricin on model surfaces: polymer brush-like behavior of a glycoprotein.* Biophys. J., 2007. **92**(5): p. 1693-1708.
111. Bayer, I., *Advances in tribology of lubricin and lubricin-like synthetic polymer nanostructures.* Lubricants, 2018. **6**(2): p. 30.
112. Winchester, R., V. Agnello, and H. Kunkel, *Gamma globulin complexes in synovial fluids of patients with rheumatoid arthritis. Partial characterization and relationship to lowered complement levels.* Clin. Exp. Immunol., 1970. **6**(5): p. 689-706.
113. *Human Gamma Globulin*. Chemicals [cited 2022 21/03]; Available from: https://www.scbt.com/p/np-hgg-human-gamma-globulin.
114. Briere, L., J. Brandt, and J. Medley, *Measurement of protein denaturation in human synovial fluid and its analogs using differential scanning calorimetry.* J. Therm. Anal. Calorim., 2010. **102**(1): p. 99-106.
115. *PubChem compound summary for CID 16132389, serum albumin (1-24)*. Compound summary 2007 [cited 2022 21/03]; Available from: https://pubchem.ncbi.nlm.nih.gov/compound/Serum-albumin-_1-24.
116. Gale, L., et al., *Boundary lubrication of joints: characterization of surface-active phospholipids found on retrieved implants.* Acta Orthop., 2007. **78**(3): p. 309-14.
117. Raj, A., et al., *Lubrication synergy: mixture of hyaluronan and dipalmitoylphosphatidylcholine vesicles.* J. Colloid Interface Sci., 2017. **488**: p. 225-233.
118. Mreła, A. and Z. Pawlak, *Articular cartilage: amphoteric nature and interfacial energy.* J. Clin. Mol. Med.. 2018. **1**: p. 1-2.
119. Zhang, Y. and J. Jordan, *Epidemiology of Osteoarthritis.* Clin. Geriatr. Med., 2010. **26**(3): p. 355-369.
120. Loeser, R., *The role of aging in the development of osteoarthritis.* Trans. Am. Clin. Climatol. Assoc., 2017. **128**: p. 44.
121. Buckwalter, J., C. Saltzman, and T. Brown, *The impact of osteoarthritis: implications for research.* Clin. Orthop. Relat. Res., 2004(427 Suppl): p. S6-15.

122. Felson, D., *Osteoarthritis as a disease of mechanics.* Osteoarthr. Cartil., 2013. **21**(1): p. 10-5.
123. Regan, E., R. Bowler, and J. Crapo, *Joint fluid antioxidants are decreased in osteoarthritic joints compared to joints with macroscopically intact cartilage and subacute injury.* Osteoarthr. Cartil., 2008. **16**(4): p. 515-21.
124. Brandt, K., et al., *Yet more evidence that osteoarthritis is not a cartilage disease*. 2006, BMJ Publishing Group Ltd.
125. MacMullan, P., G. McMahon, and G. McCarthy, *Detection of basic calcium phosphate crystals in osteoarthritis.* Jt., Bone, Spine, 2011. **78**(4): p. 358-63.
126. Imer, R., et al., *Development of atomic force microscope for arthroscopic knee cartilage inspection.* Jpn. J. Appl. Phys., 2006. **45**(3S): p. 2319.
127. Toda, Y., et al., *Change in body fat, but not body weight or metabolic correlates of obesity, is related to symptomatic relief of obese patients with knee osteoarthritis after a weight control program.* J. Rheumatol., 1998. **25**(11): p. 2181-6.
128. Desrochers, J., M. Amrein, and J. Matyas, *Microscale surface friction of articular cartilage in early osteoarthritis.* J. Mech. Behav. Biomed. Mater., 2013. **25**: p. 11-22.
129. Huang, K. and L. Wu, *Aggrecanase and aggrecan degradation in osteoarthritis: a review.* J. Int. Med. Res., 2008. **36**(6): p. 1149-1160.
130. Moshtagh, P., et al., *Micro- and nano-mechanics of osteoarthritic cartilage: The effects of tonicity and disease severity.* J. Mech. Behav. Biomed. Mater., 2016. **59**: p. 561-571.
131. Adam, N. and P. Ghosh, *Hyaluronan molecular weight and polydispersity in some commercial intra-articular injectable preparations and in synovial fluid.* Inflammation Res., 2001. **50**(6): p. 294-9.
132. Mazzucco, D., R. Scott, and M. Spector, *Composition of joint fluid in patients undergoing total knee replacement and revision arthroplasty: correlation with flow properties.* Biomaterials, 2004. **25**(18): p. 4433-4445.
133. Temple-Wong, M., et al., *Hyaluronan concentration and size distribution in human knee synovial fluid: variations with age and cartilage degeneration.* Arthritis Res. Ther., 2016. **18**: p. 18-18.
134. Lin, W. and J. Klein, *Recent progress in cartilage lubrication.* Adv. Mater., 2021. **33**(18): p. 2005513.
135. Wang, M. and Z. Peng, *Investigation of the nano-mechanical properties and surface topographies of wear particles and human knee cartilages.* Wear, 2015. **324-325**: p. 74-79.
136. Khalili, A. and M. Ahmad, *A review of cell adhesion studies for biomedical and biological applications.* IInt. J. Mol. Sci., 2015. **16**(8): p. 18149-18184.
137. Rojas, F., et al., *Molecular adhesion between cartilage extracellular matrix macromolecules.* Biomacromolecules, 2014. **15**(3): p. 772-780.
138. Schett, G., et al., *Vascular cell adhesion molecule 1 as a predictor of severe osteoarthritis of the hip and knee joints.* Arthritis Rheum., 2009. **60**(8): p. 2381-2389.
139. Wang, M., et al., *Study of the nano-mechanical properties of human knee cartilage in different wear conditions.* Wear, 2013. **301**(1–2): p. 188-191.

140. Soltes, L., et al., *Solution properties of high-molar-mass hyaluronans: the biopolymer degradation by ascorbate.* Carbohydr. Res., 2007. **342**(8): p. 1071-7.
141. Cooke, A., D. Dowson, and V. Wright, *The rheology of synovial fluid and some potential synthetic lubricants for degenerate synovial joints.* Eng. Med. , 1978. **7**(2): p. 66-72.
142. Rainer, F. and V. Ribitsch, *Viscoelastic properties of normal human synovia and their relation to biomechanics.* Z. Rheumatol., 1985. **44**(3): p. 114-119.
143. Bagga, H., et al., *Longterm effects of intraarticular hyaluronan on synovial fluid in osteoarthritis of the knee.* J. Rheumatol., 2006. **33**(5): p. 946-50.
144. Felson, D., et al., *The prevalence of knee osteoarthritis in the elderly. The Framingham osteoarthritis study.* Arthritis Rheum., 1987. **30**(8): p. 914-8.
145. Guerne, P., et al., *Growth factor responsiveness of human articular chondrocytes in aging and development.* Arthritis Rheumatol., 1995. **38**(7): p. 960-8.
146. Carlo, M. and R. Loeser, *Increased oxidative stress with aging reduces chondrocyte survival: correlation with intracellular glutathione levels.* Arthritis Rheumatol., 2003. **48**(12): p. 3419-30.
147. Dimock, A., P. Siciliano, and C. McIlwraith, *Evidence supporting an increased presence of reactive oxygen species in the diseased equine joint.* Equine Vet. J., 2000. **32**(5): p. 439-43.
148. Campisi, J., *Senescent cells, tumor suppression, and organismal aging: good citizens, bad neighbors.* Cell, 2005. **120**(4): p. 513-22.
149. Anderson, A. and R. FL., *Why is osteoarthritis an age-related disease?* Best Pract. Res., Clin. Rheumatol., 2010. **24**(1): p. 15-26.
150. Zamli, Z. and M. Sharif, *Chondrocyte apoptosis: a cause or consequence of osteoarthritis?* Int. J. Rheum. Dis., 2011. **14**(2): p. 159-66.
151. Grushko, G., R. Schneiderman, and A. Maroudas, *Some biochemical and biophysical parameters for the study of the pathogenesis of osteoarthritis: a comparison between the processes of ageing and degeneration in human hip cartilage.* Connect. Tissue Res., 1989. **19**(2-4): p. 149-76.
152. Noble, P., et al., *An equine joint friction test model using a cartilage-on-cartilage arrangement.* Vet. J., 2010. **183**(2): p. 148-52.
153. Jebens, E. and M. Monk-Jones, *On the viscosity and pH of synovial fluid and the pH of blood.* J. Bone Jt. Surg. Br. Vol., 1959. **41-B**(2): p. 388-400.
154. Jiang, L., et al., *The relationship between body mass index and hip osteoarthritis: a systematic review and meta-analysis.* Jt., Bone, Spine, 2011. **78**(2): p. 150-5.
155. Oliveria, S., et al., *Body weight, body mass index, and incident symptomatic osteoarthritis of the hand, hip, and knee.* Epidemiology, 1999. **10**(2): p. 161-6.
156. Sowers, M. and C. Karvonen-Gutierrez, *The evolving role of obesity in knee osteoarthritis.* Curr. Opin. Rheumatol., 2010. **22**(5): p. 533-7.
157. de Koning, L., et al., *Waist circumference and waist-to-hip ratio as predictors of cardiovascular events: meta-regression analysis of prospective studies.* Eur. Heart J., 2007. **28**(7): p. 850-6.
158. World_Health_Organization, *Definition, diagnosis and classification of diabetes mellitus and its complications: report of a who consultation.* 1999: Geneva.

159. Lohmander, L., et al., *Incidence of severe knee and hip osteoarthritis in relation to different measures of body mass: a population-based prospective cohort study.* Ann. Rheum. Dis., 2009. **68**(4): p. 490-6.
160. Blagojevic, M., et al., *Risk factors for onset of osteoarthritis of the knee in older adults: a systematic review and meta-analysis.* Osteoarthr. Cartil., 2010. **18**(1): p. 24-33.
161. Holliday, K., et al., *Lifetime body mass index, other anthropometric measures of obesity and risk of knee or hip osteoarthritis in the GOAL case-control study.* Osteoarthr. Cartil., 2011. **19**(1): p. 37-43.
162. Sartori-Cintra, A., P. Aikawa, and D. Cintra, *Obesity versus osteoarthritis: beyond the mechanical overload.* Einstein 2014. **12**(3): p. 374-9.
163. Visser, A., et al., *The relative contribution of mechanical stress and systemic processes in different types of osteoarthritis: the neo study.* Ann. Rheum. Dis., 2015. **74**(10): p. 1842-7.
164. Amin, S., et al., *Quadriceps strength and the risk of cartilage loss and symptom progression in knee osteoarthritis.* Arthritis Rheum., 2009. **60**(1): p. 189-98.
165. Ramage, L., G. Nuki, and D. Salter, *Signalling cascades in mechanotransduction: cell-matrix interactions and mechanical loading.* Scand. J. Med. Sc.i Sports, 2009. **19**(4): p. 457-69.
166. Yusuf, E., et al., *Association between weight or body mass index and hand osteoarthritis: a systematic review.* Ann. Rheum. Dis., 2010. **69**(4): p. 761-5.
167. Kern, P., et al., *Adipose tissue tumor necrosis factor and interleukin-6 expression in human obesity and insulin resistance.* Am. J. Physiol., 2001. **280**(5): p. 745-751.
168. Kershaw, E. and J. Flier, *Adipose tissue as an endocrine organ.* J. Clin. Endocrinol. Metab., 2004. **89**(6): p. 2548-56.
169. Figenschau, Y., et al., *Human articular chondrocytes express functional leptin receptors.* Biochem. Biophys. Res. Commun., 2001. **287**(1): p. 190-7.
170. Simopoulou, T., et al., *Differential expression of leptin and leptin's receptor isoform (Ob-Rb) mRNA between advanced and minimally affected osteoarthritic cartilage; effect on cartilage metabolism.* Osteoarthr. Cartil., 2007. **15**(8): p. 872-883.
171. Tsai, C. and T. Liu, *Osteoarthritis in women: its relationship to estrogen and current trends.* Life Sci., 1992. **50**(23): p. 1737-44.
172. Hussain, S., et al., *Female reproductive and hormonal factors and incidence of primary total knee arthroplasty due to osteoarthritis.* Arthritis Rheumatol., 2018. **70**(7): p. 1022-1029.
173. Kolhe, R., et al., *Gender-specific differential expression of exosomal mirna in synovial fluid of patients with osteoarthritis.* Sci. Rep., 2017. **7**(1): p. 2029-2029.
174. Musumeci, G., M. Szychlinska, and A. Mobasheri, *Age-related degeneration of articular cartilage in the pathogenesis of osteoarthritis: molecular markers of senescent chondrocytes.* Histol. Histopathol., 2015. **30**(1): p. 1-12.
175. Roman-Blas, J., et al., *Osteoarthritis associated with estrogen deficiency.* Arthritis Res. Ther., 2009. **11**(5): p. 241-241.
176. Musumeci, G., et al., *Osteoarthritis in the XXIst century: risk factors and behaviours that influence disease onset and progression.* Int. J. Mol. Sci., 2015. **16**(3): p. 6093-112.

177. Nakayama, Y., et al., *The effects of age and sex on chondroitin sulfates in normal synovial fluid.* Arthritis Rheumatol., 2002. **46**(8): p. 2105-8.
178. Gandhi, R., et al., *The relation between body mass index and waist-hip ratio in knee osteoarthritis.* Can. J. Surg., 2010. **53**(3): p. 151-4.
179. Kalichman, L. and E. Kobyliansky, *Age, body composition, and reproductive indices as predictors of radiographic hand osteoarthritis in Chuvashian women.* Scand. J. Rheumatol., 2007. **36**(1): p. 53-57.
180. Jordan, J., et al., *Prevalence of knee symptoms and radiographic and symptomatic knee osteoarthritis in African Americans and Caucasians: the Johnston County Osteoarthritis Project.* J. Rheumatol., 2007. **34**(1): p. 172-80.
181. Wehling, P., et al., *Effectiveness of intra-articular therapies in osteoarthritis: a literature review.* Ther. Adv. Musculoskeletal Dis., 2017. **9**(8): p. 183-196.
182. Silverstein, F., et al., *Gastrointestinal toxicity with celecoxib vs nonsteroidal anti-inflammatory drugs for osteoarthritis and rheumatoid arthritis: the class study: a randomized controlled trial.* Jama, 2000. **284**(10): p. 1247-1255.
183. Schieszer, J., *Encouraging healthy habits in patients with osteoarthritis.* Drug topics, 2019. **163**(12): p. 16-16.
184. Jordan, K., et al., *The use of conventional and complementary treatments for knee osteoarthritis in the community.* Rheumatology, 2004. **43**(3): p. 381-384.
185. Schencking, M., S. Wilm, and M. Redaelli, *A comparison of Kneipp hydrotherapy with conventional physiotherapy in the treatment of osteoarthritis: a pilot trial.* J. Integr. Med., 2013. **11**(1): p. 17-25.
186. Zochling, J., et al., *Use of complementary medicines for osteoarthritis—a prospective study.* Ann. Rheum. Dis., 2004. **63**(5): p. 549-554.
187. Jamtvedt, G., et al., *Physical therapy interventions for patients with osteoarthritis of the knee: an overview of systematic reviews.* Phys. Ther. , 2008. **88**(1): p. 123-136.
188. Guenther, L., et al., *Biochemical analyses of human osteoarthritic and periprosthetic synovial fluid.* Proc. Inst. Mech. Eng., Part H, 2014.
189. Russo, F., et al., *Platelet rich plasma and hyaluronic acid blend for the treatment of osteoarthritis: rheological and biological evaluation.* PLoS One, 2016. **11**(6).
190. Morgen, M., et al., *Nanoparticles for improved local retention after intra-articular injection into the knee joint.* Pharm. Res., 2013. **30**(1): p. 257-268.
191. Gerwin, N., C. Hops, and A. Lucke, *Intraarticular drug delivery in osteoarthritis.* Adv. Drug Delivery Rev., 2006. **58**(2): p. 226-242.
192. Ruan, M., et al., *Proteoglycan 4 expression protects against the development of osteoarthritis.* Sci. Transl. Med., 2013. **5**(176): p. 176ra34-176ra34.
193. Flannery, C., et al., *Prevention of cartilage degeneration in a rat model of osteoarthritis by intraarticular treatment with recombinant lubricin.* Arthritis & Rheum., 2009. **60**(3): p. 840-847.
194. Larsen, C., et al., *Intra-articular depot formulation principles: role in the management of postoperative pain and arthritic disorders.* J. Pharm. Sci., 2008. **97**(11): p. 4622-4654.
195. Rahimi, M., et al., *Recent developments in natural and synthetic polymeric drug delivery systems used for the treatment of osteoarthritis.* Acta Biomater., 2021.
196. Seo, E., et al., *Tribological changes in the articular cartilage of a human femoral head with avascular necrosis.* Biointerphases, 2015. **10**(2): p. 021004.

197. Schulze, K., et al., *Intraarticular application of superparamagnetic nanoparticles and their uptake by synovial membrane—an experimental study in sheep.* J. Magn. Magn. Mater., 2005. **293**(1): p. 419-432.
198. Gomes, A., et al., *Protection against osteoarthritis in experimental animals by nanogold conjugated snake venom protein toxin gold nanoparticle-naja kaouthia cytotoxin 1.* Indian J. Med. Res., 2016. **144**(6): p. 910.
199. Ratcliffe, J., et al., *Albumin microspheres for intra-articular drug delivery: investigation of their retention in normal and arthritic knee joints of rabbits.* J. Pharm. Pharmacol., 1987. **39**(4): p. 290-295.
200. Chen, Q., et al., *Recent advances in polysaccharides for osteoarthritis therapy.* Eur. J. Med. Chem., 2017. **139**: p. 926-935.
201. Adibnia, V., et al., *Bioinspired polymers for lubrication and wear resistance.* Prog. Polym. Sci., 2020. **110**: p. 101298.
202. Janoušková, O., *Synthetic polymer scaffolds for soft tissue engineering.* Physiol. Res., 2018. **67**.
203. Horisawa, E., et al., *Size-dependency of dl-lactide/glycolide copolymer particulates for intra-articular delivery system on phagocytosis in rat synovium.* Pharm. Res., 2002. **19**(2): p. 132-9.
204. Cetin, M., A. Atila, and Y. Kadioglu, *Formulation and in vitro characterization of Eudragit® l100 and Eudragit® l100-plga nanoparticles containing diclofenac sodium.* AAPS PharmSciTech, 2010. **11**(3): p. 1250-1256.
205. Narayanan, D., et al., *Poly-(ethylene glycol) modified gelatin nanoparticles for sustained delivery of the anti-inflammatory drug Ibuprofen-Sodium: An in vitro and in vivo analysis.* Nanomedicine (N. Y., NY, U. S.), 2013. **9**(6): p. 818-828.
206. Tao, W. and Z. He, *Ros-responsive drug delivery systems for biomedical applications.* Asian J. Pharm. Sci., 2018. **13**(2): p. 101-112.
207. Adibnia, V., et al., *Phytoglycogen nanoparticles: nature-derived superlubricants.* ACS Nano, 2021. **15**(5): p. 8953-8964.
208. Ahmed, E., *Hydrogel: preparation, characterization, and applications: a review.* J. Adv. Res., 2015. **6**(2): p. 105-121.
209. Balakrishnan, B., et al., *Self-crosslinked oxidized alginate/gelatin hydrogel as injectable, adhesive biomimetic scaffolds for cartilage regeneration.* Acta Biomater., 2014. **10**(8): p. 3650-3663.
210. Rong, M., et al., *High lubricity meets load capacity: cartilage mimicking bilayer structure by brushing Up stiff hydrogels from subsurface.* Adv. Funct. Mater., 2020. **30**(39): p. 2004062.
211. Lee, D., et al., *Effects of molecular weight of grafted hyaluronic acid on wear initiation.* Acta Biomater., 2014. **10**(5): p. 1817-1823.
212. Zhang, Z. and G. Huang, *Micro-and nano-carrier mediated intra-articular drug delivery systems for the treatment of osteoarthritis.* J. Nanotechnol., 2012. **2012**.
213. Faivre, J., et al., *Lubrication and wear protection of micro-structured hydrogels using bioinspired fluids.* Biomacromolecules, 2019. **20**(1): p. 326-335.
214. Liu, H., et al., *Cartilage mimics adaptive lubrication.* ACS Appl. Mater. Interfaces, 2020. **12**(45): p. 51114-51121.
215. Feng, H., et al., *Polystyrene nanospheres modified with a hydrophilic polymer brush through subsurface-initiated atom transfer radical polymerization as biolubricating additive.* Macromol. Mater. Eng., 2020. **305**(6): p. 2000135.

216. Tan, X., et al., *Mechanised lubricating silica nanoparticles for on-command cargo release on simulated surfaces of joint cavities.* Chem. Commun., 2019. **55**(18): p. 2593-2596.
217. Chen, H., et al., *Cartilage matrix-inspired biomimetic superlubricated nanospheres for treatment of osteoarthritis.* Biomaterials, 2020. **242**: p. 119931.
218. Liu, G., et al., *Charged polymer brushes-grafted hollow silica nanoparticles as a novel promising material for simultaneous joint lubrication and treatment.* J. Phys. Chem. B, 2014. **118**(18): p. 4920-4931.
219. Yan, Y., et al., *Euryale ferox seed-inspired superlubricated nanoparticles for treatment of osteoarthritis.* Adv. Funct. Mater., 2019. **29**(4): p. 1807559.
220. Liu, G., et al., *Hairy polyelectrolyte brushes-grafted thermosensitive microgels as artificial synovial fluid for simultaneous biomimetic lubrication and arthritis treatment.* ACS Appl. Mater. Interfaces, 2014. **6**(22): p. 20452-20463.
221. Zhao, W., et al., *Light-responsive dual-functional biodegradable mesoporous silica nanoparticles with drug delivery and lubrication enhancement for the treatment of osteoarthritis.* Nanoscale, 2021. **13**(13): p. 6394-6399.
222. Maudens, P., et al., *Self-assembled thermoresponsive nanostructures of hyaluronic acid conjugates for osteoarthritis therapy.* Nanoscale, 2018. **10**(4): p. 1845-1854.
223. Wan, L., et al., *Biodegradable lubricating mesoporous silica nanoparticles for osteoarthritis therapy.* Friction, 2020.
224. Wei, Y., et al., *Factors relating to the biodistribution & clearance of nanoparticles & their effects on in vivo application.* Nanomedicine (London, U. K.), 2018. **13**(12): p. 1495.
225. Yang, L., et al., *Synthesis of charged chitosan nanoparticles as functional biolubricant.* Colloids Surf., B, 2021. **206**: p. 111973.
226. Zhang, K., et al., *Thermo-sensitive dual-functional nanospheres with enhanced lubrication and drug delivery for the treatment of osteoarthritis.* Chemistry, 2020. **26**(46): p. 10564-10574.
227. Ji, X., et al., *Glucosamine sulphate-loaded distearoyl phosphocholine liposomes for osteoarthritis treatment: combination of sustained drug release and improved lubrication.* Biomater. Sci., 2019. **7**(7): p. 2716-2728.
228. Wan, L., et al., *Lubrication and drug release behaviors of mesoporous silica nanoparticles grafted with sulfobetaine-based zwitterionic polymer.* Mater. Sci. Eng. C, 2020. **112**: p. 110886.
229. Han, Y., et al., *Biomimetic injectable hydrogel microspheres with enhanced lubrication and controllable drug release for the treatment of osteoarthritis.* Bioact. Mater., 2021. **6**(10): p. 3596-3607.
230. Yang, J., et al., *Ball-bearing-inspired polyampholyte-modified microspheres as bio-lubricants attenuate osteoarthritis.* Small, 2020. **16**(44): p. e2004519-n/a.
231. Sun, T., Y. Sun, and H. Zhang, *Phospholipid-coated mesoporous silica nanoparticles acting as lubricating drug nanocarriers.* Polymers, 2018. **10**(5): p. 513.
232. Bowen, W. and N. Hilal, *Atomic force microscopy in process engineering: an introduction to afm for improved processes and products*. 2009: Butterworth-Heinemann.
233. Binnig, G., C. Quate, and C. Gerber, *Atomic force microscope.* Phys. Rev. Lett., 1986. **56**(9): p. 930.

234. Reifenberger, R., *Fundamentals of atomic force microscopy: part I: foundations*. 2016: World Scientific Publishing Company Pte. Limited.
235. Yavorskyy, A., et al., *Detection of calcium phosphate crystals in the joint fluid of patients with osteoarthritis - analytical approaches and challenges.* Analyst (Cambridge, U. K.), 2008. **133**(3): p. 302-18.
236. Wen, C., et al., *Collagen fibril stiffening in osteoarthritic cartilage of human beings revealed by atomic force microscopy.* Osteoarthr. Cartil., 2012. **20**(8): p. 916-22.
237. Frederix, P., et al., *Atomic force microscopy of biological samples.* MRS Bull., 2011. **29**(7): p. 449-455.
238. JPK_Instruments, *Nanowizard afm handbook*, in *Version 2.2a*, J.I. AG, Editor. 2012.
239. Liamas, E., et al., *Tribocorrosion behaviour of pure titanium in bovine serum albumin solution: A multiscale study.* J. Mech. Behav. Biomed. Mater., 2020. **102**: p. 103511-103511.
240. Yang, P., et al., *The stepwise process of chromium-induced dna breakage: characterization by electrochemistry, atomic force microscopy, and dna electrophoresis.* Chem. Res. Toxicol., 2005. **18**(10): p. 1563-1566.
241. DS., R., et al., *Characterization of changes to the cell surface during the life cycle of streptomyces coelicolor: atomic force microscopy of living cells.* J. Bacteriol., 2007. **189**(6): p. 2219-2225.
242. Loparic, M., et al., *Micro- and nanomechanical analysis of articular cartilage by indentation-type atomic force microscopy: validation with a gel-microfiber composite.* Biophys. J., 2010. **98**(11): p. 2731-40.
243. Majd, S., et al., *Role of hydrophobicity on the adsorption of synovial fluid proteins and biolubrication of polycarbonate urethanes: materials for permanent meniscus implants.* Mater. Des., 2015. **83**: p. 514-521.
244. Taffetani, M., et al., *Poroelastic response of articular cartilage by nanoindentation creep tests at different characteristic lengths.* Med. Eng. Phys., 2014. **36**(7): p. 850-858.
245. Butt, H., B. Cappella, and M. Kappl, *Force measurements with the atomic force microscope: technique, interpretation and applications.* Surf. Sci. Rep., 2005. **59**(1–6): p. 1-152.
246. Korolkov, V., et al., *Ultra-high resolution imaging of thin films and single strands of polythiophene using atomic force microscopy.* Nat. Commun., 2019. **10**(1): p. 1537.
247. Belikov, S., et al. *Thermal tune method for afm oscillatory resonant imaging in air and liquid*. in *American Control Conference*. 2014. IEEE.
248. Hutter, J. and J. Bechhoefer, *Calibration of atomic-force microscope tips.* Rev. Sci. Instrum., 1993. **64**(7): p. 1868-1873.
249. Park, S., et al., *Mechanical properties of bovine articular cartilage under microscale indentation loading from atomic force microscopy.* Proc. Inst. Mech. Eng., Part H, 2009. **223**(3): p. 339-347.
250. Danalache, M., et al., *Changes in stiffness and biochemical composition of the pericellular matrix as a function of spatial chondrocyte organisation in osteoarthritic cartilage.* Osteoarthr. Cartil., 2019. **27**(5): p. 823-832.
251. J Roa, J., et al., *Calculation of Young's modulus value by means of atomic force microscopy.* Recent Pat. Nanotechnol., 2011. **5**(1): p. 27-36.

252. JPK_Instruments, *Determining the elastic modulus of biological samples using atomic force microscopy*, in *Application Note*. 2014.
253. Airey, J., et al., *The effect of gas turbine lubricant base oil molecular structure on friction.* Tribol. Int., 2020. **146**: p. 106052.
254. Taylor, B. and T. Mills, *Using a three-ball-on-plate configuration for soft tribology applications.* J. Food Eng., 2020. **274**: p. 109838.
255. Timm, K., et al., *Investigation of friction and perceived skin feel after application of suspensions of various cosmetic powders.* Int. J. Cosmet. Sci., 2012. **34**(5): p. 458-465.
256. Kuszewski, H., A. Jaworski, and A. Ustrzycki, *Lubricity of ethanol–diesel blends – study with the HFRR method.* Fuel, 2017. **208**: p. 491-498.
257. Delgado, J., et al., *Hfrr and sl-bocle lubricity of paraffinic diesel fuels considering different origins and final formulations with biodiesels and additives.* Energy Fuels, 2020. **34**(3): p. 2654-2664.
258. Sukjit, E., K.D. Dearn, and A. Tsolakis, *Interrogating the surface: the effect of blended diesel fuels on lubricity.* SAE Int. J. Fuels Lubr., 2012. **5**(1): p. 154-162.
259. Hudedagaddi, C., et al., *Water molecules influence the lubricity of greases and fuel.* Wear, 2017. **376**: p. 831-835.
260. Chiampradit, N., et al., *Study of the effect of gasoline components on lubricity.* Int. J. Automot. Eng., 2017. **8**(4): p. 186-191.
261. Anastopoulos, G., et al., *The impact of fatty acid diisopropanolamides on marine gas oil lubricity.* Lubricants, 2017. **5**(3): p. 28.
262. Accardi, M., D. Dini, and P. Cann, *Experimental and numerical investigation of the behaviour of articular cartilage under shear loading—interstitial fluid pressurisation and lubrication mechanisms.* Tribol. Int., 2011. **44**(5): p. 565-578.
263. PCS-Instruments, *HFRR Brochure*, in *Brochures & Technical documents*, PCS-Instruments, Editor.: London, UK.
264. Shi, X. and Y. Zhao, *Comparison of various adhesion contact theories and the influence of dimensionless load parameter.* J. Adhes. Sci. Technol., 2004. **18**(1): p. 55-68.
265. Johnson, K., *Contact Mechanics*. 1985, Cambridge: Cambridge University Press.
266. Muller, V., V. Yushchenko, and B. Derjaguin, *On the influence of molecular forces on the deformation of an elastic sphere and its sticking to a rigid plane.* J. Colloid Interface Sci., 1980. **77**(1): p. 91-101.
267. O'Rorke, R., T. Steele, and H. Taylor, *Bioinspired fibrillar adhesives: a review of analytical models and experimental evidence for adhesion enhancement by surface patterns.* J. Adhes. Sci. Technol., 2016. **30**(4): p. 362-391.
268. Zhao, Y., L. Wang, and T. Yu, *Mechanics of adhesion in mems—a review.* J. Adhes. Sci. Technol., 2003. **17**(4): p. 519-546.
269. Cappella, B. and G. Dietler, *Force-distance curves by atomic force microscopy.* Surf. Sci. Rep., 1999. **34**(1-3): p. 1-104.
270. Wilson, D., *What is rheology?* Eye, 2018. **32**(2): p. 179-183.
271. Barnes, H., *A handbook of elementary rheology*. Vol. 1. 2000: University of Wales, Institute of Non-Newtonian Fluid Mechanics Aberystwyth.
272. Miri, T., *Viscosity and oscillatory rheology*, in *Practical food rheology: An interpretive approach*. 2011, Wiley-Blackwell: Birmingham, UK. p. 7-28.

273. Malvern_Instruments, *A basic introduction to rheology*, M.I. Limited, Editor. 2016, Malvern Instruments Limited: Worcestershire, UK.
274. Vernengo, J., C. Purdy, and S. Farrell, *Laboratory: undergraduate laboratory experiment teaching fundamental concepts of rheology in context of sickle cell anemia.* Chem. Eng. Educ., 2014. **48**(3): p. 149-156.
275. Bhuanantanondh, P., D. Grecov, and E. Kwok, *Rheological study of viscosupplements and synovial fluid in patients with osteoarthritis.* J. Med. Biol. Eng., 2012. **32**(1): p. 12-16.
276. Lakes, R. and R. Lakes, *Viscoelastic materials*. 2009: Cambridge university press.
277. Chen, T., *Rheological techniques for yield stress analysis*, T. Instruments, Editor., TA Instruments: New Castle, Delaware, USA.
278. Pecora, R., *Dynamic light scattering measurement of nanometer particles in liquids.* J. Nanopart. Res., 2000. **2**(2): p. 123-131.
279. Hassan, P., S. Rana, and G. Verma, *Making sense of brownian motion: colloid characterization by dynamic light scattering.* Langmuir, 2015. **31**(1): p. 3-12.
280. Stetefeld, J., S. McKenna, and T. Patel, *Dynamic light scattering: a practical guide and applications in biomedical sciences.* Biophys. Rev., 2016. **8**(4): p. 409-427.
281. Malvern_Instruments, *Dynamic light scattering: an introduction in 30 minutes.*, in *Technical Note Malvern, MRK656-01*. 2012. p. 1-8.
282. Vaccaro, A., J. Šefčík, and M. Morbidelli, *Characterization of colloidal polymer particles through stability ratio measurements.* Polymer, 2005. **46**(4): p. 1157-1167.
283. Finsy, R., *Particle sizing by quasi-elastic light scattering.* Adv. Colloid Interface Sci., 1994. **52**: p. 79-143.
284. Berne, B. and R. Pecora, *Dynamic light scattering: with applications to chemistry, biology, and physics*. 2000: Courier Corporation.
285. Dong, J., et al., *Intra-articular delivery of liposomal celecoxib-hyaluronate combination for the treatment of osteoarthritis in rabbit model.* Int. J. Pharm., 2013. **441**(1-2): p. 285-290.
286. Park, J., et al., *An injectable, electrostatically interacting drug depot for the treatment of rheumatoid arthritis.* Biomaterials, 2018. **154**: p. 86-98.
287. Zin, V., et al., *Tribological properties of engine oil with carbon nano-horns as nano-additives.* Tribol. Lett., 2014. **55**(1): p. 45-53.
288. Wang, A., et al., *In situ synthesis of copper nanoparticles within ionic liquid-in-vegetable oil microemulsions and their direct use as high efficient nanolubricants.* RSC Adv., 2014. **4**(85): p. 45251-45257.
289. Lee, K., et al., *Performance evaluation of nano-lubricants of fullerene nanoparticles in refrigeration mineral oil.* Curr. Appl. Phys., 2009. **9**(2): p. 128-131.
290. Lee, D., X. Banquy, and J. Israelachvili, *Stick-slip friction and wear of articular joints.* Proc. Natl. Acad. Sci. U. S. A., 2013. **110**(7): p. 567-574.
291. Schiøtz, J. and K. Jacobsen, *A maximum in the strength of nanocrystalline copper.* Science, 2003. **301**(5638): p. 1357-1359.
292. Li, D., *Encyclopedia of microfluidics and nanofluidics*. 2008: Springer Science & Business Media.

293. Morshed, A., H. Wu, and Z. Jiang, *A comprehensive review of water-based nanolubricants.* Lubricants, 2021. **9**(9): p. 89.
294. Bhattacharjee, S., *DLS and zeta potential – what they are and what they are not?* J. Controlled Release, 2016. **235**: p. 337-351.
295. Missana, T. and A. Adell, *On the applicability of dlvo theory to the prediction of clay colloids stability.* J. Colloid Interface Sci., 2000. **230**(1): p. 150-156.
296. Cano-Sarmiento, C., et al., *Zeta potential of food matrices.* Food Eng. Rev., 2018. **10**(3): p. 113-138.
297. Pischon, T., et al., *General and abdominal adiposity and risk of death in Europe.* N. Engl. J. Med., 2008. **359**(20): p. 2105-2120.
298. Gelber, A., *Osteoarthritis.* Ann. Intern. Med., 2014. **161**(1): p. ITC1-1.
299. McCutchen, C., *The frictional properties of animal joints.* Wear, 1962. **5**(1): p. 1-17.
300. Pinchuk, L., *Tribology and biophysics of artificial joints*. 1st ed. ed. Tribology and interface engineering ed. V.I. Nicholaev, E.A. Tsvetkova, and V.A. Goldade. 2006, Amsterdam: Amsterdam : Elsevier.
301. Schurz, J., *Rheology of synovial fluids and substitute polymers.* J. Macromol. Sci., Part A: Pure Appl.Chem., 1996. **33**(9): p. 1249-1262.
302. Fam, H., J. Bryant, and M. Kontopoulou, *Rheological properties of synovial fluids.* Biorheology, 2007. **44**(2): p. 59-74.
303. Meziane, A., B. Bou-Saïd, and J. Tichy, *Modelling human hip joint lubrication subject to walking cycle.* Lubr. Sci., 2008. **20**(3): p. 205-222.
304. Gao, L., D. Dowson, and R. Hewson, *A numerical study of non-Newtonian transient elastohydrodynamic lubrication of metal-on-metal hip prostheses.* Tribol. Int., 2016. **93**: p. 486-494.
305. Marx, N., et al., *Shear thinning and hydrodynamic friction of viscosity modifier-containing oils. Part I: shear thinning behaviour.* Tribol. Lett., 2018. **66**(3): p. 1-14.
306. Tichy, J. and B. Bou-Saïd, *The Phan-Thien and Tanner model applied to thin film spherical coordinates: applications for lubrication of hip joint replacement.* J. Biomech. Eng., 2008. **130**(2).
307. Naduvinamani, N. and G. Savitramma, *Squeeze film lubrication between rough poroelastic rectangular plates with micropolar fluid: a special reference to the study of synovial joint lubrication.* ISRN Tribol., 2013. **2013**: p. 431508.
308. Mathieu, P., et al., *Rheologic behavior of osteoarthritic synovial fluid after addition of hyaluronic acid: a pilot study.* Clin. Orthop. Relat. Res., 2009. **467**(11): p. 3002-3009.
309. Conrozier, T., et al., *Differences in the osteoarthritic synovial fluid composition and rheology between patients with or without flare-up. A pilot study.* Osteoarthr. Cartil., 2012. **20**: p. S244.
310. Mazzucco, D., et al., *Rheology of joint fluid in total knee arthroplasty patients.* J. Orthop. Res., 2002. **20**(6): p. 1157-1163.
311. Galandáková, A., et al., *Characteristics of synovial fluid required for optimization of lubrication fluid for biotribological experiments.* J. Biomed. Mater. Res., Part B, 2017. **105**(6): p. 1422-1431.
312. Fu, J., et al., *Synovial fluid viscosity test is promising for the diagnosis of periprosthetic joint infection.* J. Arthroplasty, 2019. **34**(6): p. 1197-1200.

313. Trivedi, M., et al., *Comparative physicochemical evaluation of biofield treated phosphate buffer saline and hanks balanced salt medium.* Am. J. BioSci., 2015. **6**(3): p. 267-277.
314. Maleki, A., A. Kjøniksen, and B. Nyström, *Anomalous viscosity behavior in aqueous solutions of hyaluronic acid.* Polym. Bull., 2007. **59**(2): p. 217-226.
315. Jin, Z., D. Dowson, and J. Fisher, *Analysis of fluid film lubrication in artificial hip joint replacements with surfaces of high elastic modulus.* Proc. Inst. Mech. Eng., Part H, 1997. **211**(3): p. 247-256.
316. Klein, J., *Molecular mechanisms of synovial joint lubrication.* Proc. Inst. Mech. Eng., Part J, 2006. **220**(8): p. 691-710.
317. Zwartele, R., et al., *Long-term results of cementless primary total hip arthroplasty with a threaded cup and a tapered, rectangular titanium stem in rheumatoid arthritis and osteoarthritis.* Int. Orthop., 2008. **32**(5): p. 581-587.
318. Cooke, A., D. Dowson, and V. Wright, *The rheology of synovial fluid and some potential synthetic lubricants for degenerate synovial joints.* Eng. Med., 1978. **7**(2): p. 66-72.
319. Chhabra, R., *Non-Newtonian fluids: an introduction*, in *Rheology of complex fluids*. 2010, Springer. p. 3-34.
320. Rudraiah, N., S. Kasiviswanathan, and P. Kaloni, *Generalized dispersion in a synovial fluid of human joints.* Biorheology, 1991. **28**(3-4): p. 207-219.
321. Hron, J., et al., *On the modeling of the synovial fluid.* Adv. Tribol., 2010. **2010**: p. 1-12.
322. Pustejovska, P. *Mathematical modeling of synovial fluids flow*. in *Proceedings of the 17th Annual Conference of Doctoral Student*. 2008.
323. Brazel, C. and S. Rosen, *Fundamental principles of polymeric materials*. 3rd ed. 2012, Toronto, Canada: John Wiley & Sons. 298-325.
324. Bhuanantanondh, P., *Rheology of synovial fluid with and without viscosupplements in patients with osteoarthritis; a pilot study*, in *The faculty of graduate studies*. 2009, The University of British Columbia: Vancouver.
325. Balazs, E., et al., *Hyaluronic acid in synovial fluid. I. Molecular parameters of hyaluronic acid in normal and arthritic human fluids.* Arthritis Rheum., 1967. **10**(4): p. 357-376.
326. Ludwig, T., et al., *Diminished cartilage-lubricating ability of human osteoarthritic synovial fluid deficient in proteoglycan 4: Restoration through proteoglycan 4 supplementation.* Arthritis Rheum., 2012. **64**(12): p. 3963-3971.
327. Hornsby, P., *Cellular senescence and tissue aging in vivo.* J. Gerontol., Ser. A, 2002. **57**(7): p. B251-B256.
328. Loeser, R., *Aging and osteoarthritis: the role of chondrocyte senescence and aging changes in the cartilage matrix.* Osteoarthr. Cartil., 2009. **17**(8): p. 971-979.
329. Baranyay, F., et al. *Association of bone marrow lesions with knee structures and risk factors for bone marrow lesions in the knees of clinically healthy, community-based adults*. in *Semin. Arthritis Rheum.* 2007. Elsevier.
330. Woo, S., et al., *Tensile properties of the human femur-anterior cruciate ligament-tibia complex: the effects of specimen age and orientation.* Am. J. Sports Med., 1991. **19**(3): p. 217-225.

331. Fukuta, S., K. Masaki, and F. Korai, *Prevalence of abnormal findings in magnetic resonance images of asymptomatic knees.* J. Orthop. Sci., 2002. **7**(3): p. 287-291.
332. Segal, N., et al., *The longitudinal relationship between thigh muscle mass and the development of knee osteoarthritis.* Osteoarthr. Cartil., 2012. **20**(12): p. 1534-1540.
333. Brooks, Y., et al., *Body mass index and percentage body fat as health indicators for young adults.* Am. J. Health Behav., 2007. **31**(6): p. 687-700.
334. Cimen, O., et al., *Obesity related measurements and joint space width in patients with knee osteoarthritis.* Upsala J. Med. Sci., 2004. **109**(2): p. 159-64.
335. Musumeci, G., et al., *Characterization of apoptosis in articular cartilage derived from the knee joints of patients with osteoarthritis.* Knee Surg. Sports Traumatol. Arthrosc., 2011. **19**(2): p. 307-13.
336. Berenbaum, F., F. Eymard, and X. Houard, *Osteoarthritis, inflammation and obesity.* Curr. Opin. Rheumatol., 2013. **25**(1): p. 114-118.
337. Mundermann, A., C. Dyrby, and T. Andriacchi, *Secondary gait changes in patients with medial compartment knee osteoarthritis: increased load at the ankle, knee, and hip during walking.* Arthritis Rheum., 2005. **52**(9): p. 2835-44.
338. Maly, M., P. Costigan, and S. Olney, *Contribution of psychosocial and mechanical variables to physical performance measures in knee osteoarthritis.* Phys. Ther., 2005. **85**(12): p. 1318-28.
339. Leal, V. and D. Mafra, *Adipokines in obesity.* Clin. Chim. Acta, 2013. **419**: p. 87-94.
340. Hame, S. and R. Alexander, *Knee osteoarthritis in women.* Curr. Rev. Musculoskelet. Med., 2013. **6**(2): p. 182-187.
341. Lawrence, J., J. Bremner, and F. Bier, *Osteo-arthrosis. Prevalence in the population and relationship between symptoms and x-ray changes.* Ann. Rheum. Dis., 1966. **25**(1): p. 1-24.
342. Akhbari, P., et al., *Differences in the composition of hip and knee synovial fluid in osteoarthritis: a nuclear magnetic resonance (NMR) spectroscopy study of metabolic profiles.* Osteoarthr. Cartil., 2019. **27**(12): p. 1768-1777.
343. Wang, X., et al., *The hip stress level analysis for human routine activities.* Biomed. Eng. (Singapore), 2005. **17**(03): p. 153-158.
344. Seedhom, B., *Conditioning of cartilage during normal activities is an important factor in the development of osteoarthritis.* Rheumatology, 2006. **45**(2): p. 146-149.
345. Roba, M., et al., *The adsorption and lubrication behavior of synovial fluid proteins and glycoproteins on the bearing-surface materials of hip replacements.* Biomaterials, 2009. **30**(11): p. 2072-2078.
346. Nečas, D., et al., *In situ observation of lubricant film formation in THR considering real conformity: the effect of model synovial fluid composition.* Tribol. Int., 2018. **117**: p. 206-216.
347. Wu, B., et al., *Characterization of adsorption and lubrication of synovial fluid proteins and HA on DLC joint bearings surface.* Surf. Coat. Technol., 2017. **320**: p. 320-332.
348. Leonardi, R., et al., *Lubricin in synovial fluid of mild and severe temporomandibular joint internal derangements.* Med. Oral Patol. Oral Cir. Bucal., 2016. **21**(6).

349. Loeser, R., et al., *Microarray analysis reveals age-related differences in gene expression during the development of osteoarthritis in mice.* Arthritis Rheum., 2012. **64**(3): p. 705-717.
350. Mustonen, A., et al., *Distinct fatty acid signatures in infrapatellar fat pad and synovial fluid of patients with osteoarthritis versus rheumatoid arthritis.* Arthritis Res. Ther., 2019. **21**(1): p. 124.
351. Van de Vyver, A., et al., *Synovial fluid fatty acid profiles differ between osteoarthritis and healthy patients.* Cartilage, 2020. **11**(4): p. 473-478.
352. Trunfio-Sfarghiu, A., et al., *Role of Nanomechanical Properties in the Tribological Performance of Phospholipid Biomimetic Surfaces.* Langmuir, 2008. **24**(16): p. 8765-8771.
353. Caballero, A., et al., *Overweight Latino children and adolescents have marked endothelial dysfunction and subclinical vascular inflammation in association with excess body fat and insulin resistance.* Diabetes care, 2008. **31**(3): p. 576-582.
354. Glowinska, B., et al., *Soluble adhesion molecules (sICAM-1, sVCAM-1) and selectins (sE selectin, sP selectin, sL selectin) levels in children and adolescents with obesity, hypertension, and diabetes.* Metabolism, 2005. **54**(8): p. 1020-1026.
355. Young, A., et al., *Proteoglycan 4 downregulation in a sheep meniscectomy model of early osteoarthritis.* Arthritis Res. Ther., 2006. **8**(2): p. 1-6.
356. Rogers, B., et al., *Topographical variation in glycosaminoglycan content in human articular cartilage.* J. Bone Joint Surg. Br., 2006. **88**(12): p. 1670-1674.
357. Froimson, M., et al., *Differences in patellofemoral joint cartilage material properties and their significance to the etiology of cartilage surface fibrillation.* Osteoarthr. Cartil., 1997. **5**(6): p. 377-86.
358. Israelachvili, J., Y. Chen, and H. Yoshizawa, *Relationship between adhesion and friction forces*, in *Fundamentals of adhesion and interfaces*. 2020, De Gruyter. p. 261-280.
359. Lawrence, A., et al., *Synthesis and characterization of a lubricin mimic (mLub) to reduce friction and adhesion on the articular cartilage surface.* Biomaterials, 2015. **73**: p. 42-50.
360. Chan, S., et al., *The role of lubricant entrapment at biological interfaces: reduction of friction and adhesion in articular cartilage.* J. Biomech., 2011. **44**(11): p. 2015-2020.
361. Brandt, K., *The role of analgesics in the management of osteoarthritis pain.* Am. J. Ther., 2000. **7**(2): p. 75-90.
362. Wang, N., et al., *High-efficient and environmental-friendly PTFE@ SiO2 core-shell additive with excellent aw/ep properties in PAO6.* Tribol. Int., 2021. **158**: p. 106930.
363. Chen, H., et al., *Synthesis of core–shell micro/nanoparticles and their tribological application: a review.* Materials, 2020. **13**(20).
364. Nasser, K., et al., *Synergistic effects of hexagonal boron nitride nanoparticles and phosphonium ionic liquids as hybrid lubricant additives.* J. Mol. Liq., 2020. **311**: p. 113343.
365. Beheshti, A., et al., *Improving tribological properties of oil-based lubricants using hybrid colloidal additives.* Tribol. Int., 2020. **144**: p. 106130.

366. Myant, C., H. Spikes, and J. Stokes, *Influence of load and elastic properties on the rolling and sliding friction of lubricated compliant contacts.* Tribol. Int., 2010. **43**(1-2): p. 55-63.
367. Asrul, M., et al., *Tribological properties and lubricant mechanism of nanoparticle in engine oil.* Procedia Eng., 2013. **68**: p. 320-325.
368. Gara, L. and Q. Zou, *Friction and wear characteristics of water-based ZnO and Al2O3 nanofluids.* Tribol. Trans., 2012. **55**(3): p. 345-350.
369. Smith, A., et al., *Development of a synovial fluid analogue with bio-relevant rheology for wear testing of orthopaedic implants.* J. Mech. Behav. Biomed. Mater., 2014. **32**: p. 177-184.
370. *Silica - Silicon Dioxide (SiO2)*. 2001 [cited 2021 06/04/2021]; Available from: https://www.azom.com/article.aspx?ArticleID=1114.
371. *PECVD Silicon Dioxide*. [cited 2021 06/04/2021]; Available from: http://www.mit.edu/~6.777/matprops/pecvd_sio2.htm.
372. *Silica Safety Data Sheet*, Merck, Editor. 2020: USA.
373. Lee, Y., et al., *Investigations on indentation size effects using a pile-up corrected hardness.* J. Phys. D: Appl. Phys., 2008. **41**(7): p. 074027.
374. Burrell, H. and B. Immergut, *Polymer Handbook*. 2nd ed. Vol. IV. 1975, New York: John Wiley.
375. *Polystyrene uniform latex particles Safety Data Sheet*, A. Scientific, Editor. 2014: UK.
376. Worzakowska, M., *Thermal and mechanical properties of polystyrene modified with esters derivatives of 3-phenylprop-2-en-1-ol.* J. Therm. Anal. Calorim., 2015. **121**(1): p. 235-243.
377. Wang, M. and C. Yu, *Silicone rubber: an alternative for repair of articular cartilage defects.* Knee Surg. Sports Traumatol. Arthrosc., 2004. **12**(6): p. 556-561.
378. Buford, A. and T. Goswami, *Review of wear mechanisms in hip implants: paper I–general.* Mater. Des., 2004. **25**(5): p. 385-393.
379. Rahaman, M., et al., *Bioactive glass in tissue engineering.* Acta Biomater., 2011. **7**(6): p. 2355-2373.
380. Gibon, E., et al., *The biological response to orthopaedic implants for joint replacement: part I: metals.* J. Biomed. Mater. Res. Part B Appl. Biomater., 2017. **105**(7): p. 2162-2173.
381. Vidal-Lesso, A., et al., *Mechanical characterization of femoral cartilage under unicompartimental osteoarthritis.* Ingeniería mecánica, tecnología y desarrollo, 2014. **4**(6): p. 239-246.
382. Stolz, M., et al., *Dynamic elastic modulus of porcine articular cartilage determined at two different levels of tissue organization by indentation-type Atomic Force Microscopy.* Biophys. J., 2004. **86**(5): p. 3269-3283.
383. Thambyah, A., A. Nather, and J. Goh, *Mechanical properties of articular cartilage covered by the meniscus.* Osteoarthr. Cartil., 2006. **14**(6): p. 580-588.
384. Ghosh, S., et al., *Investigation of techniques for the measurement of articular cartilage surface roughness.* Micron, 2013. **44**: p. 179-184.
385. Juras, V., et al., *In vitro determination of biomechanical properties of human articular cartilage in osteoarthritis using multi-parametric MRI.* J. Magn. Reson., 2009. **197**(1): p. 40-47.

386. Peters, A., et al., *The effect of ageing and osteoarthritis on the mechanical properties of cartilage and bone in the human knee joint.* Sci. Rep., 2018. **8**(1): p. 1-13.
387. Gardner-Morse, M., et al., *In situ microindentation for determining local subchondral bone compressive modulus.* J. Biomech. Eng., 2010. **132**(9).
388. Mills, T., *Development of in-vitro mouth methods for studying oral phenomena*, in *School of Chemical Engineering*. 2011, University of Birmingham: Birmingham, Uk.
389. TTV_GmbH. *Float glass, clear 1000*. Materials Technical Data Sheet 2009 [cited 2021 02 November 2021]; Available from: https://www.go-ttv.com/materials/glass/floatglass/.
390. Dowson, D., et al., *Tribological Research and Design for Engineering Systems: Proceedings of the 29th Leeds-Lyon Symposium*. 2003: Elsevier.
391. de Vicente, J., J. Stokes, and H. Spikes, *Soft lubrication of model hydrocolloids.* Food Hydrocolloids, 2006. **20**(4): p. 483-491.
392. Röchling_Engineering_Plastics, *Polystone® M (UHMW-PE) Semi-Finished Thermoplastics*. 2015.
393. Mantripragada, V., et al., *An overview of recent advances in designing orthopedic and craniofacial implants.* J. Biomed. Mater. Res. A, 2013. **101**(11): p. 3349-64.
394. Dante, R., *8 - Abrasives, ceramic, and inorganic materials*, in *Handbook of friction materials and their applications*, R. Dante, Editor. 2016, Woodhead Publishing: Boston. p. 105-121.
395. Epstein, M., et al., *The safety of metal-on-metal joint replacements with a particular focus on hip implants*. 2014, Scientific Committee on Emerging and Newly Identified Health Risks: Luxembourg.
396. Beigmoradi, R., A. Samimi, and D. Mohebbi-Kalhori, *Controllability of the hydrophilic or hydrophobic behavior of the modified polysulfone electrospun nanofiber mats.* Polym. Test., 2021. **93**: p. 106970.
397. Luo, S. and C. Wong, *IEEE Trans. Compon. Packag. Technol.* IEEE Transactions on components and packaging technologies, 2001. **24**(1): p. 43-49.
398. Coulter, B., *Dynamic light scattering detection for accurately sizing small surfactant micelles.* 2013, AZO materials.
399. Tsai, T., et al., *Effect of viscosity of base fluid on thermal conductivity of nanofluids.* Appl. Phys. Lett., 2008. **93**(23): p. 233121.
400. Watthanaphanit, A., G. Panomsuwan, and N. Saito, *A novel one-step synthesis of gold nanoparticles in an alginate gel matrix by solution plasma sputtering.* RSC Adv., 2014. **4**(4): p. 1622-1629.
401. Torres, O., et al., *Gellan gum: a new member in the dysphagia thickener family.* Biotribology, 2019. **17**: p. 8-18.
402. Lee, K. and D. Mooney, *Alginate: properties and biomedical applications.* Prog. Polym. Sci., 2012. **37**(1): p. 106-126.
403. Picone, C. and R. Cunha, *Influence of pH on formation and properties of gellan gels.* Carbohydr. Polym., 2011. **84**(1): p. 662-668.
404. Hasan, F. and D. Huang, *Characterization of colloidal silica and its adsorption phenomenon with silicon-base surfactants with relation to film strength.* J. Colloid Interface Sci., 1997. **190**(1): p. 161-170.

405. Adamczyk, Z., M. Nattich, and M. Wasilewska, *Irreversible adsorption of latex particles on fibrinogen covered mica.* Adsorption, 2010. **16**(4): p. 259-269.
406. Mishra, P., et al., *A brief review on viscosity of nanofluids.* Int. Nano Lett., 2014. **4**(4): p. 109-120.
407. Yalçın, T., et al., *The viscosity and zeta potential of bentonite dispersions in presence of anionic surfactants.* Mater. Lett., 2002. **57**(2): p. 420-424.
408. Chen, H., Y. Ding, and C. Tan, *Rheological behaviour of nanofluids.* New J. Phys., 2007. **9**(10): p. 367.
409. Bongaerts, J., K. Fourtouni, and J. Stokes, *Soft-tribology: lubrication in a compliant pdms–pdms contact.* Tribol. Int., 2007. **40**(10-12): p. 1531-1542.
410. Hwang, Y., et al., *Effect of the size and morphology of particles dispersed in nano-oil on friction performance between rotating discs.* J. Mech. Sci. Technol., 2011. **25**(11): p. 2853-2857.
411. Azman, S., et al., *Study of tribological properties of lubricating oil blend added with graphene nanoplatelets.* J. Mater. Res., 2016. **31**(13): p. 1932-1938.
412. Hamrock, B., B. Schmid, and B. Jacobson, *Fundamentals of fluid film lubrication*. Vol. 169. 2004: CRC press.
413. Gan, B., *Using machine learning algorithms to analyse data pertaining to osteoarthritis*, in *School of Computer Science*. 2019, University of Birmingham: Birmingham, UK.
414. Chen, D., et al., *Osteoarthritis: toward a comprehensive understanding of pathological mechanism.* Bone Res., 2017. **5**: p. 16044-16044.
415. Zhang, Q., et al., *Neutrophil membrane-coated nanoparticles inhibit synovial inflammation and alleviate joint damage in inflammatory arthritis.* Nat. Nanotechnol., 2018. **13**(12): p. 1182-1190.
416. Kang, C., et al., *Acid-activatable polymeric curcumin nanoparticles as therapeutic agents for osteoarthritis.* Nanomedicine (N. Y., NY, U. S.), 2020. **23**: p. 102104.
417. Liggins, R., et al., *Intra-articular treatment of arthritis with microsphere formulations of paclitaxel: biocompatibility and efficacy determinations in rabbits.* Inflammation Res., 2004. **53**(8): p. 363-72.
418. Bettencourt, A. and A. Almeida, *Poly(methyl methacrylate) particulate carriers in drug delivery.* J. Microencapsulation, 2012. **29**(4): p. 353-67.
419. Food_and_Drug_Administration, *Class II Special Controls Guidance Document: Polymethylmethacrylate (PMMA) Bone Cement - Guidance for Industry and FDA*, in *668*, F.a.D. Administration, Editor. 2002, Food and Drug Administration: U.S.A.
420. Tyler, B., et al., *Polylactic acid (PLA) controlled delivery carriers for biomedical applications.* Adv. Drug Delivery Rev., 2016. **107**: p. 163-175.
421. Malikmammadov, E., et al., *PCL and PCL-based materials in biomedical applications.* J. Biomater. Sci., Polym. Ed., 2018. **29**(7-9): p. 863-893.
422. Ulery, B., L. Nair, and C. Laurencin, *Biomedical applications of biodegradable polymers.* J. Polym. Sci. B Polym. Phys., 2011. **49**(12): p. 832-864.
423. Balos, S., et al., *Modulus of elasticity, flexural strength and biocompatibility of poly(methyl methacrylate) resins with low addition of nanosilica.* Research & Reviews: J. Dent. Sci., 2016. **4**(1): p. 26-33.
424. Park, S., M. Chao, and P. Raj, *Mechanical properties of surface-charged poly (methyl methacrylate) as denture resins.* Int. J. Dent., 2009. **2009**.

425. Tröster, S. and J. Kreuter, *Influence of the surface properties of low contact angle surfactants on the body distribution of 14C-poly (methyl methacrylate) nanoparticles.* J. Microencapsulation, 1992. **9**(1): p. 19-28.
426. Holmes, R., R. Burford, and C. Bertram, *Preparation and characterization of poly(methyl methacrylate) beads.* J. Appl. Polym. Sci., 2008. **109**(3): p. 1814-1822.
427. Spasojevic, P., et al., *The mechanical properties of a poly (methyl methacrylate) denture base material modified with dimethyl itaconate and di-n-butyl itaconate.* Int. J. Polym. Sci., 2015. **2015**.
428. Dziadek, M., et al., *New generation poly (ε-caprolactone)/gel-derived bioactive glass composites for bone tissue engineering: Part I. Material properties.* Mater. Sci. Eng. C, 2015. **56**: p. 9-21.
429. Chen, B. and K. Sun, *Poly (ε-caprolactone)/hydroxyapatite composites: effects of particle size, molecular weight distribution and irradiation on interfacial interaction and properties.* Polym. Test., 2005. **24**(1): p. 64-70.
430. Tamjid, E., et al., *Effect of particle size on the in vitro bioactivity, hydrophilicity and mechanical properties of bioactive glass-reinforced polycaprolactone composites.* Mater. Sci. Eng. C, 2011. **31**(7): p. 1526-1533.
431. Salmoria, G., et al., *The effects of laser energy density and particle size in the selective laser sintering of polycaprolactone/progesterone specimens: morphology and drug release.* Int. J. Adv. Manuf. Technol., 2013. **66**(5-8): p. 1113-1118.
432. Rudnik, E., *Compostable polymer materials*. 2010: Elsevier.
433. Kasuga, T., et al., *Preparation and mechanical properties of polylactic acid composites containing hydroxyapatite fibers.* Biomaterials, 2000. **22**(1): p. 19-23.
434. Mathew, A., K. Oksman, and M. Sain, *Mechanical properties of biodegradable composites from poly lactic acid (PLA) and microcrystalline cellulose (MCC).* J. Appl. Polym. Sci., 2005. **97**(5): p. 2014-2025.
435. Ouyang, P., et al., *Fabrication of hydrophilic paclitaxel-loaded pla-peg-pla microparticles via seds process.* Front. Mater. Sci. China, 2009. **3**(1): p. 15-24.
436. Farah, S., D. Anderson, and R. Langer, *Physical and mechanical properties of pla, and their functions in widespread applications—a comprehensive review.* Adv. Drug Delivery Rev., 2016. **107**: p. 367-392.
437. Ferri, J., et al., *Poly (lactic acid) formulations with improved toughness by physical blending with thermoplastic starch.* J. Appl. Polym. Sci., 2018. **135**(4): p. 45751.
438. Dunkers, J., M. Cicerone, and N. Washburn, *Collinear optical coherence and confocal fluorescence microscopies for tissue engineering.* Opt. Express, 2003. **11**(23): p. 3074-9.
439. Goncalves, C., J. Coutinho, and I. Marrucho, *Optical Properties*, in *Poly(Lactic Acid): Synthesis, Structures, Properties, Processing, and Applications*, R. Auras, et al., Editors. 2010.
440. El-kharrag, R., A. Amin, and Y. Greish, *Synthesis and characterization of mesoporous sodium dodecyl sulfate-coated magnetite nanoparticles.* J. Ceram. Sci. Tech., 2011. **2**(4): p. 203-210.
441. Necas, J., et al., *Hyaluronic acid (hyaluronan): a review.* Vet. Med., 2008. **53**(8): p. 397-411.

442. Ye, X., et al., *Depletion interactions in colloid-polymer mixtures.* Phys. Rev. E, 1996. **54**(6): p. 6500.
443. Fallacara, A., et al., *Hyaluronic acid in the third millennium.* Polymers, 2018. **10**(7): p. 701.
444. Georgiev, G., et al., *Surface chemistry study of the interactions of hyaluronic acid and benzalkonium chloride with meibomian and corneal cell lipids.* Soft Matter, 2013. **9**(45): p. 10841-10856.
445. Sahu, A., P. Solanki, and S. Mitra, *Curcuminoid-loaded poly (methyl methacrylate) nanoparticles for cancer therapy.* Int. J. Nanomed., 2018. **13**: p. 101.
446. Hendrick, E. and M. Frey, *Increasing surface hydrophilicity in poly(lactic acid) electrospun fibers by addition of pla-b-peg co-polymers.* J. Eng. Fibers Fabr., 2014. **9**(2): p. 153-164.
447. Rosen, M. and J. Kunjappu, *Surfactants and interfacial phenomena*. 2012: John Wiley & Sons.
448. McClements, D., *Food emulsions: principles, practices, and techniques*. 2015: CRC Press.
449. Pancharoen, M., *Physical properties of associative polymer solutions*, in *Energy Resources Engineering*. 2009, Stanford University: California, USA.
450. De Vicente, J., J. Stokes, and H. Spikes, *Lubrication properties of non-adsorbing polymer solutions in soft elastohydrodynamic (EHD) contacts.* Tribol. Int., 2005. **38**(5): p. 515-526.
451. Rudyak, V., *Viscosity of nanofluids. Why it is not described by the classical theories.* Adv. Nanopart., 2013. **2**(03): p. 266.
452. Haward, S., et al., *Extensional flow of hyaluronic acid solutions in an optimized microfluidic cross-slot device.* Biomicrofluidics, 2013. **7**(4).
453. Huang, R., G. Moon, and R. Pal, *Chitosan/anionic surfactant complex membranes for the pervaporation separation of methanol/mtbe and characterization of the polymer/surfactant system.* J. Membr. Sci., 2001. **184**(1): p. 1-15.
454. Thomas, S. and C. Sobhan, *A review of experimental investigations on thermal phenomena in nanofluids.* Nanoscale Res. Lett., 2011. **6**(1): p. 377.
455. Sulek, M., T. Wasilewski, and K. Kurzydłowski, *The effect of concentration on lubricating properties of aqueous solutions of sodium lauryl sulfate and ethoxylated sodium lauryl sulfate.* Tribol. Lett., 2010. **40**(3): p. 337-345.
456. Zhang, J. and Y. Meng, *Stick–slip friction of stainless steel in sodium dodecyl sulfate aqueous solution in the boundary lubrication regime.* Tribol. Lett., 2014. **56**(3): p. 543-552.
457. Shimizu, Y. and H. Spikes, *The influence of slide–roll ratio on zddp tribofilm formation.* Tribol. Lett., 2016. **64**(2): p. 19.
458. Kamada, K., et al., *Surfactant-induced friction reduction for hydrogels in the boundary lubrication regime.* J. Phys.: Condens. Matter, 2011. **23**(28): p. 284107.
459. Hachiya, K. and T. Nitta, *Relationship between friction coefficient, viscosity and compressibility of polyethylene glycol.* Tribol. Online, 2008. **3**(2): p. 70-75.
460. Kang, M. and G. Im, *Drug delivery systems for intra-articular treatment of osteoarthritis.* Expert Opin. Drug Delivery, 2014. **11**(2): p. 269-82.

461. Wieland, H., et al., *Osteoarthritis - an untreatable disease?* Nat. Rev. Drug Discovery, 2005. **4**(4): p. 331-44.
462. Larsen, C., et al., *Intra-articular depot formulation principles: role in the management of postoperative pain and arthritic disorders.* J. Pharm. Sci., 2008. **97**(11): p. 4622-54.
463. Guo, Y., Z. Hao, and C. Wan, *Tribological characteristics of polyvinylpyrrolidone (pvp) as a lubrication additive for artificial knee joint.* Tribol. Int., 2016. **93**: p. 214-219.
464. Larson, K., et al., *Reduction of friction by recombinant human proteoglycan 4 in il-1alpha stimulated bovine cartilage explants.* J. Orthop. Res., 2017. **35**(3): p. 580-589.
465. Shirani, A., et al., *Nanodiamonds for improving lubrication of titanium surfaces in simulated body fluid.* Carbon, 2019. **143**: p. 890-896.
466. Permatasari, D., et al., *Quercetin prevent proteoglycan destruction by inhibits matrix metalloproteinase-9, matrix metalloproteinase-13, a disintegrin and metalloproteinase with thrombospondin motifs-5 expressions on osteoarthritis model rats.* J. Adv. Pharm. Technol. Res., 2019. **10**(1): p. 2-8.
467. Shi, D., et al., *Photo-cross-linked scaffold with kartogenin-encapsulated nanoparticles for cartilage regeneration.* ACS Nano, 2016. **10**(1): p. 1292-9.
468. Saeedi, T., H. Alotaibi, and P. Prokopovich, *Polymer colloids as drug delivery systems for the treatment of arthritis.* Adv. Colloid Interface Sci., 2020: p. 102273.
469. Liu, G., et al., *Magnetite-loaded thermosensitive nanogels for bioinspired lubrication and multimodal friction control.* ACS Macro Lett., 2016. **5**(1): p. 144-148.
470. Clemett, D. and K. Goa, *Celecoxib: a review of its use in osteoarthritis, rheumatoid arthritis and acute pain.* Drugs, 2000. **59**(4): p. 957-80.
471. Zweers, M., et al., *Celecoxib: considerations regarding its potential disease-modifying properties in osteoarthritis.* Arthritis Res. Ther., 2011. **13**(5): p. 239.
472. Park, S., et al., *Cartilage mechanical response under dynamic compression at physiological stress levels following collagenase digestion.* Ann. Biomed. Eng., 2008. **36**(3): p. 425-34.
473. Huang, X., et al., *A practical model of quartz crystal microbalance in actual applications.* Sensors, 2017. **17**(8).
474. openQCM. *Quartz specs*. [cited 2019 25/06]; Available from: https://openqcm.com/openqcm-next-tech-specs.
475. Cooke, M., et al., *Matrix degradation in osteoarthritis primes the superficial region of cartilage for mechanical damage.* Acta Biomater., 2018. **78**: p. 320-328.
476. Curtis, C., et al., *A comparative study of the nanoscale and macroscale tribological attributes of alumina and stainless steel surfaces immersed in aqueous suspensions of positively or negatively charged nanodiamonds.* Beilstein J. Nanotechnol., 2017. **8**: p. 2045-2059.
477. Ünal, H., *15 - Antibiofilm coatings*, in *Handbook of antimicrobial coatings*, A. Tiwari, Editor. 2018, Elsevier. p. 301-319.
478. Goda, T., et al., *Protein adsorption resistance and oxygen permeability of chemically crosslinked phospholipid polymer hydrogel for ophthalmologic biomaterials.* J. Biomed. Mater. Res., Part B, 2009. **89**(1): p. 184-190.

479. Riley, J. and R. Tilton, *Sequential adsorption of nanoparticulate polymer brushes as a strategy to control adhesion and friction.* Langmuir, 2016. **32**(44): p. 11440-11447.
480. Acharya, B., et al., *Nanotribological performance factors for aqueous suspensions of oxide nanoparticles and their relation to macroscale lubricity.* Lubricants, 2019. **7**(6): p. 49.
481. Kumar, N., et al., *One-pot synthesis and first-principles elasticity analysis of polymorphic MnO2 nanorods for tribological assessment as friction modifiers.* RSC Adv., 2017. **7**(54): p. 34138-34148.
482. Koshy, C., P. Rajendrakumar, and M. Thottackkad, *Evaluation of the tribological and thermo-physical properties of coconut oil added with MoS2 nanoparticles at elevated temperatures.* Wear, 2015. **330-331**: p. 288-308.
483. Trivedi, K., K. Parekh, and R. Upadhyay, *Nanolubricant: magnetic nanoparticle based.* Mater. Res. Express, 2017. **4**(11): p. 114003.
484. Ramakrishna, S., et al., *Controlling adhesion force by means of nanoscale surface roughness.* Langmuir, 2011. **27**(16): p. 9972-9978.
485. Ramakrishna, S., et al., *Study of adhesion and friction properties on a nanoparticle gradient surface: transition from JKR to DMT contact mechanics.* Langmuir, 2013. **29**(1): p. 175-182.
486. Wang, X., et al., *Investigations on the mechanical properties of conducting polymer coating-substrate structures and their influencing factors.* Int. J. Mol. Sci., 2009. **10**(12): p. 5257-5284.
487. Wan, C. and S. Gorb, *Friction reduction mechanism of the cuticle surface in the sandhopper talitrus saltator (Amphipoda, talitridae).* Acta Biomater., 2020. **101**: p. 414-421.
488. Kim, K., et al., *An injectable, click-cross-linked small intestinal submucosa drug depot for the treatment of rheumatoid arthritis.* Adv. Healthcare Mater., 2016. **5**(24): p. 3105-3117.
489. Ujhelyi, Z., et al., *Evaluation of cytotoxicity of surfactants used in self-micro emulsifying drug delivery systems and their effects on paracellular transport in Caco-2 cell monolayer.* Eur. J. Pharm. Sci., 2012. **47**(3): p. 564-73.
490. Gratzer, P., R. Harrison, and T. Woods, *Matrix alteration and not residual sodium dodecyl sulfate cytotoxicity affects the cellular repopulation of a decellularized matrix.* Tissue Eng., 2006. **12**(10): p. 2975-83.
491. Dong, L., et al., *Cytotoxicity of single-walled carbon nanotubes suspended in various surfactants.* Nanotechnol., 2008. **19**(25): p. 255702.
492. da Luz, C., et al., *Poly-lactic acid nanoparticles (PLA-NP) promote physiological modifications in lung epithelial cells and are internalized by clathrin-coated pits and lipid rafts.* J. Nanobiotechnol., 2017. **15**(1): p. 11-11.
493. Bulcão, R., et al., *Acute and subchronic toxicity evaluation of poly(ε-caprolactone) lipid-core nanocapsules in rats.* Toxicol. Sci., 2012. **132**(1): p. 162-176.
494. Changerath, R., et al., *Poly(methyl methacrylate)-grafted chitosan microspheres for controlled release of ampicillin.* J. Biomed. Mater. Res., Part B, 2009. **89**(1): p. 65-76.
495. Dhana Lekshmi, U., et al., *In vitro characterization and invivo toxicity study of repaglinide loaded poly (methyl methacrylate) nanoparticles.* Int. J. Pharm., 2010. **396**(1-2): p. 194-203.

496. Hashemipour, M., et al., *In vitro cytotoxic effects of celecoxib, mefenamic acid, aspirin and indometacin on several cells lines.* J. Dent. (Shiraz, Islamic Repub. Iran), 2016. **17**(3): p. 219-225.
497. Lu, Y., et al., *Celecoxib suppresses autophagy and enhances cytotoxicity of imatinib in imatinib-resistant chronic myeloid leukemia cells.* J. Transl. Med., 2016. **14**: p. 270-270.
498. Zafarvahedian, E., et al., *Effect of metformin and celecoxib on cytotoxicity and release of GDF-15 from human mesenchymal stem cells in high glucose condition.* Cell Biochem. Funct., 2017. **35**(7): p. 407-413.
499. Hossen, S., et al., *Smart nanocarrier-based drug delivery systems for cancer therapy and toxicity studies: a review.* J. Adv. Res., 2018. **15**: p. 1-18.
500. Feng, M. and P. Li, *Amine-containing core-shell nanoparticles as potential drug carriers for intracellular delivery.* J. Biomed. Mater. Res., Part A, 2007. **80**(1): p. 184-93.
501. Streubel, A., J. Siepmann, and R. Bodmeier, *Multiple unit gastroretentive drug delivery systems: a new preparation method for low density microparticles.* J. Microencapsulation, 2003. **20**(3): p. 329-47.
502. Chiesa, E., et al., *Hyaluronic acid-decorated chitosan nanoparticles for CD44-targeted delivery of everolimus.* Int. J. Mol. Sci., 2018. **19**(8).
503. Gamarra, A., et al., *Comblike ionic complexes of hyaluronic acid and alkanoylcholine surfactants as a platform for drug delivery systems.* Biomacromolecules, 2018. **19**(9): p. 3669-3681.
504. Chen, Z., et al., *Development of brucine-loaded microsphere/thermally responsive hydrogel combination system for intra-articular administration.* J. Controlled Release, 2012. **162**(3): p. 628-35.
505. Thakkar, H., R. Kumar Sharma, and R. Murthy, *Enhanced retention of celecoxib-loaded solid lipid nanoparticles after intra-articular administration.* Drugs R. D., 2007. **8**(5): p. 275-85.
506. Bruce, C., et al., *Molecular dynamics simulation of sodium dodecyl sulfate micelle in water: micellar structural characteristics and counterion distribution.* J. Phys. Chem. B, 2002. **106**(15): p. 3788-3793.
507. Azmi, W., et al., *Experimental determination of turbulent forced convection heat transfer and friction factor with SiO2 nanofluid.* Exp. Therm. Fluid Sci., 2013. **51**: p. 103-111.
508. Wang, Z., S. Nania, and S. Shaw, *Structure of aqueous water films on textured−OH-terminated self-assembled monolayers.* Langmuir, 2015. **31**(8): p. 2382-2389.